

**Long-baseline laser interferometry for the detection of  
binary black-hole mergers**

Thesis by  
**Evan D. Hall**

In Partial Fulfillment of the Requirements for the  
degree of  
**Doctor of Philosophy**

CALIFORNIA INSTITUTE OF TECHNOLOGY  
Pasadena, California

2017  
(Defended 14 November 2016)

© 2017

Evan D. Hall  
ORCID: 0000–0001–9018–666X

All rights reserved except where otherwise noted

# Abstract

Late in 2015, gravitational physics reached a watershed moment with the first direct detections of gravitational waves. Two events, each from the coalescence of a binary black hole system, were detected by the Laser Interferometer Gravitational-wave Observatory (LIGO). At present, LIGO comprises two 4 km laser interferometers, one in Washington and the other in Louisiana; a third detector is planned to be installed in India. These interferometers, known as Advanced LIGO, belong to the so-called “second generation” of gravitational-wave detectors. Compared to the first-generation LIGO detectors (Initial and Enhanced LIGO), these instruments use multi-stage active seismic isolation, heavier and higher-quality mirrors, and more laser power to achieve an unprecedented sensitivity to gravitational waves. In 2015, both Advanced LIGO detectors achieved a strain sensitivity better than  $10^{-23}/\text{Hz}^{1/2}$  at a few hundred hertz; ultimately, these detectors are designed to achieve a sensitivity of a few parts in  $10^{-24}/\text{Hz}^{1/2}$  at a few hundred hertz.

This thesis covers several topics in gravitational physics and laser interferometry. First, it presents the design, control scheme, and noise performance of the Advanced LIGO detector in Washington during the first observing run (O1). Second, it discusses some issues relating to interferometer calibration, and the impact of calibration errors on astrophysical parameter estimation. Third, it discusses the prospects for using terrestrial and space-based laser interferometers as dark matter detectors.

This thesis has the internal LIGO document number [P1600295](#).

## Acknowledgments

Over the past years, I have benefited from the support of many wise and wonderful people without whom this work would not have been possible.

Thanks to Steve and Sam for throwing me into the deep end with electronics and lasers at Chicago. And thanks to Bobby, Lee, Brittany, and everyone else in the old meson tunnel for putting up with me.

Thanks to Rana for the opportunity to work on optical cavities from 4 cm to 4 km, for always being a source of advice and motivation, and for going to bat for his students when needed. Thanks to Nic and Jamie for dealing with my incessant questions. Thanks to Tara, David, Zach, Eric, Koji, Aidan, and Gabriele for making the subbasement a little less monastic.

Thanks to Daniel, Keita, and Peter for always being able to dredge up a plan of attack from the bog of loop tweaks, signal rewiring, and noise projections at the Hanford detector. Thanks to Sheila, Kiwamu, Jenne, Jeff, Alexa, Dan, Terra, and everyone else at Hanford who was part of the mad dash to the first observing run. And thanks to Stefan, Matt, and Lisa for showing up from time to time to help us not repeat the mistakes of the past.

Finally, I'd like to thank my parents and family for their many years of unwavering support.

ותם מן לא ינתהו לדרגה יצי טלאמה בברק בל בגשם סקל או נחוה מן אחנארה  
וגיראה אתי חזי פי טלאמת אליל ولو דלק אצז איסיר יצא אדי ישrok עלינה  
ليس هو دائمًا بل يلوح ويقفز كأنه لheat الحرب المتألفة

— רמב"ם

And then there are some whose darkness is illumined not by lightning,  
but by some kind of crystal or similar stone, or other substance that  
possesses the property of shining during the night; and to them even  
this small amount of light is not continuous, but now it shines and now  
it vanishes, as if it were the Flame of the Rotating Sword.

— Maimonides

## TABLE OF CONTENTS

<b>Abstract</b>	iii
<b>Acknowledgments</b>	iv
<b>Table of Contents</b>	vi
<b>List of Illustrations</b>	viii
<b>List of Tables</b>	xi
<b>Published Content and Contributions</b>	xii
<b>Chapter I: General relativity and gravitational radiation</b>	1
1.1 Basic equations	1
1.2 Weak-field limit	3
1.3 Gravitational radiation	3
1.4 Terrestrial detection	4
1.5 Other detection methods	7
<b>Chapter II: The Advanced LIGO interferometers: design and control</b>	8
2.1 Topology overview	8
2.2 Laser frequency control	18
2.3 Differential arm length control	26
2.4 Noise from vertex length controls	32
2.5 Angular control	40
2.6 Suspension control	49
2.7 Intensity control	52
<b>Chapter III: Noise in the Advanced LIGO detectors</b>	55
3.1 Quantum noise	55
3.2 Thermal noise	57
3.3 Seismic and Newtonian noise	65
3.4 Gas noise	66
3.5 Frequency noise	68
3.6 Intensity noise	72
3.7 Photodiode noise	74
3.8 Actuator noise	74
3.9 Noise from vertex degrees of freedom	79
3.10 Noise from angular degrees of freedom	80
3.11 Jitter noise	81
3.12 Noise budget	81
<b>Chapter IV: Observational results</b>	84
4.1 GW150914	84
4.2 LVT151012	85
4.3 GW151226	85
<b>Chapter V: Some topics in calibration</b>	87
5.1 Overview	87

5.2	Differential arm length optomechanical plant . . . . .	89
5.3	Systematic calibration errors . . . . .	93
5.4	Optimal transfer function measurements from the Fisher matrix . .	99
Chapter VI:	Searching for dark matter with laser interferometers . . . . .	111
6.1	Previous work . . . . .	111
6.2	Newtonian and Yukawa-type interactions . . . . .	112
6.3	Detection with laser interferometers . . . . .	113
6.4	Search strategy . . . . .	118
Chapter VII:	Future work . . . . .	119
7.1	Interferometry . . . . .	119
7.2	Calibration . . . . .	124
Appendix A:	Preliminary notions about loops . . . . .	125
A.1	Introduction . . . . .	125
A.2	Crossovers . . . . .	127
A.3	Measurements . . . . .	127
A.4	Noise . . . . .	129
Appendix B:	Median estimation of amplitude spectral densities . . . . .	131
B.1	Problem statement . . . . .	131
B.2	Gauss and Rayleigh distributions . . . . .	132
B.3	rms versus median averaging . . . . .	133
B.4	Real-world example . . . . .	134
Appendix C:	Optical cavities . . . . .	137
C.1	Definitions . . . . .	137
C.2	Pound–Drever–Hall locking . . . . .	139
C.3	Michelson locking . . . . .	141
Appendix D:	Some algebra for the differential arm length plant . . . . .	143
Appendix E:	In-situ test mass ringdown measurement . . . . .	146
Bibliography	. . . . .	150

## LIST OF ILLUSTRATIONS

<i>Number</i>	<i>Page</i>
1.1 Strain sensitivities for some past, current, and future gravitational wave experiments. . . . .	5
2.1 Diagram of a Michelson interferometer. . . . .	9
2.2 Diagram of a Fabry–Pérot interferometer. . . . .	11
2.3 Overview of the Advanced LIGO interferometer. . . . .	16
2.4 Diagram of the Advanced LIGO frequency and intensity stabilization systems . . . . .	17
2.5 Open-loop transfer function of the reference cavity stabilization servo . . . . .	20
2.6 Open-loop transfer function (model and measurement) of the input modecleaner frequency locking loop, with no feedback from the interferometer. . . . .	22
2.7 Open-loop transfer function (model and measurement) of the laser frequency locking to the interferometer common-mode arm length. . . . .	24
2.8 Crossover (model and measurement) from the laser frequency feedback to the modecleaner length feedback. . . . .	25
2.9 Block diagram of the Advanced LIGO frequency stabilization system. . . . .	26
2.10 Differential arm length optomechanical response as a function of SRC detuning . . . . .	29
2.11 Open-loop transfer function of the differential arm length control. . . . .	31
2.12 Crossover transfer functions for the penultimate and upper-intermediate actuator offloading for the differential arm length control. . . . .	32
2.13 Sensing matrix of the vertex degrees of freedom . . . . .	33
2.14 OLTFs of the vertex length degrees of freedom . . . . .	35
2.15 Feedforward subtraction diagram . . . . .	36
2.16 PRC length coupling into differential arm length . . . . .	37
2.17 Beamsplitter motion coupling into differential arm length . . . . .	38
2.18 SRC length coupling into differential arm length . . . . .	39
2.19 Diagram of hard and soft cavity optic motions. . . . .	42
2.20 Open-loop transfer functions for angular control of the differential hard arm mode. . . . .	43
2.21 Open-loop transfer functions for angular control of the beamsplitter. . . . .	46

2.22	Open-loop transfer functions for angular control of the signal recycling cavity pointing. . . . .	47
2.23	Diagram of the Advanced LIGO quadruple suspension. . . . .	50
3.1	GW photodiode auto- and cross-spectral densities from O1. . . . .	56
3.2	Diagram of the signal recycling mirror holder. . . . .	64
3.3	Budget of frequency noise in H1. . . . .	69
3.4	Frequency noise coupling into the differential arm length readout. . . . .	71
3.5	Relative intensity noise at the interferometer input. . . . .	72
3.6	Intensity noise coupling into the differential arm length readout, in terms of input RIN into antisymmetric-port RIN. . . . .	73
3.7	Noises associated with the test mass electrostatic actuator. . . . .	74
3.8	Freerunning and residual length noises for the power recycling cavity. . . . .	79
3.9	Freerunning and residual length noises for the signal recycling cavity. . . . .	80
3.10	Freerunning and residual length noises for the Michelson degree of freedom. . . . .	81
3.11	Noise budget of Advanced LIGO fundamental noises. . . . .	82
3.12	Noise budget of Advanced LIGO Hanford at the start of the first observing run. . . . .	83
4.1	Spectrogram of the GW150914 signal in the H1 detector. . . . .	85
4.2	Advanced LIGO H1 strain spectra during the three events GW150914, LVT151012, and GW151226. . . . .	86
5.1	Simplified diagram of the Advanced LIGO differential arm length sensing and control. . . . .	88
5.2	Advanced LIGO differential arm length optomechanical plants . . . . .	90
5.3	Open- and closed-loop transfer functions of the differential arm length loop used in the simulations in this chapter. . . . .	97
5.5	Normalized Cramér–Rao bounds on the covariance matrix for a single-frequency transfer function estimate of a one-pole system, assuming a fixed excitation amplitude. . . . .	103
5.6	Normalized Cramér–Rao bounds on the covariance matrix for a single-frequency transfer function estimate of a one-pole system, assuming a fixed excitation SNR. . . . .	104
5.7	Posterior for optimal calibration line placement for NS/NS-detuned operation at 125 W. . . . .	106
5.8	Frequency-dependent statistical errors in the NS/NS-optimized detuned interferometer response function for an optimized calibration line scheme.	107

5.9	Frequency-dependent statistical errors in an O2-like response function for a by-hand choice of calibration lines. . . . .	109
5.10	Frequency-dependent statistical errors in an O2-like response function for an optimized choice of calibration lines. . . . .	110
6.1	Example acceleration time series for dark matter interactions with Advanced LIGO. . . . .	114
6.2	Example acceleration spectra for dark matter interactions with Advanced LIGO. . . . .	115
6.3	Event rates for Newtonian dark matter interaction with laser interferometers. . . . .	116
6.4	Event rates for Yukawa dark matter interaction with Advanced LIGO. . . . .	117
6.5	Event rates for Yukawa dark matter interaction with LISA. . . . .	117
7.1	Expected frequency noise coupling with and without a signal recycling mirror. . . . .	120
7.2	Expected intensity noise coupling with and without a signal recycling mirror. . . . .	121
7.3	Expected frequency noise coupling for a possible 40 km detector. . . . .	123
A.1	Anatomy of a generalized servo loop. . . . .	126
B.1	Mean versus median averaging for the H1 OMC null stream. . . . .	135
B.2	Histogram of ASD values for the H1 OMC null stream at 100 Hz. . . . .	135
E.1	Posterior pdf of Advanced LIGO test mass loss angles, as determined from end Y ringdown data. . . . .	148

## LIST OF TABLES

<i>Number</i>	<i>Page</i>
2.1 Optomechanical parameters for the Advanced LIGO Hanford detector during O1. . . . .	18
2.2 Paramters for aLIGO H1 laser frequency stabilization. . . . .	19
2.3 Paramters for differential arm length sensing and control during O1 . . . . .	30
2.4 Parameters for vertex length sensing and control during O1 . . . . .	33
2.5 Sensors and bandwidths for angular control during O1 . . . . .	41
5.1 Parameters for the Advanced LIGO optomechanical plant. . . . .	91
B.1 Median bias factor $b$ (to four decimal places) for $N$ non-overlapping segments. . . . .	134
E.1 Data for determining coating and substrate losses via end Y test mass ringdowns. . . . .	147

## Published Content and Contributions

1. E. D. Hall, V. V. Frolov, T. Callister, H. Müller, M. Pospelov, and R. X. Adhikari. [Laser interferometers as dark matter detectors](#). *ArXiv e-prints* (2016).  
E.D.H. performed numerical simulations for Newtonian and Yukawa event rates and wrote portions of the manuscript. [arXiv:1605.01103].
2. Evan Hall for the LIGO Scientific Collaboration. [Laser Frequency and Intensity Stabilization for Advanced LIGO](#). *18th Coherent Laser Radar Conference (CLRC 2016)*. Cooperative Institute for Research in Environmental Sciences (CIRES), 2016, pp. 197–200. ISBN: 9781510828544.  
E.D.H. wrote this overview on behalf of the LIGO Scientific Collaboration. [URL: <https://clrc.cires.colorado.edu/4pagesummaries/W/W2.pdf>].
3. D. V. Martynov, E. D. Hall, B. P. Abbott, R. Abbott, T. D. Abbott, C. Adams, R. X. Adhikari, R. A. Anderson, S. B. Anderson, K. Arai, et al. [Sensitivity of the Advanced LIGO detectors at the beginning of gravitational wave astronomy](#). *Phys. Rev. D* 93 (11) (2016), p. 112004.  
E.D.H. contributed a high-frequency strain noise budget and a brief discussion of laser frequency noise. [DOI: 10.1103/PhysRevD.93.112004].

# 1 General relativity and gravitational radiation

In this chapter, we'll review some basics of general relativity and gravitational radiation. Largely we will follow Creighton and Anderson.<sup>1</sup> A good overview of general relativity is given by Zee.<sup>2</sup>

## 1.1 Basic equations

### Geodesic equation

A central postulate in general relativity is that massive particles move to extremize their proper time  $\tau$ . In other words, the spacetime trajectory  $X^\mu(\tau)$  is found by extremizing the action

$$S = \int_{s_A}^{s_B} ds = \int_{\tau_A}^{\tau_B} d\tau \left( g_{\alpha\beta} \frac{dX^\alpha}{d\tau} \frac{dX^\beta}{d\tau} \right)^{1/2}. \quad (1.1)$$

The result of this extremization is the **geodesic equation**

$$\frac{d^2 X^\mu}{d\tau^2} = \Gamma_{\nu\rho}^\mu \frac{dX^\nu}{d\tau} \frac{dX^\rho}{d\tau}, \quad (1.2)$$

where

$$\Gamma_{\nu\rho}^\mu = \frac{1}{2} g^{\mu\lambda} \left( \frac{\partial g_{\rho\lambda}}{\partial x^\sigma} + \frac{\partial g_{\sigma\lambda}}{\partial x^\rho} - \frac{\partial g_{\rho\sigma}}{\partial x^\lambda} \right) \quad (1.3)$$

is the **connection coefficient**. Additional forces (from electromagnetism, elastodynamics, and so on) go on the right-hand side of equation 1.2.

## Equation of geodesic deviation

How can one tell whether a particular metric describes flat spacetime or a spacetime with gravity? One prescription is to start with two test masses, initially separated by a small spacetime vector  $\zeta^\mu$ , and set them in motion with some four-velocity  $U^\rho = dX^\rho/d\tau$ . Then the relative acceleration of the two masses is given by the equation of **geodesic deviation**:

$$\frac{D^2\zeta^\mu}{D\tau^2} = -R^\mu_{\nu\rho\sigma} U^\nu U^\rho \zeta^\sigma, \quad (1.4)$$

where  $D^2\zeta^\mu/D\tau^2 = U^\lambda \nabla_\lambda (U^\sigma \nabla_\sigma \zeta^\mu)$  and

$$R^\mu_{\nu\rho\sigma} = 2\partial_{[\rho}\Gamma^\mu_{\sigma]\nu} - 2\Gamma^\lambda_{\nu[\rho}\Gamma^\mu_{\sigma]\lambda} \quad (1.5)$$

is the **Riemann tensor**. If  $D^2\zeta^\mu/D\tau^2$  is nonzero, the spacetime is curved. Geodesic deviation is the principle that underpins gravitational wave detection.

## Einstein field equation

The relationship between spacetime curvature and matter/energy is given by the **Einstein field equation**, which tells us how to calculate the metric tensor  $g_{\alpha\beta}$  given a certain stress-energy tensor  $T_{\alpha\beta}$ :

$$G_{\alpha\beta} = \frac{8\pi}{c^4} T_{\alpha\beta}, \quad (1.6)$$

where

$$R_{\alpha\beta} = R^\gamma_{\alpha\gamma\beta} \quad (\text{Ricci tensor}) \quad (1.7)$$

$$R = R^\gamma_\gamma \quad (\text{scalar curvature}) \quad (1.8)$$

$$G_{\alpha\beta} = R_{\alpha\beta} - \frac{1}{2}g_{\alpha\beta}R \quad (\text{Einstein tensor}). \quad (1.9)$$

In the following sections we will see that in empty space ( $T_{\alpha\beta} = 0$ ), the Einstein equation can be linearized and then admits plane wave solutions, which are gravitational waves.

Observations of type Ia supernovae and of anisotropies of the cosmic microwave background indicate that (at least on cosmological scales) the behavior of “empty” space is consistent with the presence of a constant, nonzero stress-energy  $T_{\alpha\beta} = -\Lambda g_{\alpha\beta}$  (so-called “**dark energy**”), which is about 70 % of the closure density of the universe.<sup>3</sup>

## 1.2 Weak-field limit

Many experimental tests of general relativity (including the detection of gravitational waves from distant astrophysical sources) operate in a regime where the spacetime curvature is small. In this so-called **weak-field limit**, the metric  $g_{\alpha\beta}$  is approximately the Minkowski metric  $\eta_{\alpha\beta}$  with a perturbation  $h_{\alpha\beta}$  satisfying  $|h_{\alpha\beta}| \ll |\eta_{\alpha\beta}|$ . In this regime, terms involving products of  $h_{\alpha\beta}$  with itself are ignored.

In the weak-field limit, the spacelike components of the geodesic deviation equation are

$$\ddot{\zeta}^i = -R^i{}_{0j0}\zeta^j. \quad (1.10)$$

This shows that the components  $R^i{}_{0j0}$  of the Riemann tensor manifest physically as tidal accelerations. For example, in the case of a spacetime sourced by a Newtonian potential  $\Phi(x^i)$ , these components  $R^i{}_{0j0}$  are the tidal field  $-\partial^2\Phi/\partial x^i\partial x^j$ . Turning this statement around, we can say that one can measure the Riemann tensor (and hence the curvature of spacetime) by measuring a tidal acceleration.

## 1.3 Gravitational radiation

In the weak-field limit, the Einstein field equations can be recast as a wave equation in  $h_{\alpha\beta}$ , sourced by some stress–energy tensor  $T_{\alpha\beta}$ . Solving this wave equation in vacuum ( $T_{\alpha\beta} = 0$ ) yields a class of plane wave solutions, called **gravitational waves**. For a wave travelling along the  $z$  axis, the weak-field metric perturbation has the form

$$h_{\alpha\beta} = \begin{pmatrix} 0 & 0 & 0 & 0 \\ 0 & h_+ & h_x & 0 \\ 0 & h_x & -h_+ & 0 \\ 0 & 0 & 0 & 0 \end{pmatrix}, \quad (1.11)$$

where the coefficients  $h_+$  and  $h_x$  are (potentially) time-dependent.<sup>a</sup> Equivalently, the line element for this metric is

$$ds^2 = -c^2 dt^2 + (1 + h_+) dx^2 + (1 - h_+) dy^2 + 2h_x dx dy + dz^2. \quad (1.12)$$

---

<sup>a</sup> Note that there are only two independent components in this metric, despite the fact that the metric can have up to ten independent components in general. In this case, eight of these ten components are eliminated when fixing the gauge. This gauge is referred to as the **transverse traceless (TT) gauge**, and freely falling masses have fixed coordinates in this gauge, even in the presence of a time-varying metric.

In this case, the geodesic deviation equations are

$$\ddot{\zeta}^x = \frac{1}{2} (\ddot{h}_+ \zeta^x + \ddot{h}_\times \zeta^y) \quad (1.13a)$$

$$\ddot{\zeta}^y = \frac{1}{2} (\ddot{h}_\times \zeta^x - \ddot{h}_+ \zeta^y) \quad (1.13b)$$

$$\ddot{\zeta}^z = 0, \quad (1.13c)$$

where the baseline separation vector is  $\zeta = \zeta^x \hat{\mathbf{x}} + \zeta^y \hat{\mathbf{y}} + \zeta^z \hat{\mathbf{z}}$ . These equations show explicitly that a gravitational wave exerts a tidal force on any matter that it passes through.

## 1.4 Terrestrial detection

Terrestrial detection efforts revolve around trying to make very sensitive tidal force measurements in the audio band.

### Bars

Resonant bar detectors are the oldest class of gravitational wave detection experiments.<sup>1</sup> In these experiments, a high- $Q$  object (often a bar, and often made of high-quality aluminum) is used to detect the tidal force of a passing gravitational wave. A wave with appropriate frequency content can pump energy into one of the bar's normal modes, setting the ends of the bar in motion with a strain that is much greater (by a factor  $Q$ ) compared to the intrinsic strain of the gravitational wave. Modern resonant bar detectors are able to achieve narrow-band strain sensitivities of order  $10^{-21}/\text{Hz}^{1/2}$ .<sup>1,4</sup>

### Planets and moons

Just like a metal bar, a celestial body such as a planet or moon will respond to the stress of a passing gravitational wave. The response produces local seismic disturbances at the body's surface,<sup>7</sup> which can be measured using a network of seismometers. Coughlin and Harms used data from seismometer networks on the Earth<sup>8</sup> and the Moon<sup>9</sup> to place upper limits on the stochastic GW background  $\Omega_{\text{GW}}$  from 0.1 to 1 Hz, yielding a limit  $\Omega_{\text{GW}} < 1.2 \times 10^5$ .

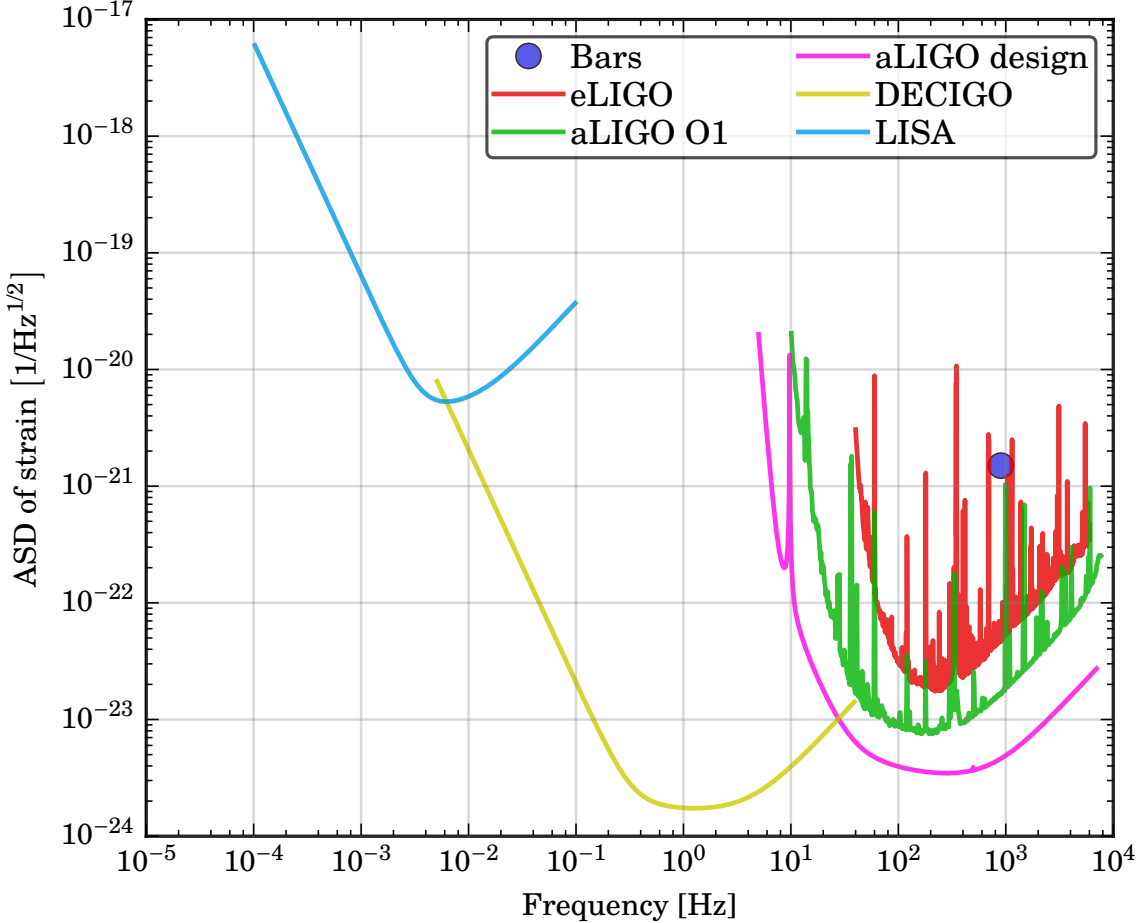


Figure 1.1: Strain sensitivities for some past, current, and future gravitational wave experiments. “Bars” refers to the joint AURIGA–EXPLORER–NAUTILUS–Virgo run described by Acernese et al.<sup>4</sup> “DECIGO” refers to a proposed space-based laser interferometer experiment with a 1000 km baseline.<sup>5</sup> “LISA” refers to a proposed space-based laser interferometer experiment with a  $5 \times 10^6$  km baseline.<sup>6</sup>

## Laser interferometers

An optical interferometer monitors the relative displacement (and hence relative acceleration) of multiple freefalling (or quasi-freefalling) test masses.

In the case of a simple Michelson interferometer, one mirror (test mass) is displaced by an amount  $\zeta_x \hat{\mathbf{x}}$  from a beamsplitter, and another is displaced an amount  $\zeta_y \hat{\mathbf{y}}$  from a beamsplitter. One port of the beamsplitter is illuminated with laser light of wavelength  $\lambda_0$ , and a photodetector is used to monitor the amount of light exiting the other port. If the relative displacement is zero ( $\zeta_x = \zeta_y = \zeta$ ), the interferometer’s antisymmetric port will be dark, since the round-trip phases  $\phi_x$  and  $\phi_y$  are equal.

Explicitly,

$$\phi_x = 2c \int_0^{\zeta/c} \frac{2\pi}{\lambda_0} dt = \frac{4\pi}{\lambda} \int_0^\zeta dx = \frac{4\pi}{\lambda} \zeta, \quad (1.14)$$

and the calculation for  $\phi_y$  yields the same answer.

We now consider what happens when a gravitational wave passes through the detector. We are interested in waves with frequency  $f$  of less than a few kilohertz, so the period  $T = 1/f$  is on the order of milliseconds or more. On the other hand, the light travel time in a kilometer-scale Michelson is tens of microseconds. Therefore, the response of the interferometer to the wave can be treated adiabatically. Suppose at some particular time the GW strain is  $h_+$ . We again want to compute the phases  $\phi_x$  and  $\phi_y$  of the light that is sent into the interferometer in the presence of this strain. For light traveling along the  $x$  arm,  $dt$  and  $dx$  are related by  $0 = -c^2 dt^2 + (1 + h_+) dx^2$  because light always travels along a null path. Therefore, the phase accumulated in the  $x$  arm is<sup>b</sup>

$$\phi_x = 2 \int_0^{\zeta/c} \frac{2\pi c}{\lambda_0} dt = \frac{4\pi}{\lambda_0} \int_0^\zeta \sqrt{1 + h_+} dx \approx \frac{4\pi}{\lambda_0} \int_0^\zeta \left(1 + \frac{h_+}{2}\right) dx = \frac{4\pi}{\lambda_0} \left(1 + \frac{h_+}{2}\right) \zeta, \quad (1.15)$$

and similarly,

$$\phi_y = \frac{4\pi}{\lambda_0} \left(1 - \frac{h_+}{2}\right) \zeta, \quad (1.16)$$

so that

$$\Delta\phi = \phi_x - \phi_y = \frac{4\pi}{\lambda_0} h_+ \zeta. \quad (1.17)$$

This shows that a Michelson interferometer will register a phase shift  $\Delta\phi$  that is directly proportional to both the applied spacetime strain  $h_+$  and the length of the interferometer's baseline  $\zeta$ .

We assumed the light was sent into the interferometer *after* the strain had already been applied, so that the wavelength is the same in both arms. However, any light already circulating in the interferometer as the strain is applied will be gravitationally frequency-shifted, with the light in one arm being redshifted and the light in the other arm being blueshifted.<sup>10</sup> As the light in the arms returns to the beam-splitter, a phase difference accumulates, causing power to appear at the dark port. This is the resolution to the common question of how one can use light to detect gravitational waves, given that gravitational waves cause redshift of the light in the arms.

---

<sup>b</sup> Even in the presence of nonzero strain, the limits of the integration are still 0 and  $\zeta$ , because the masses are assumed to be freely falling, and therefore their coordinates do not change in the TT gauge.

## 1.5 Other detection methods

### Pulsar timing

Millisecond pulsars are excellent clocks that can be used for GW detection.<sup>11</sup> If a GW passes between the line of sight from a pulsar to a radio telescope, then the arrival times of the pulses will be perturbed. There are many non-GW effects which could perturb the pulse arrival time for a particular pulsar, so in practice many pulsars are observed simultaneously. This makes it possible to extract the correlated arrival time perturbation due to the GW. Pulsar timing is particularly well-suited to measurement of  $\Omega_{\text{GW}}(f)$  on year-long timescales; the Parkes Pulsar Timing Array has been able so far to set a limit  $\Omega_{\text{GW}}(1/\text{yr}) < 2.3 \times 10^{-10}$  assuming  $\Omega_{\text{GW}}(f) \propto f^{0.5}$ .<sup>12</sup>

### Cosmic microwave background polarization

A detection of gravitational waves from the early universe can be made by careful measurement of the cosmic microwave background (CMB) polarization.<sup>13</sup> If the inflationary paradigm is correct, then the present observable universe evolved from a small, causally connected region that was blown up by a large factor ( $\sim 10$  to  $\sim 60$  e-foldings) less than  $10^{-32}$  s after the big bang. Consequently, quantum fluctuations in the fields present during the inflationary period—for example, the inflaton field and the gravitational field—were similarly blown up and should appear today as perturbations to the temperature and polarization of the CMB on large angular scales. While several different fields can produce large-angle curl-free (*E*-mode) perturbations in the CMB polarization in the early universe, *only* the gravitational field can produce large-angle divergence-free (*B*-mode) CMB perturbations. Therefore, detecting primordial *B*-modes in the CMB would provide evidence for the existence of gravitational waves in the early universe. Detecting primordial *B*-modes is the current aim of several ground-based, balloon-borne, and space-based CMB polarimetry experiments.

## 2 The Advanced LIGO interferometers: design and control

This chapter discusses the optical topology of the Advanced LIGO interferometers, and how the interferometer lengths, angles, and laser are controlled. This thesis will not discuss the lock acquisition system (green auxiliary lasers for the arms and third-harmonic heterodyne sensing for the vertex)<sup>14</sup> used to bring the interferometer onto resonance from its initial uncontrolled state. This system has already been discussed in detail by Staley<sup>15</sup> and Martynov.<sup>16</sup>

We will make heavy use of the analytical formulas found by Sigg<sup>17</sup> and Izumi and Sigg<sup>18–21</sup> for length readout and control of resonant interferometers.

### 2.1 Topology overview

This section will review Michelson and Fabry–Pérot interferometer topologies, and how these are combined to form a dual-recycled Fabry–Pérot Michelson interferometer.

#### **Michelson interferometer**

Consider a Michelson interferometer with two reflective test masses and a 50% beamsplitter (figure 2.1).

Suppose the input (symmetric) port of the Michelson is illuminated with a laser with frequency  $\omega_0/2\pi$  and field amplitude  $E_0$ . If  $\phi_X = 2\omega_0 \ell_X/c$  and  $\phi_Y = 2\omega_0 \ell_Y/c$  are the round-trip phases from the beamsplitter to the test masses and back, then the

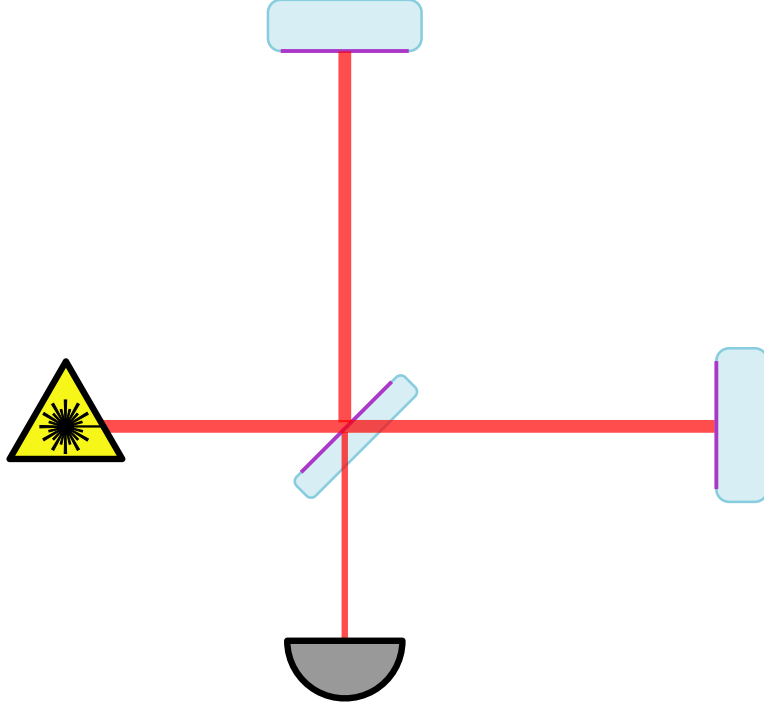


Figure 2.1: Diagram of a Michelson interferometer. A laser beam is injected into the symmetric (bright) port, and the differential arm length signal is read out at the antisymmetric (dark) port.

field at the antisymmetric port is

$$E_{AS} = \frac{E_0}{2} (e^{i\phi_X} - e^{i\phi_Y}) \quad (2.1)$$

$$= i E_0 e^{i\phi_+} \sin \phi_-, \quad (2.2)$$

with  $\phi_{\pm} = (\phi_X \pm \phi_Y)/2$ . Correspondingly, the power  $P_{AS} = |E_{AS}|^2$  at the antisymmetric port is

$$P_{AS} = P_0 \sin^2 \phi_-. \quad (2.3)$$

Implicit in this equation is the statement that common-mode phase fluctuations do not make a signal at the antisymmetric port. This common-mode rejection is crucial for interferometric gravitational wave detection, since all realistic lasers have phase noise that is many orders of magnitude higher than the phase fluctuation induced by a passing gravitational wave.

How is the anti-symmetric fringe condition maintained? One possibility is to servo the laser frequency so that  $P_{AS} = P_0/2$  (the half-fringe condition). This method is simple, but has the disadvantage that fluctuations in  $P_0$  appear directly at the antisymmetric port.

Another possibility (closer to what is actually employed) is to modulate the laser at some radio frequency  $\Omega/2\pi$  and then operate the Michelson at a dark fringe ( $P_{AS} = 0$ ). This requires choosing  $\ell_X \neq \ell_Y$  by some macroscopic amount (that is, by many multiples of the laser wavelength), so that the transmission of light from the input port to the anti-symmetric port becomes frequency-dependent. In the field of gravitational wave detection, this intentional length offset is called the Schnupp asymmetry.<sup>a</sup>

Writing  $\phi_{\pm}(\omega) = 2\omega\ell_{\pm}/c$ , we see that

$$E_{AS}(\omega) = iE_0(\omega)e^{2i\omega\ell_+/c} \sin(2\omega\ell_-/c). \quad (2.4)$$

We write  $\ell_- = \bar{\ell}_- + \delta\ell_-$ , where  $\bar{\ell}_-$  is the Schnupp asymmetry (i.e., the macroscopic part of the differential length), and  $\delta\ell_-$  is the microscopic detuning. We assume the Michelson is operated at the dark fringe, so we are trying to keep  $\delta\ell_-$  at 0. The field incident on the beamsplitter is

$$E_0 e^{i\omega_0 t} e^{i\Gamma \cos \Omega t} \simeq E_0 e^{i\omega_0 t} \left( 1 + \frac{i\Gamma}{2} e^{i\Omega t} + \frac{i\Gamma}{2} e^{-i\Omega t} \right), \quad (2.5)$$

where  $\Gamma$  is the modulation index and  $\Omega$  is the angular modulation frequency. After some algebra (see section C.3), it can be shown that, to linear order in  $\delta\phi_-$ , the demodulated rf power at the antisymmetric port at  $\Omega$  is

$$P_{AS} = P_0 \Gamma \sin \bar{\phi}_- \delta\phi_-, \quad (2.6)$$

where  $\bar{\phi}_- = 2\omega\bar{\ell}_-/c$  is the macroscopic portion of the differential phase.

What is the phase sensitivity of a Michelson interferometer? In the case of either dc or rf readout, it is set by the power incident on the beamsplitter.

In the case of dc readout, if the antisymmetric port is kept nearly dark, then  $P_{AS} \simeq P_0\phi_-^2$ , so that the optical gain is  $s_{dc} = \partial P_{AS}/\partial\phi_-|_{\phi_0} = 2P_0\phi_0$ , where  $\phi_0$  is the static differential phase offset for the carrier in the arms. The shot noise of the light in the antisymmetric port is  $S_{PP}^{1/2}(f) = (2h\nu_0 P_{AS})^{1/2} = (2h\nu_0 P_0)^{1/2}\phi_0$ , and hence the equivalent phase noise is  $(h\nu_0/2P_0)^{1/2}$ .<sup>23</sup>

In the case of rf readout, the optical gain is  $s_{rf} = P_0\Gamma \sin \bar{\phi}_-$ , and the shot noise (which comes from the two sidebands) is  $[(3/2)h\nu_0 P_0]^{1/2}\Gamma \sin \bar{\phi}_-$ ; the shot-noise-limited

---

<sup>a</sup>This is the same basic principle that underlies Fourier transform spectroscopy, which has been used (among other things) to verify the thermal nature of the cosmic microwave background.<sup>22</sup>



Figure 2.2: Diagram of a Fabry–Pérot interferometer. The photodiode may also be placed in so as to monitor the reflected light, rather than the transmitted light.

phase sensitivity is then  $[3hv_0/2P_0]^{1/2}$ , independent of both  $\Gamma$  and  $\bar{\phi}_-$ .<sup>b</sup> We can refer this noise to strain via the relation  $\delta\phi = (\pi/\lambda_0)L\delta h$ . This results in a shot-noise-limited strain ASD of

$$S_{hh}^{(\text{shot})}(f)^{1/2} = \frac{1}{\pi L} \left( \frac{3hc\lambda_0}{2P_0} \right)^{1/2}. \quad (2.7)$$

For  $P_0 = 1\text{ W}$ ,  $\lambda_0 = 1064\text{ nm}$ , and  $L = 4\text{ km}$ , this results in a strain of  $4 \times 10^{-20}/\text{Hz}^{1/2}$ . This strain sensitivity is good, but not good enough for regular detection of gravitational wave events. Improving this sensitivity requires either increasing the laser power by many orders of magnitude or augmenting the optical topology to improve the shot-noise-limited SNR. In the next section we show that the sensitivity can be greatly enhanced through the use of Fabry–Pérot interferometry.

## Fabry–Pérot interferometer

The basic definitions for a Fabry–Pérot interferometer are given in appendix C. This appendix also reviews the standard control scheme [the Pound–Drever–Hall (PDH) technique] for locking a laser to a cavity, or vice versa.

We consider a two-mirror Fabry–Pérot interferometer with length  $L$  (figure 2.2). For simplicity we assume the input mirror has transmissivity  $T$ , and the output mirror has zero transmissivity. Therefore, the cavity is overcoupled, with a pole  $f_p = cT/8\pi L$ . We now compute the shot-noise-limited sensitivity of this cavity when it is kept resonant using PDH reflection locking. Given a modulation depth  $\Gamma$ , the optical gain (in watts per meter) of the PDH readout is<sup>c</sup>

$$s(f) = \frac{c}{L\lambda_0} \times \frac{4P_0J_0(\Gamma)J_1(\Gamma)/f_p}{1 + if/f_p}. \quad (2.8)$$

The shot noise on the photodiode is

$$S_{PP}^{(\text{shot})}(f) = 4hv_0P_0 [(1-v)J_0(\Gamma)^2 + 3J_1(\Gamma)^2]. \quad (2.9)$$

<sup>b</sup> The factor of 3 (rather than 2) in these rf shot noise formulas arises from the cyclostationary nature of the noise in the demodulated sidebands.<sup>24,25</sup>

<sup>c</sup> See appendix C.

Assuming the visibility is perfect ( $v = 1$ ), the shot-noise limited strain ASD is therefore

$$S_{hh}^{(\text{shot})}(f)^{1/2} = \frac{1}{L} \times \frac{S_{PP}^{(\text{shot})}(f)^{1/2}}{|s(f)|} = \frac{1}{2} \left( \frac{3h\lambda_0}{cP_0} \right)^{1/2} |f_p + if|. \quad (2.10)$$

For  $L = 4\text{ km}$  and  $f_p = 42\text{ Hz}$ , we have  $S_{hh}^{(\text{shot})}(f \ll f_p)^{1/2} = 2 \times 10^{-24}/\text{Hz}^{1/2}$ , an improvement of  $c/\sqrt{2}\pi L f_p = 4\mathcal{F}/\sqrt{2}\pi \approx 400$  over the Michelson sensitivity as given by (2.7). Above the cavity pole, the sensitivity rises like  $f$ , crossing the Michelson sensitivity at  $f = c/\sqrt{2}\pi L \approx 17\text{ kHz}$ .<sup>d</sup>

It is therefore highly advantageous to use optical cavities when using a laser to sense small audio-band strains. In the next section, we examine the Fabry–Pérot-enhanced Michelson topology that is used in Advanced LIGO and other gravitational-wave interferometers.

## Fabry–Pérot Michelson interferometer with recycling

The Advanced LIGO instruments are dual-recycled Fabry–Pérot Michelson interferometers, as shown in figure 2.3. This means that they are Michelson interferometers whose arms are Fabry–Pérot cavities. Additionally, a power-recycling mirror is placed between the laser and the beamsplitter in order to enhance the amount of power circulating in the Fabry–Pérot arms. Finally, a signal-recycling mirror is placed between the beamsplitter and the antisymmetric port readout to tune the bandwidth of the instrument.

A dual-recycled Fabry–Pérot Michelson has five length degrees of freedom:

$$L_+ = \frac{L_X + L_Y}{2} \quad (2.11)$$

$$L_- = \frac{L_X - L_Y}{2} \quad (2.12)$$

$$L_P = -x_P + x_B + \frac{x_{IX} - x_B}{2} + \frac{y_{IY} - y_B}{2} \quad (2.13)$$

$$L_M = \frac{x_{IX} - x_B}{2} - \frac{y_{IY} - y_B}{2} \quad (2.14)$$

$$L_S = -y_S + y_B + \frac{x_{IX} - x_B}{2} + \frac{y_{IY} - y_B}{2}. \quad (2.15)$$

---

<sup>d</sup> We note in passing that the shot-noise-limited sensitivity of a Fabry–Pérot cavity is independent of  $f_p$  for  $f > f_p$ ; in other words, there is no penalty in terms of shot-noise-limited sensitivity for choosing  $f_p$  to be as small as possible.<sup>26</sup>

These are, respectively, the common-mode arm length (CARM), the differential arm length (DARM), the power recycling cavity (PRC) length, the Michelson length (MICH), and the signal-recycling cavity (SRC) length.<sup>e;f</sup>

We now want to answer the question: how do we choose the interferometric lengths and the optic reflectivities?

We should choose the end test masses to be highly reflective, since there is no benefit in letting light leak out the end mirrors, other than the small amount (about 1 W) required for diagnostic and control purposes. In Advanced LIGO, we have  $T_e = 4 \text{ ppm}$ .

The input test mass transmissivity  $T_i$  and signal recycling mirror transmissivity  $T_s$  are chosen jointly to set the interferometer's signal bandwidth and to optimize a number of technical effects; we discuss these transmissivity choices later.

We now discuss how to choose the power-recycling mirror transmissivity  $T_p$ . We want to choose the mirror transmissivity so as to provide the lowest possible strain-referred shot noise, which means maximizing the amount of power entering the arms. For the time being, suppose we have chosen some fiducial input test mass transmissivity  $T_i$ , and suppose each arm has a round-trip loss  $\eta_a$  of order 100 ppm. With  $r_i \simeq 1 - T_i/2 - \eta_i/2$  and  $r_e \simeq 1 - \eta_e/2$ , the arm reflectivity is<sup>18</sup>

$$r_a = \frac{r_e(1 - \eta_i) - r_i}{1 - r_i r_e} \simeq \frac{T_i - \eta_a}{T_i + \eta_a} \simeq 1 - \frac{2\eta_a}{T_i}, \quad (2.16)$$

---

<sup>e</sup> Note that the differential arm length is sometimes defined as  $L_- = L_X - L_Y$ , particularly for the purposes of noise budgeting and data analysis. In particular, the equivalent GW strain estimate stored in the science data is  $h = (L_X - L_Y)/L$ , where  $L$  is the nominal average arm length.

<sup>f</sup> Why are there only five interferometric degrees of freedom if a dual-recycled Fabry-Pérot Michelson interferometer has seven mirrors? If each mirror is constrained to lie in the  $xy$  plane, then there are fourteen translational degrees of freedom (two for each mirror). Moving any of the seven optics transverse to their surface normals will obviously produce no signal, so this eliminates seven degrees of freedom. The other two non-interferometric degrees of freedom involve the simultaneous motion of multiple optics:

1. The four test masses move away from the beamsplitter along the beamline directions (which has no effect on  $L_+$ ,  $L_-$ , or  $L_M$ ), and the power- and signal-recycling mirrors move toward the beamsplitter in order to null the change in  $L_p$  and  $L_s$ .
2. The IX and EX masses move away from the beamsplitter, and the IY and EY masses move toward the beamsplitter. This has no effect on  $L_+$ ,  $L_-$ ,  $L_p$ , or  $L_s$ , but it lengthens  $L_M$ . Therefore, the beamsplitter and the recycling mirrors are moved in order to cancel the effect in  $L_M$ .

where  $\eta_a = \eta_i + \eta_e$ . Then

$$\frac{P_b}{P_0} = g_p^2 = \left| \frac{t_p}{1 - r_p r_a} \right|^2 \quad (2.17a)$$

$$\approx \frac{T_p}{(T_p/2 + \eta_p/2 + 2\eta_a/T_i)^2}, \quad (2.17b)$$

where  $\eta_p$  is the round-trip PRC loss.<sup>g</sup> If  $\eta_p \ll 4\eta_a/T_i$ , the PRC loss is negligible and hence the PRC gain  $P_b/P_0$  is maximized by choosing

$$T_p = 4\eta_a/T_i, \quad (2.18)$$

giving  $g_p^2 = T_i/4\eta_a$ .

We now discuss how to choose  $T_i$  and  $T_s$ . In a non-signal-recycled interferometer, the quantum noise limit depends crucially on the choice of arm finesse. However, a signal-recycled interferometer has a quantum noise limit that is determined jointly by the arm finesse and the signal recycling mirror transmissivity. Therefore, the arm finesse may be determined from any number of other criteria, and the signal recycling mirror transmissivity may be adjusted to give the desired quantum noise curve. Some of these finesse criteria are as follows.

- The coupling of Michelson motion into the antisymmetric port is given by  $1/G_a = \pi/2\mathcal{F}$ .<sup>27</sup> To ensure that thermal noise from the beamsplitter suspension contributes negligibly to the differential arm length readout, we should choose  $\mathcal{F} \geq 350$  for Advanced LIGO.<sup>28</sup>
- The coupling of low-frequency SRC length motion into the antisymmetric port is proportional to the stored arm power, the arm finesse, and the dc readout offset.<sup>27</sup> To ensure that thermal noise from the signal recycling mirror suspension contributes negligibly to the differential arm length readout, we should choose  $\mathcal{F} \leq 625$  for Advanced LIGO.<sup>28</sup>
- A lower finesse arm easier to lock, since it spends more time crossing each fringe.
- Lower power stored in the arms leads to fewer parametric instabilities.

The Advanced LIGO arms are chosen to have a finesse of 440, corresponding to an input test mass transmissivity of  $T_i = 1.4\%$ . This means that each arm has a natural bandwidth (cavity pole)  $f_a = cT_i/8\pi L = 42\text{Hz}$ . For the final Advanced LIGO design, the signal recycling mirror is chosen to have a transmissivity  $T_s = 20\%$ , corresponding to a bandwidth (differential arm pole)  $f_- \simeq f_a \times (1 + r_s)/(1 - r_s) = 750\text{Hz}$ ,

---

<sup>g</sup> This follows by writing  $r_p = \sqrt{1 - T_p - \eta_p} \simeq 1 - T_p/2 - \eta_p/2$ .

where  $r_s = \sqrt{1 - T_s}$ . However, for lower power operation (as during the first observing run), the transmissivity is instead  $T_s = 37\%$ , giving a bandwidth  $f_- \approx 365\text{ Hz}$ .

The exact expressions for the common-mode (+) and differential (−) arm poles are<sup>18</sup>

$$2\pi f_+ = \frac{c}{2L_+} \ln \left[ \frac{1 + r_i r_p}{r_e r_i + r_e r_p (1 - \eta_j)} \right] \quad (2.19)$$

$$2\pi f_- = \frac{c}{2L_+} \ln \left[ \frac{1 - r_i r_s}{r_e r_i - r_e r_s (1 - \eta_j)} \right]. \quad (2.20)$$

Fixing  $T_i$  also fixes the value of the PRM transmissivity required to achieve maximal power buildup (that is, critical carrier coupling) in the interferometer, according to equation 2.17b. However, choosing critical carrier coupling means that certain reflection error signals that depend on the beat of the carrier against the sidebands will vanish (the 45 MHz reflection angular signals are one such example—see section 2.5). Therefore, the PRM transmissivity is chosen to be  $T_p = 3.0\%$ , which slightly overcouples the carrier.

Finally, we consider how to choose the macroscopic cavity lengths. The macroscopic lengths of the common-mode and differential arm lengths should be obvious: the common-mode length should be as long as possible, so as to get the best strain sensitivity, and the differential arm length should be zero, so that the interferometer is balanced.

For the vertex lengths, the rough goal is to have one set of sidebands (at frequency  $f_1$ ) resonant in the PRC and another (at frequency  $f_2$ ) resonant in the SRC, with both sidebands nonresonant in the arms. To achieve nonresonance in the arms, the sideband frequency must be significantly different from a multiple of  $c/2L_+ = 37.5\text{ kHz}$ . Once the sideband frequencies are chosen, the macroscopic PRC and SRC lengths (and the Schnupp asymmetry for the Michelson degree of freedom) must be chosen to give the appropriate resonance condition. In particular, the PRC length  $\bar{l}_p$  must be a half-integer multiple of  $c/2f_1$ , so that the carrier and the sideband are simultaneously resonant. If the rf modulation is applied before the input modecleaner (as is the case in Advanced LIGO), the modecleaner length must also be a multiple of  $c/2f_1$ . The SRC length  $\bar{l}_s$  is then chosen to be a half-integer multiple of  $c/2f_2$ , such that the  $f_1$  sidebands do not also resonate. Finally, the Schnupp asymmetry  $\bar{l}_m$  is chosen to critically couple the  $f_2$  sidebands into the SRC.<sup>27</sup>

Numerical values for the Advanced LIGO optical configuration are given in table 2.1, and an overview diagram is given in figure 2.3.

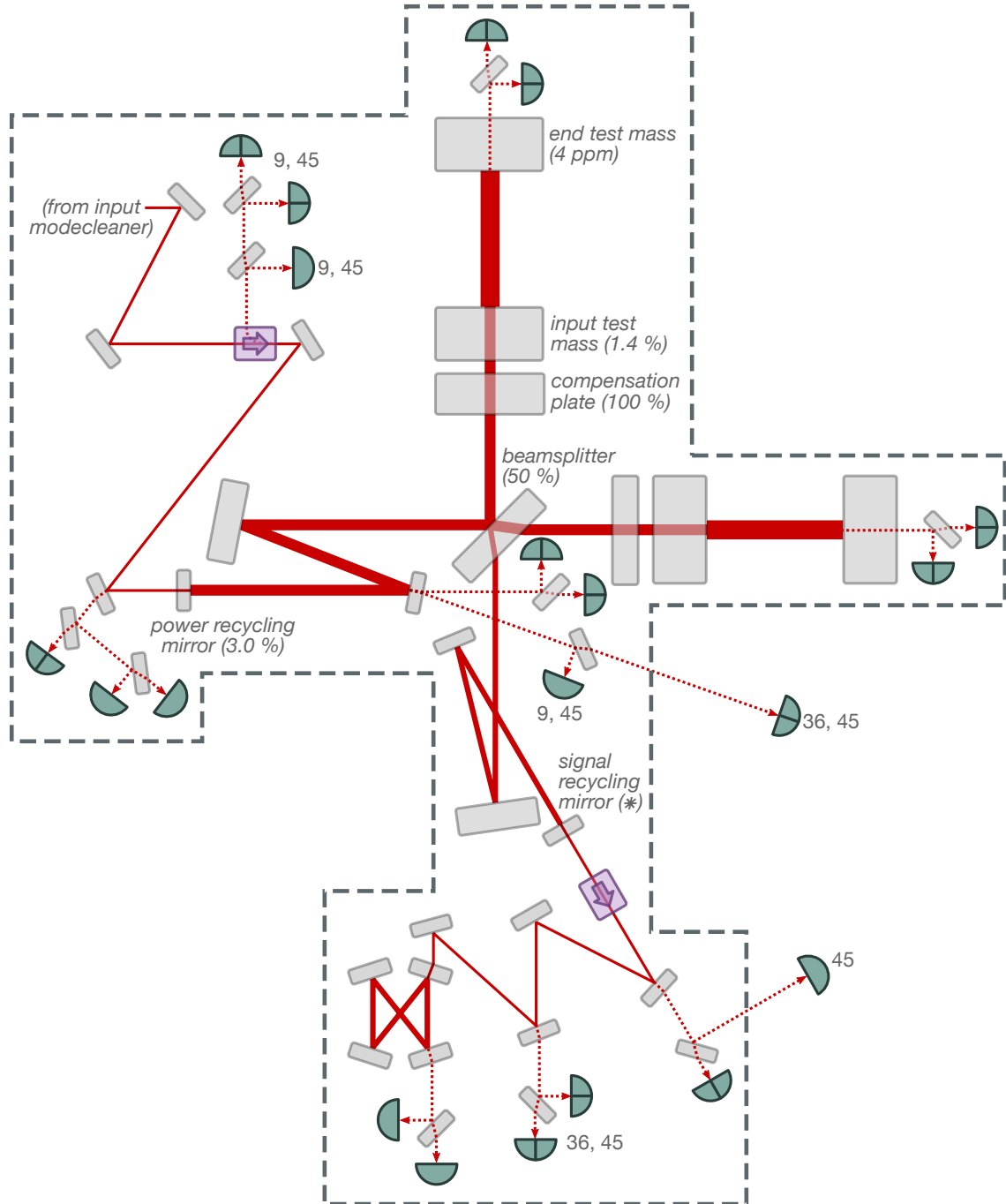


Figure 2.3: Overview of the Advanced LIGO interferometer. Optics and photodetectors inside the dashed box are in vacuum and seismically isolated. Numbers next to photodetectors indicate resonant rf detection at those frequencies. Additionally, each resonant rf length sensor has a corresponding broadband rf detector placed in air (for detecting frequencies from 9 to 135 MHz). Numbers next to optics indicate transmissivities. The signal recycling mirror has a transmissivity of 37 % for O1 and O2; the design value, for use at full laser power (125 W), is 20 %.

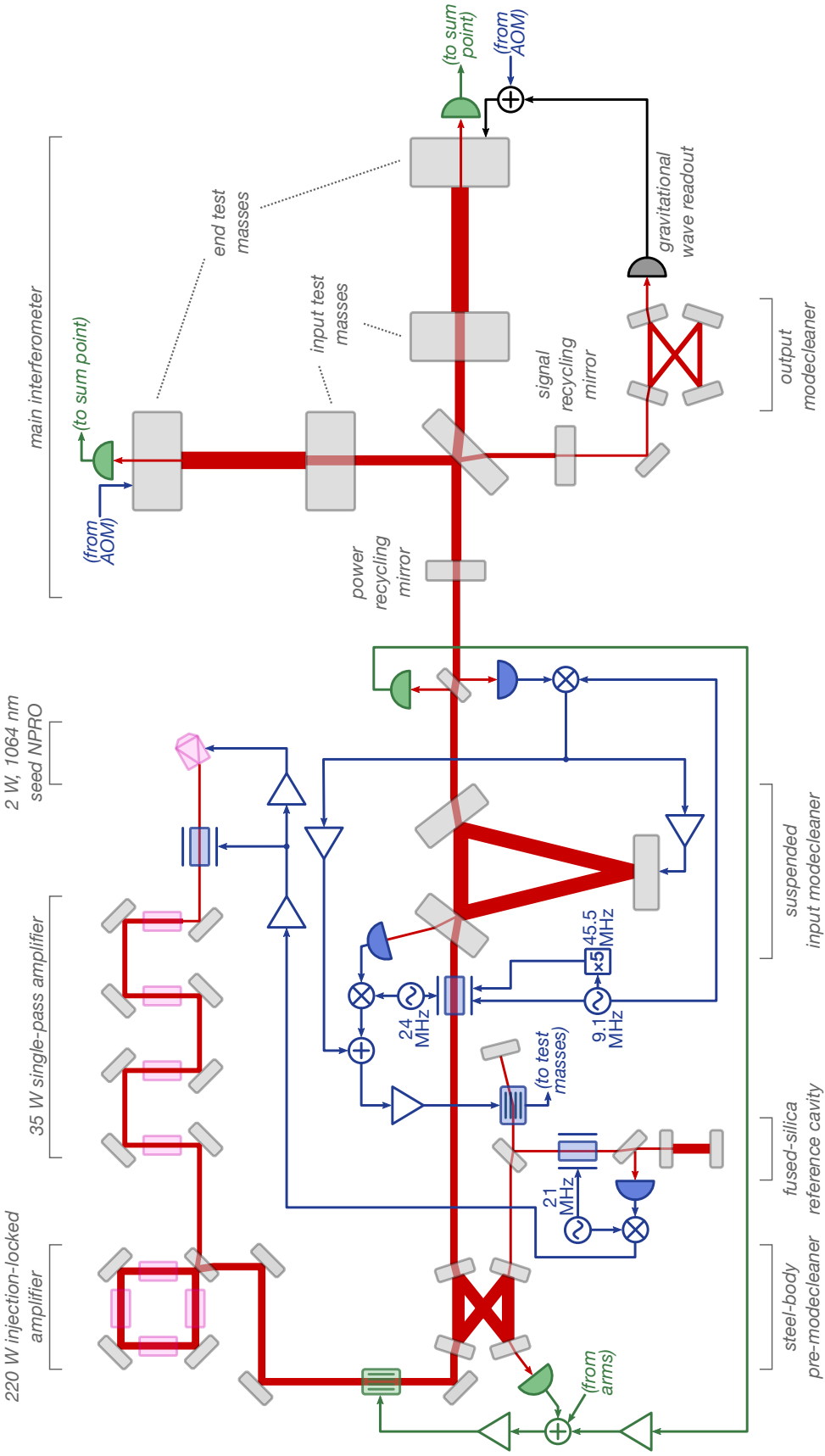


Figure 2.4: Simplified diagram of the Advanced LIGO laser system, including frequency stabilization (blue lines) and intensity stabilization (green lines). The differential arm length control and the strain readout are shown with black lines. Some liberties have been taken with folding and pickoff mirrors. Components for sensing and control of the injection-locked amplifier, pre-modecleaner, beamsplitter, recycling mirrors, and output modecleaner are not shown. The outermost intensity stabilization path (feeding the transmitted arm powers to the inner servo error point) was not used during the first observing run. Symbols:  $\square$  photodiode;  $\odot$  rf oscillator;  $\square$  electro-optic modulator;  $\blacksquare$  acousto-optic modulator;  $\otimes$  mixer.

Arm length	3994.5 m
PRC length	55 m
Michelson length	3 m
Schnupp asymmetry	8 cm
SRC length	56 m
Input modecleaner length <sup>29</sup>	33 m
Output modecleaner length <sup>30</sup>	1.132 m
End test mass transmission	4 ppm
Input test mass transmission	1.4 %
Power recycling mirror transmission	3.0 %
Signal recycling mirror transmission	37 %
Arm loss <sup>31</sup>	100(20) ppm
Interferometer rf modulation frequency 1	9.100230 MHz
Interferometer rf modulation frequency 2	45.501150 MHz
IMC rf modulation frequency	24.078360 MHz
OMC dither frequency	4.1 kHz
Interferometer rf modulation depth 1	0.22 rad
Interferometer rf modulation depth 2	0.28 rad
IMC rf modulation depth	0.01 rad
Laser wavelength	1064 nm
Interferometer input power	19 to 21 W
Carrier power recycling gain	38 to 42 W/W
Carrier arm gain	280 W/W
Carrier visibility	> 97 %

Table 2.1: Optomechanical parameters for the Advanced LIGO Hanford detector during the first observing run. The parameters for the Livingston detector are similar.

## 2.2 Laser frequency control

### Overview

Reducing the laser frequency noise to an astrophysically competitive level is challenging. As said above, the interferometer's Michelson topology should reject common-mode noises such as laser frequency noise. However, this common-mode rejection is

Reference cavity length <sup>32</sup>	20.3 cm
Reference cavity spot size <sup>32</sup>	290 $\mu$ m
Reference cavity pole <sup>32</sup>	30 kHz
Reference cavity servo bandwidth	200 kHz
Input modecleaner round-trip length <sup>33</sup>	32.9 m
Input modecleaner spot size <sup>34</sup>	2–3 mm
Input modecleaner pole	9 kHz
Input modecleaner servo bandwidth	40 kHz
Common-mode arm length <sup>33</sup>	3994.5 m
Common-mode spot size <sup>34</sup>	5–6 cm
Common-mode cavity pole	0.63 Hz
Common-mode servo bandwidth	15 kHz

Table 2.2: Paramters for aLIGO H1 laser frequency stabilization.

finite; in practice, it is a factor of a few hundred. To make the laser noise contribute negligibly to the interferometer’s GW strain readout, a phase noise of  $10^{-8}$  rad/Hz $^{1/2}$  at 100 Hz is required at the interferometer’s input.<sup>35</sup> (The common-mode cavity then provides a factor of  $\sim 100$  suppression for light circulating in the arms.) On the other hand, the fractional phase fluctuation of a good solid-state laser such as a 1064 nm Nd:YAG NPRO has a freerunning noise of about 100 Hz/Hz $^{1/2}$  at 100 Hz,<sup>36</sup> which amounts to a phase fluctuation of 1 rad/Hz $^{1/2}$ .

How can we achieve eight orders of magnitude of phase noise suppression below 1 kHz? First, we need an optical reference cavity whose phase noise is at least as good as the phase noise requirement. Such a length reference is handily furnished by the interferometer’s common-mode arm length: within the gravitational wave band (10 Hz to 7 kHz), the displacement noise of this degree of freedom should be limited by radiation pressure noise, coating thermal noise, squeezed film damping, and perhaps a few other displacement noises which nonetheless are too small to cause the resulting laser phase noise to contaminate the differential arm length readout.

How do we build a loop to frequency-stabilize the laser to the common-mode arm length? We might imagine building a simple frequency-locking loop in which the freerunning laser is directly locked to the common-mode arm length. However, this loop would need its final unity-gain frequency to be 1 MHz or more. Such a

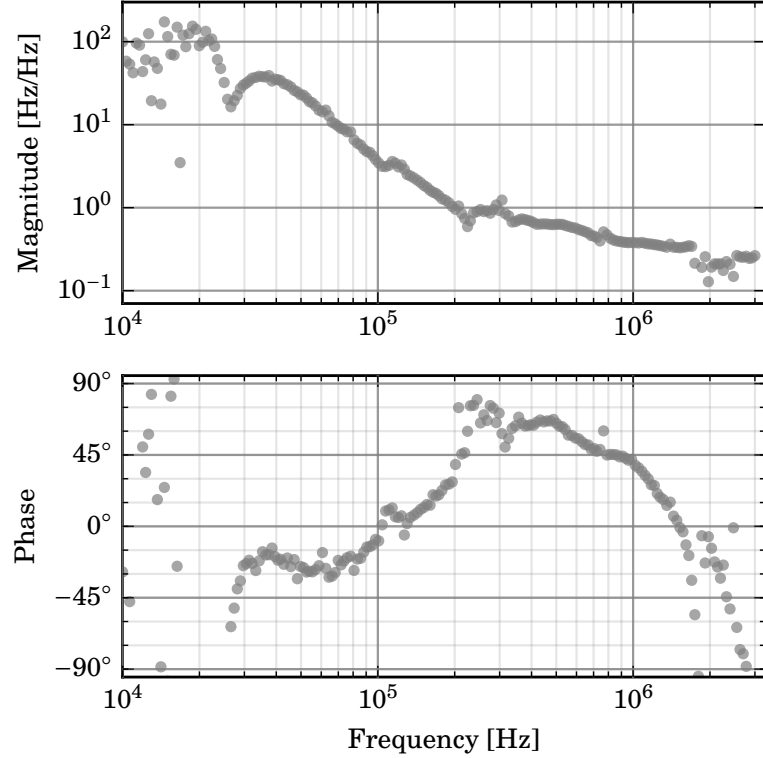


Figure 2.5: Open-loop transfer function of the reference cavity stabilization servo, with no feedback from the input modecleaner or the interferometer. The dip in the transfer function around 26 kHz arises from the actuation crossover between the laser PZT and the broadband EOM.

high UGF is difficult to achieve, since a 4 km cavity has a phase delay of  $L/c = 13 \mu\text{s}$  in its PDH signal.<sup>37</sup> Instead, Advanced LIGO (as with other initial/advanced gravitational-wave laser interferometers) employs a multi-cavity stabilization approach: the laser is first stabilized to a table-top reference cavity using a loop with a bandwidth of hundreds of kilohertz, then to a suspended cavity (the input modecleaner) with a bandwidth around 50 kHz, and finally to the common-mode arm length with a bandwidth of about 20 kHz. Table 2.2 gives parameters relevant to the laser frequency stabilization, and a diagram of the frequency (and intensity) stabilization scheme is shown in figure 2.4.

## Reference cavity stabilization

The goal of the reference cavity loop is to suppress the freerunning frequency noise of the NPRO—about  $(100 \text{ Hz}/\text{Hz}^{1/2}) \times (100 \text{ Hz}/f)$ —down to the length noise of a

20.3 cm fused-silica reference cavity. The noise performance of this stabilization scheme was investigated at length by Chalermongsak et al.<sup>32</sup>

This cavity is 20.3 cm long, has a finesse of roughly  $10^4$ , and is designed to be critically coupled. It is suspended inside a small vacuum chamber that sits on the main pre-stabilized laser table. In the absence of scatter, rf amplitude modulation, excess intensity noise, and so on, this design should produce a cavity frequency noise that is limited by the Brownian noise of the mirror coatings—about  $(6\text{mHz}/\text{Hz}^{1/2}) \times (100\text{Hz}/f)^{1/2}$ .

About 20 mW of light from the main laser beam is incident on the cavity. 21 MHz phase sidebands are applied with a resonant electro-optic modulator, and the resulting beat note is sensed in reflection of the cavity. The cavity visibility is typically 80 %.

The servo loop is designed to have a UGF of more than 100 kHz (in principle, nearly 1 MHz), so that several orders of magnitude of noise suppression can be achieved in the GW band. A typical open-loop transfer function (OLTF) of the reference cavity stabilization servo from O1 is shown in figure 2.5.

The main features of the optical (frequency-to-power) transfer function in this loop are the reference cavity pole at 25 kHz, and the pole of the pre-modecleaner<sup>36</sup> at 560 kHz (since the frequency actuator is located before the PMC, but the reference cavity is located after it). On the actuation side, we need an actuator that can actuate with minimal phase delay up to 1 MHz, with enough range to cancel the freerunning NPRO noise in and above the GW band. Additionally, it must be able to adjust the laser frequency by several gigahertz on thermal timescales ( $\lesssim 1\text{Hz}$ ), in order to compensate for long-term drifts in either the NPRO length or the reference cavity length. To achieve all these requirements, three actuators are employed:

1. on thermal timescales, control is applied to a thermoelectric cooler attached to the NPRO crystal, with a coefficient of order 1 GHz/V;
2. for frequencies between  $\approx 1\text{Hz}$  and  $\approx 10\text{kHz}$ , control is applied to a piezoelectric transducer mounted to the NPRO crystal, with an actuation coefficient of order 1 MHz/V; and
3. for frequencies above  $\approx 10\text{kHz}$ , control is applied to a broadband electro-optic modulator placed at the output of the laser resonator, with an actuation coefficient of order 10 mrad/V.

Finally, we note here that the light used to illuminate the reference cavity is frequency-modulated at 79 MHz with an acousto-optic modulator (AOM) placed in a double-

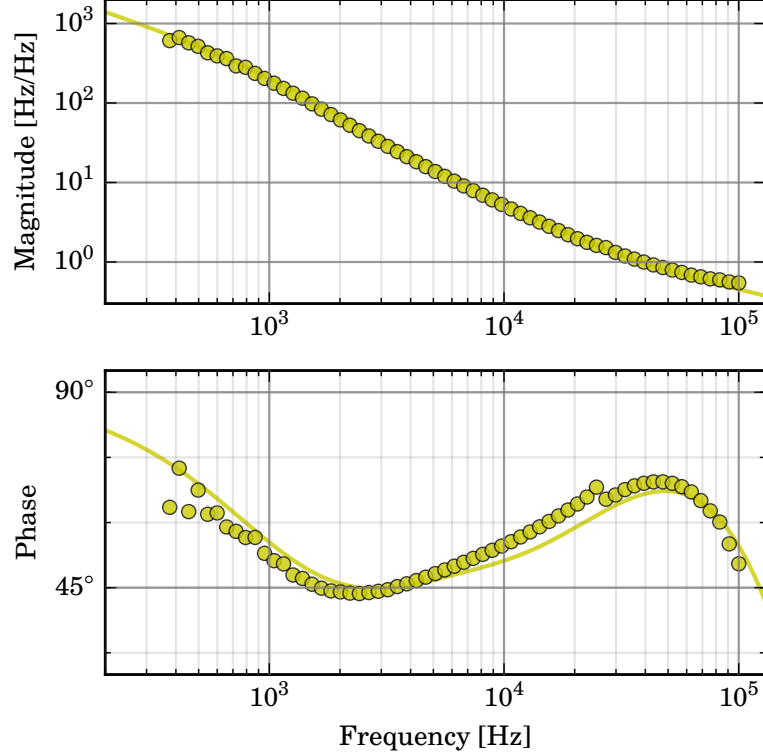


Figure 2.6: Open-loop transfer function (model and measurement) of the input modecleaner frequency locking loop, with no feedback from the interferometer.

pass configuration.<sup>h</sup> This provides a mechanism for changing the main laser frequency while keeping the light in the reference cavity on resonance: within the bandwidth of the reference cavity servo, adjusting the rf modulation frequency of the AOM produces an offset in the PDH error signal, which the servo cancels by adjusting the frequency of the main laser.

### Input modecleaner stabilization

The input modecleaner consists of three mirrors suspended in vacuum, forming a ring cavity with a 32.9 m round-trip length. The input and output coupling mirrors each have a 0.6 % transmissivity, and the third mirror is a high reflector. The cavity pole is  $f_{IMC} = 8.8 \text{ kHz}$ .

The resonance condition between the main laser and the input modecleaner is sensed with PDH reflection locking, using 24 MHz sidebands with a modulation

---

<sup>h</sup> That is, the beam is sent through the AOM, then the first-order diffracted beam is retroreflected (with a 90° polarization rotation) back into the AOM, producing light modulated at twice the AOM's rf modulation frequency. This cancels pointing fluctuations in the first-order modulated beam induced, for example, by variations in the rf modulation frequency.<sup>38</sup>

index of  $\Gamma \simeq 0.01$  rad. With 20 W of laser power incident on the modecleaner, the power on the PDH photodiode is  $P_{\text{IMC}} = 50$  mW when the modecleaner is unlocked. If the modecleaner is critically coupled (carrier visibility  $v = 1$ ), the reflected light on the photodiode when locked is entirely from the PDH sidebands, and this sets the shot-noise-limited performance of the loop at  $\sqrt{3(hc/\lambda_0)P_{\text{IMC}}\Gamma^2}/(2P_{\text{IMC}}\Gamma/f_{\text{IMC}}) = (f_{\text{IMC}}/2)\sqrt{3(hc/\lambda_0)/P_{\text{IMC}}} \simeq 15 \mu\text{Hz}/\text{Hz}^{1/2}$ . In practice, the modecleaner is not critically coupled ( $v < 1$ ) and the reflected light on the photodiode (when locked) is dominated by a few milliwatts of carrier light, giving a shot-noise limited performance  $\sqrt{2(hc/\lambda_0)(1-v)P_{\text{IMC}}}/(2P_{\text{IMC}}/f_{\text{IMC}}) = (f_{\text{IMC}}/2\Gamma)\sqrt{3(hc/\lambda_0)(1-v)/P_{\text{IMC}}} \simeq 0.4 \text{ mHz}/\text{Hz}^{1/2}$ .

Resonance is maintained by feeding the servo control signal to the AOM in front of the reference cavity, yielding a loop with roughly 50 kHz bandwidth (figure 2.6). When the interferometer is not locked, the low frequency portion of the AOM control signal is relieved by adjusting the modecleaner length, with a crossover frequency of a few tens of hertz. When the interferometer is locked, the modecleaner length is instead adjusted using the PDH error signal from the main interferometer (explained below).

## Common-mode arm length stabilization

Frequency stabilization of the laser to the common-mode arm length is again achieved with PDH locking, using the 9.1 MHz signal in reflection of the power recycling mirror.

The optomechanical transfer function from common-mode arm length fluctuation to reflected demodulated power is<sup>18</sup>

$$\delta P_{\text{refl}}^{(9I)} = 4N_1 g_p^2 r'_a r_{\text{sb}} \frac{(2\pi/c)(v_0 \delta L_+ + L_+ \delta v)}{1 + i f/f_+}, \quad (2.21)$$

where  $N_1 = 2J_0(\Gamma_9)J_1(\Gamma_9)P_0$ ,  $g_p^2$  is the power recycling gain,  $r'_a$  is the derivative of the arm reflectivity for the carrier,  $r_{\text{sb}}$  is the arm reflectivity for the sidebands, and  $f_+ \simeq 0.6$  Hz is the common-mode pole (defined in equations 2.19). Based on budgeting of the test masses and the laser, we assume that in the GW band the length fluctuations  $\delta L_+$  are negligible compared to the frequency fluctuations  $\delta v$ . Additionally,  $\delta P_{\text{refl}}^{(9I)}$  is sensitive to fluctuations in the PRC length  $\delta L_p$ , albeit to a lesser extent than common-mode fluctuations.

On this basis,  $\delta P_{\text{refl}}^{(9I)}$  is used as an error signal for frequency-stabilizing the laser to the common-mode arm length. Feedback is achieved by adjusting the modecleaner

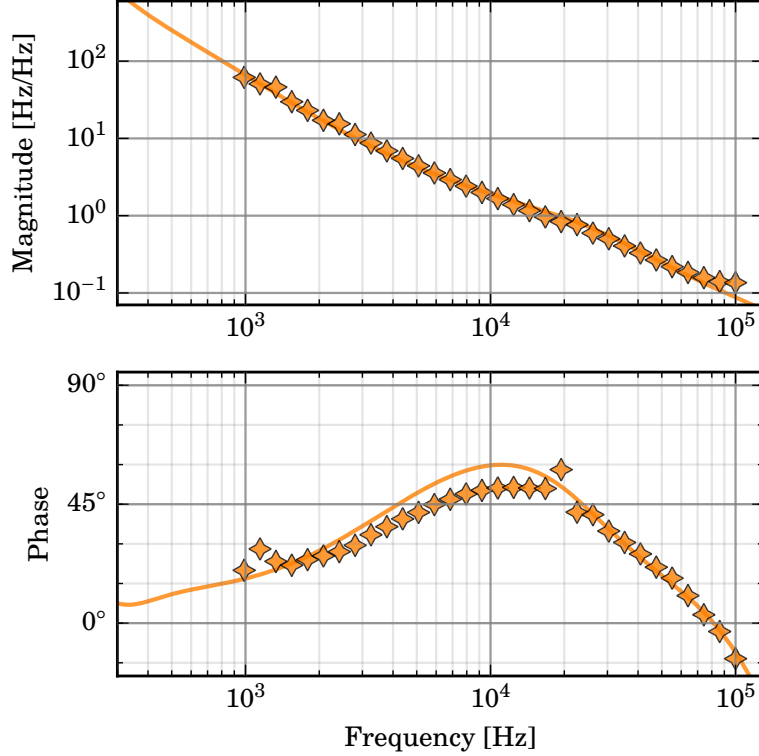


Figure 2.7: Open-loop transfer function (model and measurement) of the laser frequency locking to the interferometer common-mode arm length.

length, which is equivalent to adding an error point offset to the modecleaner frequency servo loop. Because this actuator is mechanical, it is not feasible to achieve a multi-kilohertz actuator this way. Therefore, in addition to the mechanical mode-cleaner length adjustment, the common-mode error signal is also summed directly into the modecleaner’s electronic error point (another example of “additive offset”). The open-loop transfer function of the common-mode loop is shown in figure 2.7, and the crossover between the mechanical feedback and the additive offset is shown in figure 2.8. This electronic additive offset scheme causes the modecleaner to be slightly detuned from resonance for frequencies above the additive offset crossover, but the bandwidth of the modecleaner is wide enough ( $f_{\text{IMC}} = 8.8\text{kHz}$ ) that this detuning is negligible.

The final piece of the common-mode arm length stabilization scheme is the tidal feedback. The above servo topology uses the common-mode error signal to adjust the modecleaner length, and the resulting modecleaner error signal is used to adjust the rf drive frequency of the reference cavity AOM. As the common-mode arm length drifts relative to the reference cavity length, a low-frequency control signal accumulates on the VCO driving the AOM. This VCO has a control range of  $\pm 1\text{MHz}$ ,

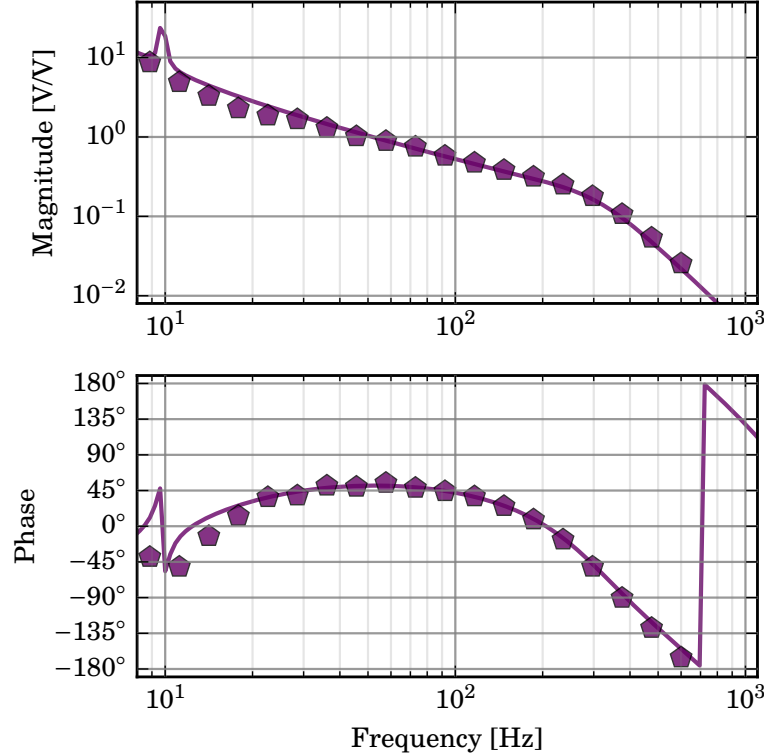


Figure 2.8: Crossover (model and measurement) from the laser frequency feedback to the modecleaner length feedback.

which means that the common-mode arm length can drift by at most  $\pm 13 \mu\text{m}$  before the VCO saturates. On the other hand, daily earth tides can produce several hundreds of microns of displacement over a 4 km baseline. To keep the interferometer locked for many hours, tidal compensation is required. To do this, the VCO control signal is offloaded to the upper-intermediate end masses, which each have a dc longitudinal range of  $13 \mu\text{m}$ .<sup>39</sup> The bandwidth of this offloading is of order 1 Hz. The low-frequency control that accumulates on each upper-intermediate mass is then offloaded to the hydraulic isolator supporting the suspension,<sup>40</sup> with a bandwidth of about 10 mHz. The range of this actuator is about 1 mm.

## Block diagram

A block diagram of the laser frequency stabilization system is given in figure 2.9. The open-loop transfer function of the common-mode arm length stabilization loop is

$$H = \frac{\bar{G}AKP(F/K + M)}{1 - \bar{G}AK}, \quad (2.22)$$

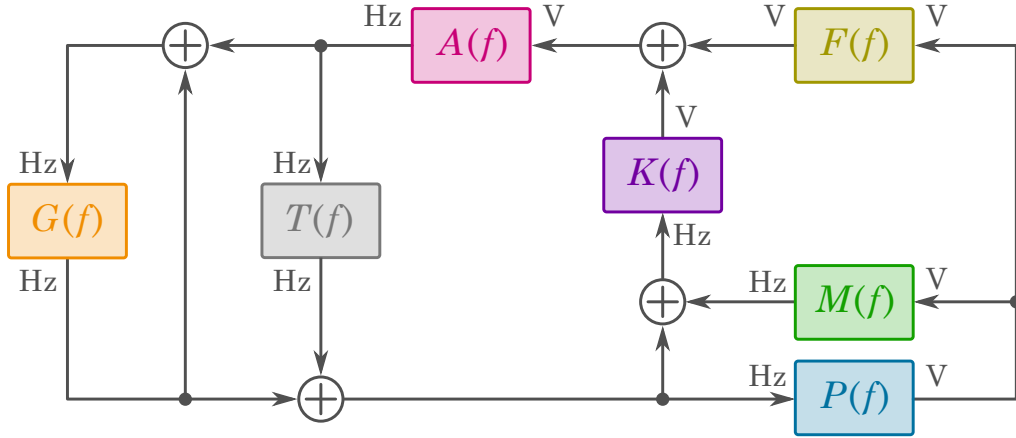


Figure 2.9: Block diagram of the Advanced LIGO frequency stabilization system.  $G(f)$  refers to the main laser and the reference cavity stabilization.  $A(f)$  refers to the AOM and its VCO, and servo electronics for feeding the input modecleaner error signal to the VCO.  $K(f)$  refers to the modecleaner and its PDH photodiode.  $P(f)$  refers to the interferometer, its PDH photodiode, and the servo electronics common to the fast and slow feedback paths.  $M(f)$  refers to the slow feedback electronics.  $F(f)$  refers to the fast feedback electronics.  $T(f)$  refers to the tidal feedback path.

where  $\bar{G} = G/(1-G)$  is the closed-loop transfer function of the reference cavity stabilization, and we have neglected the tidal offloading  $T$ . Since the UGF of  $G$  is above 100 kHz, we have  $\bar{G} \approx -1$  below a few tens of kilohertz. Note that since

$$J \equiv \bar{G}AK \quad (2.23)$$

is the open-loop transfer function of the input modecleaner length loop in the absence of any interferometer feedback, we can write  $H$  as

$$H = \frac{JP(F/K + M)}{1 - J} = \bar{J}P(F/K + M), \quad (2.24)$$

with  $\bar{J} = J/(1 - J)$ .

The crossover transfer function from the modecleaner length control to the additive offset control is given by

$$X = \frac{\bar{G}AKMP}{1 - \bar{G}AK(1 + FP/K)} = \frac{JMP}{1 - J(1 + FP/K)}. \quad (2.25)$$

## 2.3 Differential arm length control

Differential arm length is controlled by sensing the fluctuations in the carrier light at the interferometer's dark port and feeding the signal back to one of the end test

masses. Since dark port fluctuations are also used to estimate the strain  $h(t)$  incident on the detector, the sensing and control of this degree of freedom must be exceptionally low noise, and the transfer function from differential test mass force to dark port power must be well characterized. Table 2.3 lists parameters relevant to the differential arm length control.

## Optomechanical response

The interferometer's optomechanical response determines how differential test mass force  $F$  (for example, from a GW strain  $h$ ) produces power fluctuation  $P$  at the dark port. While this quantity is fundamentally a force-to-power transfer function  $P(\omega)/F(\omega)$ , we often cast it instead as a displacement-to-power transfer function  $P(\omega)/L_-(\omega)$ , where  $L_- = F/(-M\omega^2)$  is the differential arm length displacement for free masses each with mass  $M$ . In the GW band, deviation from the free-mass assumption can arise if the interferometer is operated with a microscopic phase offset in the SRC length, as such detuned configurations induce an optical spring.<sup>41</sup>

While the initial LIGO detectors used PDH sensing to read out the dark port signal, the enhanced and advanced detectors instead use a self-homodyne technique called “dc readout”.<sup>42</sup> The differential arm length is held with an intentional dc offset (of order 10 pm), so that carrier light from the arms appears at the dark port. When the differential arm length fluctuates (for example, from a GW), it creates carrier audio sidebands that also appear at the dark port and modulate the amplitude of the dark port field. For pure signal extraction, the transfer function from free differential test mass displacement to antisymmetric port fluctuation is<sup>18</sup>

$$\delta P_{\text{as}}(f) = 2N_{\text{dc}} g_p^2 g_s^2 r_a'^2 \left( \frac{2\pi}{\lambda_0} \right)^2 \frac{\delta L_-^{(0)} \delta L_-(f)}{1 + if/f_-}, \quad (2.26)$$

where  $\delta L_-^{(0)}$  is the microscopic differential length offset,  $f_-$  is the optical pole given by (2.20), and

$$N_{\text{dc}} = 4J_0(\Gamma_9)^2 J_0(\Gamma_{45})^2 P_{\text{in}}. \quad (2.27)$$

In any case other than pure signal extraction or pure signal recycling, the optomechanical response involves two additional quantities.

The first parameter is the homodyne angle. Homodyne detection techniques such as dc readout work by beating a signal-modulated field  $\sqrt{2}E_0[1+\alpha(t)]\cos[\omega_0 t + \phi(t)]$  against an unmodulated local oscillator field  $\sqrt{2}E_0 \cos[\omega_0 t + \zeta]$ , where  $\zeta$  is a static

phase offset known as the homodyne angle. For certain homodyne detection topologies (for example, a Mach–Zender interferometer), the homodyne angle may be adjusted by varying the relative path length traveled between the local oscillator field and the signal field (for example, using a piezoelectrically actuated mirror). In ideal dc readout, however, both the local oscillator field and the signal field co-propagate inside the interferometer, meaning that the homodyne angle is fixed at  $\zeta = \pi/2 = 90^\circ$ . The addition of a contrast defect produces carrier light in the quadrature orthogonal to the local oscillator light, causing a rotation of the homodyne angle. The condition  $\zeta = 90^\circ$  is known to have been satisfied to better than  $3^\circ$  during O1, based on the total amount of contrast defect light exiting the dark port with no dc readout light.

The second parameter is the SRC detuning. The static, one-way microscopic SRC detuning phase is  $\phi_s^{(0)} = (2\pi/\lambda_0) \delta L_s^{(0)}$ .  $\phi_s^{(0)} = 0$  corresponds to pure signal recycling, and  $\phi_s^{(0)} = \pi/2$  corresponds to pure signal extraction. Other detuning phases result in an optical spring that reduces the displacement-to-power transfer function below the spring frequency; a fuller discussion of this effect is given in chapter 5. Nominally, Advanced LIGO is configured to operate with pure signal extraction for the first few observing runs. However, during O1, H1 operated with about  $0.5^\circ$  of unintentional positive (antispring) detuning, likely due to an offset in the angular control of the signal recycling mirror. This was observed as a loss of gain in the optomechanical response around 10 Hz and below, as measured by a calibrated differential arm length radiation pressure actuator (the photon calibrator). The antispring effect was subsequently confirmed by measuring the optomechanical response as a function of (intentional) microscopic SRC length detuning (figure 2.10).

## Readout

The laser light exiting the antisymmetric port contains the dc readout carrier light, the audio-band signal field, the rf control sidebands (mostly the 45.5 MHz sidebands), and carrier light that is not mode-matched into the arm cavities (the “contrast defect” light).

The goal of dc readout is to sense the audio-band beat note between the dc carrier light and the carrier audio sidebands (rather than the rf beatnote between the 45.5 MHz light and the carrier audio sidebands, which is the idea of PDH). To do this, an output modecleaner is used to separate the carrier light from the rf sideband light; the carrier light (and its audio sidebands) are then directed onto

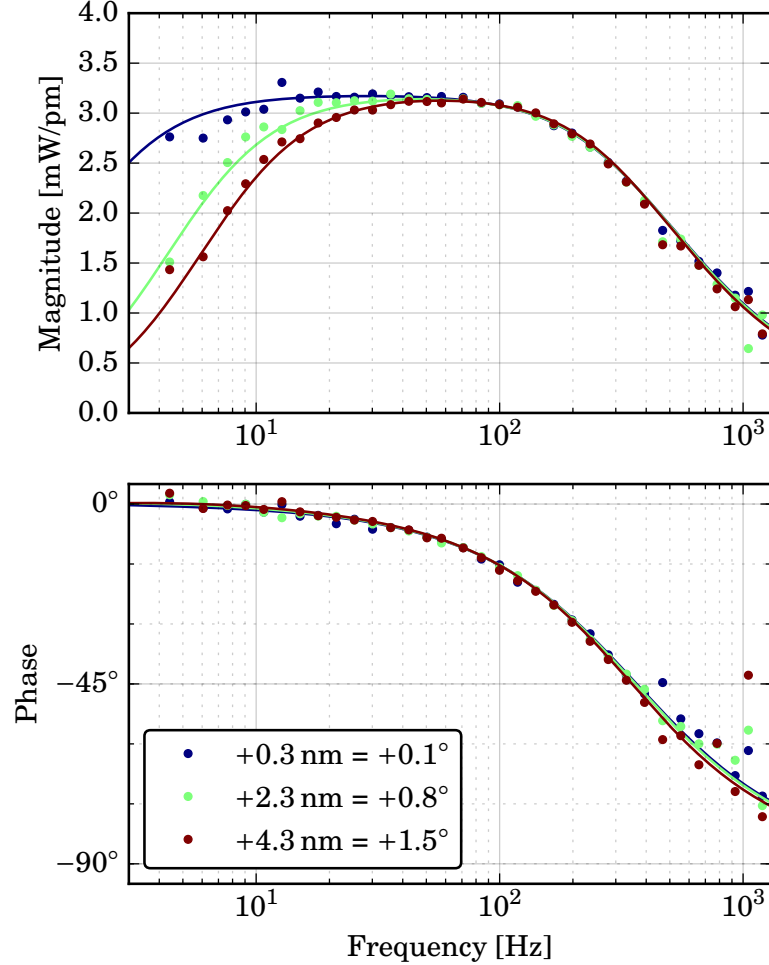


Figure 2.10: Optomechanical response of the interferometer’s differential arm length, shown for several different SRC detunings at 10 W of input power. Solid lines show estimated theory curves. Fundamentally, this transfer function is a force-to-power transfer function  $P(f)/F(f)$ , but here (as is customary) the force is referred to the displacement  $x = -F/M\omega^2$  of a free mass.

two InGaAs photodiodes, each with a 3.0 mm diameter. Each photodiode is reverse-biased with +12 V.<sup>49</sup> In vacuum, the photocurrent from each photodiode is shunted across a resistor, and the resulting voltage is read out with an LT1128 op-amp. The shunt resistor is selectable, and may be either  $100\Omega$  or  $400\Omega$ .<sup>50</sup> The summed photocurrent of these two photodiodes is the differential arm length error signal. Two photodiodes (rather than one) allow for a greater amount of dc offset light to be used, and also provide an important diagnostic tool (the “null stream”), formed by differencing the two photocurrents.

The output modecleaner is kept resonant by adjusting one of its two piezoelectri-

Photodiode current (total)	20 mA dc
Photodiode quantum efficiency	0.88
Photodiode responsivity	0.75 A/W
Optical gain <sup>43</sup>	4.2(2) mW/pm
Optical pole <sup>43</sup>	340(20) Hz
Microscopic arm detuning ( $L_x - L_y$ )	12.5(4) pm
Microscopic RSE detuning (one-way) <sup>44</sup>	1.5(6) nm
Homodyne angle <sup>45</sup>	90(3) °
Time delay <sup>i;46</sup>	427 μs
Freerunning noise <sup>47</sup>	0.6 μm rms
Residual noise <sup>47</sup>	60 fm rms
Actuator	EY
Loop bandwidth	45 Hz
Relief bandwidth to penultimate mass	20 Hz
Relief bandwidth to antipenultimate mass	2 Hz
Relief bandwidth to hydraulic actuator	11 mHz

<sup>i</sup>Includes optical time delay ( $L/c = 13 \mu\text{s}$ ),<sup>37</sup> digital delays,<sup>48</sup> and the delay from uncompensated high-frequency transfer function features.<sup>46</sup>

Table 2.3: Parameters for differential arm length sensing and control for aLIGO H1 during the first observing run. The parameters for L1 are similar, although no RSE detuning was observed.

cally actuated mirrors. The resonance condition is sensed by applying a 4.1 kHz dither to this mirror and demodulating the resulting line in the GW signal.

## Control

The differential arm length control signal is fed back to one test mass only. This also alters the interferometer's common-mode arm length, but the frequency stabilization servo strongly suppresses these fluctuations. The UGF of the differential arm length loop is about 50 Hz. The OLTF is shown in figure 2.11. Three out of the four stages of the suspension are used to displace the test mass; the crossover transfer functions for this control hierarchy are shown in figure 2.12.

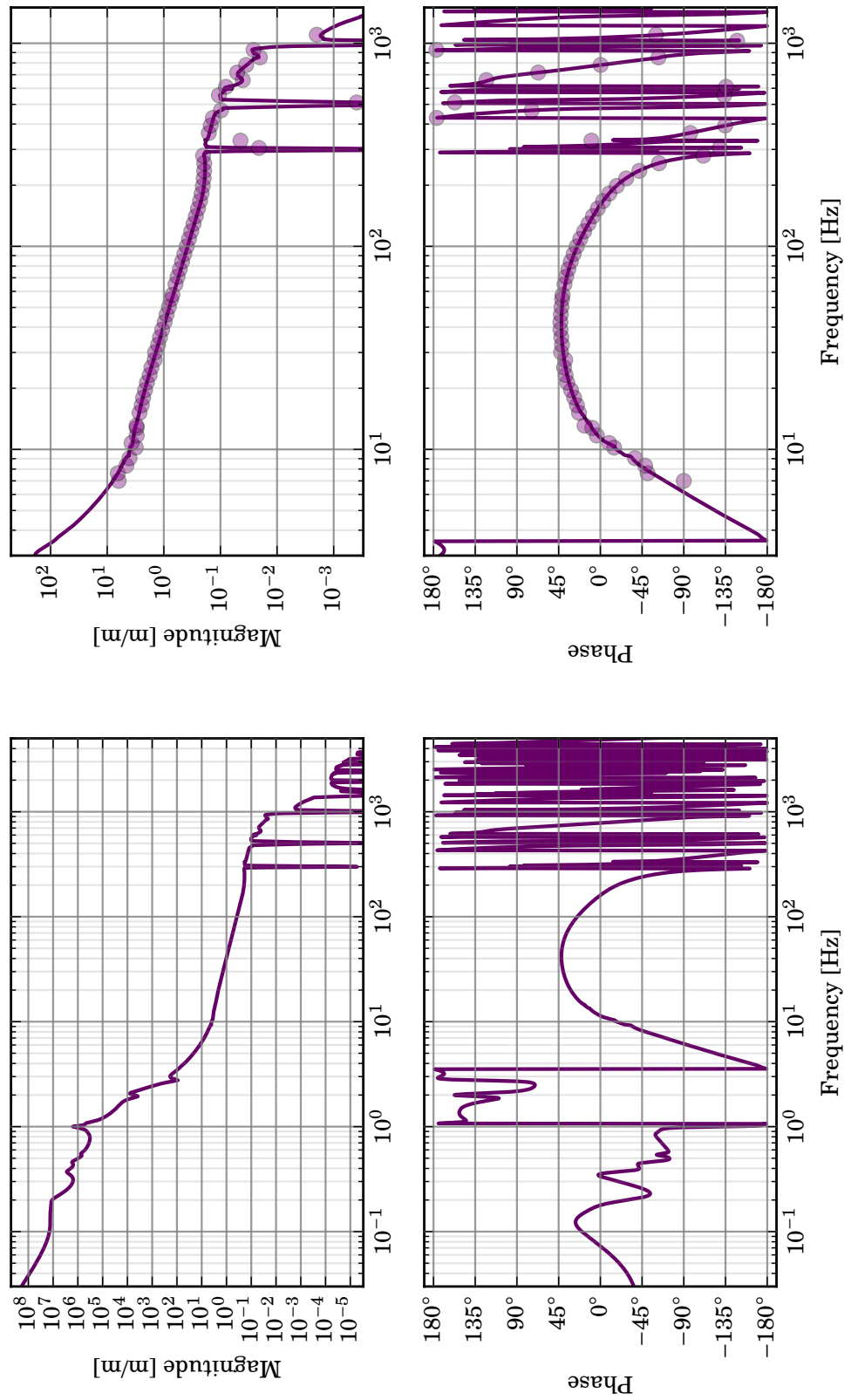


Figure 2.11: Open-loop transfer function model of the differential arm length control. The right-hand plot is a zoomed-in version of the left-hand plot, with the measurement shown.<sup>51</sup>

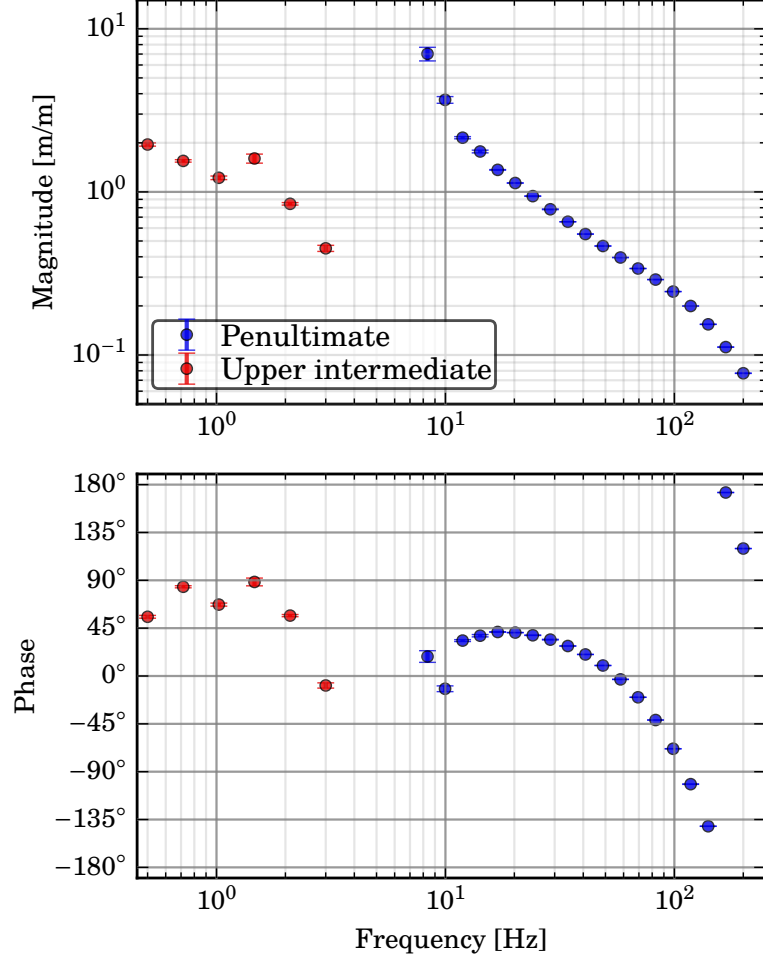


Figure 2.12: Crossover transfer functions for the penultimate and upper-intermediate actuator offloading for the differential arm length control.

Since dc readout is intrinsically quadratic, differential arm length motion at a frequency  $f$  can produce upconverted fluctuation in the readout at a frequency  $2f$ . To keep this upconverted noise well below the true differential arm length noise, the allowed residual differential arm length fluctuation is set at 1 fm.<sup>35</sup> During the first observing run, the residual fluctuation was instead a few tens of femtometers.<sup>47</sup> However, dc readout upconversion could not be shown to limit the interferometer noise performance in the GW band.<sup>52</sup>

## 2.4 Noise from vertex length controls

	PRC	Michelson	SRC
Photodiode power	17 mW dc	17 mW dc	17 mW dc
Optical gain	3.6 W/ $\mu\text{m}$	0.60 W/ $\mu\text{m}$	0.13 W/ $\mu\text{m}$
Freerunning noise	0.9 $\mu\text{m}$ rms	0.4 $\mu\text{m}$ rms	0.1 $\mu\text{m}$ rms
Residual noise	1.0 pm rms	5 pm rms	20 pm rms
Actuator	PRM	Beamsplitter	SRM
Loop bandwidth	65 Hz	10 Hz	25 Hz
Upper mass relief bandwidth	60 mHz	30 mHz	60 mHz

Table 2.4: Parameters for vertex length sensing and control for aLIGO H1 during the first observing run. The parameters for L1 are similar.

#### H1 vertex length sensing, 2016-01-13

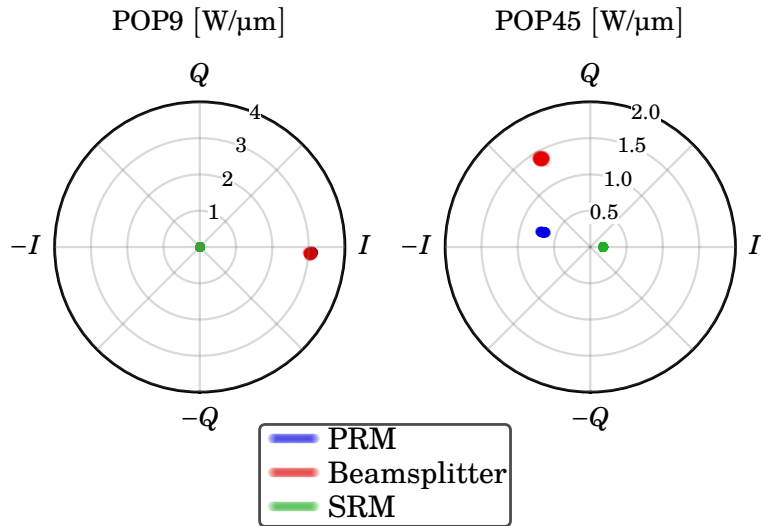


Figure 2.13: Sensing matrix of the vertex degrees of freedom. The cross-coupling of the beamsplitter from a  $Q$  (pure Michelson) signal into  $I$  (PRC or SRC) signal can be seen in the 45 MHz channel. In the 9 MHz measurement, the PRC and beamsplitter elements are on top of each other.

### Optical response and readout

Per watt of incident photodiode power, the vertex degrees of freedom are best sensed at the power-recycling pick-off port (POP), rather than the reflected port or the antisymmetric port. Using POP to sense the vertex lengths requires very strong suppression of common-mode fluctuations, as this signal shows up more strongly

in POP9I and POP45I than any of the vertex lengths. Once this requirement is satisfied, the next strongest signal is the PRC length, which shows up most strongly in POP9I. The Michelson length shows up most strongly in POP45Q. Finally, the SRC length shows up most strongly in POP45I. However, the PRC length also shows up in POP45I, with greater strength than the SRC length.<sup>18</sup> Therefore, the error signal for the SRC length control uses a combination of POP45I and POP9I which is insensitive to PRC length fluctuation. The sensing matrix of the POP sensors is shown in the radar plots in figure 2.13.

There remains the question of how to choose the UGFs of these three loops. First, PRC length fluctuations show up more strongly than SRC length fluctuations in both POP9 and POP45; therefore, the PRC length UGF should be higher than the SRC length UGF. Second, if the beamsplitter is used to control the Michelson length, there will be cross-coupling of Michelson actuation into power- and signal-recycling lengths; therefore, the UGF of the Michelson loop should be lower than either the PRC and SRC loops. These two considerations set the Michelson loop as the lowest UGF loop, and the PRC loop as the highest UGF loop. Table 2.4 gives relevant parameters for these loops.

The residual rms requirement for the vertex length loops is set at 1 pm, based on the linearity limit of the photodetector.<sup>35</sup> During the first observing run, the actual residual rms of the loops was less than 20 pm (figures 3.8, 3.9, and 3.10).

The OLTFs of the vertex loops are shown in figure 2.14.

## Cross-coupling into differential arm length

### Optomechanical cross-coupling

The differential arm length error signal  $e_-$  has contributions not only from freerunning displacement noise ( $L_-$ ) and photodiode sensing noise ( $n_-$ ), but also from residual noises from other degrees of freedom—particularly the Michelson length and the SRC length.

The Michelson coupling into the differential arm length readout is a straightforward phase coupling: Michelson motion produces differential phase sidebands, which are converted to amplitude sidebands at the antisymmetric port in the same manner as differential phase sidebands from the arms. Because the length-to-phase conversion for differential arm length fluctuations is enhanced by  $g_a^2 = 2\mathcal{F}/\pi \approx 280$

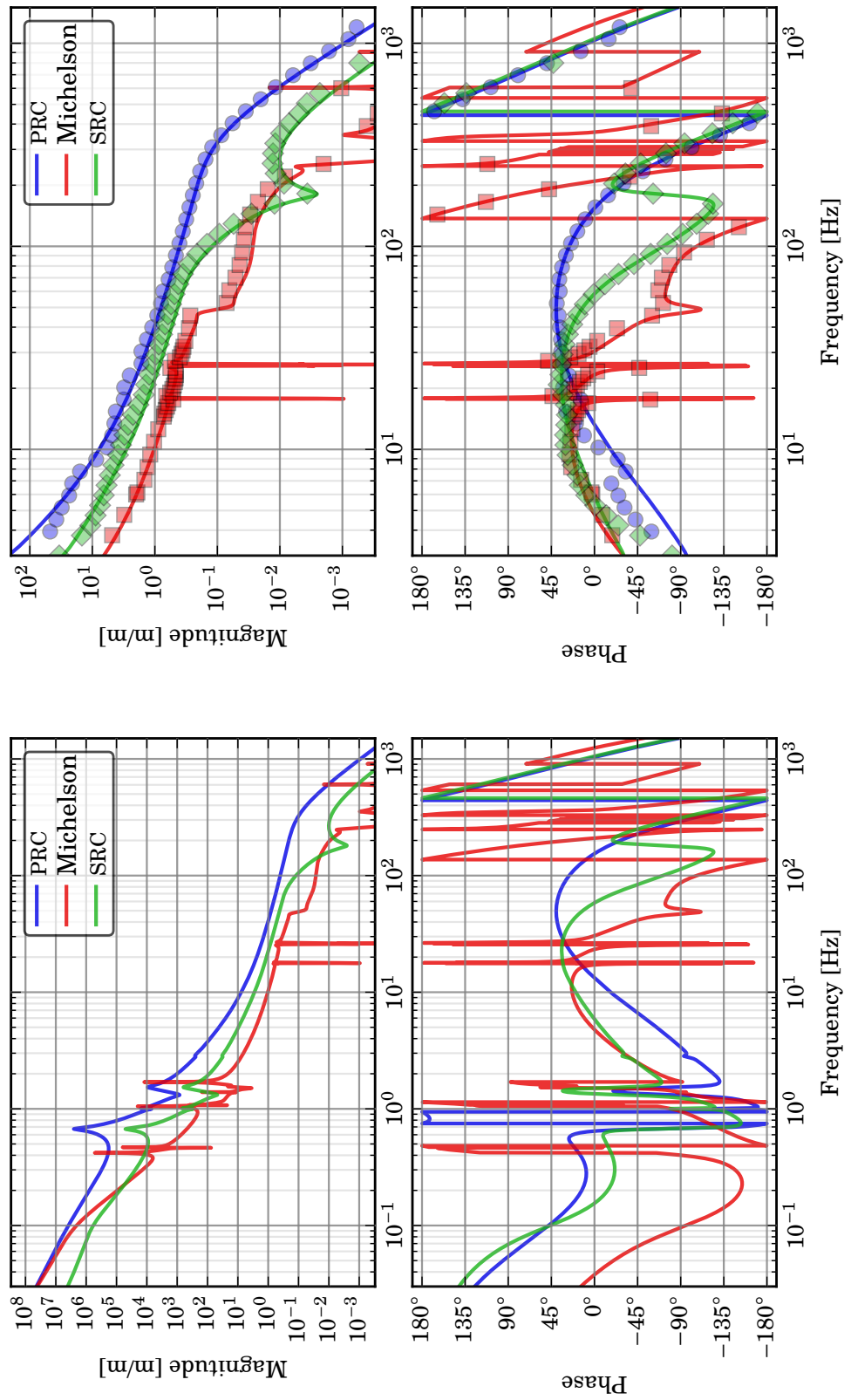


Figure 2.14: OLTFs of the vertex length degrees of freedom, shown across two different frequency ranges. Points show the results of measurements; lines show the corresponding models. The right-hand plots are zoomed in from the left-hand plots.

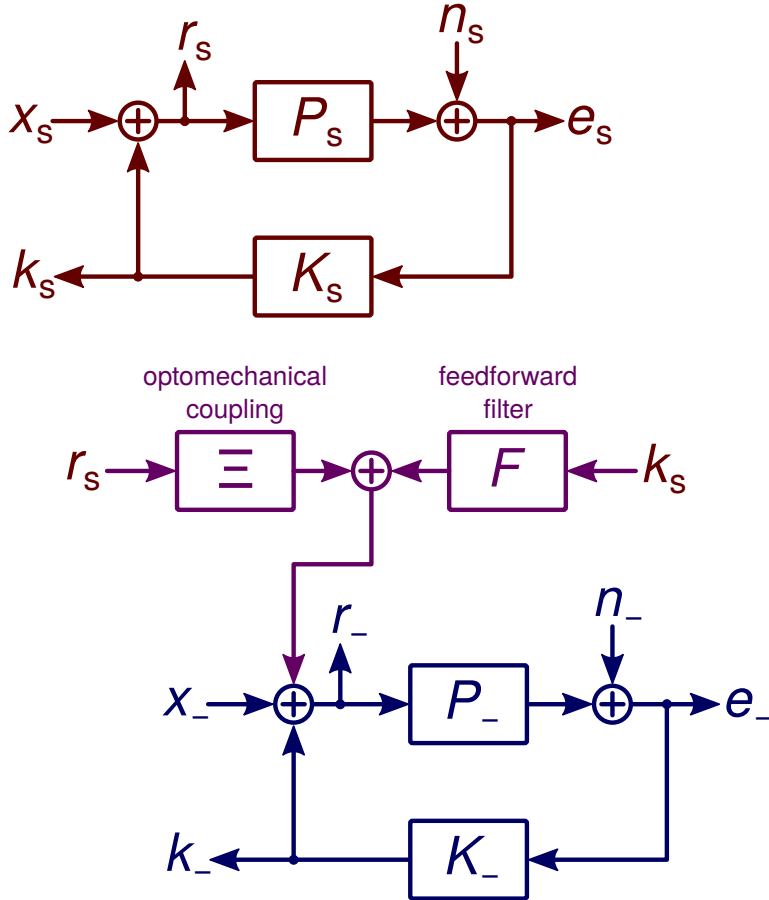


Figure 2.15: Illustration of optomechanical coupling and feedforward subtraction, here for the SRC length loop coupling into differential arm length. Residual SRC length fluctuation  $r_s$ , which comprises both suppressed displacement noise  $x_s/(1 - H_s)$  and impressed sensing noise  $H_s n_s/(1 - H_s)$ , couples into the differential arm length readout via some optomechanical coupling  $\Xi$ . To reduce the influence of this coupling on the differential arm length readout, the SRC length control signal  $k_s$  is summed (either mechanically, digitally, or analogly) into the differential arm length error point via some feedforward filter  $F$ . In general, it is not possible to construct a filter  $F$  which simultaneously cancels the displacement and sensing noise contributions to  $r_s$ .

relative to the length-to-phase conversion for Michelson fluctuations, the expected coupling of Michelson motion into differential arm length readout (expressed as an equivalent differential arm length motion) is<sup>27</sup>

$$\Xi_m = \frac{1}{g_a^2} = \frac{\pi}{2\mathcal{F}} \approx 3.6 \times 10^{-3} \text{ m/m.} \quad (2.28)$$

The measured coupling is shown in figure 2.17.

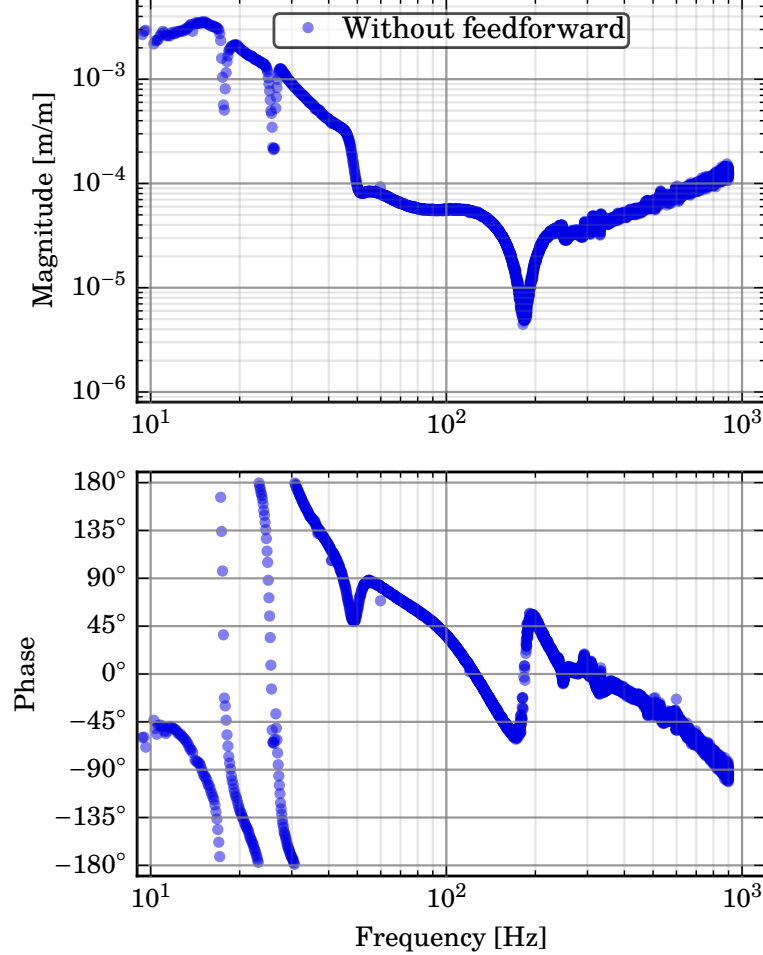


Figure 2.16: Coupling of power recycling mirror motion into differential arm length readout.

The signal recycling length coupling into the differential arm length readout has several parts. The first is a  $1/f^2$  coupling mediated by radiation pressure: SRC phase sidebands propagate into the arms and produce differential intensity fluctuations, which are converted to differential length fluctuations via radiation pressure.<sup>18,27</sup> The second is a high-frequency coupling rising like  $f^2$ ; it appears if the SRC is microscopically detuned from pure resonant sideband extraction.<sup>27</sup> These two effects together imply a coupling of SRC motion into differential arm length motion:<sup>27</sup>

$$\begin{aligned} \Xi_s = & 0.012 \text{ m/m} \times \frac{P_a}{750 \text{ kW}} \times \frac{\delta L_-^{(0)}}{10 \text{ pm}} \times \frac{\mathcal{F}}{450} \times \left( \frac{10 \text{ Hz}}{f} \right)^2 \\ & + 3 \times 10^{-5} \text{ m/m} \times \frac{\phi_s^{(0)}}{10^\circ} \times \frac{\delta L_-^{(0)}}{10 \text{ pm}} \times \frac{\mathcal{F}}{450} \times \left( \frac{f}{100 \text{ Hz}} \right)^2. \end{aligned} \quad (2.29)$$

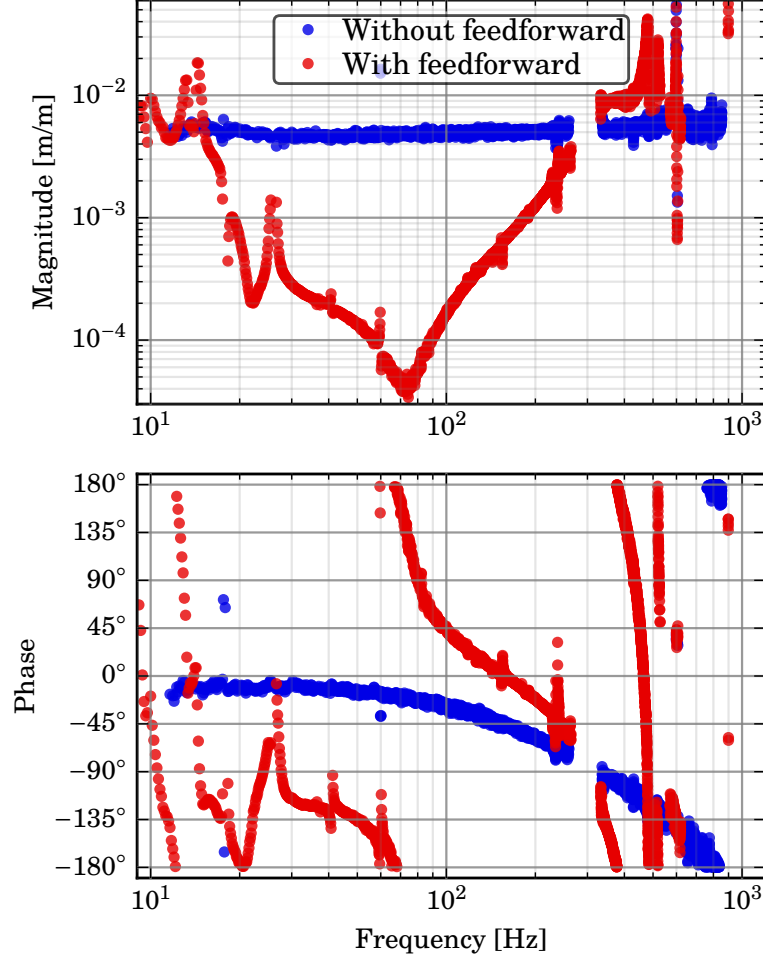


Figure 2.17: Coupling of beamsplitter motion into differential arm length readout.

Finally, another class of high-frequency couplings, generally rising like  $f$  or faster, can arise from nonidealities such as arm imbalances and angular control offsets,<sup>53</sup> but these effects are not easily quantified analytically. The measured SRC length coupling into the differential arm length readout is shown in figure 2.18.

Additionally, the measured PRC length coupling into the differential arm length readout is shown in figure 2.16.

### Feedforward subtraction

The cross-couplings described above seem to set a hard limit on the allowed residual fluctuation of the vertex degrees of freedom, based only on the desired differential arm length sensitivity and the magnitude of the cross-coupling. However, because the residual vertex fluctuations are witnessed by other sensors, it is possible to sub-

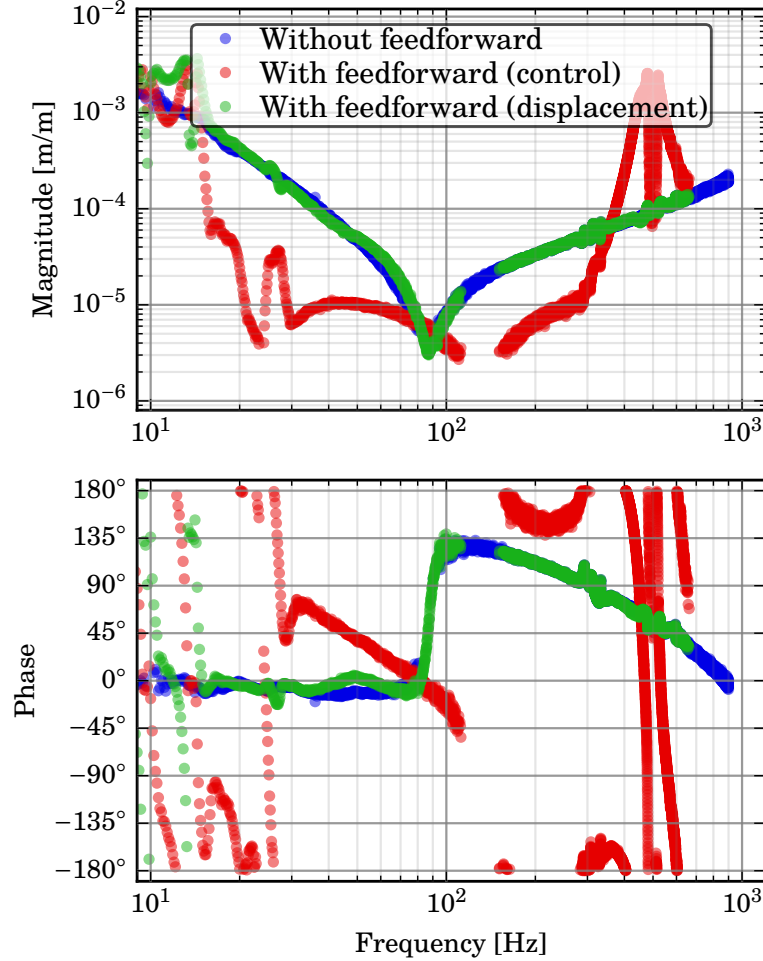


Figure 2.18: Coupling of signal recycling mirror motion into differential arm length readout. Note in this case that because the bandwidth of the SRC loop is low, the application of feedforward subtraction does not worsen the displacement noise coupling into the differential arm length readout.

tract off these cross-coupled signals from the differential arm length.<sup>54</sup> This may be done after the fact—using stored sensor data—or it may be done mechanically in real time by feeding the expected cross-coupled signals forward onto the test masses. This latter strategy was employed for the first observing run.

Figure 2.15 shows an implementation of feedforward subtraction of SRC length into differential arm length. The residual SRC length noise is

$$r_s = \frac{x_s + K_s n_s}{1 - H_s}, \quad (2.30)$$

where  $x_s$  is the loop’s freerunning displacement noise, and  $n_s$  is the loop’s sensing noise. The term  $K_s n_s / (1 - H_s)$  is therefore the “control noise” impressed onto the SRC length by the sensor.

An optomechanical coupling  $\Xi(f)$  produces an apparent noise  $\Xi \times r_s$  in the differential arm length readout. To cancel this coupling, we can design a filter  $F(f)$ , apply it to the SRC length control signal  $k_s$ , and apply the product  $F \times k_s$  to the differential arm length actuation to cancel  $\Xi \times r_s$ . However, since

$$k_s = \frac{P_s x_s + K_s n_s}{1 - H_s} \neq r_s, \quad (2.31)$$

it is in general not possible to design a filter  $F$  which simultaneously cancels the couplings from both  $x_s$  and  $n_s$ . If we wish to cancel the coupling from  $x_s$ , we should choose  $F = \Xi/P_s$ . On the other hand, if we wish to cancel the coupling from  $n_s$ , we should choose  $F = \Xi$ . Note that feedforward that is tuned to cancel the coupling of  $x_s$  may worsen the coupling of  $n_s$ , and vice versa.

For the first observing run, feedforward was employed for the Michelson and SRC lengths by actuating on the penultimate stages of the input test masses. The feedforward was tuned so as to cancel sensing noise, since this noise was expected to dominate over the intrinsic cavity noise. However, because the Michelson and SRC loop bandwidths are relatively low, the feedforward filters are able to cancel sensing noise without appreciably worsening the displacement noise couplings.

## 2.5 Angular control

This section presents an overview of the angular sensing and control for the Hanford interferometer. Table 2.5 enumerates the angular loops and gives their bandwidths.

### Readout techniques

Two general classes of interferometric angular readout are employed in Advanced LIGO: wavefront sensing, which is an extension of the PDH technique, and audio-band pointing.

Both types of loop operate on the principle that misalignment of a  $\text{TEM}_{00}$  beam relative to an optical cavity (and vice versa) generates  $\text{TEM}_{01}$  light. Beat notes involving  $\text{TEM}_{01}$  light against  $\text{TEM}_{00}$  light are sensed using quadrant photodetectors, with the photocurrents differenced as appropriate to generate either pitch or yaw signals. In the case of wavefront sensing, the signal of interest is generated from the beat of  $\text{TEM}_{00}$  audio-band light against  $\text{TEM}_{00}$  rf sideband light, or vice

Loop	Sensor	Bandwidth [Hz]	
		Pitch	Yaw
Diff. hard	AS 45 MHz	2.1 $\diamond$	3.6 $\diamond$
Comm. hard	Refl. 9 MHz	<0.1	<0.1
Diff. soft	Arm trans. dc	<0.05	<0.05
Comm. soft	Arm trans. dc	<0.05	<0.05
PRM	POP dc	0.03	0.2
PR2	—	—	—
PR3	Refl. 9+45 MHz	0.12	0.08
Beamsplitter	AS 36 MHz	2 $\diamond$	3 $\diamond$
SRM	AS 36 MHz	0.13	0.4
SR2	AS dc	1.2 $\diamond$	2 $\diamond$
SR3	Shadow sensor	~0.03	—
ITM	Optical lever	—	—
Input pointing	Refl. 9 MHz	0.10	0.06

Table 2.5: Sensors for and bandwidths of the angular control loops for H1. Values marked by  $\diamond$  were determined by OLTF measurement, and refer to the highest UGF where applicable. All others were determined by step response. No yaw control was implemented for SR3, and no control was implemented for PR2.

versa.<sup>j;55,56</sup> In the case of audio-band pointing, the signal of interest is generated by TEM<sub>01</sub> audio sideband light against TEM<sub>00</sub> carrier light, or vice versa.

Beam misalignment may take the form of a tilt, a translation, or both, and hence fully sensing the misalignment requires at least two quadrant detectors, separated by some amount of Gouy phase (preferably 90°).

## Arm loops

### Optomechanical plants

The eight arm loops constitute the most phenomenologically rich angular control loops. The power stored in the arms generates not only radiation pressure that affects the interferometer's length responses, but also radiation torques that affect

<sup>j</sup> That is, TEM<sub>01</sub> rf light against TEM<sub>00</sub> carrier light.

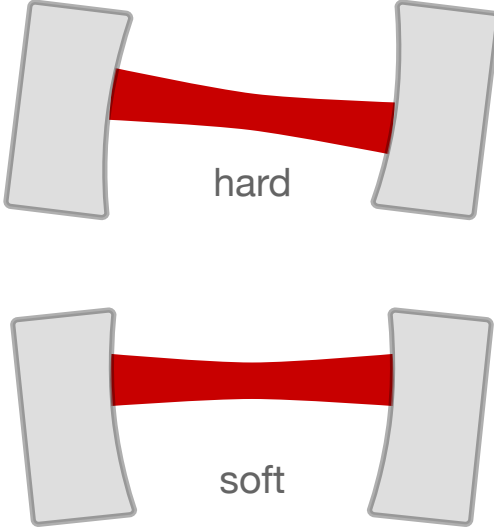


Figure 2.19: Diagram of hard and soft cavity optic motions. The hard mode is so named because the radiation torque enhances the mechanical stiffness of the optic suspensions, while the soft mode diminishes it.

the interferometer's angular responses. The effect of these radiation torques was first analyzed by Sidles and Sigg,<sup>57</sup> and we summarize the relevant points here.

In the absence of radiation pressure, the transfer function taking test mass torque to test mass angle is determined only by the mechanics of the mass and its suspension; for Advanced LIGO, the relevant torsional constants are  $\kappa_p = 9.7 \text{ N m/rad}$  and  $\kappa_y = 9.4 \text{ N m/rad}$ .<sup>58</sup> The corresponding angular frequencies are  $f_{p,y} = (1/2\pi)\sqrt{\kappa_{p,y}/I_{p,y}}$ .

In the presence of radiation pressure, the four test masses are coupled together, and the eigenmodes of the coupled system involve simultaneous motions of the test masses together. The eigenvalues of the system give two optical torsional constants:<sup>58</sup>

$$\kappa_{s,h} = \frac{LP}{c} \times \frac{(g_e + g_i) \pm \sqrt{(g_e - g_i)^2 + 4}}{g_e g_i - 1}, \quad (2.32)$$

where  $g_{i,e} = 1 - L/\mathcal{R}_{i,e}$  is the  $g$  factor of each test mass. These torsional constants are added to the mechanical torsional constant of the suspension in order to give the overall torsional constant of the mode. The hard and soft modes of a two-mirror cavity are illustrated in figure 2.19.

An important consequence of this particular eigenvalue problem is that one of these eigenvalues ( $\kappa_h$ ) is always positive, and the other is always negative ( $\kappa_s$ ). Therefore, one set of modes has a torsional constant  $\kappa = \kappa_{p,y} + \kappa_h$  that is stiffer than the

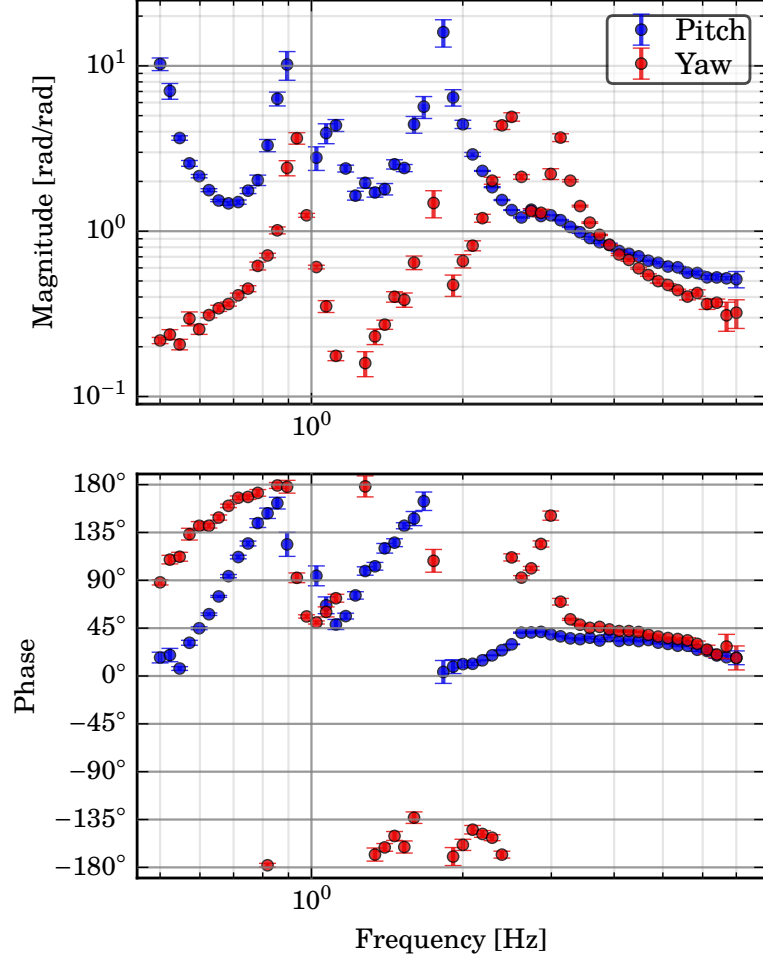


Figure 2.20: Open-loop transfer functions for angular control of the differential hard mode. The multiple UGFs arise from imbalances between the test mass actuators, overly aggressive test-mass bounce-mode cutoff filters, and insufficient boosting in the digital compensator. These issues were resolved after O1.

mechanical torsion (the “hard modes”), and the other set has a torsional constant  $\kappa = \kappa_{p,y} + \kappa_s$  that is softer than the mechanical torsion (the “soft modes”). If  $|\kappa_s| > \kappa_{p,y}$ , the soft modes become unstable, and require active control with a bandwidth sufficient to stabilize the unstable poles. In Advanced LIGO, the test mass  $g$  factors ( $g_i = -0.78$  and  $g_e = -1.06$ ) are chosen in part to make  $|\kappa_s|$  small: with 800 kW of power in each arm, the primary hard mode resonance frequency is expected to be around 3 Hz, and the soft mode resonance is expected to be around -0.3 Hz.

## Sensing and actuation

Based on simulations by Barsotti et al.<sup>58</sup> and some experimental trial and error, the following sensors were chosen for the arm modes:

- the 45 MHz antisymmetric port WFSs are used to sense the differential hard mode (OLTF shown in figure 2.20);
- the 9 MHz WFSs in reflection are used to sense the common hard mode; and
- the end station dc QPDs are used to sense the common and differential soft modes.

For the WFS loops, the general procedure for producing a suitable error signal is given in the following.

1. Ensure that a suitable centering loop is closed around each WFS.
2. Drive a line in the relevant DOF. Verify that the line appears in every quadrant of the relevant WFSs.
3. Rotate the (digital) demodulation phases so that the signal shows up in the same quadrature for each quadrant. Verify that the line appears with roughly the same amplitude in each quadrant.
4. Choose a linear combination of the WFSs that gives a usable error signal. “Usable” here is somewhat ill-defined, but we can identify some desirable characteristics.
  - a) The error signal crosses zero in the appropriate place; for example, in a place where some power buildup is maximized. If each individual WFS signal has an undesired dc offset, an appropriate combination of two signals may sometimes be found with a zero crossing in the right place.
  - b) The error signal is relatively insensitive to other DOF(s). If each individual WFS senses some DOF much more strongly than the DOF of interest, an appropriate combination of two signals may sometimes be found which is sensitive to the DOF of interest but insensitive to the other DOF. Rejection of other DOFs in the error signal may be achieved after the fact by diagonalizing the interferometer’s angular sensing matrix.

For the hard loops, the error signals were initially chosen to give good zero crossings (no suppression of other DOFs was considered). For the differential hard loops, a relatively high bandwidth (more than 3 Hz) is required to keep the antisymmetric port power stable enough to keep the interferometer locked with zero common-mode arm length offset. The common-mode hard loops may also be operated at

similarly high bandwidths. However, during O1, the coupling of the sensor noise from the 9 MHz reflection WFSs into the differential arm length readout was so high that these loops were operated with lower bandwidth.

For the pointing loops, the procedure signal selection procedure is similar, although no phasing is required. For the soft loops, the QPD combination at each end station was chosen to minimize the sensitivity of the signal to motion of the suspension which supports the QPDs.<sup>59</sup> Importantly, this does *not* minimize the sensitivity of the resulting error signals to hard motion, and indeed hard motion is seen with good SNR in the soft loop error signals. Therefore, the stable operation of these loops relies on gain hierarchy, with the soft loop UGFs kept well below the hard loop UGFs. The positions of the end station spots were chosen to maximize the interferometer recycling gain.

For all the arm loops, the penultimate test masses are used as actuators. Importantly, in order for the loops to be properly coupled into the hard/soft basis, the test mass actuation transfer functions must be made uniform; this requires that top-stage local damping is uniform, and that the penultimate stage actuators are balanced. The relatively sharp zeros observed in 2.20 are indicative of actuator mismatch between test masses.

In addition to the interferometric loops listed here, local pitch damping (via optical levers) was also applied to the input test masses during O1 in order to avoid the common-mode soft instability (see below). This also contributes to the actuator mismatch for the hard and soft loops.

## Symmetric port loops

On the symmetric port side, six degrees of freedom are controlled.

1. The difference of the 9 MHz reflection WFSs is used to sense the input pointing of the beam into the interferometer. The actuator is the final steering mirror into the interferometer (IM4).
2. During O1, a combination of the 45 MHz reflection WFSs is used as an error signal to control the angle of the large PRC folding mirror (PR3). The 9 MHz WFS were also used to subtract common-mode hard motion from the PR3 error signal.
3. The pointing of the PRC light onto one of the PRC QPDs is used to control the angle of the power recycling mirror.

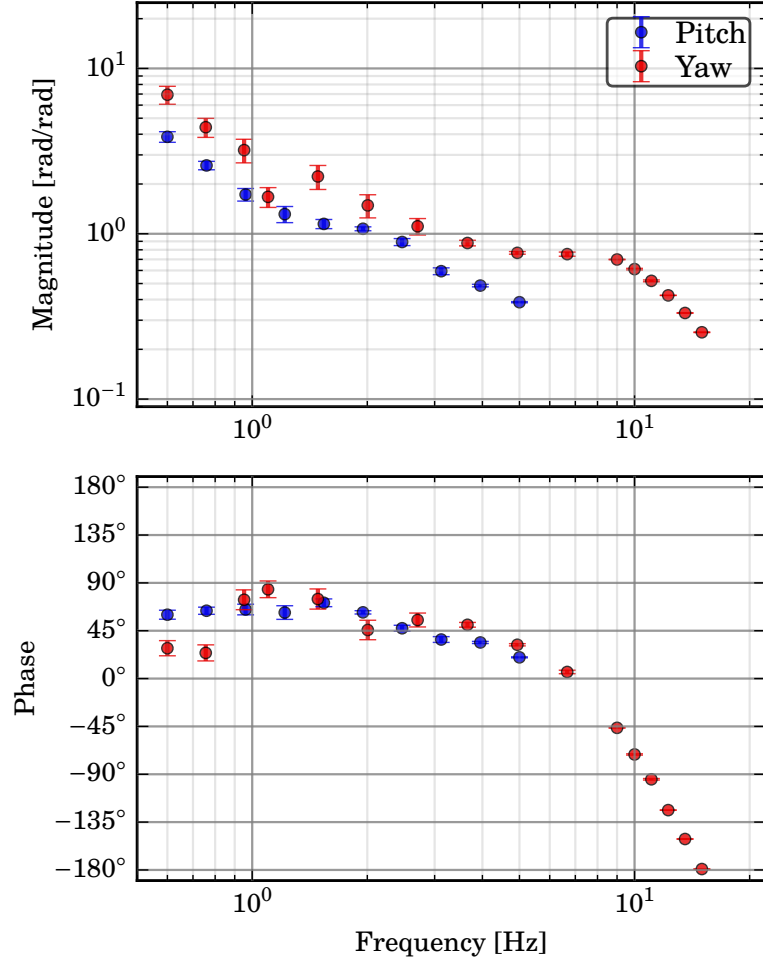


Figure 2.21: Open-loop transfer functions for angular control of the beamsplitter.

For both H1 and L1, the 45 MHz reflection error signal suffered from the problem that the optical gain would flip sign as the interferometer's recycling gain crossed a certain threshold (somewhere in the region from 30 to 33 W/W). For H1, this so-called "Arai singularity" was avoided in practice by adjusting the green initial alignment references so that the interferometer would have a high recycling gain (more than 36 W/W) as soon as arm resonance was achieved. To get rid of the Arai singularity for good, both L1 and H1 installed an in-air WFS to monitor the PRC light, with L1 using the 36 MHz signal and H1 using the 45 MHz signal.

## Beamsplitter and antisymmetric port loops

Four degrees of freedom are controlled:

1. A combination of 36 MHz antisymmetric port wavefront sensors are used to control the beamsplitter angles (OLTFs shown in figure 2.21).

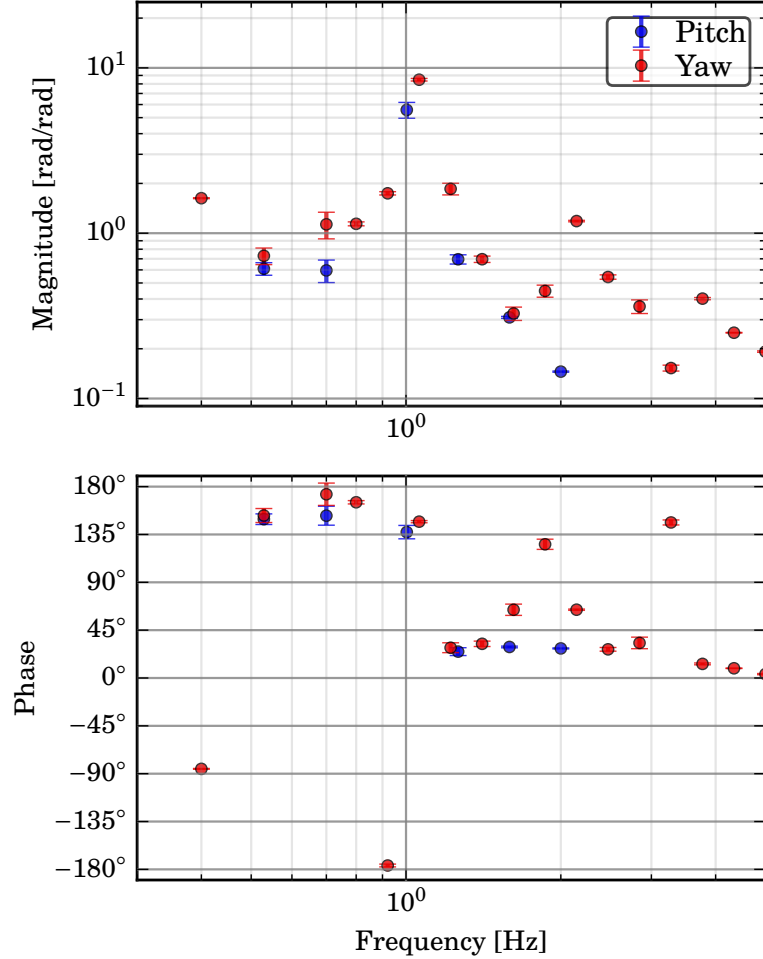


Figure 2.22: Open-loop transfer functions for angular control of the signal recycling cavity pointing.

2. A combination of 36 MHz antisymmetric port wavefront sensors are used to control the angles of the signal recycling mirror.
3. A QPD at the output of the SRC is used to control the angles of the small SRC folding mirror (SR2) (OLTFs shown in figure 2.22).
4. A shadow sensor is used to control the pitch of the large SRC folding mirror (SR3).

The antisymmetric port 36 MHz wavefront sensors presented little difficulty for L1, but were extremely problematic for H1, and their (mis)behavior is part of the constellation of issues surrounding the Hanford signal recycling cavity. Phasing the 36 MHz sensors was difficult: certain quadrants showed little to no response to optical signals, or sometimes showed different responses depending on whether an optic was driven in pitch or yaw. Loops could still be closed around the beamsplitter

and SRM angles, but the error signals at 2 W were unusable at 25 W. For O1, stable 25 W operation was achieved by choosing a combination of 36 MHz signals that kept the rf sideband powers high in the recycling cavities.

## Input modecleaner

Angular control of the input modecleaner is achieved with a combination of rf wavefront sensing and dc pointing sensing. Two wavefront sensors are placed in reflection of the modecleaner, and these are used to control (relative to the input beam) the angle of the high reflector and the common-mode angle of the input/output coupling mirrors. The third degree of freedom of the mirrors (the differential angle of the input and output coupling mirrors) is left uncontrolled. Finally, the pointing of the beam on the high reflector is controlled by closing a loop around a dc quadrant photodetector placed in transmission of the high reflector.

## Output modecleaner

To keep the output modecleaner aligned with respect to the antisymmetric port beam, four dither lines are applied to the first and third (out of three) antisymmetric-port steering mirrors that steer the beam from the output Faraday isolator into the output modecleaner. These lines are demodulated in the GW signal and used as error signals to drive the third steering mirror and the modecleaner suspension.<sup>60,61</sup> For future observing runs, this dither alignment scheme may be replaced by a test mass drumhead sensing scheme, as was employed in Enhanced LIGO.<sup>26</sup>

## Cross-coupling into differential arm length

Several effects cause angular control signals to produce differential arm length motion via simple linear coupling. First, if the beam spot is miscentered on the test mass by an amount  $\delta$ , angular motion  $\theta$  of the mass will produce a length coupling  $\theta\delta$ . Second, imbalance of the suspension actuators can convert an angular drive signal into a partially longitudinal drive signal. Finally, when driving the penultimate stage in pitch, there is an intrinsic mechanical coupling to test mass length.

To reduce this linear angular coupling, frequency-independent feedforward is employed on each test mass. A line in pitch or yaw is injected into the relevant penultimate stage angular control signal, and this line then appears in the differential

arm length readout because of the linear angular cross-coupling. The angular control signal is then summed into the penultimate stage longitudinal control signal, with some coefficient that is optimized to minimize the appearance of the line in the differential arm length.

More generally, the differential arm length noise due to angular fluctuations is the frequency-domain convolution of the motion of the interferometer mirrors.<sup>58,62</sup> This means that the angle-to-length mechanism is bilinear, and therefore cannot be subtracted off with linear feedforward. When the dominant angular noise contribution to the differential arm length is no longer linear, the best strategy may be to reduce the mirror motion, for example, by improving the seismic isolation of the mirrors or decreasing the angle-referred shot noise of the sensors.

## 2.6 Suspension control

### Test mass suspensions

Each test mass suspension comprises two quadruple suspensions, mounted from an active seismic isolation platform<sup>40</sup> inside the vacuum system. One of these suspensions contains the test mass as its final payload; it serves to isolate the test mass from external vibrations, with a transfer function magnitude of  $(10^{-15} \text{ m/m}) \times (100 \text{ Hz}/f)^8$  in the GW band. The upper three masses are fitted with permanent magnets so that they may be magnetically actuated. The other suspension contains masses fitted with sensors and actuators for controlling the main suspension. On the upper three masses, the actuators are solenoids that act on the permanent magnets of the main suspension masses, and the sensors are shadow sensors. On the bottom mass, the actuator comprises a set of electrodes which actuate capacitively on the test mass itself. The choice of electrostatic—rather than magnetic—actuation is driven by the desire to avoid direct coupling of ambient magnetic fields to the test mass, and to avoid spoiling the  $Q$  of the test mass by attaching magnets onto it. The angle of each test mass can be sensed with an optical lever. A diagram of the test mass and the associated suspensions is shown in figure 2.23.

#### Test mass and electrostatic actuator

To actuate on the test mass, the outer annulus of the face of the glass reaction mass is patterned with five interdigitated gold electrodes. Four of these electrodes

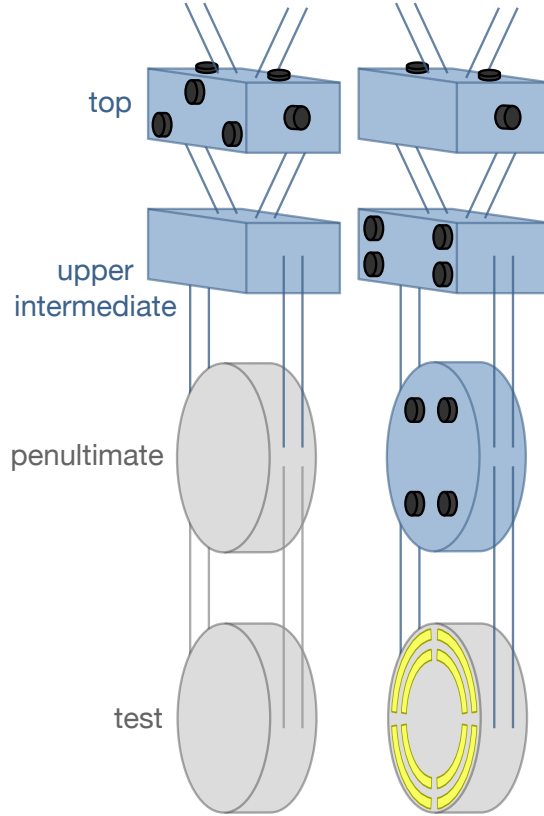


Figure 2.23: Diagram of the Advanced LIGO quadruple suspension. The test mass and penultimate mass are made from fused silica, and are attached with four fused silica fibers. The reaction mass is also made from fused silica. The remainder of the masses and wires are steel.

are each confined to a specific quadrant of the reaction mass; the fifth extends throughout the patterned area. Applying differential voltage between any of these electrodes produces a fringing field  $\mathbf{E}$  inside the test mass, which induces a polarization field  $\mathbf{P} = \epsilon_0 \chi \mathbf{E}$ , and hence a force  $\mathbf{F} = \nabla [\int d^3r \mathbf{P} \cdot \mathbf{E}]$ .

Since  $F$  is proportional to  $E^2$ , this actuator is intrinsically nonlinear. To achieve linear actuation, a fixed bias voltage  $V_b$  is applied to the fifth, extended electrode. Then applying a signal voltage  $v$  to any of the other electrodes will produce a corresponding force proportional to  $(V_b + v)^2 \approx V_b^2 + 2V_b v$ . For longitudinal actuation on the end test masses, the proportionality constant is  $\alpha \approx 1.5 \times 10^{-10} \text{ N/V}^2$ . This is set by the geometry of the fringing field with respect to the test mass, as well as the presence of charge on the mass.<sup>16</sup> For the input test masses, the proportionality constant is weaker, because the gap between the reaction mass and the test mass

is larger for the input suspensions (20 mm versus 5 mm) in order to reduce squeeze film damping.

During O1, the end Y electrostatic actuator was used to control the differential arm length, with 380 V of bias, and a signal range of  $\pm 20$  V on each quadrant. The electrostatic actuation strength is affected by the presence of charge on and around the test mass.<sup>16</sup>

### **Penultimate mass**

The penultimate mass is fabricated from fused silica, and is fitted with four magnets. On all four suspensions, this stage is used as the main actuator for the test mass angular control. On the end Y suspension, this stage is used for differential arm length feedback (along with the upper intermediate and test stages). On the input X and input Y suspensions, this stage is used for feedforward cancellation of Michelson and SRC length control.

Additionally, this stage is used to damp the eight silica violin modes on each test mass. The first harmonics of these modes have frequencies close to  $f_v = 500$  Hz. These modes become problematic if their rms amplitude produces more than  $10^{-14}$  m of differential arm length motion, as this will saturate the dc readout photodiodes when operated in high-sensitivity mode. Worse still, violin modes exhibit dilution damping,<sup>63</sup> with  $Q > 10^8$ . This implies a time constant  $\tau = Q/\pi f_v > 17$  h, so it is imperative that they be actively damped if they ring up. Violin modes are sensed in the differential arm length readout, which is bandpassed to produce various control signals. These signals are sent to the penultimate stage, with the option of driving in some combination of length, pitch, or yaw.

### **Upper intermediate mass**

The upper intermediate mass is made from steel, and is fitted with four magnets, giving longitudinal, pitch, and yaw control. During the first observing run, the end Y upper intermediate mass was used to offload differential arm length control from the test mass. Additionally, both the end X and end Y upper intermediate masses were used to offload the VCO control signal for the reference cavity AOM. The input X and Y upper intermediate masses were not used for H1.

### Top mass

The top mass is made from steel, and is fitted with six magnets. A key feature of the suspension design is that all degrees of freedom of the pendulum masses are supposed to be observable using the top mass sensors. This allows six ac-coupled servo loops to be closed around the top mass in order to damp these degrees of freedom from roughly 0.1 to 1 Hz. The modes are considered well damped if a step response applied to each top mass degree of freedom produces a response with a  $Q$  of a few.

In the lead-up to O1, it was found that the test mass bounce and roll modes could not adequately be damped using the top-mass sensors alone; the modes would ring up and saturate the differential arm length readout. The bulk of the energy in these modes is stored in the silica fibers between the penultimate mass and the test mass, so these modes are long-lived, with a  $Q$  of the same order as the intrinsic silica  $Q$  (more than  $10^5$ ). Generally, these modes are considered problematic if their amplitude in the differential arm length readout exceeds  $10^{-13} \text{ m}_{\text{rms}}$ . The coupling of the bounce mode is thought to be well understood: if the local gravity at the test mass does not lie in the plane normal to the beamline, then bounce mode motion produces a small amount of beamline motion. For a perfectly spherical earth with a homogeneous local gravity field, the expected bounce coupling is  $(2.0 \text{ km}/6400 \text{ km}) = 3 \times 10^{-4} \text{ m/m}$ ; in reality, gravimetry measurements imply bounce couplings ranging from  $8 \times 10^{-6} \text{ m/m}$  to  $6.4 \times 10^{-4} \text{ m/m}$ .<sup>64</sup> The coupling of the roll mode occurs when the plane of the mode rotation is not parallel to the test mass face; this could arise, for example, from the wedge of the test mass substrate.<sup>65</sup> During O1, the four bounce modes were sensed by bandpassing the differential arm length readout, and feeding the resulting to the vertical actuators on the top mass with an experimentally determined phase delay. The four roll modes were sensed by bandpassing the 45 MHz antisymmetric-port wavefront sensor signals and feeding the result to the top mass vertical actuators.

Additionally, the top mass receives low-frequency pitch and yaw control signals from the penultimate stage.

## 2.7 Intensity control

Several orders of magnitude of intensity noise suppression are required for Advanced LIGO to achieve its designed sensitivity. The injection-locked amplifier pro-

duces a typical RIN of less than  $(10^{-5}/\text{Hz}^{1/2}) \times (100\text{ Hz}/f)$  for  $f < 1\text{ kHz}$ . The requirement for the light at the interferometer input is  $10^{-7}/\text{Hz}^{1/2}$  at 100 Hz and  $2 \times 10^{-9}/\text{Hz}^{1/2}$  at 10 Hz.<sup>35</sup> Two intensity stabilization loops are implemented to achieve this suppression. A third loop is available to suppress optomechanical instabilities around the test mass suspension resonances.

## Inner loop

For the inner loop, a pair of photodiodes (one in-loop and one out-of-loop) is used to sense the light exiting one of the high-reflector ports of the pre-modecleaner. The in-loop signal is filtered and then used to actuate on a single-pass AOM located immediately before the pre-modecleaner (figure 2.4). The bandwidth of this loop is approximately 50 kHz, and the shot-noise-limited performance of the loop is sufficient to achieve a RIN of a few parts in  $10^{-8}/\text{Hz}^{1/2}$  from 30 Hz to 1 kHz.<sup>36</sup>

However, after the high-power oscillator was activated in H1, the inner loop ceased to properly stabilize the laser intensity, leading to 40 times more RIN entering the interferometer at 100 Hz.<sup>66,67</sup> This behavior could be explained by the inner loop diodes seeing a common intensity noise (for example, from jitter or polarization) that is not seen on the other two transmission ports of the pre-modecleaner.

## Outer loop

Additional intensity noise suppression is achieved with an outer loop located in transmission of the input modecleaner. This loop uses an array of four in-loop and four out-of-loop photodiodes, and the loop bandwidth is about 10 kHz. In principle, at 10 Hz the loop can achieve a RIN of  $2 \times 10^{-9}/\text{Hz}^{1/2}$ . Additionally, the interferometer passively filters the intensity noise above the common-mode cavity pole,  $f_+ \approx 0.6\text{ Hz}$ .

## Outermost loop

For powers above 10 W in H1, an optomechanical instability was sometimes observed, producing test mass pitch motion in the common-mode soft degree of freedom at a frequency close to the primary suspension resonances (around 0.5 Hz). This instability could not be cured by adjusting spot positions on the test masses. To reduce the frequency of occurrence, optical lever damping was applied to the

input test masses. While generally sufficient for O1, this did not resolve the issue, and the instability again started to appear as commissioning progressed to more than 30 W.

Driggers et al.<sup>68</sup> eventually determined that this instability could be explained by a nonzero coupling from test mass angle into arm power (of unknown origin), with a magnitude  $\partial P/\partial\theta \sim 10^{10}$  W/rad at 0.5 Hz. The arm power fluctuation drives the test masses longitudinally, which also drives the test mass angles (in a common-mode soft configuration) because of mechanical length-to-pitch coupling in the test mass suspensions, with an expected magnitude  $\partial\theta/\partial F \simeq 4 \times 10^{-2}$  rad/N at 0.5 Hz. Therefore, common-mode soft test mass motion propagates around an optomechanical feedback loop, with an open-loop gain  $(2/c)(\partial P/\partial\theta)(\partial\theta/\partial F)$  that can exceed unity at 0.5 Hz.

To suppress this instability, a third intensity stabilization loop was created in order to stabilize the power in the arms around the suspension resonance frequencies. The transmitted powers from each end station (measured by the in-vacuum QPDs) are summed, giving an error signal that measures the average transmitted arm power. The digitally filtered error signal is summed electronically into the outer loop, giving an open-loop gain that is above unity between 0.2 and 0.7 Hz.<sup>69,70</sup>

# 3 Noise in the Advanced LIGO detectors

This chapter presents a budget of the noise in the Advanced LIGO Hanford detector. Noise analysis of the Livingston detector is given by Martynov<sup>16</sup> and Martynov et al.<sup>43</sup> Similar budgets for the initial detectors have been given, for example, by Adhikari<sup>71</sup> and Ballmer.<sup>72</sup> As of this writing, the budgets for both Advanced LIGO detectors fail to explain the differential arm length sensitivity between 50 Hz and 200 Hz; the source of this noise is under active investigation.

## 3.1 Quantum noise

### Overview

Quantum noise refers to the joint contributions of radiation pressure noise (a displacement noise) and shot noise (a sensing noise) to the differential arm length readout. Quantum noise has been explained by Caves<sup>73</sup> as the effect of vacuum fluctuations which enter the unused ports of the interferometer—particularly the antisymmetric port.

In the case of no signal recycling mirror, the quantum noise of a lossless interferometer is<sup>41,74</sup>

$$S_{hh}(f) = \left( \mathcal{K} + \frac{1}{\mathcal{K}} \right) \frac{h_{\text{SQL}}^2}{2}, \quad (3.1)$$

where

$$h_{\text{SQL}}^2 = \frac{h}{\pi^3 M L^2 f_a^2} \quad (3.2)$$

and

$$\mathcal{K} = \frac{P_b c}{\pi^3 \lambda_0 M L^2 f_a^2 f^2} \times \frac{1}{1 + (f/f_a)^2}.$$

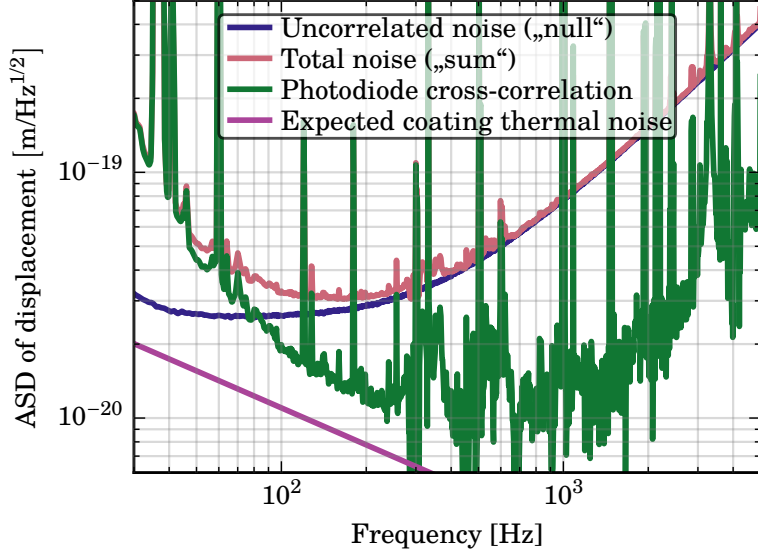


Figure 3.1: GW photodiode auto- and cross-spectral densities from the first observing run, referred to freerunning differential arm length. The photodiode sum is the usual freerunning DARM estimate. The photodiode null shows only uncorrelated noises, such as shot noise and photodiode electronics noise. The cross-correlation shows only correlated noises, such as displacement noise and sensing noises arising in the interferometer.

The effect of adding a signal recycling mirror with resonant sideband extraction (that is,  $\pi/2$ -detuned signal recycling) is to make the substitutions

$$f_a \rightarrow y f_a \quad \text{and} \quad P_b \rightarrow P_b/y, \quad (3.3)$$

with  $y = (1 + r_s)/(1 - r_s)$ . The effect of resonant sideband extraction, then, is to decrease the effective power on the beamsplitter and broaden the linewidth of the arms.

## Photodiode cross-correlation

The GW readout is sensed with two photodiodes (called “A” and “B”), each receiving half the light transmitted through the output modecleaner. The shot noise on these photodiodes is uncorrelated. Therefore, the cross-spectral density  $S_{AB}(f)$  of the two photocurrents  $i_A$  and  $i_B$  can be used to estimate the amount of correlated noise  $i_0$  present in the interferometer or the GW readout, since the shot noise will average away. An example is provided in figure 3.1, which shows the correlated differential arm length noise during the first observing run.

How many averages are required to resolve the correlated noise? The estimated coherence  $\hat{\gamma}_{AB,(N)}^2$  after  $N$  averages is

$$\hat{\gamma}_{AB,(N)}^2(f) = \frac{|\langle i_A^* i_B \rangle_N|^2}{\langle i_A^* i_A \rangle_N \langle i_B^* i_B \rangle_N} \quad (3.4a)$$

$$= \frac{|\langle i_0^* i_0 \rangle_N + \langle i_A'^* i_0 \rangle_N + \langle i_0^* i_B' \rangle_N + \langle i_A'^* i_B \rangle_N|^2}{\langle i_A^* i_A \rangle_N \langle i_B^* i_B \rangle_N}, \quad (3.4b)$$

where  $i'_{A,B} = i_{A,B} - i_0$  is the uncorrelated noise component of each diode. In the limit that  $|i_0| \ll |i'_{A,B}|$  (that is, we are trying to resolve a small coherent component buried underneath shot noise), then the middle two terms will always be subdominant to the last term, regardless of  $N$ , so we can ignore them.

Upon each noise realization, the vectors  $i_0$ ,  $i'_A$ , and  $i'_B$  have magnitudes which are drawn from Rayleigh distributions with means  $\sqrt{S_{00}}$ ,  $\sqrt{S_{A'A'}}$ , and  $\sqrt{S_{B'B'}}$ , respectively. Their phases are all random. However, the two products  $i_0^* i_0$  and  $i_A'^* i_B'$  behave differently upon summation over a large number  $N$  of noise realizations. Since  $i_0^* i_0$  is always real (i.e., the phase is always 0), the summation  $\sum_k i_0^{(k)*} i_0^{(k)}$  grows like  $N$ . On the other hand, since  $i_A'^* i_B'$  has a random phase, the summation  $\sum_k i_A'^{(k)*} i_B'^{(k)}$  grows like  $\sqrt{N}$ . Hence, after a large number of averages,  $\langle i_0^* i_0 \rangle_N \rightarrow S_{00}$  and  $\langle i_A'^* i_B' \rangle_N \rightarrow \sqrt{S_{A'A'} S_{B'B'}} / \sqrt{N}$ . Therefore, these two terms will be equal when  $N = S_{AA}(f) S_{BB}(f) / S_{00}^2(f) = 1/\gamma_{AB}^2$ . So at least  $1/\gamma_{AB}^2$  averages are required to resolve a coherence  $\gamma_{AB}^2$  in this case.

## 3.2 Thermal noise

### The fluctuation–dissipation theorem

The fluctuation–dissipation theorem is a general result in statistical mechanics that quantifies how losses in a system give rise to fluctuations of the system's coordinates. A derivation of this theorem was first given by Callen and Welton.<sup>75</sup> The theorem has found wide use in various areas of precision measurement. In gravitational wave physics, it provides important results for thermally driven noise in mirrors, suspensions, and electronics.

Consider a system with some generalized coordinate  $x$ , and a corresponding generalized force  $F$ . If an oscillatory force  $F(t) = F_0(f) \cos(2\pi f t)$  is applied to the system at frequency  $f$ , the system's coordinate will respond with a velocity  $\dot{x}(t) =$

$\dot{x}_0(f) \sin[2\pi f t + \phi(f)]$ , where the amplitude  $\dot{x}_0(f)$  and phase lag  $\phi(f)$  are determined by the system's equation of motion. Often,  $\phi(f)$  arises from some kind of loss mechanism; for example, mechanical, electrical, or thermodynamic dissipation in the system.

The fluctuation–dissipation theorem says that the time-averaged power dissipation  $W(f) = \langle F(t)\dot{x}(t) \rangle$  causes stochastic fluctuation  $S_{xx}(f)$  in the coordinate  $x$ :<sup>a</sup>

$$S_{xx}(f) = \frac{2k_B T}{\pi^2 f^2} \frac{W(f)}{F_0(f)^2}. \quad (3.6)$$

Note that

$$W(f) = \langle F(t)\dot{x}(t) \rangle = F_0 \dot{x}_0 \langle \cos(2\pi f t) \sin(2\pi f t + \phi) \rangle = \frac{1}{2} F_0 \dot{x}_0 \sin \phi \simeq \frac{1}{2} F_0 \dot{x}_0 \phi, \quad (3.7)$$

where the approximation holds for  $\phi \ll 1$ . This shows that the energy dissipated (and hence the amount of fluctuation) depends on the phase lag  $\phi$ .

Equivalently, if we can express the system's equation of motion in the Fourier domain, then we can extract the transfer function  $Y(f) = \dot{x}(f)/F(f)$  (commonly called the admittance) which relates the complex amplitudes  $\dot{x}(f) = \dot{x}_0(f)e^{i\phi(f)}$  and  $F(f) = F_0(f)e^{i\psi_F(f)}$ . Then by computing  $W(f)$ , we find

$$S_{xx}(f) = \frac{k_B T}{\pi^2 f^2} |\operatorname{Re} Y(f)| = \frac{2k_B T}{\pi f} |\operatorname{Im} \chi(f)|, \quad (3.8)$$

where  $\chi(f) = x(f)/F(f) = Y(f)/(2\pi i f)$  is the system's susceptibility.

## Types of thermal noise

The fundamentals of mechanical and thermodynamical thermal noises are described by Saulson.<sup>77</sup> A more detailed overview of thermal noises relevant to gravitational wave detection is given by Narwodt et al.<sup>78</sup>

### Brownian noise

Brownian noise refers to fluctuation arising from friction in a mechanical system. Such friction may arise from rubbing, gas damping, or—of particular concern to low-noise mechanical experiments—internal friction within the bulk or on the surface

---

<sup>a</sup> This is the classical version of the fluctuation–dissipation theorem, valid in the limit  $k_B T \gg 2\pi\hbar f$ . The fully quantum version of the theorem is obtained by the substitution<sup>76</sup>

$$k_B T \rightarrow \frac{2\pi\hbar f}{1 - \exp(-2\pi\hbar f/k_B T)}. \quad (3.5)$$

of the system. In solid materials like glasses, metals, or plastics, internal friction is quantified by the material's mechanical  $Q$  factor or, equivalently, the loss angle  $\phi = 1/Q$  (which may be frequency-dependent). This loss angle produces a phase lag in the system's response to an applied force, and therefore produces a loss in accordance with equation 3.6. In the particular case that  $\phi$  is frequency-independent, the loss is called *structural*. If  $\phi \propto f$ , the loss is called *viscous*.

### Thermodynamic noise

Every macroscopic system in thermodynamic equilibrium continually wanders between the many different microstates available to it. This wandering leads to random fluctuations in the system's state variables, such as temperature, entropy, pressure, volume, and so on. In particular, temperature fluctuations will propagate to fluctuations in other material parameters—such as volume, refractive index, elasticity, and so on—because of the temperature dependence of these parameters.<sup>79</sup> The effects of these fluctuations on the optical readout of a mechanical system due to temperature fluctuations are collectively referred to as thermodynamic noise. In particular,

- fluctuation from the coefficient of thermal expansion  $\alpha = (1/L)\partial L/\partial T$  is called thermoelastic noise;
- fluctuation from the coefficient of thermorefraction  $\beta = \partial n/\partial T$  is called thermorefractive noise;
- fluctuation from  $\alpha$  and  $\beta$  considered together coherently is called thermo-optic noise; and
- fluctuation from the fractional temperature dependence  $(1/E)\partial E/\partial T$  of the Young modulus  $E$  is also said to contribute to thermoelastic noise.

### Johnson–Nyquist noise

Johnson–Nyquist noise<sup>80,81</sup> refers to the thermal noise in an electronic circuit arising from its lossy (that is, resistive) components.

Consider the simple case of computing the charge fluctuation (or equivalently, the voltage fluctuation) across a capacitor with capacitance  $C$  whose plates are connected by a resistor with resistance  $R$ . From elementary electrodynamics, we know that if a voltage  $V$  is applied to the capacitor, then the charge  $q$  on the plates

amounts to a stored energy  $U = qV$ . Therefore, we can view  $q$  as the coordinate for the system and  $V$  as the corresponding force, and we should be able to use the fluctuation–dissipation theorem to calculate the stochastic fluctuations in  $q$  (or  $V$ ) even in the absence of an applied voltage.

The system's admittance can be read off from the system's equation of motion, which in this case is already known from elementary circuit analysis:

$$\dot{q}(f) = Y(f)V(f) = \frac{1}{Z_R \parallel Z_C} V(f) = \frac{1 + 2\pi i f R C}{R} V(f). \quad (3.9)$$

We now suppose we are only interested in the effect of the resistor; that is, we stick to frequencies  $f \ll 1/RC$ , where the dynamics of the capacitor does not affect the behavior of the circuit. Then  $Y(f) \approx 1/R$ . Then from the fluctuation–dissipation theorem, the charge fluctuation across the capacitor in the absence of an applied voltage is

$$S_{qq}(f) = \frac{k_B T}{\pi^2 f^2} |\text{Re } Y(f)| = \frac{k_B T / R}{\pi^2 f^2}, \quad (3.10)$$

and the voltage fluctuation is

$$S_{VV}(f) = \frac{S_{qq}(f)}{|Y(f)/2\pi i f|^2} = 4k_B T R, \quad (3.11)$$

which is the usual expression for Johnson–Nyquist noise in terms of the voltage fluctuation across the resistor.

## In suspensions

Suspension thermal noise has both Brownian and thermoelastic contributions, which have been characterized by Cumming et al.<sup>82</sup> in a modal analysis that considers the suspension fibers, the test mass ears, and the welds connecting the fibers to the ears.

### Brownian noise

Each element of the suspension has Brownian dissipation in the bulk of the glass, and on the glass surface. The bulk loss is very small and nearly viscous, with a loss angle  $\phi_b = (1.2 \times 10^{-11}) \times (f/1\text{Hz})^{0.77}$ . The surface loss is structural, and depends on the intrinsic loss angle  $\phi_s$  of the surface material, the depth  $h$  of the surface, and the thickness  $d$  of the suspension element: the loss is  $8h\phi_s/d \approx 1.2 \times 10^{-7}$  for  $d = 400 \mu\text{m}$ , which is the thinnest element (highest surface-to-volume ratio) of the suspension.<sup>82</sup>

## Thermodynamic noise

The thermoelastic loss angle  $\phi^{(\text{susTE})}$  of each suspension element depends on contributions from the CTE  $\alpha$  of the silica, and the temperature dependence  $\partial E/\partial T$  of its Young modulus. At each point  $z$  along the fiber, the loss is given by<sup>82</sup>

$$\phi^{(\text{susTE})}(\omega, z) = \frac{ET}{C} \left( \alpha - \frac{\sigma(z)}{E^2} \frac{\partial E}{\partial T} \right) \times \frac{\omega \tau(z)}{1 + [\omega \tau(z)]^2}, \quad (3.12)$$

where  $\sigma(z)$  is the static stress in the fiber,  $C$  is the volumetric heat capacity of the silica, and  $\tau(z)$  is the thermal time constant of the suspension element, which depends on its material properties and geometry. The negative sign between the thermoelastic and Young modulus terms in equation 3.12 indicates that the thermoelastic loss can be minimized by engineering the appropriate amount of static stress  $\sigma$ . In the Advanced LIGO suspensions, thermoelastic cancellation in the fiber is achieved by making the end portions of the fiber twice the diameter of the central section (800  $\mu\text{m}$  versus 400  $\mu\text{m}$ ).<sup>82</sup>

The main suspension thermal noise contributions to differential arm length fluctuation are from the longitudinal and bounce modes, since these modes produce motion in the beamline direction.

## In substrates

### Brownian noise

Levin<sup>83</sup> computed the Brownian noise for a cylindrical mirror substrate of radius  $R$  interrogated by a Gaussian beam with spot size  $w \ll R$ ; this was later extended by Bondu et al.<sup>84</sup> and Liu and Thorne<sup>85</sup> for cases where  $w \ll R$  is violated. The Levin expression is

$$S_{xx}^{(\text{subBr})}(f) = \frac{4k_B T}{f} \frac{\sqrt{2}}{\pi^3} \frac{1 - \sigma^2}{Ew} \phi I, \quad (3.13)$$

where  $E$  is the Young modulus,  $\sigma$  is the Poisson ratio,  $\phi$  is the loss angle in the bulk, and  $I \approx 1.9$  is a numerical factor. For Advanced LIGO, with  $w \approx 6\text{ cm}$  and  $R = 17\text{ cm}$ , the corrections of Bondu et al. and Liu and Thorne amount to a substrate Brownian noise that is roughly 70 % of the Levin expression in terms of amplitude. The bulk loss angle is assumed to be  $\phi = (7.6 \times 10^{-12}) \times (f / 1\text{ Hz})^{0.77}$ .<sup>86</sup> Additionally, Brownian loss at the substrate surface can be treated in the same way as coating loss, with a thickness-loss product of  $d\phi_s = 5 \times 10^{-12}\text{ m}$ .<sup>86</sup>

## Thermodynamic noise

The thermoelastic noise of test mass substrates have been described by Braginsky et al.<sup>79</sup> and Cerdonio et al.<sup>87</sup> This noise (per test mass) is given by

$$S_{xx}^{(\text{subTE})}(f) = \frac{4k_B T^2}{\pi^{1/2}} \frac{\alpha^2(1+\sigma)^2 w}{\kappa} J(f/f_T), \quad (3.14)$$

where<sup>88</sup>

$$J(\Omega) = -\text{Re} \left\{ \frac{e^{i\Omega/2}(1-i\Omega)}{\Omega^2} \text{erfc} \left[ \frac{\Omega^{1/2}(1+i)}{2} \right] \right\} + \frac{1}{\Omega^2} - \frac{1}{(\pi\Omega^3)^{1/2}} \quad (3.15)$$

and  $f_T = \kappa/\pi w^2 C$ , and the material parameters refer to the substrate. The function  $J(\Omega)$  has asymptotes  $1/\sqrt{8\Omega}$  for  $\Omega \ll 1$  and  $1/\Omega^2$  for  $\Omega \gg 1$ .

## In coatings

### Brownian noise

Brownian noise in coatings is analyzed in detail by Hong et al.,<sup>89</sup> who derive a general expression for the noise in a multilayer dielectric stack interrogated by a laser beam. In general, any isotropic and homogeneous material has two elastic loss angles: a loss angle  $\phi_K$  corresponding to the bulk modulus  $K$ , and a loss angle  $\phi_G$  corresponding to the shear modulus  $G$ . However, these individual loss angles are (so far) poorly constrained in the coating materials used in GW detection, and are usually assumed to be equal.

The Advanced LIGO coatings consist of multilayer stacks of silica ( $\text{SiO}_2$ ) and titania-doped tantalum ( $\text{Ti}:\text{Ta}_2\text{O}_5$ ). Silica has a loss angle of about  $5 \times 10^{-5}$ , while titania-doped tantalum has a much larger loss angle—about  $3 \times 10^{-4}$ .<sup>90</sup> The tantalum loss is the dominant thermal noise contributor to the Advanced LIGO strain sensitivity. Measurements by Gras et al.<sup>90</sup> on Advanced LIGO coating witness samples indicate that the expected coating thermal noise contribution to the differential arm length sensitivity is

$$S_{xx}^{(\text{cBr})}(f)^{1/2} = (1.15 \times 10^{-20} \text{ m/Hz}^{1/2}) \times \left( \frac{100 \text{ Hz}}{f} \right)^{1/2}. \quad (3.16)$$

## Thermodynamic noise

Thermodynamic noise in coatings is computed by finding the spectrum  $S_{TT}$  of temperature fluctuations corresponding to a Gaussian pressure profile.<sup>79,85,91–93</sup> This

spectrum is

$$S_{TT}(f) = \frac{2^{3/2} k_B T^2}{\pi \kappa_s w} \int_0^\infty du \operatorname{Re} \left[ \frac{ue^{-u^2/2}}{(u^2 - if/f_T)^{1/2}} \right], \quad (3.17)$$

with  $f_T = \kappa_c/\pi C_c w^2$ . The integral goes to  $\sqrt{\pi/2}$  for  $f \ll f_T$ , and to  $\sqrt{f_T/2f}$  for  $f \gg f_T$ . For the Advanced LIGO coatings,  $\kappa_c \sim 10 \text{ W}/(\text{m K})$  and  $C_c \sim 1 \text{ J}/(\text{m}^3 \text{ K})$ , so for  $w \approx 6 \text{ cm}$  we have  $f_T < 10^{-4} \text{ Hz}$ .

Evans et al.<sup>92</sup> then considered thermo-optic noise by propagating  $S_{TT}(f)$  to reflected phase fluctuations arising from the coefficient of thermal expansion  $\alpha = (1/L)\partial L/\partial T$  and coefficient of thermorefraction  $\beta = \partial n/\partial T$  for the coating layers. The resulting reflected phase noise (referred to effective mirror displacement) is

$$S_{xx}(f) = S_{TT}(f) \Gamma(f) (\alpha_c d - \beta_c \lambda - \alpha_s d C_c / C_s)^2, \quad (3.18)$$

where

- $\alpha_c$ ,  $\beta_c$ , and  $C_c$  are the CTE, CTR, and heat capacity of the coating;
- $\alpha_s$  and  $C_s$  are the CTE and heat capacity of the substrate;
- $d$  is the coating thickness; and
- $\Gamma$  is a frequency-dependent factor accounting for the nonzero thickness of the coating.

Importantly, the relative sign of the  $\alpha_c$  and  $\beta_c$  is negative, indicating that an uncorrelated analysis of the thermoelastic and thermorefractive noises overestimates the thermo-optic noise for positive  $\alpha_c$  and  $\beta_c$  (as is the case for silica/tantala coatings). In fact, the coating layer structure can be optimized to cancel the thermoelastic and thermorefractive terms, thereby suppressing the total thermo-optic noise.<sup>94</sup> The Advanced LIGO coatings were not optimized in this way, but nonetheless some thermo-optic cancellation is present.

For Advanced LIGO, the expected thermo-optic noise contribution to the differential arm length sensitivity does not exactly follow a power law. It is expected to be  $4.1 \times 10^{-21} \text{ m}/\text{Hz}^{1/2}$  at 10 Hz and  $2.2 \times 10^{-21} \text{ m}/\text{Hz}^{1/2}$  at 100 Hz.<sup>92</sup>

### Photothermal noise

For a homogeneous test mass, the photothermal transfer function, taking incident power to mirror surface displacement, is<sup>79,87,95</sup>

$$\frac{x(f)}{P(f)} = -\frac{\alpha(1+\sigma)}{\pi^2 w^2 C} \times \frac{\mathcal{A}}{if}, \quad (3.19)$$

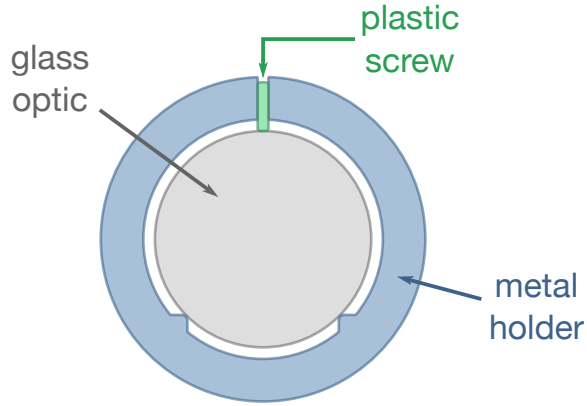


Figure 3.2: Cross-sectional diagram of the signal recycling mirror holder. The SRM is 5.08 cm in diameter and is held inside an aluminum ring with two PEEK set screws.

valid for  $f \gg f_T \equiv \kappa/\pi C w^2 \simeq 0.1 \text{ mHz}$ .

The absorptivity of the test mass coatings is excellent, with typical values that are a few hundred parts per billion. With  $\alpha = 5.1 \times 10^{-7} \text{ K}^{-1}$ ,  $\sigma = 0.17$ ,  $C = 1.6 \times 10^6 \text{ J}/(\text{m}^3 \text{ K})$ , and  $w = 5 \text{ cm}$ , this implies a transfer function magnitude

$$\left| \frac{x}{P} \right| = (5 \times 10^{-19} \text{ m/W}) \times \left( \frac{100 \text{ Hz}}{f} \right) \times \left( \frac{\mathcal{A}}{1 \text{ ppm}} \right). \quad (3.20)$$

With  $P_{\text{arm}} = 100 \text{ kW}$ , this implies a shot noise  $\sqrt{2h\nu P} \simeq 2 \times 10^{-7} \text{ W/Hz}^{1/2}$ , this implies a photothermal shot noise per test mass of  $2.5 \times 10^{-26} \text{ m/Hz}^{1/2}$  for  $\mathcal{A} = 250 \text{ ppb}$ . This is completely negligible for Advanced LIGO even at design sensitivity. Even with excess intensity noise in the arms arising from a RIN of  $10^{-8}/\text{Hz}$  at the interferometer input (figure 3.5), the resulting photothermal noise is  $7.5 \times 10^{-25} \text{ m/Hz}^{1/2}$  per test mass at 100 Hz, which is still negligible.

A more exact expression for the test mass photothermal transfer function, including terms accounting specifically for coating thermo-optic noise and substrate thermoelastic noise, is given by Farsi et al.;<sup>95</sup> however, this will not bring the expected photothermal noise (either from shot noise or classical intensity noise) to a level which limits Advanced LIGO.

## Elsewhere

During O1, the signal recycling mirror was unique among the interferometer optics in that it was set inside a metal holder using two 8-32 PEEK plastic screws

(figure 3.2). Finite element analysis of the assembly indicated the shear vibration of these screws should have a resonance at about 3 kHz,<sup>96</sup> and indeed a resonance in the transfer function from SRM motion into POP45 light was seen at 3.3 kHz in H1 and 2.4 kHz in L1.<sup>97,98</sup> This frequency is consistent with an effective free vibration length  $\ell$  of roughly 0.9 mm: the shear compliance per screw is  $x/F = \ell/GA$ , where  $G \approx 1.4$  GPa is the shear modulus for PEEK and  $A = \pi(4.2\text{ mm})^2 = 54.5\text{ mm}^2$  is the area of each screw. With an effective mass  $m = 100\text{ g}$  for this mode, the resonant frequency is then  $f_0 = \sqrt{GA/2\ell m}/2\pi$ . The width of the resonance in H1 implies a Q factor of 170, or equivalently a loss angle  $\phi = 1/Q = 6 \times 10^{-3}$ , assuming structural damping. This implies a Brownian SRM motion of<sup>77</sup>

$$S_{xx}(f) = \frac{2k_B T}{\pi f} \frac{\phi/(4\pi^2 m f_0^2)}{(1 - f^2/f_0^2)^2 + \phi^2}, \quad (3.21)$$

which amounts to an SRM displacement of  $(6 \times 10^{-17}\text{ m/Hz}^{1/2}) \times (100\text{ Hz}/f)^{1/2}$  for  $f \ll f_0$ . The agreement between the expected peak height from equation 3.21 and the observed peak height in the displacement-calibrated SRC length error signal is excellent,<sup>99</sup> as is the agreement between the expected peak height and the observed height in the differential arm length readout (using the measured coupling shown in figure 2.18). Note, however, that the behavior of the noise around the resonance frequency cannot constrain the slope of the loss angle, so the assumption here that the loss is structural has not been confirmed.

The thermoelastic contribution from the plastic is expected to be small: most of the energy of the mode is stored in shear strain, while thermoelastic noise arises only from bulk strain.

### 3.3 Seismic and Newtonian noise

#### Seismic noise

Ground motion is subject to daily and seasonal variations, particularly for frequencies below 1 Hz.<sup>100</sup> However, for quiet above-ground sites like Hanford and Livingston, the motion above 1 Hz in each direction has the approximate displacement ASD<sup>101</sup>

$$S(f) = (10^{-8}\text{ m/Hz}^{1/2}) \times \left(\frac{1\text{ Hz}}{f}\right)^2. \quad (3.22)$$

Coupling of this noise into differential arm length comes from ground motion in the beamline direction for each test mass, and from ground motion in the vertical direction that couples to beamline motion because the earth's curvature (see

section 2.6). Below the GW band, seismic noise is suppressed by an active seismic isolation system,<sup>40</sup> and within the GW band the noise is passively filtered by the mechanical transfer functions of the mirror suspensions.

## Newtonian noise

Newtonian noise refers to displacement caused by fluctuations in the gradient of the Newtonian potential  $\Phi(\mathbf{r})$  at each test mass. Such gradient fluctuations can be sourced by seismic noise, vibration of structures and equipment nearby the masses, and (of lesser concern to current gravitational wave detectors) fluctuations in atmospheric pressure.<sup>102</sup>

In future observing runs, the effect of Newtonian noise on the differential arm length readout may be estimated using seismometer arrays. This effect can then be subtracted from the differential arm length signal, either online or offline.<sup>103</sup>

## 3.4 Gas noise

The LIGO vacuum system is designed to be held at about  $0.1 \mu\text{Pa}$ , with the dominant species of residual gas being  $\text{H}_2$ .<sup>104</sup> The small amount of residual gas leads to two kinds of gas noise; these are included in the budget in figure 3.12.

### Optical scattering

The first kind of gas noise is a sensing noise induced by gas molecules wandering across the beam path and scattering light out of the beam. This noise has a flat phase spectrum up to a cutoff frequency that depends on the species of the gas.<sup>101,105</sup> For some particular species of gas, the displacement-referred noise induced along a single arm is

$$S_{xx}(f) = \frac{(4\pi\alpha)^2 n}{v} \int_0^L dz \frac{\exp[-2\pi f w(z)/v]}{w(z)}, \quad (3.23)$$

where  $\alpha$ ,  $n$ , and  $v$  are the polarizability, number density, and speed of the gas, and  $w(z)$  is the spot size along the arm.

## Squeeze film damping

The second kind of gas noise is a displacement noise induced by gas molecules hitting the test masses.<sup>106,107</sup> This is particularly problematic for the Advanced LIGO end test masses because of the small gap (5 mm) between the test mass and the reaction mass. A single molecule may bounce between the masses many times as it passes through the gap; this is referred to as “proximity-enhanced gas damping” or “squeeze-film damping”. For a given test mass geometry, the presence of the gas induces a mechanical impedance  $Z(f) = F(f)/\dot{x}(f)$  that is proportional to the gas pressure  $p$  and the time  $\tau$  required for the gas to diffuse into or out of the gap. Additionally, the impedance has a pole at  $1/\tau$ . The full expression for the force noise from squeezed-film damping is well-modeled by the formula<sup>106</sup>

$$S_{FF}^{(sfd)}(f) = S_{FF}^{(\infty)} + \frac{\Delta S_{FF}}{1 + (2\pi f \tau)^2}, \quad (3.24)$$

where  $S_{FF}^{(\infty)}$  is a white force noise that accounts for molecular collisions against the test mass in the absence of the reaction mass, and  $\Delta S_{FF}$  accounts for the proximity-enhancement effect.

To accurately compute the quantities in equation 3.24, numerical simulations are required (and the results are quoted below). However, analytical calculations by Dolesi et al. yield approximate expressions for  $\tau$  and  $\Delta S_{FF}$ :<sup>106</sup>

$$\tau = \left( \frac{\pi m_g}{2k_B T} \right)^{1/2} \frac{R^2/d}{\ln [1 + (R/d)^2]} \quad (3.25)$$

$$\Delta S_{FF} = 4k_B T \times \pi R^2 \times \frac{p \tau / d}{1 + (2\pi f \tau)^2}, \quad (3.26)$$

where  $T$  is the temperature,  $R$  is the test mass radius,  $d$  is the gap size,  $p$  is the pressure, and  $m_g$  is the mass of the gas species.

Numerical simulations of the Advanced LIGO end test mass geometry indicate that for 1  $\mu\text{Pa}$  of  $\text{H}_2$ , the expected force spectrum for a single end test mass is flat up to  $1/2\pi\tau = 1/(2\pi \times 800 \mu\text{s}) = 200 \text{ Hz}$ , with a dc value  $\sqrt{\Delta S_{FF}} = 1.2 \times 10^{-14} \text{ N/Hz}^{1/2}$ . The ac value is  $\sqrt{S_{FF}^{(\infty)}} = 1.4 \times 10^{-15} \text{ N/Hz}^{1/2}$ .<sup>108</sup>

We can use the known compliance of the test masses to convert the force spectrum into a displacement spectrum. The displacement noise from squeeze-film damping for two independent end test masses in the presence of residual  $\text{H}_2$  is then

$$S_{xx}^{(sfd)}(f) = (1.2 \times 10^{-20} \text{ m/Hz}^{1/2}) \times \left( \frac{p_{\text{H}_2}}{1 \mu\text{Pa}} \right) \times \left( \frac{30 \text{ Hz}}{f} \right)^2 \quad \text{for } f < 200 \text{ Hz}. \quad (3.27)$$

## 3.5 Frequency noise

### Budget of frequency noise in the interferometer

In this section we discuss the noises contributing to the frequency stabilization system. The topology of the frequency stabilization loop was discussed in detail in section 2.2, and a block diagram reduction of the loop was given in figure 2.9.

Our objective in this section is to produce a budget of the residual frequency noise  $r$  at the input of the interferometer; this input frequency noise is filtered by the common-mode cavity and then propagates to the differential arm length readout via a coupling function presented later. A loop analysis will show that

$$r = \frac{1}{1 + if/f_{IMC}} \times \frac{-A[(F + KM)Pn_p + Fn_f + KMn_m + Kn_k + n_a] - n_g}{A[(F + KM)P + K] + 1}, \quad (3.28)$$

where  $n_X$  refers to noise injected immediately before block  $X$  in the figure 2.9. The budget of noises considered in this section is shown in figure 3.3.

#### Noise in the laser

The typical freerunning noise of the NPRO (including the injection-locked oscillator) is  $(100\text{ Hz}/\text{Hz}^{1/2}) \times (100\text{ Hz}/f)$ .<sup>36</sup> At sufficiently high frequencies, this noise eventually becomes subdominant to the Schawlow–Townes limit<sup>109</sup>

$$S_{vv}^{(\text{ST})}(f) = \frac{1}{2\pi\tau} \sqrt{\frac{h\nu_0}{P}}, \quad (3.29)$$

which is a fundamental limit depending only on the laser frequency  $\nu_0$ , the output power  $P$ , and the storage time  $\tau$  of the laser resonator. For a resonator round-trip length  $L \sim 10\text{ cm}$  and a coupler transmissivity  $T \sim 1\%$ , the storage time is  $\tau = -2L/c\ln(1-T) \sim 70\text{ ns}$ . For  $P \sim 1\text{ W}$  of output, the Schawlow–Townes limit is then  $S_{vv}^{(\text{ST})}(f)^{1/2} \sim 1\text{ mHz}/\text{Hz}^{1/2}$ , which is subdominant to the aforementioned  $1/f$  noise below 1 MHz.

#### Noise in reference cavity

The goal of the reference cavity loop is to stabilize the laser frequency noise down to the (apparent) length noise of the fused-silica reference cavity. The performance

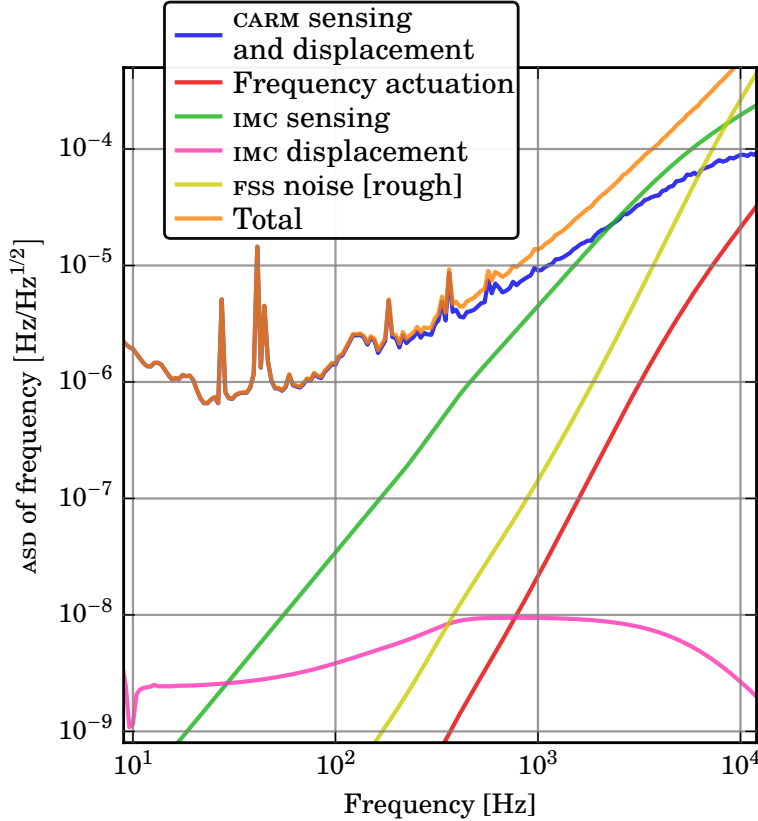


Figure 3.3: Budget of frequency noise of the light at the input of the Advanced LIGO Hanford detector.

of the Advanced LIGO reference cavity stabilization system was investigated extensively by Chalermongsak<sup>110</sup> and Chalermongsak et al.<sup>32</sup> in a test setup at Caltech. At best, this stabilization system should be limited by the Brownian noise of the reference cavity mirrors, about  $(6\text{ mHz}/\text{Hz}^{1/2}) \times (100\text{ Hz}/f)^{1/2}$ . However, even in the test setup this performance was degraded by a number of technical noise sources below a few tens of hertz, with the largest technical noise contributors being scattered light and seismic motion. Additionally, the apparent length noise at a few hundred hertz is additionally susceptible to acoustic noise.<sup>32</sup> Therefore, one might say more conservatively that in the presence of some common technical issues, the reference cavity stabilization loop is able to stabilize the laser frequency to better than  $0.1\text{ Hz}/\text{Hz}^{1/2}$  above 30 Hz.

One must also consider the frequency noise on the VCO used to drive the reference cavity AOM. Modeling<sup>111</sup> and measurement<sup>112</sup> indicate that the double-pass frequency noise is better than  $6\text{ mHz}/\text{Hz}^{1/2}$  above 10 Hz.

### Noise in the input modecleaner

In the GW band, the frequency stabilization to the input modecleaner should be limited by the shot noise of the light on the PDH photodiode. With 25 W of input light into the modecleaner, about  $P_{\text{IMC}} = 50 \text{ mW}$  is incident on the PDH photodiode with the modecleaner unlocked. Assuming the reflected light from the locked modecleaner is dominated by sideband light, and assuming  $\Gamma_{\text{IMC}} = 0.01 \text{ rad}$ , this sets the shot noise limit at  $(f_{\text{IMC}}/2)\sqrt{3hc/\lambda_0 P_{\text{IMC}}} = 15 \mu\text{Hz}/\text{Hz}^{1/2}$ . Because the bandwidth of the IMC loop is tens of kilohertz, the loop impresses this shot noise onto the laser frequency. In practice, because of imperfect modematching into the modecleaner, a few milliwatts of carrier light remains on the PDH detector even when the modecleaner is locked, making the shot-noise-limited frequency spectrum more like a few parts in  $10^{-4} \text{ Hz}/\text{Hz}^{1/2}$ .

### Noise in the common-mode and PRC lengths

The noise performance of this loop is limited by the shot noise on the PDH photodiode, along with the photodiode dark noise and the electronics noise of the first few electronic amplifiers. With 25 W of power at the interferometer input, these sources together limit the frequency noise performance to roughly  $1 \mu\text{Hz}/\text{Hz}^{1/2}$  between 10 and 100 Hz, and roughly  $10 \mu\text{Hz}/\text{Hz}^{1/2}$  at 1 kHz. The interferometer passively filters this input frequency noise above the common-mode pole  $f_+ \simeq 0.6 \text{ Hz}$ , attenuating the frequency noise on the circulating light to less than  $10^{-8} \text{ Hz}/\text{Hz}^{1/2}$  at 100 Hz.

The 9.1 MHz reflection PDH sensor additionally senses PRC length fluctuation, as seen in equation 2.21; therefore, PRC length fluctuation acts as an error point offset for the common-mode arm length stabilization loop.

### Coupling into differential arm length readout

The basic coupling mechanism can be understood by considering an asymmetric Michelson with differential mirror reflectivities:

$$\begin{aligned} E_{\text{out}}(\omega) &= \frac{E_{\text{in}}(\omega)}{2} \left[ r_X e^{2i\omega\ell_X/c} + r_Y e^{2i\omega\ell_Y/c} \right] \\ &= E_{\text{in}}(\omega) e^{2i\omega\ell_+} [r_+ \cos(2\omega\ell_-/c) + ir_- \sin(2\omega\ell_-/c)], \end{aligned} \quad (3.30)$$

with  $r_\pm = (r_X \pm r_Y)/2$  and  $\ell_\pm = (\ell_X \pm \ell_Y)/2$ . The cosine term in brackets in equation 3.30 is the usual Michelson response given a certain amount of length offset  $\ell_-$ . This

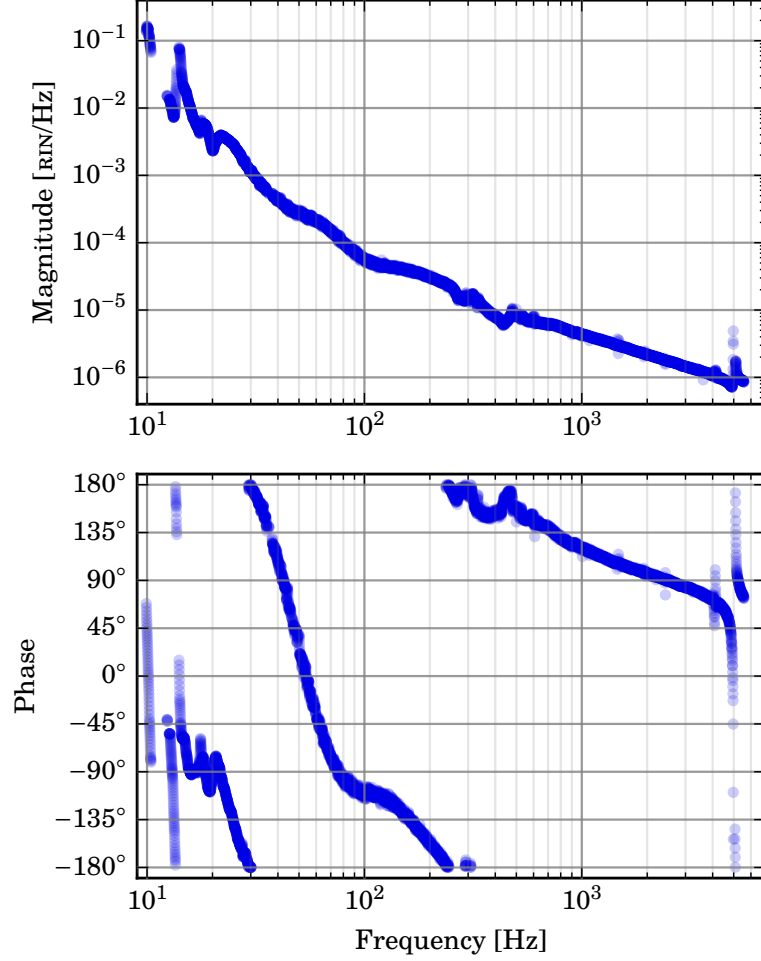


Figure 3.4: Frequency noise coupling into the differential arm length readout.

offset may include a macroscopic Schnupp offset  $\bar{\ell}_-$ , as well as a microscopic dc readout offset  $\delta\ell_-^{(0)}$ . The sine term in brackets in equation 3.30 is the “contrast defect” light. It converts phase sidebands at the interferometer input into amplitude sidebands at the output: a sideband of the form  $\pm i\Gamma e^{i(\omega_0 \pm \omega)t}$  at the input emerges as  $\mp \Gamma r_- \sin[2(\omega_0 \pm \omega)\ell_-/c]e^{i(\omega_0 \pm \omega)t}$  at the output.

Importantly, in the plane-wave approximation, and in the absence of radiation pressure, *both* a reflectivity imbalance and a length imbalance are required to produce a contrast defect. Advanced LIGO has two (intentional) sources of length imbalance; namely, the macroscopic Schnupp asymmetry in the Michelson length and the microscopic dc readout offset in the differential arm length. There are also (unintentional) arm reflectivity imbalances, which can manifest as dc reflectivity imbalances or as imbalances in the arm pole frequencies.

If radiation pressure is included, then a length imbalance alone is sufficient to pro-

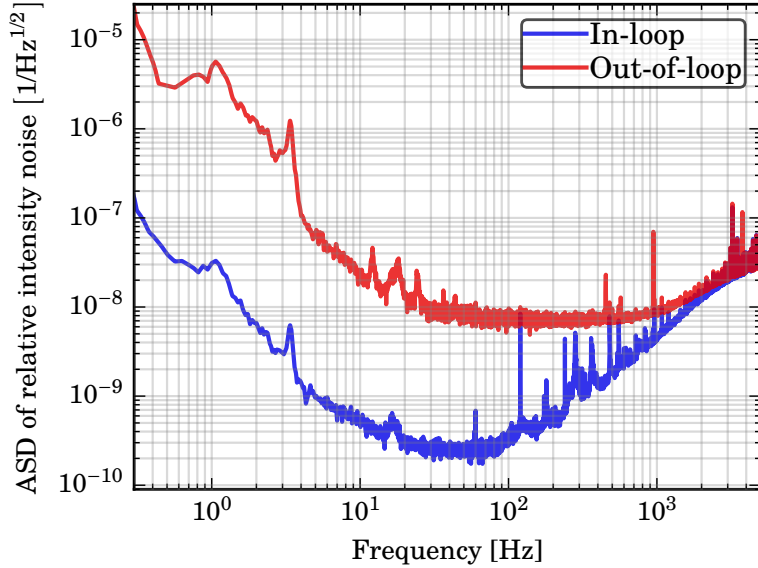


Figure 3.5: Relative intensity noise at the interferometer input, as measured by the in-loop and out-of-loop photodiodes for the outer intensity loop.

duce a frequency noise coupling into differential arm length. In Advanced LIGO, the dc readout offset in the differential arm length causes laser frequency fluctuations to convert to differential arm power fluctuations, since each arm is slightly detuned from resonance.<sup>21</sup>

Approximate analytical expressions for frequency coupling into differential arm length readout have been computed by Izumi and Sigg,<sup>20,21</sup> taking into account the aforementioned length and reflectivity imbalances, radiation pressure, and also a static common-mode arm length offset.

The measured H1 frequency noise coupling into the differential arm length readout is shown in figure 3.4.

## 3.6 Intensity noise

The out-of-loop sensor of the outer loop measures the amount of RIN at the interferometer input. A plot of this RIN is given in figure 3.5.

### Coupling into differential arm length readout

Approximate analytical expressions for intensity coupling into differential arm length readout have been computed by Izumi and Sigg.<sup>18,20,21</sup> The intensity cou-

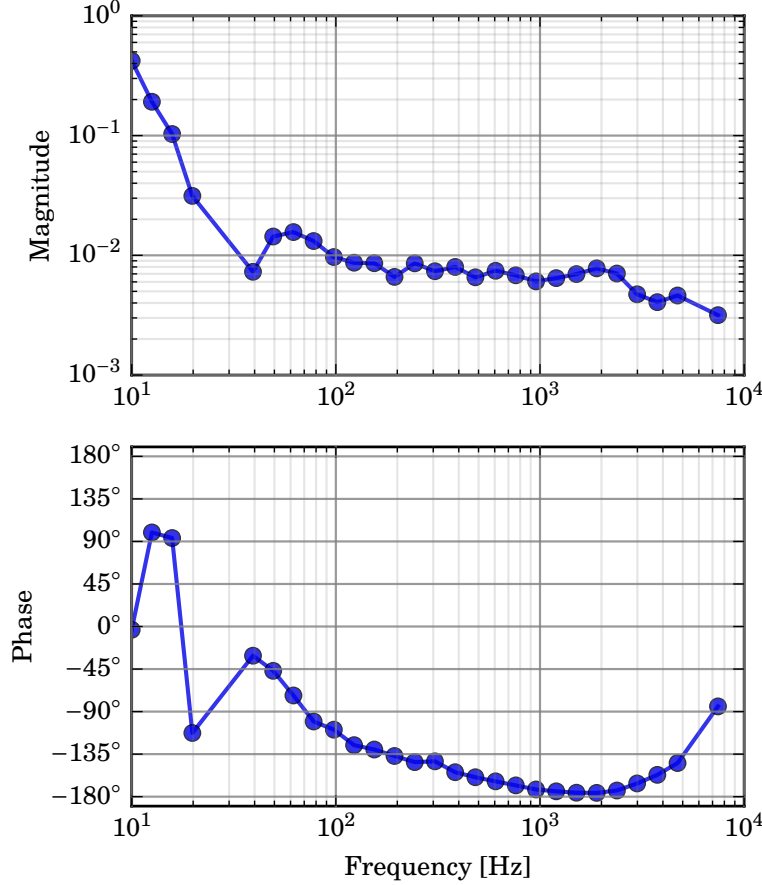


Figure 3.6: Intensity noise coupling into the differential arm length readout, in terms of input RIN into antisymmetric-port RIN.

pling arises through a few different mechanisms.

1. *dc readout*: Input intensity fluctuation modulates the amount of dc readout light exiting the interferometer.
2. *Contrast defect*: Similarly, input intensity fluctuation modulates the amount of contrast defect light exiting the interferometer. As with the frequency noise coupling, the magnitude of this effect depends on arm imbalances such as Schnupp asymmetry and differential frequency-dependent reflectivity.
3. *Radiation pressure*: Input intensity fluctuations produce radiation pressure fluctuations in the arms. If the arms are perfectly balanced, this fluctuation is purely common-mode. However, any of the aforementioned arm imbalances (as well as an imbalance in the reduced masses of the arms) will produce a differential signal.
4. *rf sidebands*: Because the attenuation of the rf sidebands through the OMC is finite ( $T = 60$  ppm for the 45.5 MHz sidebands), intensity noise of the sideband

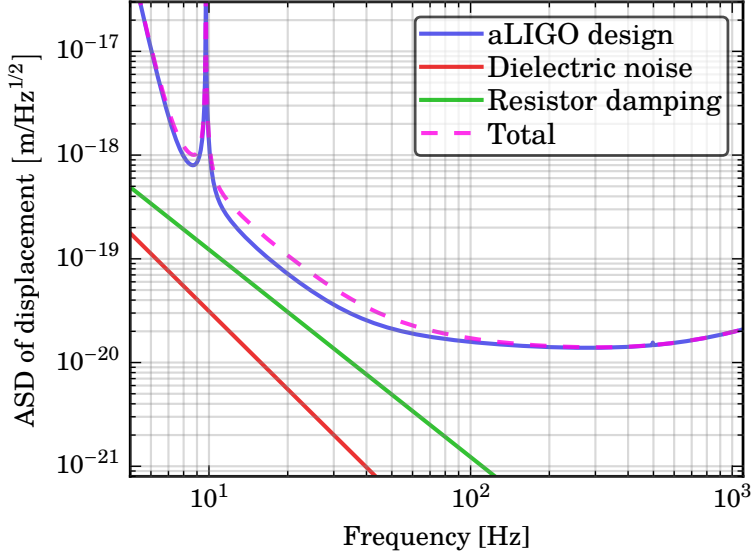


Figure 3.7: Noises associated with the test mass electrostatic actuator, along with the Advanced LIGO design sensitivity. The noises shown here scale with the bias voltage  $V_b$  applied to the test mass.

light can create signal on the GW photodiodes. Furthermore, because the rf sidebands are not resonant in the arms, they are not filtered by the common-mode cavity pole, so input intensity fluctuations light appear directly on the sideband light at the antisymmetric port.

The measured H1 intensity noise coupling into the differential arm length readout is shown in figure 3.6. The projection onto the differential arm length readout is then given in figure 3.12.

### 3.7 Photodiode noise

The photodiodes, their readout electronics, and the analog-to-digital conversion produce noise even in the absence of light. This noise amounts to  $1.0 \times 10^{-8}$  mA/Hz $^{1/2}$  (equivalent to 0.3 mA of photocurrent) per diode, with a  $1/f$  knee around 60 Hz.<sup>113</sup>

### 3.8 Actuator noise

In this section we discuss some actuator noises associated with the test masses. Estimates of these noises are shown in figure 3.7.

## DAC noise

The 18-bit DAC used to drive each suspension actuator has a typical voltage noise of<sup>14</sup>

$$S_{VV}^{(\text{DAC})}(f)^{1/2} = (300 \text{ nV/Hz}^{1/2}) \times \sqrt{1 + \left(\frac{50 \text{ Hz}}{f}\right)^2}. \quad (3.31)$$

Only the test mass DACs are expected to have the capacity to significantly impact the differential arm length sensitivity. During O1, the low-noise test mass actuator electronics had a dc gain of 2 V/V, with poles at 2.2 Hz, 2.2 Hz, and 152 Hz, and zeros at 50 Hz and 50 Hz. Combined with a force coefficient of  $2\alpha V_b \approx 2 \times (2 \times 10^{-10} \text{ N/V}^2) \times (380 \text{ V}) = 1.1 \times 10^{-7} \text{ N/V}$  and a mechanical compliance of  $2.6 \times 10^{-3} \text{ m/N} \times (0.4 \text{ Hz}/f)^2$ , this implies a DAC-induced displacement noise of  $1.2 \times 10^{-22} \text{ m/Hz}^{1/2}$  at 50 Hz for each test mass, rising like  $f^3$  below 50 Hz.

## Electrostatic damping

### Dielectric loss

In this section we examine noise arising from dielectric loss in the test mass substrate, which couples into test mass displacement via the electric field of the electrostatic driver.

The principle of the electrostatic driver is that an electric field  $\mathbf{E}$  applied to the test mass creates a polarization density  $\mathbf{P} = \epsilon_0 \chi \mathbf{E}$  in the substrate. Here  $\chi$  is the susceptibility of the substrate. To include the dielectric loss, we add a small imaginary component to the susceptibility:  $\chi = \chi_0(1 + i\phi_\chi)$ . Equivalently, if the test mass and the electrostatic driver are viewed as a capacitor, then the dielectric loss of the substrate makes the capacitance complex:  $C = C_0(1 + i\phi_C)$ . The dielectric loss of Suprasil glasses is quoted as  $5 \times 10^{-4}$  at 1 kHz,<sup>b</sup> although other measurements on fused silica indicate a much lower audio-band dielectric loss—less than  $4 \times 10^{-6}$ .<sup>c</sup> If a significant fraction of the capacitance comes from the field in the substrate (rather than field in the vacuum gap between the masses), then the loss angle of the capacitance will nearly equal the loss angle of the substrate.

<sup>b</sup> Heraeus, *Quartz Glass for Optics: Data and Properties*, HQS-MO\_01.4/E/07.2015

<sup>c</sup> Dynasil quotes this measurement as being “performed at Laboratory of A. R. Von Hippel, Laboratory for Insulation Research, Massachusetts Institute of Technology, May 1970.” (<http://www.dynasilsilicafusedsilica.com/techinfo.phtml?tid=9>)

If a sinusoidal voltage  $V(t) = V_0 \cos(\omega t)$  is applied to the ESD, a charge  $q$  will accumulate on the electrodes, with  $q(t) = C_0 V_0 [\cos(\omega t) + \phi_C \sin(\omega t)]$ . Then the time-averaged power dissipation in the dielectric is

$$W = \langle qV \rangle = \frac{1}{2} C_0 V_0^2 \phi_C \omega, \quad (3.32)$$

and from the fluctuation-dissipation theorem, the PSD of voltage fluctuation is therefore

$$S_{VV}(f) = \left| \frac{V(f)}{q(f)} \right|^2 \times \frac{2k_B T}{\pi^2 f^2} \frac{W(f)}{V_0^2} = \frac{2k_B T}{\pi f} \frac{\phi_C}{C_0}. \quad (3.33)$$

Given a drive voltage  $V$  on the electrode, the force exerted on the test mass is

$$F = -\frac{\partial U}{\partial x} = -\frac{\partial}{\partial x} \left[ \frac{1}{2} C(x) V^2 \right] = -\frac{1}{2} \frac{\partial C}{\partial x} V^2. \quad (3.34)$$

The coefficient  $\alpha = \frac{1}{2} \partial C / \partial x$  is known from measurement to be about  $2 \times 10^{-10} \text{ N/V}^2$ . Given some static bias voltage  $V_b$ , the small-signal voltage-to-force coefficient is then  $(\partial C / \partial x)V_b \simeq 8 \times 10^{-8} \text{ N/V}$  for  $V_b = 380 \text{ V}$ . This measurement can also be used to infer the capacitance of the system: assuming  $C_0(x) = 2\alpha d / (1 + x/d)$ , we have  $\partial C / \partial x|_0 \simeq 2\alpha$ , so  $C_0(0) \simeq 2 \text{ pF}$  for  $d = 5 \text{ mm}$ .<sup>d</sup> These numbers are sufficient to compute  $S_{VV}(f)$  and  $S_{FF}(f)$ .  $S_{xx}(f)$  is then computed from  $S_{FF}(f)$  via the free-mass compliance  $1/M\omega^2$ , with  $M = 40 \text{ kg}$ .

The resulting estimate for the displacement noise from dielectric loss is

$$S_{xx}(f)^{1/2} = (9.2 \times 10^{-24} \text{ m/Hz}^{1/2}) \times \left( \frac{\phi_C}{1 \times 10^{-6}} \right)^{1/2} \times \left( \frac{V_b}{100 \text{ V}} \right) \times \left( \frac{100 \text{ Hz}}{f} \right)^{5/2}, \quad (3.36)$$

which gives  $S_{xx}(f)^{1/2} = (7.0 \times 10^{-23} \text{ m/Hz}^{1/2}) \times (100 \text{ Hz}/f)^{5/2}$  for  $\phi_C = 4 \times 10^{-6}$  and  $V_b = 380 \text{ V}$ . This noise term is shown in figure 3.7.

This estimate does not consider effects from nearby conductors (for example, the ring heaters) or other capacitive effects from the cables connecting the electrodes to the flange.

---

<sup>d</sup> Numerical simulations by Evans and Miller<sup>115</sup> instead suggest

$$C_0(x) \simeq \frac{2\alpha d/b}{(1 + x/d)^b} \quad (3.35)$$

with  $b = 1.38$ , but quantitatively this does not affect the result too much.

## Circuit damping

We now examine noise arising from the circuit that drives the reaction mass electrodes.<sup>116,117</sup> Between each amplifier and each electrode there is a series resistor that protects against overcurrent. Each resistor injects Johnson–Nyquist noise (that is, charge fluctuation) into the electrodes, which adds damping to the test mass.

Assuming the bias electrode is held at  $V_b = V_0$  and each signal electrode is held at 0 V, the steady-state relationship between the bias voltage and the charge on the electrode is  $V_0 = q_0/C_0$ . Here we assume (again) that the position-dependent capacitance is given by  $C(x) = C_0/(1 + x/d)$ , where  $d = 5\text{ mm}$  is the position of the mass when the bias is 0 V.

We'll compute the  $Q$  of the pendulum mode in the presence of damping by first computing the peak energy stored in the mode, and the energy dissipated per cycle in the resistor.

The position dependence of the potential energy of the total electromechanical system is

$$U(x) = \frac{1}{2}C(x)V_0^2 + \frac{1}{2}\mu\omega_0^2x^2 \quad (3.37a)$$

$$= \frac{\alpha d V_0^2}{1 + x/d} + \frac{1}{2}\mu\omega_0^2x^2 \quad (3.37b)$$

$$\simeq \alpha d V_0^2 \left(1 - \frac{x}{d} + \frac{x^2}{d^2}\right) + \frac{1}{2}\mu\omega_0^2x^2 \quad (3.37c)$$

$$= \frac{1}{2}k(x - x_0)^2 + U_0 \quad (3.37d)$$

$$\equiv \frac{1}{2}k\xi^2 + U_0, \quad (3.37e)$$

where

$$\xi = x - x_0 \quad (3.38)$$

$$k = \frac{2\alpha V_0^2}{d} + \mu\omega_0^2 \simeq \mu\omega_0^2 \quad (3.39)$$

$$x_0 = \alpha V_0^2/k \simeq \alpha V_0^2/\mu\omega_0^2, \quad (3.40)$$

and  $U_0$  is a constant energy which we ignore henceforth. Note that the approximation in equations 3.39 and 3.40 is good to about 100 ppm for Advanced LIGO; in other words, the presence of the charged electrode does not significantly alter the pendulum dynamics.

Suppose the pendulum oscillates by an amount  $\xi(t) = \Xi \cos \omega t$ . The peak energy stored is  $U(\Xi) = \frac{1}{2}k\Xi^2$ . To compute the energy  $\Delta U$  dissipated as the pendulum swings, we need to compute the current flowing through the resistor. First, we compute the charge stored on the capacitor:

$$q = C(x)V_0 \simeq 2\alpha d V_0 \left(1 - \frac{x}{d} + \frac{x^2}{d^2}\right). \quad (3.41)$$

Therefore, the current flowing across the resistor is

$$\dot{q} = 2\alpha V_0 \dot{\xi} \left(\frac{2x}{d} - 1\right) \simeq -2\alpha V_0 \dot{\xi}, \quad (3.42)$$

where we have used the facts that  $\dot{x} = \dot{\xi}$  and  $x/d \ll 1$ . The energy dissipated in the resistor over one cycle  $2\pi/\omega$  of the pendulum motion is therefore

$$\Delta U(\Xi) = \frac{2\pi}{\omega} \times \langle \dot{q}^2 \rangle R \quad (3.43a)$$

$$= \frac{2\pi}{\omega} \times (2\alpha V_0)^2 \langle \dot{\xi}^2 \rangle R \quad (3.43b)$$

$$= \frac{2\pi}{\omega} \times (2\alpha V_0)^2 \times \frac{(\omega \Xi)^2}{2} \times R \quad (3.43c)$$

$$= \pi \omega (2\alpha V_0 \Xi)^2 R, \quad (3.43d)$$

and therefore the  $Q$  factor of the motion is

$$Q(\omega) = \frac{U(\Xi)}{\Delta U(\Xi)} = \frac{\frac{1}{2}k\Xi^2}{\pi \omega (2\alpha V_0 \omega \Xi)^2 R} = \frac{\mu \omega_0^2}{2\pi \omega (2\alpha V_0)^2 R}. \quad (3.44)$$

Since  $1/Q \propto \omega$ , the damping is viscous. Setting  $\omega = \omega_0$  gives the  $Q$  for the pendulum mode:

$$Q(\omega_0) = \frac{\mu \omega_0}{2\pi (2\alpha V_0)^2 R}. \quad (3.45)$$

For  $\mu = 16 \text{ kg}$ ,  $\omega_0/2\pi = 0.4 \text{ Hz}$ ,  $\alpha = 2 \times 10^{-10} \text{ N/V}^2$ ,  $V_0 = 380 \text{ V}$ , and  $R = 10 \text{ k}\Omega$ , the expected  $Q$  is then  $1.1 \times 10^{10}$ , which is greater than the expected mechanical  $Q$  of the pendulum alone. However, the shallower slope of the electrical damping ( $1/f^2$ ) compared to the mechanical damping ( $1/f^{5/2}$ ) means that the resistive damping noise overtakes the structural mechanical noise above 10 Hz.

The same answer could have been reached more simply by computing the Johnson–Nyquist noise of the electrode resistors and propagating the resulting voltage noise into test mass displacement. However, the above calculation shows that this simplified approach is not guaranteed to work if (1) the electromechanical stiffness  $k$  (equation 3.39) is significantly different from the mechanical stiffness  $\mu \omega_0^2$ , or (2) the thermal motion of the pendulum is a significant fraction of the gap size, so that the approximation  $x/d \ll 1$  in equation 3.42 does not hold.

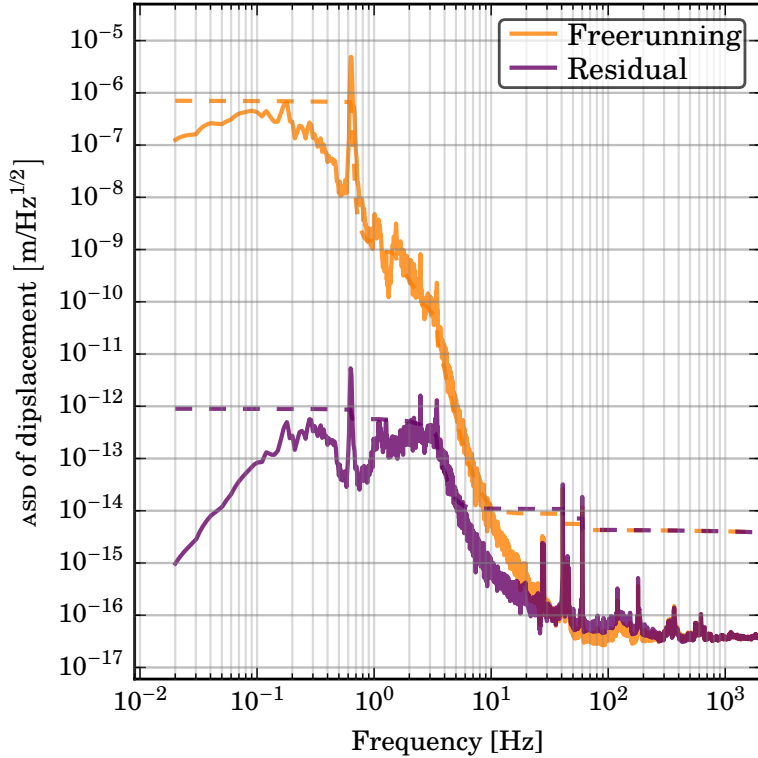


Figure 3.8: Freerunning and residual length noises for the power recycling cavity.

### 3.9 Noise from vertex degrees of freedom

Figures 3.8, 3.9, and 3.10 show the residual and freerunning displacement noises for the power-recycling cavity length, the Michelson length, and the signal-recycling cavity length. The residual displacement noise of each degree of freedom—particularly the Michelson and SRC lengths—can couple into the differential arm length readout. Above a few tens of hertz, the residual displacement noise comes mostly from sensing noise that is injected into the loops. The effect of this reinjected sensing noise is cancelled in the differential arm length readout using feedforward subtraction for the Michelson and SRC lengths, as described in 2.4. Nonetheless, residual noises in these three degrees of freedom can still couple into the differential arm length readout, potentially because of imperfect feedforward cancellation, the presence of significant displacement noises not arising from sensing noise, or bilinear couplings (which cannot be subtracted with an LTI feedforward scheme).

To measure the amount of vertex noise in the differential arm length readout, noise is injected into each vertex degree of freedom, with an amplitude sufficient to produce a clear excess in the differential arm length readout above the quiescent level.

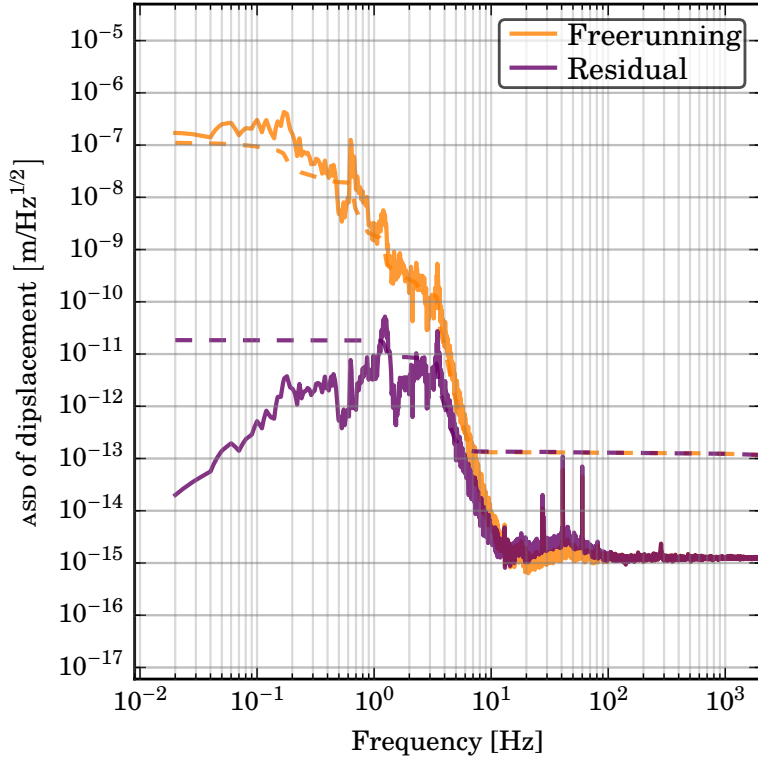


Figure 3.9: Freerunning and residual length noises for the signal recycling cavity.

One could use this data to produce a transfer function from the vertex degree of freedom to the differential arm length (as is shown in figures 2.16, 2.17, and 2.18), and then use the transfer function to propagate the quiescent vertex residual noise into the differential arm length. However, to account for bilinear couplings it is better to compute the excess power ratio between the vertex residual and the differential arm length readout, and use this power-based coupling to propagate the quiescent vertex residual noise into the differential arm length. This is the technique that is used for the noise budget presented in this chapter.

### 3.10 Noise from angular degrees of freedom

The impact of residual angular fluctuations on the differential arm length readout is budgeted in a fashion similar to the vertex length degrees of freedom, as described in section 3.9. Only the differential hard loops, the Michelson loops, and the SRC pointing loops are measured and budgeted, because the other loops are low-bandwidth and their impact on the differential arm length noise is expected to be minimal.

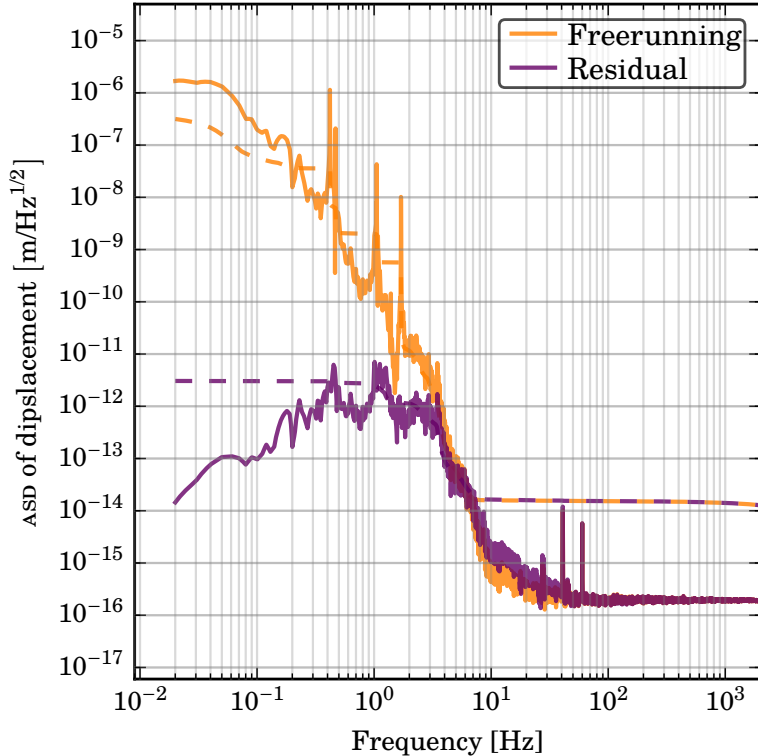


Figure 3.10: Freerunning and residual length noises for the Michelson degree of freedom.

### 3.11 Jitter noise

Jitter coupling was measured by exciting the pointing into the input modecleaner, and using the modecleaner wavefront sensor error signals as a witness for the amount of jitter being injected. The modecleaner suppresses, but does not completely remove, the jitter that is sent into the interferometer. The quiescent level of the wavefront sensor error signals represents an upper limit to the amount of jitter entering the interferometer.

### 3.12 Noise budget

In figure 3.11 we show a budget of fundamental noises limiting the differential arm length sensitivity for H1 during the first observing run. In figure 3.12 we show a budget that includes both the fundamental noises and the known technical noises described previously.

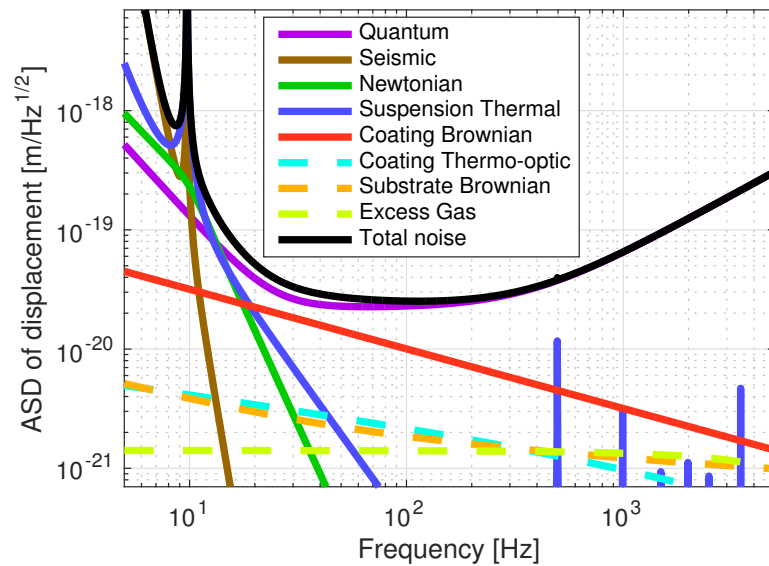


Figure 3.11: Noise budget of Advanced LIGO fundamental noises for the first observing run, computed using GWINC.<sup>86</sup>

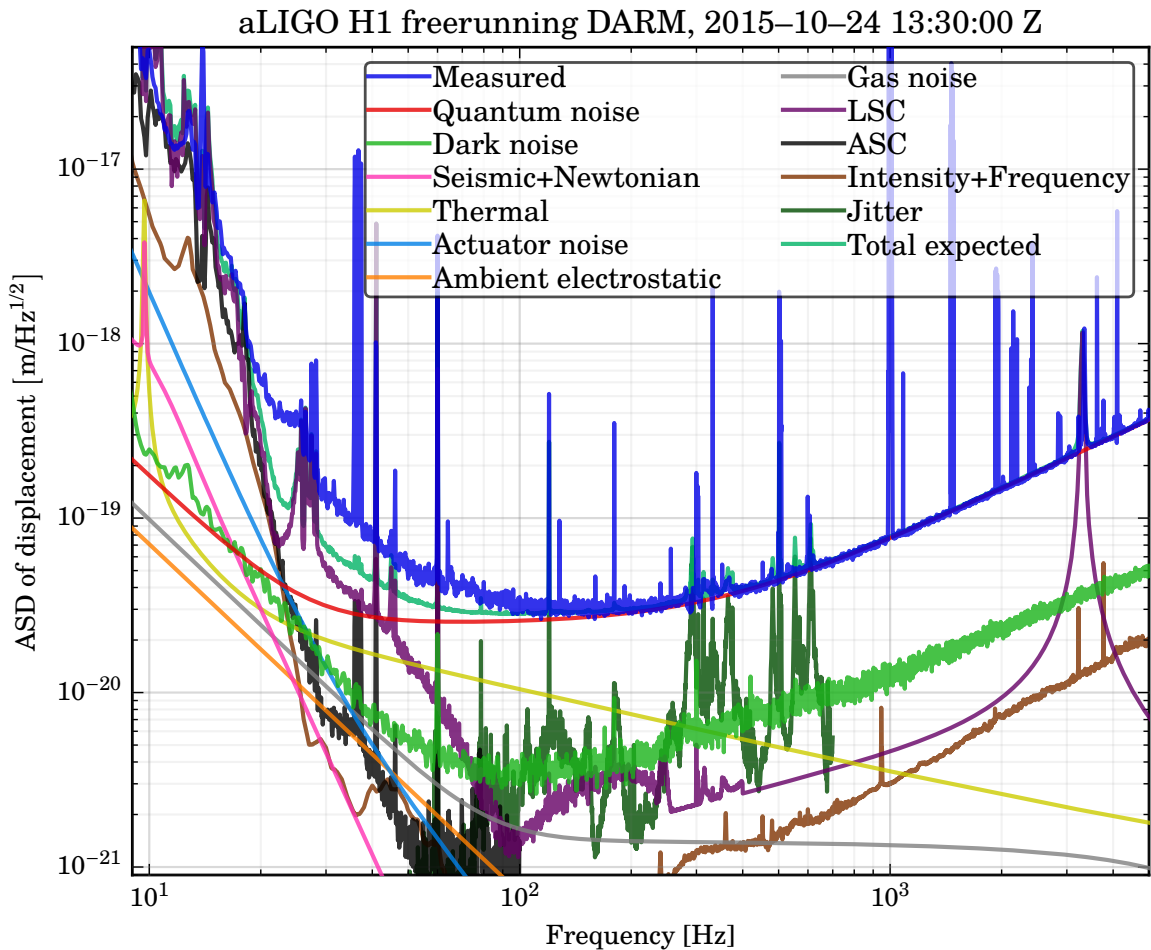


Figure 3.12: Noise budget of Advanced LIGO Hanford at the start of the first observing run.

## 4 Observational results

Advanced LIGO’s first observing run resulted in the first detection of gravitational waves,<sup>118</sup> with the second detection following soon after.<sup>119</sup> Both events resulted from the coalescence of heavy stellar-mass black holes (on the order of tens of solar masses) merging at redshift  $z \sim 0.1$ . In addition to furnishing the first direct detection of gravitational waves, these events also provide the first evidence for binary black hole systems and binary black hole coalescences.<sup>120</sup>

This chapter recapitulates the main astrophysical results of the first observing run; these results are the culmination of work performed by the entire LIGO–Virgo scientific collaboration. We will not comprehensively review the great variety of searches that are performed on the strain data, or the technical details of these searches.

### 4.1 GW150914

GW150914<sup>118,122</sup> was a gravitational wave event generated by the coalescence of two black holes, each a few tens of solar masses. The waveform was loud enough that it could be seen by eye in the bandpassed strain time series. The signal spent 8 cycles between 35 and 150 Hz. At 150 Hz, the strain reached its peak of about  $1.0 \times 10^{-21}$ , after which the signal rang down. A time–frequency plot of the signal is shown in figure 4.1, and the noise performance of the Hanford detector during this event (and the subsequent events) is shown in figure 4.2.

This event was initially found in low-latency by the burst pipeline,<sup>123</sup> and was later also extracted from the data using the compact-binary-coalescence pipeline.<sup>124</sup> The parameters of the event (masses, spins, and so on) were later estimated using a dedicated parameter estimation pipeline.<sup>125</sup>

GW150914 enabled new tests of general relativity<sup>126</sup> and inferences about the rate of binary black hole mergers.<sup>127,128</sup>

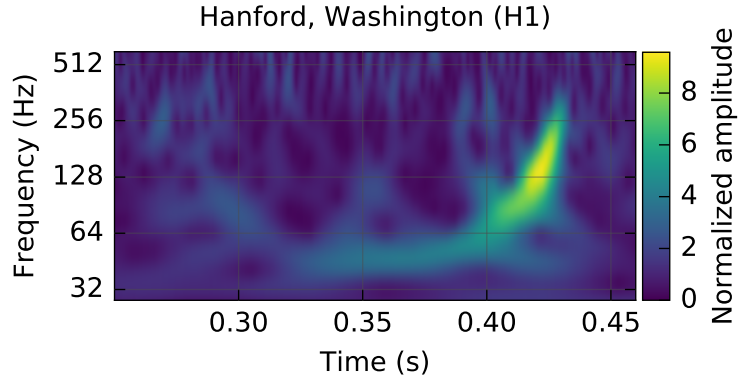


Figure 4.1: Spectrogram of the GW150914 signal in the H1 detector. Reproduced from Abbott et al.<sup>118</sup>

## 4.2 LVT151012

LVT151012<sup>122</sup> was a  $1.7\sigma$  event<sup>a</sup> that showed up with an SNR 9.7 between the two detectors. If indeed it came from a binary coalescence, it would correspond to a binary black hole system that is somewhat lighter than GW150914 (a chirp mass  $\simeq 15 M_\odot$ ) and somewhat further away ( $z \simeq 0.2$ ), with a ringdown frequency of 400 to 500 Hz.

## 4.3 GW151226

GW151226<sup>119,122</sup> was produced by another lighter binary black hole coalescence. Compared to GW150914, the SNR is slightly lower and accumulated over a larger number of cycles: the waveform spent about 45 cycles between 35 and 100 Hz, and then about 10 cycles from 100 to 450 Hz.

---

<sup>a</sup> The low statistical significance of this signal ( $< 5\sigma$ ) is the reason that is designated “LVT” (LIGO–VIRGO trigger) and is not given the “GW” designation.

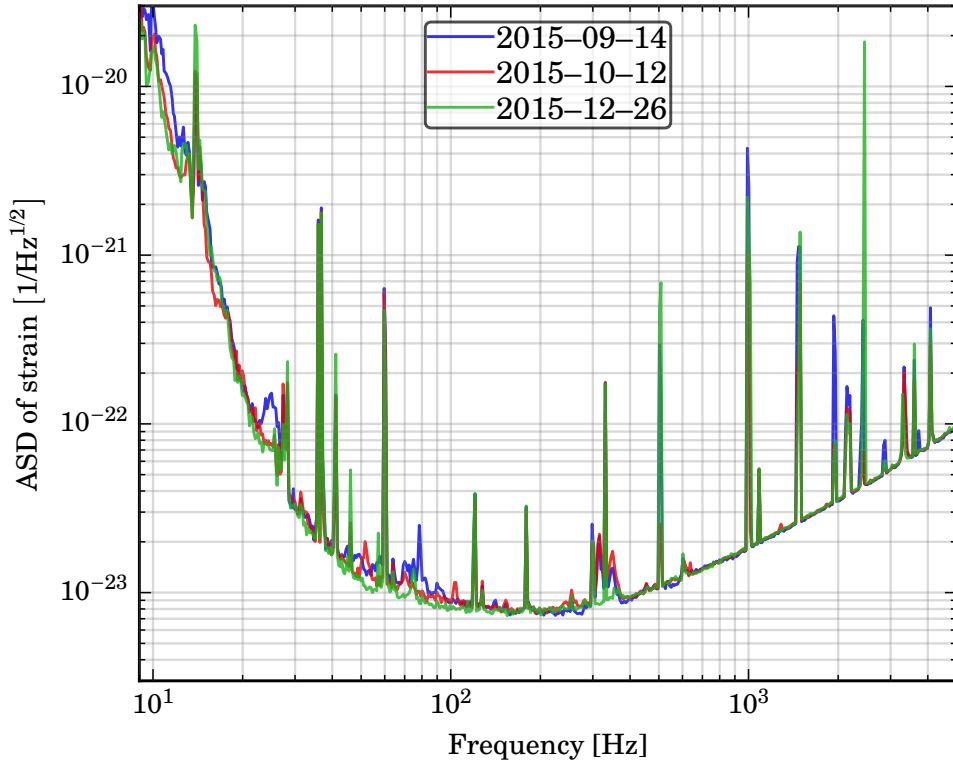


Figure 4.2: Advanced LIGO H1 strain spectra during the three events GW150914, LVT151012, and GW151226. The peaks around 300 Hz are jitter from a piezoelectrically actuated mirror mount that is used to inject the laser light into the vacuum system. These peaks were reduced midway through the observing run by applying epoxy to the mount.<sup>121</sup> The change in the noise floor between 40 Hz and 200 Hz occurs in the region where the spectrum is dominated by unknown noise. In addition to the mains line (60 Hz) and harmonics, one can see calibration lines at 35, 332, and 1080 Hz, the test mass roll mode at 13 Hz, a triple suspension roll mode at 41 Hz, test mass violin modes at 500 Hz and harmonics, the OMC length dither line at 4.1 kHz, and the OMC angle dither lines around 2.1 kHz. Noise analysis of these spectra can be found in chapter 3 and the references therein, particularly Martynov et al.<sup>43</sup>

# 5 Some topics in calibration

This chapter aims to introduce some concepts and computations that will be useful for current and future calibration efforts.

- In section 5.1 we give a brief overview of why and how GW interferometers are calibrated into strain.
- In section 5.2 we review the differential arm length optomechanical plant in the case of detuned signal recycling and arbitrary homodyne angle. We present a reparametrization of this function that is amenable to real-world calibration.
- In section 5.3 we examine how systematic errors in the interferometer calibration induce systematic errors in the parameter estimation of compact binary systems.
- In section 5.4 we show how to choose calibration line frequencies so as to minimize the uncertainty in the estimated calibration parameters.

## 5.1 Overview

The goal of interferometer calibration is to take the GW readout signal  $\delta P(t)$  (measured in counts, millamps, milliwatts, or some other kind of hardware unit) and produce an estimate of the freerunning spacetime strain  $\delta h(t) = \delta L_-/L$  incident along the detector arms. This requires characterizing both the optical dynamics of the interferometer (that is, the transfer function describing how length fluctuation  $\delta L_-$  is transduced into power fluctuation  $\delta P$ ) and the feedback control system (figure 5.1), since this system suppresses power fluctuations within the servo bandwidth.

Currently, Advanced LIGO uses several methods to calibrate the interferometer readout.<sup>51</sup> The “photon calibrator” is the main method used to measure the interferometer’s inverse sensing function, and can be operated while the interferometer is

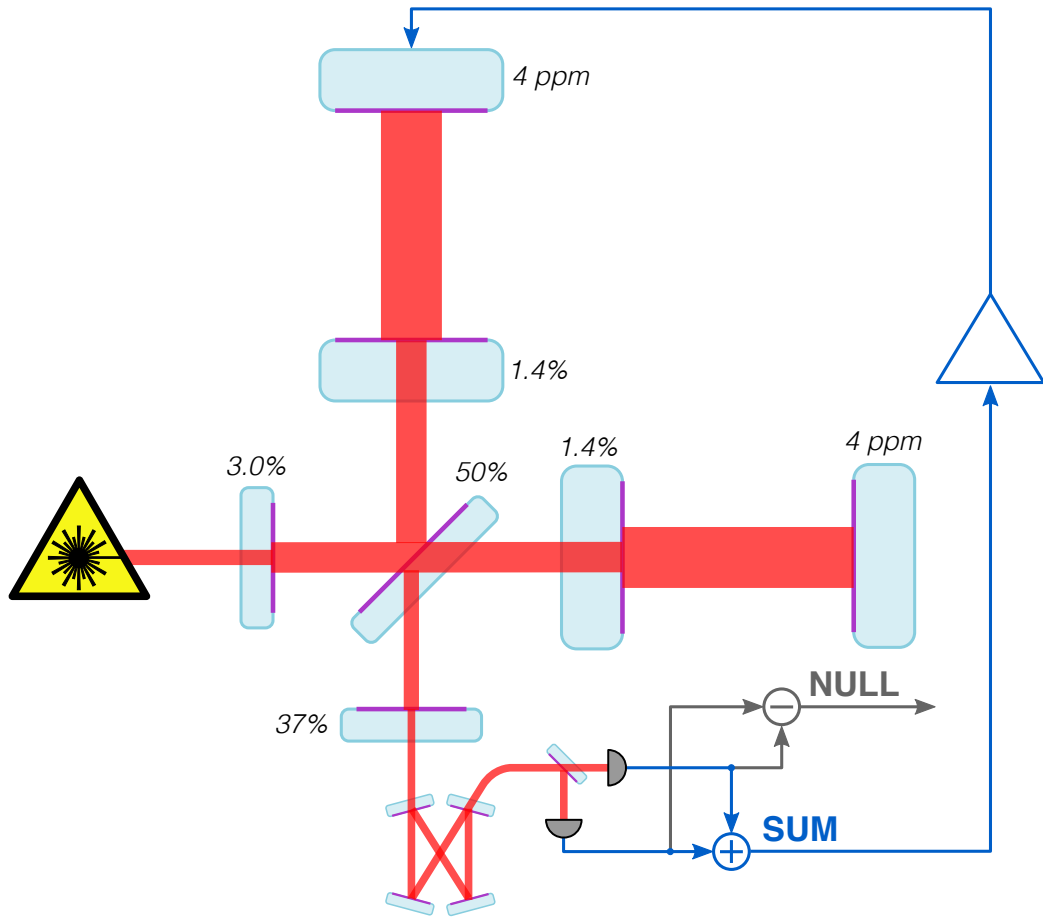


Figure 5.1: Simplified diagram of the Advanced LIGO differential arm length sensing and control. The summed photocurrent (“SUM”) is directly proportional to the power fluctuation  $\delta P$  at the interferometer’s antisymmetric port, which is related to the differential arm length fluctuation  $\delta L_-$  by a transfer function  $C(f) = \delta P(f)/\delta L_-(f)$ . The photocurrent is amplified and fed back to one of the end test masses with a bandwidth  $\sim 50$  Hz; the open-loop transfer function of this feedback loop is  $G(f)$ . Relating the observed power fluctuation  $\delta P$  to the incident freerunning strain requires characterizing the response function  $[1 - G(f)]/C(f)$ . The differenced photocurrent (“NULL”) is used for diagnostic purposes only. Numbers next to the mirrors give the power transmissivities. (For certain portions of this chapter, the SRM is assumed to be 20 % transmissive.)

in its nominal operating state. An auxiliary, amplitude-modulatable  $1\text{ }\mu\text{m}$  laser is reflected from one of the end test masses, thereby producing a radiation force. The applied power is measured with a NIST-traceable photodiode, so that the amount of applied force (assuming no in-vacuum clipping or other nonidealities) is known to better than 1 %.<sup>129</sup> With a knowledge of the test mass suspension dynamics, this known force can be expressed as an equivalent free-mass displacement. Therefore, when the interferometer is locked, the inverse sensing function [that is, the transfer function from freerunning free-mass displacement (in meters) to GW readout (in milliwatts, millamps, or digital counts)] can be measured directly.

Two other methods are used as cross-checks, and require the interferometer to be unlocked.

1. One method uses a simple Michelson formed by the beamsplitter and the input test masses to calibrate an input test mass actuator against the main laser wavelength. Then a single arm is locked with the main laser, allowing the end test mass actuator to be calibrated against the input test mass actuator. Therefore, the end test mass control signal (in counts) can be calibrated into meters.
2. The other method uses the auxiliary green locking system. A green laser is locked to each arm, producing an rf beat note. A VCO with a known voltage-to-frequency actuation strength is locked to this beat note. An end test mass actuator (with a control signal in counts) can then be calibrated against the VCO control signal (in hertz).

## 5.2 Differential arm length optomechanical plant

In chapter 2 we showed that the differential arm length optomechanical plant during the first observing run corresponded to nearly pure resonant sideband extraction, with a small amount of antispring detuning. In this section we explore more fully the effect of optical springs on this optomechanical plant.

Buonanno and Chen<sup>41</sup> derived input-output relations for a signal-recycled Fabry-Pérot interferometer including radiation pressure. From this one can write down the displacement-to-power transfer function,<sup>a</sup> up to a constant (see, for example,

---

<sup>a</sup> This transfer function is fundamentally a *force*-to-power transfer function. However, for consistency with the simple RSE case, the force is referred to an equivalent freerunning displacement via the free-mass compliance  $1/M\omega^2$ .

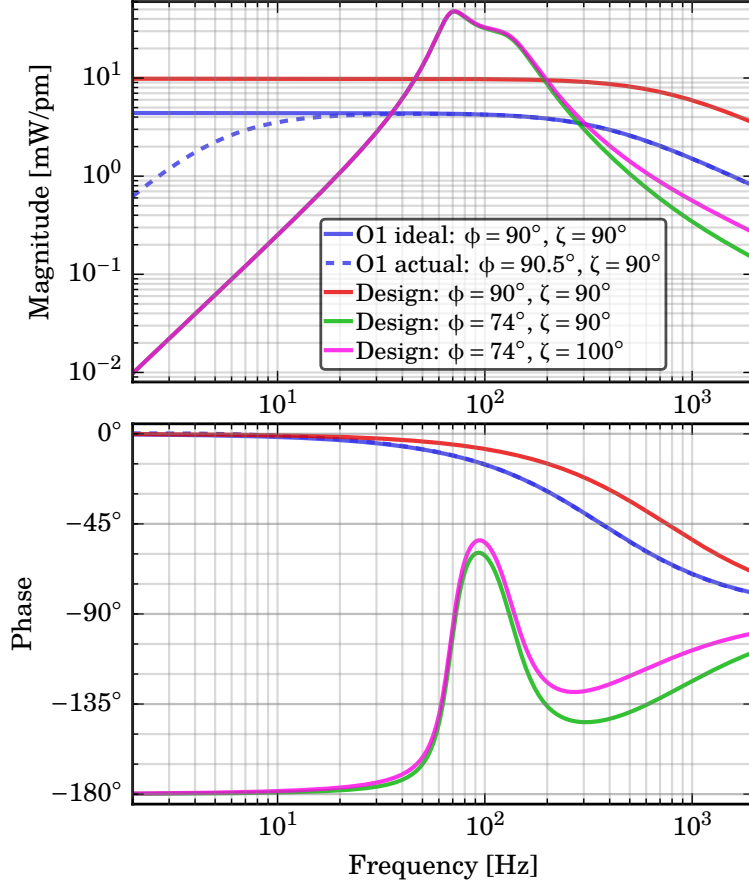


Figure 5.2: Advanced LIGO differential arm length plant, shown for both O1 ( $T_s = 37\%$ ,  $P_{bs} = 700\text{ W}$ ) and for the final design ( $T_s = 20\%$ ,  $P_{bs} = 3500\text{ W}$ ). In both cases, 20 mA (= 27 mW) of dc readout light is assumed.

Ward<sup>130)</sup>:

$$\frac{\delta P}{\delta L_-} \propto \frac{t_s e^{i\beta} [(1 - r_s e^{2i\beta}) \cos \phi \cos \zeta - (1 + r_s e^{2i\beta}) \sin \phi \sin \zeta]}{1 + r_s^2 e^{4i\beta} - 2r_s e^{2i\beta} [\cos 2\phi + (\mathcal{K}/2) \sin 2\phi]} \sqrt{\frac{2P_{bs}\omega_0^2}{\omega_a^2 + \omega^2}}, \quad (5.1)$$

where the quantities are defined in appendix D.

With some algebra (done in appendix D), this can be transformed to

$$\frac{\delta P}{\delta L_-} = g \times \frac{1 + if/z}{(1 + if/|p|Q_p - f^2/|p|^2) - \xi^2/f^2}, \quad (5.2)$$

with quantities defined as follows.

- $g$  is an optical gain (in milliwatts per picometer, or something similar).
- $z$  is a zero of the transfer function, given by

$$z = f_a \times \frac{\cos(\phi + \zeta) - r_s \cos(\phi - \zeta)}{\cos(\phi + \zeta) + r_s \cos(\phi - \zeta)}, \quad (5.3)$$

<i>Quantity</i>	$O_1/O_2,$ <i>nominal</i>	$O_1/O_2,$ <i>actual H1</i>	<i>Design, no</i> <i>detuning</i>	<i>Design, NS/NS</i> <i>detuning</i>
$f_a$	42 Hz	42 Hz	42 Hz	42 Hz
$T_s$	37 %	37 %	20 %	20 %
$\phi$	90 °	90.5 °	90 °	74 °
$\zeta$	90 °	90(3) °	90 °	100 °
$P_{bs}$	700 W	700 W	6250 W	6250 W
$g$	4.4 mW/pm	4.4 mW/pm	9.8 mW/pm	9.8 mW/pm
$z$	365.2 Hz	365.2 Hz	753.7 Hz	396.3 Hz
$ p $	365.2 Hz	364.2 Hz	753.7 Hz	143.8 Hz
$Q_p$	0.5	0.501	0.5	2.422
$\xi^2$	$0^2 \text{ Hz}^2$	$-4.93^2 \text{ Hz}^2$	$0^2 \text{ Hz}^2$	$+63.45^2 \text{ Hz}^2$

Table 5.1: Parameters for the Advanced LIGO optomechanical plant.

where  $f_a$  is the arm pole.

- $p$  is a complex frequency given by

$$p = f_a \times \frac{1 - r_s e^{2i\phi}}{1 + r_s e^{2i\phi}}, \quad (5.4)$$

so that

$$|p| = f_a \sqrt{\frac{1 - 2r_s \cos 2\phi + r_s^2}{1 + 2r_s \cos 2\phi + r_s^2}} \quad (5.5)$$

and

$$Q_p = \frac{|p|}{2 \operatorname{Re} p} = \frac{1}{2} \frac{\sqrt{1 - 2r_s^2 \cos 4\phi + r_s^4}}{1 - r_s^2}. \quad (5.6)$$

Note that  $Q_p$  attains a minimum value of 1/2 when  $p$  is real.

- $\xi^2$  is the square of the spring frequency:

$$\xi^2 = f_a^2 \times \frac{2\alpha r_s \sin 2\phi}{1 - 2r_s \cos 2\phi + r_s^2}, \quad (5.7)$$

and may be positive or negative. Here  $\alpha = 4P_{bs}\omega_0/(\omega_a^4 M L^2)$ .

The transfer function in equation 5.2 is *not* given in a pole-zero representation, since the denominator has not been factorized. Because the denominator is quartic,

one can always write down analytic expressions for its roots (that is, the poles of the transfer function), but these expressions are quite complicated. Instead, we will make some general remarks and then give pole-zero representations of this transfer function in some limiting cases.

First, we remark on the general features of this transfer function, which has three zeros and four poles. In both the spring and antispring cases, it has two zeros at 0 Hz, a left-handed real zero at the frequency  $z$ , and a left-handed complex pole pair with a magnitude roughly equal to the frequency  $|p|$ . In the spring case, the final two poles constitute a right-handed complex pair with magnitude roughly equal to  $|\xi^2|^{1/2}$ . In the antispring case, the final two poles are both real, with one left-handed and one right-handed, and the magnitudes are again roughly equal to  $|\xi^2|^{1/2}$ .

Second, we remark that this transfer function reduces to the simple RSE case in the limit that  $\phi = \pi/2$ . In this case, we have  $\text{Im } p = 0$ , so  $\alpha = 0$ . The denominator then comprises exactly two real poles at the RSE pole frequency  $f_- = f_a \times (1+r_s)/(1-r_s)$ . In the numerator, the zero becomes  $f_-$  (regardless of the value of  $\zeta$ ), and it therefore cancels one of the poles in the denominator. Therefore, the bracketed portion of equation 5.2 becomes  $1/(1+if/f_-)$ , as expected.

Third, we quantitatively analyze the limit that the frequency of the spring is much less than the frequency of the RSE pole. This situation may be encountered if either  $\phi - \pi/2$  or  $P_{BS}$  is sufficiently small, or if  $M$  or  $L$  are sufficiently large. In this situation, the denominator can be written *approximately* as the product of two pole pairs:

1. One pair, located in the left-hand  $s$  plane, is complex and produces the high-frequency rolloff in the RSE response. The magnitude and  $Q$  of this pair are  $|p|$  and  $Q_p$ , as given above.
2. The second pair produces the spring (or antispring) feature at low frequencies.
  - a) In the spring case ( $\xi^2 > 0$ ), the pole pair is complex and lies in the right-hand  $s$  plane. The magnitude of this pair can be determined by examining the phase  $\theta_D(f)$  of the denominator:

$$\tan[\theta_D(f)] = \frac{f/|p|Q_p}{1-f^2/|p|^2-\xi^2/f^2} \simeq \frac{f/|p|Q_p}{1-\xi^2/f^2}. \quad (5.8)$$

The maximum of the spring feature should occur when  $\theta_D(f) = -\pi/2$ ; that is,  $\tan \theta_D = -\infty$ . This occurs when  $f = \pm|\xi^2|^{1/2}$ . So  $|\xi^2|^{1/2}$  is the magnitude of this right-handed pole pair. To find the  $Q$  of the pair, we note that when

$f = |\xi^2|^{1/2}$ , the denominator is (approximately)  $i|\xi^2|^{1/2}/|p|Q_p$ . Therefore,

$$Q_\xi \approx \frac{|p|}{|\xi^2|^{1/2}} Q_p. \quad (5.9)$$

- b) In the antispring case ( $\xi^2 < 0$ ), the pole pair is real, with one pole being right-handed and the other left-handed. Correspondingly, there is a gentle rolloff instead of a sharp resonance feature, and there is no phase loss at low frequencies.

In either case, the denominator can be written as

$$\left( \operatorname{sgn} \xi^2 - \frac{if}{|\xi^2|^{1/2} Q_\xi} - \frac{f^2}{|\xi^2|} \right) \left( 1 + \frac{if}{|p|Q_p} - \frac{f^2}{|p|^2} \right). \quad (5.10)$$

The optomechanical plant parameters for various Advanced LIGO configurations are given in table 5.1, and the corresponding transfer functions are shown in figure 5.2.

### 5.3 Systematic calibration errors

In this section we will examine how systematic errors in the interferometer calibration affect astrophysical parameter estimation.

#### General discussion and formalism

Suppose we have some frequency-domain detector waveform  $d(f)$  which is known to contain an astrophysical signal—here assumed to be a compact binary coalescence. We want to estimate the astrophysical parameters  $\theta$  that best correspond to  $d$ . This analysis is commonly done in a Bayesian framework,<sup>131</sup> where the name of the game is to use Bayes's theorem arrive at a probability density function (pdf) for  $\theta$  given the measured waveform.

Bayes's theorem says

$$p(\theta|d) = \frac{p(d|\theta)p(\theta)}{p(d)}, \quad (5.11)$$

with the quantities defined as follows.

1.  $p(\theta)$  is the prior pdf for  $\theta$  (that is, our initial guess at a pdf of  $\theta$ ).
  2.  $p(d|\theta)$  is the probability of observing the waveform  $d$  given a certain value of  $\theta$ .
- This conditional pdf is determined by the underlying physics that is assumed

to generate  $d$  from  $\boldsymbol{\theta}$  (in our case, a combination of analytic and numerical relativity). Any quantity proportional to  $p(d|\boldsymbol{\theta})$  is referred to as a likelihood function.

3.  $p(d)$  is a normalizing constant referred to as the evidence.
4.  $p(\boldsymbol{\theta}|d)$  is the posterior pdf for  $\boldsymbol{\theta}$  (that is, our updated pdf for  $\boldsymbol{\theta}$  in light of  $d$ ).

If the detector noise in each frequency bin is Gaussian, we can assume the following for the logarithm of the likelihood function:

$$\ell \equiv \ln p[d(f;\lambda) | \boldsymbol{\theta}] \propto -\frac{1}{2} \int_0^\infty df \frac{|h(f;\boldsymbol{\theta}) - d(f;\lambda)|^2}{S_{nn}(f;\lambda)}. \quad (5.12)$$

Here  $h(f;\boldsymbol{\theta})$  is the relativistic waveform expected from a system with parameters  $\boldsymbol{\theta}$ , and  $S_{nn}(f)$  is the noise PSD of the detector.  $d(f)$  is (again) the waveform from the detector. For both  $d$  and  $S_{nn}$  we have now explicitly written the dependence on  $\lambda$ , which refers to the calibration parameters used to estimate the freerunning strain from the detector error signal  $e(f)$ . Estimating  $d$  from  $e$  requires estimating a transfer function referred to as the interferometer's response function,  $R$ :

$$d(f;\lambda) = R(f;\lambda) e(f) \quad (5.13)$$

$$S_{nn}(f;\lambda) = |R(f;\lambda)|^2 S_{ee}(f). \quad (5.14)$$

We now want to know how the maximum of  $\ell$  shifts if small calibration errors are introduced.

Suppose  $e(f)$  is generated from a GW waveform  $h(f;\boldsymbol{\theta}_{\text{true}})$  with parameters  $\boldsymbol{\theta}_{\text{true}}$ . Suppose also the interferometer's calibration parameters are  $\lambda_{\text{true}}$ , but we've instead made a slightly wrong estimate  $\lambda$ . Then  $d(f) = h(f;\boldsymbol{\theta}_{\text{true}}) \times R(f;\lambda) / R(f;\lambda_{\text{true}})$ , and  $S_{nn}(f) = S_{nn}^{(\text{true})}(f) \times |R(f;\lambda) / R(f;\lambda_{\text{true}})|^2$ .

Therefore,

$$\begin{aligned} \ell(\boldsymbol{\theta}, \lambda) &\equiv \ln p(d|\boldsymbol{\theta}, \lambda) \\ &\propto -\frac{1}{2} \int_0^\infty df \frac{|h(f;\boldsymbol{\theta}_{\text{true}})|^2}{S_{nn}^{(\text{true})}(f)} \times \left| 1 - \frac{R(f;\lambda_{\text{true}})}{R(f;\lambda)} \frac{h(f;\boldsymbol{\theta})}{h(f;\boldsymbol{\theta}_{\text{true}})} \right|^2, \end{aligned} \quad (5.15)$$

where we now explicitly indicate the functional dependence on  $\lambda$  as well as  $\boldsymbol{\theta}$ .

For brevity, we'll find it convenient to define

$$r(\boldsymbol{\theta}, \lambda) = \frac{R(f;\lambda_{\text{true}})}{R(f;\lambda)} h(f;\boldsymbol{\theta}) - h(f;\boldsymbol{\theta}_{\text{true}}). \quad (5.16)$$

We want to know how the maximum of  $\ell$  changes in the presence of nonzero  $\Delta\lambda = \lambda - \lambda_{\text{true}}$ , and how this maps to an equivalent  $\Delta\theta = \theta - \theta_{\text{true}}$ .

With a little calculus, it is straightforward to show

$$\underbrace{\begin{bmatrix} \ell_{\theta_1\theta_1} & \ell_{\theta_1\theta_2} & \cdots & \ell_{\theta_1\theta_M} \\ \ell_{\theta_2\theta_1} & \ell_{\theta_2\theta_2} & \cdots & \ell_{\theta_2\theta_M} \\ \vdots & \vdots & \ddots & \vdots \\ \ell_{\theta_M\theta_1} & \ell_{\theta_M\theta_2} & \cdots & \ell_{\theta_M\theta_M} \end{bmatrix}}_{\equiv \mathcal{H}} \begin{bmatrix} \Delta\theta_1 \\ \Delta\theta_2 \\ \vdots \\ \Delta\theta_M \end{bmatrix} = \underbrace{\begin{bmatrix} \ell_{\theta_1\lambda_1} & \ell_{\theta_1\lambda_2} & \cdots & \ell_{\theta_1\lambda_N} \\ \ell_{\theta_2\lambda_1} & \ell_{\theta_2\lambda_2} & \cdots & \ell_{\theta_2\lambda_N} \\ \vdots & \vdots & \ddots & \vdots \\ \ell_{\theta_M\lambda_1} & \ell_{\theta_M\lambda_2} & \cdots & \ell_{\theta_M\lambda_N} \end{bmatrix}}_{\equiv \mathcal{M}} \begin{bmatrix} \Delta\lambda_1 \\ \Delta\lambda_2 \\ \vdots \\ \Delta\lambda_N \end{bmatrix}, \quad (5.17)$$

where  $\ell_{\mu_i\mu_j}$  is the second partial derivative of  $\ell$  with respect to parameters  $\mu_i$  and  $\mu_j$ :

$$\ell_{\mu_i\mu_j} = \frac{\partial^2 \ell}{\partial \mu_i \partial \mu_j} = -\frac{1}{2} \int_0^\infty \frac{df}{S_{nn}^{(\text{true})}(f)} \times 2 \operatorname{Re} \left[ \frac{\partial^2 r^*}{\partial \mu_i \partial \mu_j} r + \frac{\partial r^*}{\partial \mu_i} \frac{\partial r}{\partial \mu_j} \right]. \quad (5.18)$$

In equation 5.17 we have made note of the fact that the matrix  $\mathcal{H}$  on the left-hand side is the Hessian of  $\ell$  with respect to  $\theta$ . Additionally, to the matrix on the right-hand side we have assigned the letter  $\mathcal{M}$ . This allows us to write the relationship between calibration errors  $\Delta\lambda$  and parameter estimation errors  $\Delta\theta$  as

$$\Delta\theta = \mathbf{J} \Delta\lambda \quad \text{with } \mathbf{J} = \mathcal{H}^{-1} \mathcal{M}. \quad (5.19)$$

The letter  $\mathbf{J}$  is chosen to remind the reader of a Jacobian matrix, since this equation expresses how first-order changes in  $\lambda$  are related to first-order changes in  $\theta$ .

## Application to 2 pN parameter estimation

For the purpose of this simulation, we want to examine the effect of calibration errors on a simple Bayesian parameter estimation using stationary-phase 2 pN waveforms (see Röver et al.<sup>132</sup> for an example of this kind of parameter estimation).

In the 2 pN approximation, the parameters comprising  $\theta$  are

- the total mass  $M = M_1 + M_2$ ,
- the symmetric mass ratio  $\eta = M_1 M_2 / (M_1 + M_2)^2$ ,
- the coalescence time  $t_c$ ,
- the coalescence phase  $\phi_c$ , and
- the luminosity distance  $D$ , which is degenerate with the inclination angle of the source.

The 2 pN stationary-phase waveform (expressed as a frequency-domain strain) is then

$$h(f; \boldsymbol{\theta}) = \frac{1}{2\pi^{2/3} c^{3/2}} \frac{(GM)^{5/6}}{D} \left( \frac{5\eta}{6} \right)^{1/2} f^{-7/6} \times \exp \left\{ -i[2\pi f t_c + \phi_c + \psi_{2pN}(f; M, \eta)] \right\}, \quad (5.20)$$

where  $\psi_{2pN}$  is a polynomial in  $(\pi GMf)^{1/3}/c$ , with coefficients involving  $\eta$ .<sup>132</sup>

For the calibration model, we assume  $\boldsymbol{\lambda}$  comprises six parameters ( $g, z, |p|, Q_p, \xi^2$ , and  $a$ ), and the response function is given by

$$R(f; \boldsymbol{\lambda}) = \frac{1}{C(f; g, z, |p|, Q_p, \xi^2)} - A(f; a)D(f). \quad (5.21)$$

Here  $C$  is the interferometer sensing function, with parameters given by equation 5.2.  $A$  is the suspension transfer function. In this simulation, the ultimate (electrostatic) and penultimate (magnetic) actuators are used, with a crossover around 20 Hz. The strength of the penultimate actuator is assumed to be constant for the duration of the run, while the strength  $a$  of the ultimate actuator (in newtons per volt) is assumed to drift because of charge accumulated on or near the test mass.  $D$  is a set of (known) analog and filters connecting the error signal (in millamps) to the control signal (in volts). The resulting open-loop transfer function has a UGF of 180 Hz, which is required to stabilize the right-handed poles of the spring feature; this OLTF is shown in figure 5.3. The total response function  $R = 1/S$  is shown in figure 5.4.

The true astrophysical parameters were chosen to be  $M = 65 M_\odot$ ,  $\eta = 0.247$ ,  $t_c = 0.250\text{ms}$ ,  $\phi_c = 0.60\text{rad}$ , and  $D = 410\text{Mpc}$ . The true calibration parameters were chosen to be the detuned RSE NS/NS-optimized configuration given in table 5.1. We compute  $\mathbf{J}$  in equation 5.19 using an automatic differentiation routine.<sup>b</sup> This yields the following relationship between systematic errors in the calibration parameters and systematic errors in the astrophysical parameters:

$$\begin{bmatrix} \Delta M/M \\ \Delta \eta/\eta \\ \Delta t_c/(1\text{ms}) \\ \Delta \phi_c/(1\text{rad}) \\ \Delta D/D \end{bmatrix} = \frac{1}{10^3} \begin{bmatrix} -80 & -21 & -80 & -64 & -51 & -129 \\ 177 & 40 & 198 & 136 & 94 & 274 \\ 260 & 851 & -1689 & 812 & 857 & 570 \\ -2174 & -819 & -1218 & -1913 & -1751 & -3148 \\ -180 & -71 & 329 & 3 & 194 & 961 \end{bmatrix} \begin{bmatrix} \Delta g/g \\ \Delta z/z \\ \Delta |p|/|p| \\ \Delta Q_p/Q_p \\ \Delta \xi^2/\xi^2 \\ \Delta a/a \end{bmatrix}. \quad (5.22)$$

---

<sup>b</sup> ad in python.

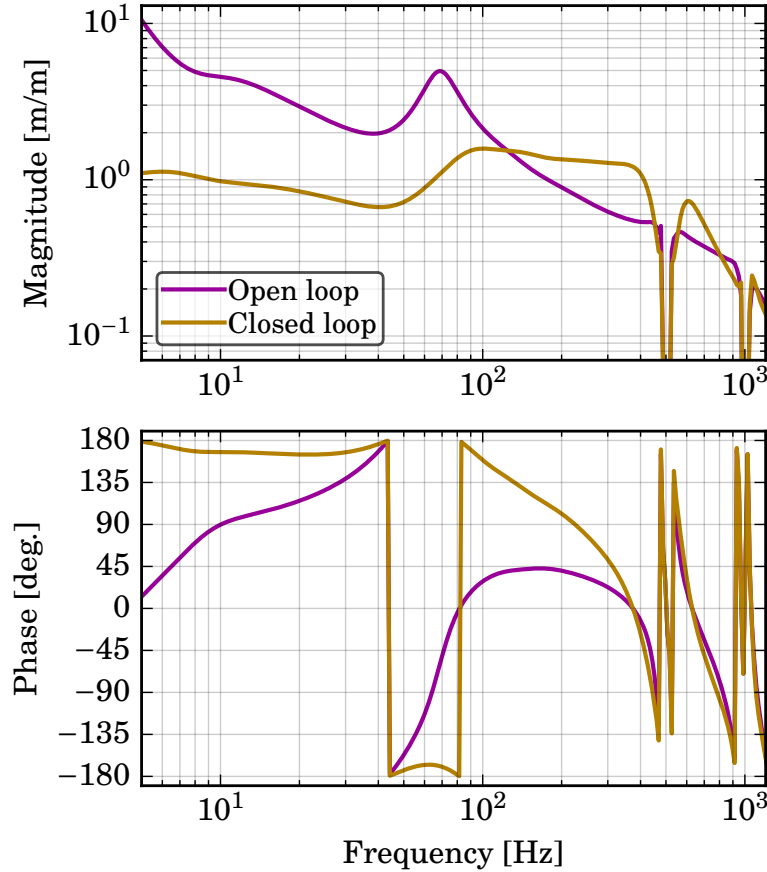


Figure 5.3: Open- and closed-loop transfer functions of the differential arm length loop used in the simulations in this chapter corresponding to NS/NS-optimized detuned RSE. Compared to O1, the UGF has been increased by a factor of 3, the time delay of the loop has been reduced, and additional digital shaping is applied to compensate the complex RSE feature around 150 Hz.

We can use this matrix to set astrophysically motivated requirements on our calibration. For example, if we wish to determine the system's total mass to better than 1 %, then we should aim for no more than 2.4 % fractional systematic error on each of the calibration parameters, since  $2.4\% \times (80 + 21 + 80 + 64 + 51 + 129) \times 10^{-3} = 1.0\%$ .

## Application to tests of general relativity

The above analysis can be used to examine the impact of calibration errors on GW-based tests of general relativity (GR). These tests often involve augmenting the waveform model with adding additional parameters that should be equal to zero in GR.<sup>126,133</sup> One example is the use of GW merger data to bound the mass  $m$  (or equivalently the Compton wavelength  $\lambda = h/mc$ ) of the graviton.<sup>134</sup>

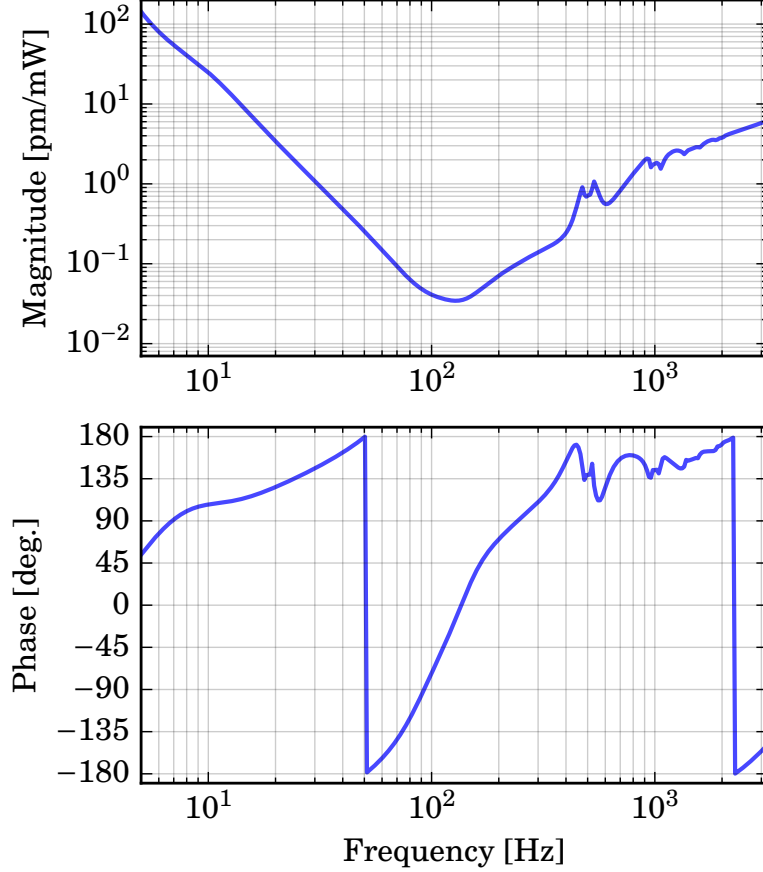


Figure 5.4: Response function  $1/S$  for the 125 W detuned RSE scheme considered here.

A massive graviton is subject to the dispersion relation  $E^2 = m^2 c^4 + p^2 c^2$ , which implies that a gravitational wave with wavelength  $\lambda$  propagates with a speed given by

$$\frac{v^2}{c^2} = \frac{p^2 c^2}{E^2} \simeq 1 - \left( \frac{hc}{\lambda E} \right)^2. \quad (5.23)$$

For a GW inspiral, this has the effect of introducing a 1 pN phase term  $\phi_g(f)$  to the inspiral waveform:

$$\phi_g(f) = -\frac{\pi \mathcal{D} c}{\lambda^2 (1+z) f} \equiv -\frac{B}{f}, \quad (5.24)$$

where  $\mathcal{D}$  is a distance-like quantity (*not* necessarily equal to the luminosity distance  $D$ ) defined by Will,<sup>134</sup> and  $z$  is the source redshift. Note that  $B$  has the dimensions of a frequency. In standard GR,  $m = 0$ , so  $\lambda = \infty$  and hence  $B = 0$  Hz. Analysis of the GW150914 signal set a limit  $\lambda > 10^{13}$  km at 90 % confidence.<sup>126</sup>

Repeating the above analysis with the  $B$  parameter included yields the following matrix equation:

$$\begin{bmatrix} \Delta M/M \\ \Delta\eta/\eta \\ \Delta t_c/(1\text{ms}) \\ \Delta\phi_c/(1\text{rad}) \\ \Delta D/D \\ \Delta B/(1\text{kHz}) \end{bmatrix} = \frac{1}{10^3} \begin{bmatrix} -2392 & 280 & -6577 & -1003 & 1111 & -2769 \\ 3563 & -401 & 9713 & 1512 & -1607 & 4140 \\ 2723 & 530 & 5231 & 1812 & -380 & 3382 \\ -10380 & 250 & -24280 & -5246 & 2373 & -12518 \\ -414 & -40 & -327 & -92 & 312 & 694 \\ 2259 & -294 & 6349 & 918 & -1135 & 2580 \end{bmatrix} \begin{bmatrix} \Delta g/g \\ \Delta z/z \\ \Delta|p|/|p| \\ \Delta Q_p/Q_p \\ \Delta\xi^2/\xi^2 \\ \Delta a/a \end{bmatrix}. \quad (5.25)$$

In the standard GR case  $B = 0$  (that is,  $\lambda = \infty$ ), a systematic error  $\Delta B$  will result in a reportedly finite wavelength  $\lambda$  according to equation 5.24. For  $\mathcal{D}/(1+z) \sim 400 \text{ Mpc}$  and  $\Delta B \sim 100 \text{ Hz}$  (a typical value expected from equation 5.25 assuming a few-percent systematic error in the calibration parameters), the resulting Compton wavelength is  $\lambda \sim 10^{13} \text{ km}$ . Note that this is of the same order as the upper limit placed on GW150914. This indicates that unmodeled systematic calibration errors at the few-percent level could already produce a fictitious finite value for the graviton Compton wavelength, at least in the detuned interferometer configuration discussed here.

## 5.4 Optimal transfer function measurements from the Fisher matrix

Many optical, mechanical, and optomechanical systems are often assumed to be linear and time-invariant. Under this assumption, the parameters of such a system can be estimated by measuring the system's transfer function. Although one can always measure a transfer function with a standard swept-sine routine, there are several situations that lead us to think more carefully about our measurement strategy.

1. In the case of systems such as alignment control systems, seismic isolation systems, and mechanical suspensions, transfer function measurement can be quite expensive, as it can require exciting the system down to millihertz frequencies.
2. In the case of important data channels such as the differential arm length readout of Advanced LIGO, transfer function measurement is expensive because such measurements necessarily invalidate certain parts of the data.

This is particularly true for the continuous transfer function measurement required to track time-varying changes in the interferometer calibration (the “calibration lines”); data at the line frequencies must be thrown out.

With a little forethought, one can choose the measurements so as to maximize the amount of information learned about the system’s parameters. One method for quantifying the amount of information gained is to compute the Fisher matrix of the measurement.<sup>135</sup> The inverse of the Fisher matrix provides a lower bound (the so-called Cramér–Rao bound) on the covariance matrix of the estimated parameters. Good, straightforward explanations of the Fisher matrix and the Cramér–Rao bound are few and far between. Two such resources are David Wittman’s “Fisher Matrix for Beginners”<sup>136</sup> and the technical appendix to the Dark Energy Task Force report.<sup>137</sup>

## General discussion

We define the following notation: we have a linear, time-invariant (LTI) system whose transfer function  $H(f)$  depends on a certain set of parameters  $\boldsymbol{\theta} = (\theta_1, \theta_2, \dots, \theta_M)$ . We can probe this system by exciting its input with a signal  $x(f)$  and reading back the response  $y(f) = H(f)x(f) + n(f)$ , where  $n(f)$  is some readout noise. Our goal is to produce an estimate  $\hat{H}(\boldsymbol{\theta}; f)$  given our observed response  $y(f)$ , our excitation  $x(f)$ , and our estimate of the noise  $n(f)$ .

In practice, we excite the system with sinusoids at frequencies  $f_1, f_2, \dots, f_N$ . We record the complex excitation amplitudes  $x_1, x_2, \dots, x_N$  and the response amplitudes  $y_1, y_2, \dots, y_N$ . These amplitudes have been corrupted by noise whose amplitudes are  $n_1, n_2, \dots, n_N$ ; in general, we have

$$y_\alpha = H_\alpha x_\alpha + n_\alpha; \quad \alpha = 1, 2, \dots, N, \quad (5.26)$$

where  $H_\alpha = H(f_\alpha)$ . On the other hand, given an estimate  $\hat{H}(\boldsymbol{\theta}; f)$  of the system, we can write down a set of estimated amplitudes  $\hat{y}_1, \hat{y}_2, \dots, \hat{y}_N$ , with

$$\hat{y}_\alpha = \hat{H}_\alpha(\boldsymbol{\theta})x_\alpha; \quad \alpha = 1, 2, \dots, N, \quad (5.27)$$

Our goal is to find the value of  $\boldsymbol{\theta}$  which makes the estimated responses  $\{\hat{y}_\alpha\}$  approach the observed responses  $\{y_\alpha\}$ . To this end, we can write down a likelihood function  $\mathcal{L}(\boldsymbol{\theta}) \propto p(\{y_\alpha\}|\boldsymbol{\theta})$ , where  $p(\{y_\alpha\}|\boldsymbol{\theta})$  is the probability of having observed the

amplitudes  $\{y_\alpha\}$  given a certain value of  $\boldsymbol{\theta}$ . From here on we will assume that the noise is Gaussian, which results in a likelihood function<sup>c</sup>

$$\mathcal{L}(\boldsymbol{\theta}) \propto \exp \left[ - \sum_{\alpha=0}^{N-1} \frac{|y_\alpha - \hat{y}_\alpha(\boldsymbol{\theta})|^2}{2|n_\alpha|^2} \right]. \quad (5.28)$$

How should we place our  $N$  frequencies so as to maximize the amount of information we can learn about  $H$ ? Intuitively, we know we should choose our frequencies so as to maximize the curvature of  $\mathcal{L}$  (or, equivalently, the curvature of  $\ln \mathcal{L}$ ) with respect to  $\boldsymbol{\theta}$ . To find an expression for the curvature, we vary  $\boldsymbol{\theta}$  and keep track of terms up to second order:

$$\ln \mathcal{L}(\boldsymbol{\theta} + \delta \boldsymbol{\theta}) \approx \ln \mathcal{L}|_{\boldsymbol{\theta}} + \sum_i \frac{\partial [\ln \mathcal{L}]}{\partial \theta_i} \Bigg|_{\boldsymbol{\theta}} \delta \theta_i + \frac{1}{2} \sum_i \sum_j \frac{\partial^2 [\ln \mathcal{L}]}{\partial \theta_i \partial \theta_j} \Bigg|_{\boldsymbol{\theta}} \delta \theta_i \delta \theta_j. \quad (5.29)$$

Once we have found parameters  $\boldsymbol{\theta}_0$  which maximize  $\ln \mathcal{L}$ , the first-derivative terms will vanish, leaving only the second-derivative (that is, curvature) terms. These curvature terms are the elements of the Fisher matrix  $\mathcal{F}$ :<sup>d</sup>

$$\mathcal{F}_{ij} = - \frac{\partial^2 [\ln \mathcal{L}]}{\partial \theta_i \partial \theta_j} \Bigg|_{\boldsymbol{\theta}_0} \quad (5.30a)$$

$$= \frac{\partial^2}{\partial \theta_i \partial \theta_j} \left[ \sum_{\alpha} \frac{|y_\alpha - \hat{y}_\alpha(\boldsymbol{\theta})|^2}{2|n_\alpha|^2} \right] \Bigg|_{\boldsymbol{\theta}_0} \quad (5.30b)$$

$$= \sum_{\alpha} \frac{1}{2|n_\alpha|^2} \left[ \frac{\partial \hat{y}_\alpha^*}{\partial \theta_i} \frac{\partial \hat{y}_\alpha}{\partial \theta_j} - (y_\alpha^* - \hat{y}_\alpha^*) \frac{\partial^2 \hat{y}_\alpha}{\partial \theta_i \partial \theta_j} + \text{cc} \right] \Bigg|_{\boldsymbol{\theta}_0}. \quad (5.30c)$$

If our estimate  $\hat{y}$  is unbiased, we expect  $y_\alpha - \hat{y}_\alpha \rightarrow 0$ , and thus

$$\mathcal{F}_{ij} = \sum_{\alpha} \frac{1}{|n_\alpha|^2} \text{Re} \left[ \frac{\partial \hat{y}_\alpha^*}{\partial \theta_i} \frac{\partial \hat{y}_\alpha}{\partial \theta_j} \right] \Bigg|_{\boldsymbol{\theta}_0}. \quad (5.31)$$

Since  $\hat{y}_\alpha = \hat{H}_\alpha x_\alpha$ , we have

$$\mathcal{F}_{ij} = \sum_{\alpha} \frac{|x_\alpha|^2}{|n_\alpha|^2} \text{Re} \left[ \frac{\partial \hat{H}_\alpha^*}{\partial \theta_i} \frac{\partial \hat{H}_\alpha}{\partial \theta_j} \right] \Bigg|_{\boldsymbol{\theta}_0}, \quad (5.32)$$

---

<sup>c</sup> If one is not comfortable with likelihood functions, note that  $-\ln \mathcal{L}$  is equivalent to the usual  $\chi^2$  statistic used for curve fitting.

<sup>d</sup> Note that  $\mathcal{F} = -\mathcal{H}$ , where  $\mathcal{H}$  is the Hessian of  $\ln \mathcal{L}$  evaluated at  $\boldsymbol{\theta}_0$ . Strictly speaking  $\mathcal{F}$  is the *observed Fisher information*, which is to be contrasted with the *expected Fisher information*. See Efron and Hinkley<sup>138</sup> for more information.

which is the discrete-frequency equivalent of the expression found by L. Price.<sup>135</sup> Following the usual convention, we'll write  $\sigma(H_\alpha) = |n_\alpha/x_\alpha|$ .<sup>e</sup>

The inverse of the Fisher matrix provides a lower bound for the covariance matrix:

$$\Sigma \geq \mathcal{F}^{-1}, \quad (5.34)$$

where the inequality is understood to be elementwise. This is the so-called Cramér–Rao bound.

## Single-frequency excitations

As an example, we apply the above concepts to the problem of estimating the parameters of a single-pole system  $H(f) = g/(1 + if/p)$  using an excitation at only one frequency. This system describes, for example, the optical response of a resonant Fabry–Pérot cavity to length or frequency perturbations. In this context,  $g$  is called the optical gain and  $p$  is called the cavity pole. For concreteness we can consider the Advanced LIGO differential arm length plant, for which (during O1) we have  $g \simeq 3.2 \text{ mA/pm}$  and  $p \simeq 350 \text{ Hz}$ .

For this system, our parameter vector is  $\theta = (g, p)$ , so the Fisher matrix will be  $2 \times 2$ . As a start, we'll consider the case where we have only a single excitation at a frequency  $f_1$ . This results in only a single observation  $y_1$ .<sup>f</sup>

In this instance, the Fisher matrix is

$$\mathcal{F} = \frac{1}{\sigma_1^2} \begin{bmatrix} \frac{p^2}{p^2 + f_1^2} & \frac{gp f_1^2}{(p^2 + f_1^2)^2} \\ \frac{gp f_1^2}{(p^2 + f_1^2)^2} & \frac{g^2 f_1^2}{(p^2 + f_1^2)^2} \end{bmatrix}, \quad (5.35)$$

and as a result, the covariance matrix  $\Sigma$  is bounded elementwise from below by  $\mathcal{F}^{-1}$ :

$$\Sigma \geq \sigma_1^2 \begin{bmatrix} \frac{1}{p^4} (p^2 + f_1^2)^2 & -\frac{(p^2 + f_1^2)^2}{gp^3} \\ -\frac{(p^2 + f_1^2)^2}{gp^3} & \frac{(p^2 + f_1^2)^3}{g^2 p^2 f_1^2} \end{bmatrix}. \quad (5.36)$$

<sup>e</sup> Alternatively, we can decompose each observation into real/imaginary parts:  $y_\alpha = y_\alpha^{(r)} + iy_\alpha^{(i)}$ , and likewise for  $H_\alpha$  and  $n_\alpha$ . Then we can write down an alternative Fisher matrix

$$\mathcal{F}_{ij} = \sum_{\alpha=1}^N \sum_{\beta \in \{r,i\}} \frac{|x_\alpha|^2}{|n_\alpha^{(\beta)}|^2} \frac{\partial \hat{H}_\alpha^{(\beta)}}{\partial \theta_i} \frac{\partial \hat{H}_\alpha^{(\beta)}}{\partial \theta_j}. \quad (5.33)$$

In the case  $n_\alpha^{(r)} = n_\alpha^{(i)}$ , this reduces to the definition given above.

<sup>f</sup> However, since  $y_1$  is complex, it contains two pieces of information:  $y_1 = y_1^{(r)} + iy_1^{(i)}$ .

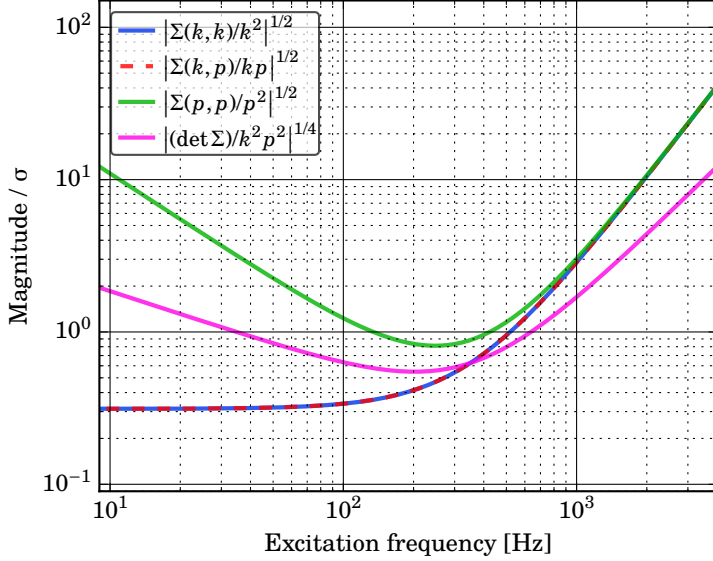


Figure 5.5: Normalized Cramér–Rao bounds on the covariance matrix  $\Sigma$  for a single-frequency transfer function estimate of the system  $H(f) = g/(1 + if/p)$ , with  $g = 3.2\text{mA}/\text{pm}$  and  $p = 350\text{Hz}$ . Here we have assumed a white readout noise and a flat excitation amplitude.

From here, the goal is to choose  $f_1$  so as to provide the “optimal”  $\Sigma$ . To make progress, we need to make assumptions about  $\sigma_1$ , which means making assumptions about the excitation amplitude  $x_1$  and the readout noise amplitudes  $n_1$ . The next sections explore two simple cases for  $x_1$  and  $n_1$ .

### Flat excitation and white readout noise

To start with, we’ll assume that the readout noise  $n_\alpha$  is Gaussian and white as a function of frequency. (In the case of the differential arm length in Advanced LIGO, the assumption of whiteness is true only above 100 Hz or so.) We’ll also assume that the excitation amplitude is flat:  $x_\alpha = x_0$  for all  $\alpha$ . Then  $\sigma_1 = \sigma(f_1) \equiv \sigma$  (that is, it is independent of frequency). In this case, the elements of  $\Sigma$  are minimized as follows:

1. To minimize  $\Sigma(g,g)$ , one should choose  $f_1 = 0\text{Hz}$ . This results in

$$\Sigma(0) \geq \begin{bmatrix} \sigma^2 & -\sigma^2 p/g \\ -\sigma^2 p/g & \infty \end{bmatrix}, \quad (5.37)$$

which is evidently unacceptable for simultaneous estimation of  $g$  and  $p$ .

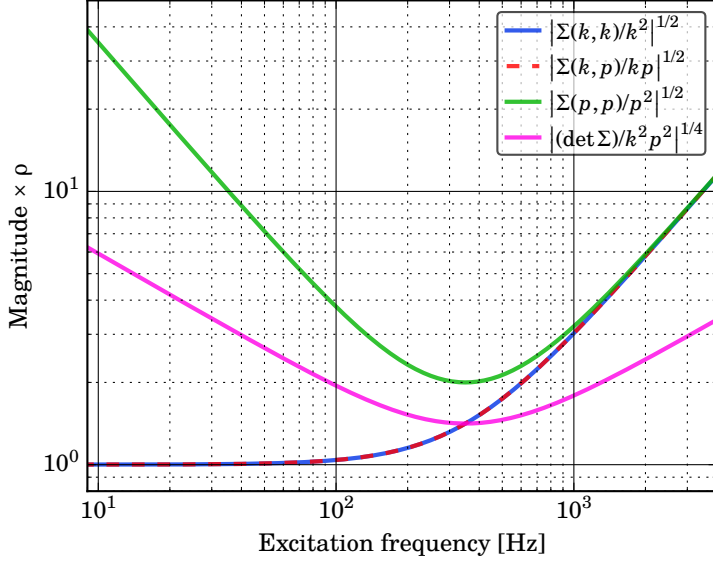


Figure 5.6: Normalized Cramér–Rao bounds on the covariance matrix  $\Sigma$  for a single-frequency transfer function estimate of the system  $H(f) = g/(1 + if/p)$ , with  $g = 3.2\text{mA}/\text{pm}$  and  $p = 350\text{Hz}$ . Here we have assumed that the response  $y$  has a constant SNR  $\rho$  above the readout noise  $n$ .

2. To minimize  $\Sigma(g, p)$ , one should again choose  $f_1 = 0\text{Hz}$ .
3. To minimize  $\Sigma(p, p)$ , one should choose  $f_1 = p/\sqrt{2}$ . This results in

$$\Sigma(p/\sqrt{2}) \geq \frac{9}{4} \begin{bmatrix} \sigma^2 & -\sigma^2 p/g \\ -\sigma^2 p/g & 3\sigma^2 p^2/g^2 \end{bmatrix}. \quad (5.38)$$

4. To minimize  $\det \Sigma$ , one should choose  $f_1 = p/\sqrt{3}$ . This results in

$$\Sigma(p/\sqrt{3}) \geq \frac{16}{9} \begin{bmatrix} \sigma^2 & -\sigma^2 p/g \\ -\sigma^2 p/g & 4\sigma^2 p^2/g^2 \end{bmatrix}. \quad (5.39)$$

In figure 5.5 we plot the elements of  $\Sigma$ , along with  $\det \Sigma$ , as a function of  $f_1$ , assuming that the Cramér–Rao bound is saturated.

### Constant-SNR excitation

Often we can do better than a flat excitation amplitude. If we already have reasonable knowledge of  $g$ ,  $p$ , and  $n$ , it is desirable to aim for the measurement to have a constant SNR. For our purposes, we define this as  $\rho_\alpha = |y_\alpha/n_\alpha| = |x_\alpha H_\alpha/n_\alpha|$ . Therefore, we choose  $|x_\alpha| = \rho|n_\alpha|/|H_\alpha|$ , where  $\rho$  is our target SNR, and hence  $\sigma_\alpha^{(r,i)} = |H_\alpha|/\rho$ .

With this choice of excitation amplitude, the Fisher matrix is

$$\mathcal{F} = \rho^2 \begin{bmatrix} \frac{1}{g^2} & \frac{f_1^2}{gp(p^2 + f_1^2)} \\ \frac{f_1^2}{gp(p^2 + f_1^2)} & \frac{f_1^2}{p^2(p^2 + f_1^2)} \end{bmatrix} \quad (5.40)$$

and the covariance matrix satisfies

$$\Sigma \geq \frac{1}{\rho^2} \begin{bmatrix} \frac{g^2}{p^2}(p^2 + f_1^2) & -\frac{g}{p}(p^2 + f_1^2) \\ -\frac{g}{p}(p^2 + f_1^2) & \frac{1}{f_1^2}(p^2 + f_1^2)^2 \end{bmatrix}. \quad (5.41)$$

As expected, the bound on the covariance goes down like  $\rho^2$ . To minimize the bounds on both  $\Sigma(g, g)$  and  $\Sigma(g, p)$ , one should again choose  $f_1 = 0$  Hz. However, this again results in  $\Sigma(p, p) = \infty$ :

$$\Sigma(0) \geq \begin{bmatrix} g^2/\rho^2 & -gp/\rho^2 \\ -gp/\rho^2 & \infty \end{bmatrix}. \quad (5.42)$$

This time, the bounds on both  $\Sigma(p, p)$  and  $\det \Sigma$  are minimized by choosing  $f_1 = p$ :

$$\Sigma(p) \geq 2 \begin{bmatrix} g^2/\rho^2 & -gp/\rho^2 \\ -gp/\rho^2 & 2p^2/\rho^2 \end{bmatrix}. \quad (5.43)$$

In figure 5.6 we plot the elements of  $\Sigma$ , along with  $\det \Sigma$ , as a function of  $f_1$ , assuming that the Cramér–Rao bound is saturated.

## Application to differential arm length calibration

### For NS/NS-optimized detuned operation at full power

We want to apply the above formalism to the problem of estimating the parameters of the differential arm length loop using photon radiation pressure. A known radiation force  $F(f) = -M\omega^2 x(f)$  is applied to the test mass, resulting in a power fluctuation  $P(f)$  at the dark port.  $x(f)$  and  $P(f)$  are related via the reciprocal response function  $S(f) = 1/R(f)$ , whose parameters  $g$ ,  $z$ ,  $|p|$ ,  $Q_p$ ,  $\xi^2$ , and  $a$  we would like to constrain. We assume the calibration will consist of five lines placed somewhere between 7 Hz and 3 kHz, each with the same, fixed SNR  $\rho$ . The Fisher matrix in this case is

$$\mathcal{F}_{ij} = \rho^2 \sum_{\alpha=1}^5 \frac{1}{|\hat{S}_\alpha|^2} \operatorname{Re} \left( \frac{\partial \hat{S}_\alpha^*}{\partial \lambda_i} \frac{\partial \hat{S}_\alpha}{\partial \lambda_j} \right), \quad (5.44)$$

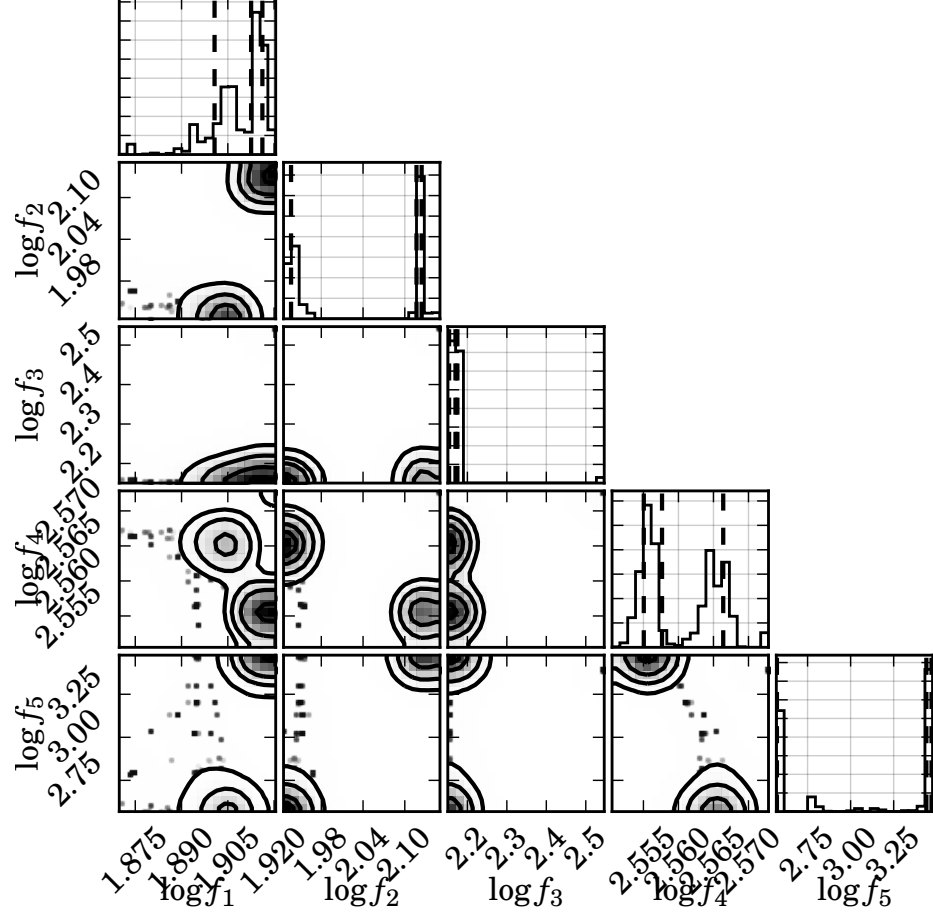


Figure 5.7: Posterior distribution of optimal line frequencies for differential arm length optical plant estimation, as determined by maximizing the volume of the Fisher information of the measurement. The differential arm length optical plant assumed here is the 125 W NS/NS-optimized plant described in table 5.1, with a loop shown in figure 5.3.

with  $\lambda = \begin{pmatrix} g & z & |p| & Q_p & \xi^2 & a \end{pmatrix}^\top$ . The Fisher matrix determinant  $\det \mathcal{F}$  is maximized with respect to the five line frequencies via MCMC. In the MCMC, it is important to enforce  $f_1 \leq f_2 \leq f_3 \leq f_4 \leq f_5$  in order to produce well-localized posteriors on the frequencies. The posterior pdf of the frequencies is shown in figure 5.7. The maximum a posteriori frequencies are 82, 133, 145, 359, and 2847 Hz.

The Fisher matrix (evaluated at the maximum a posteriori frequencies) is inverted to yield a bound on the covariance matrix  $\Sigma$ . The resulting relative covariance ma-

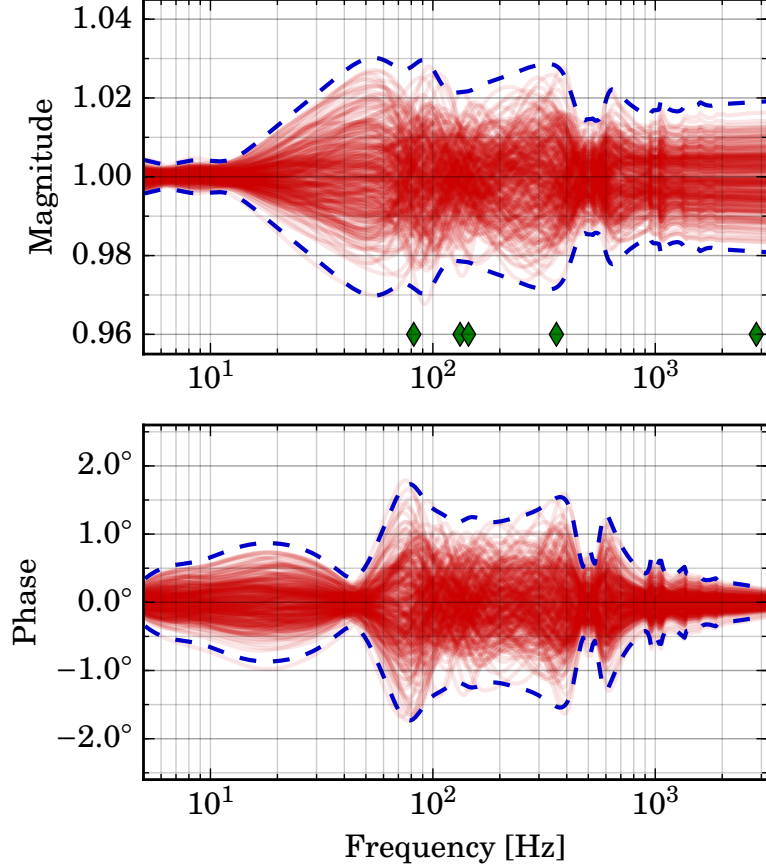


Figure 5.8: 300 randomly generated realizations of statistical errors in the parameters  $g$ ,  $z$ ,  $|p|$ ,  $Q_p$ ,  $\xi^2$ , and  $a$  for the response function  $1/S$  corresponding to the NS/NS-optimized, detuned, full-power operation described in the text. The green diamonds indicate the chosen calibration line frequencies. The realizations are drawn according to the covariance matrix given in equation 5.45 with an SNR of  $\rho = 100$ . The blue dashed lines give the envelope of the  $3\sigma$  uncertainties associated with these errors. This shows that the frequency-dependent statistical error of the five-line sensing scheme considered here is better than 3 % in magnitude and 2  $^\circ$  in phase in the GW band.

trix  $\Sigma^{(\text{rel})}$  (with elements  $\Sigma_{ij}^{(\text{rel})} = \Sigma_{ij}/\lambda_i \lambda_j$ ) is

$$\Sigma^{(\text{rel})} = \frac{1}{\rho^2} \begin{bmatrix} 1.12^2 & & & & & \\ 0.855^2 & 1.05^2 & & & & \\ -0.556^2 & -0.203^2 & 0.387^2 & & & \\ -1.17^2 & -0.988^2 & 0.606^2 & 1.49^2 & & \\ -1.02^2 & -0.535^2 & 0.656^2 & 1.04^2 & 1.40^2 & \\ 0.533^2 & 0.341^2 & -0.424^2 & -0.781^2 & -0.62^2 & 0.658^2 \end{bmatrix}. \quad (5.45)$$

Since none of these values is significantly larger than unity, if the line SNRs are chosen to be  $\rho = 100$  then the parameter uncertainties and covariances can be constrained to about 1% or better. In figure 5.8 we show the expected frequency-dependent statistical uncertainty in the interferometer response function, with the errors drawn from a distribution given by the optimal covariance matrix written above with  $\rho = 100$ . Evidently, the Cramér–Rao bound implies that we can achieve better than 3% uncertainty in magnitude and  $2^\circ$  in phase with this scheme.

### For nearly pure RSE operation at lower power

We repeat the above analysis for an O2-like configuration with 50 W of input power, no significant homodyne angle offset, and an 8 Hz antispring. Explicitly,  $g = 6.0 \text{ mW/pm}$ ,  $z = 365.2 \text{ Hz}$ ,  $|p| = 364.2 \text{ Hz}$ ,  $Q_p = 0.501$ ,  $\xi^2 = -8.0 \text{ Hz}^2$ , and  $a = 2.2 \times 10^{-7} \text{ N/V}$ . Because  $z$  and  $|p|$  are nearly equal, and  $Q_p$  is nearly 1/2, attempting to estimate all six parameters will result in excessively large uncertainties. Therefore, we assume that  $z$  and  $Q_p$  are known and fixed, and we include only  $g$ ,  $|p|$ ,  $\xi^2$ , and  $a$  in the Fisher matrix.

For O2, a sensible “by-hand” choice of lines is 8, 37, 330, and 1080 Hz. This results in a relative covariance matrix

$$\Sigma^{(\text{rel})} = \frac{1}{\rho^2} \begin{bmatrix} 0.886^2 & & & \\ -0.625^2 & 0.602^2 & & \\ -0.651^2 & 0.461^2 & 1.29^2 & \\ -0.102^2 & -0.0225^2 & 0.102^2 & 0.291^2 \end{bmatrix}. \quad (5.46)$$

Figure 5.9 shows the resulting frequency-dependent errors in the response function.

On the other hand, optimizing the four calibration line frequencies to maximize the determinant of the Fisher matrix yields lines at 10.4, 49, 199, and 2807 Hz. The resulting relative covariance matrix is

$$\Sigma^{(\text{rel})} = \frac{1}{\rho^2} \begin{bmatrix} 0.652^2 & & & \\ -0.447^2 & 0.513^2 & & \\ -0.538^2 & 0.357^2 & 1.25^2 & \\ -0.198^2 & -0.0691^2 & 0.246^2 & 0.274^2 \end{bmatrix}. \quad (5.47)$$

Figure 5.10 shows the resulting frequency-dependent errors in the response function.

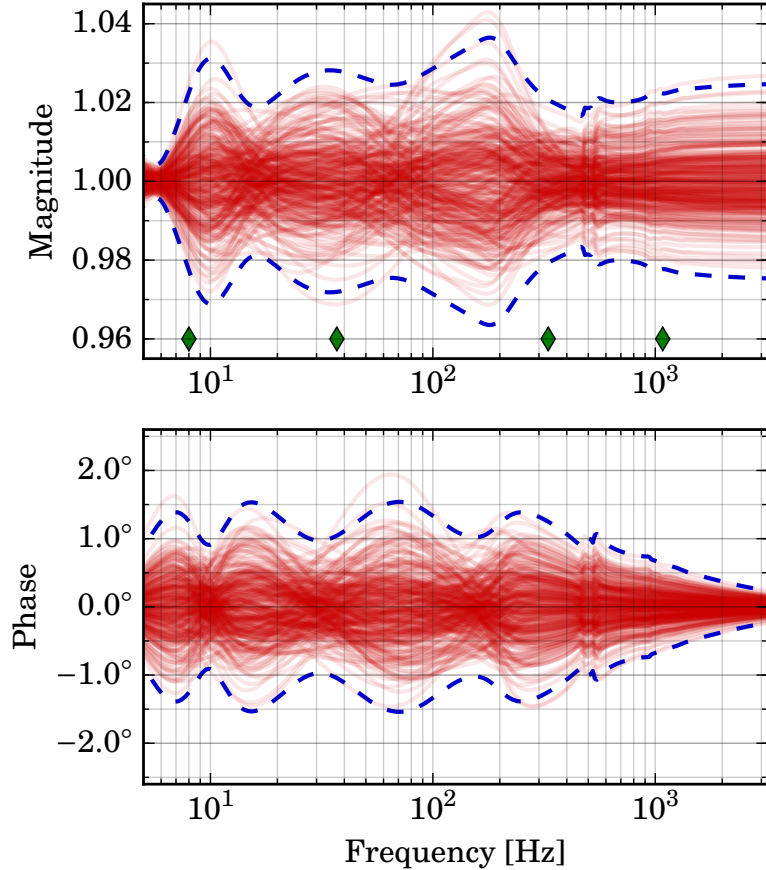


Figure 5.9: Response function errors (analogous to figure 5.8) for four calibration line frequencies picked by hand for an O2-like configuration.

The hand-picked calibration lines result in a Cramér–Rao bound  $\det \Sigma \geq 2.6 \times 10^9$  for  $\rho = 100$ , while the optimized calibration lines have a bound  $\det \Sigma \geq 1.0 \times 10^9$ . By comparing figures 5.9 and 5.10, one can see that this does correspond to an improvement in the response function uncertainty; however, the improvement is modest: the maximal error of 3.6 % and  $1.6^\circ$  is reduced to 3.0 % and  $1.4^\circ$ .

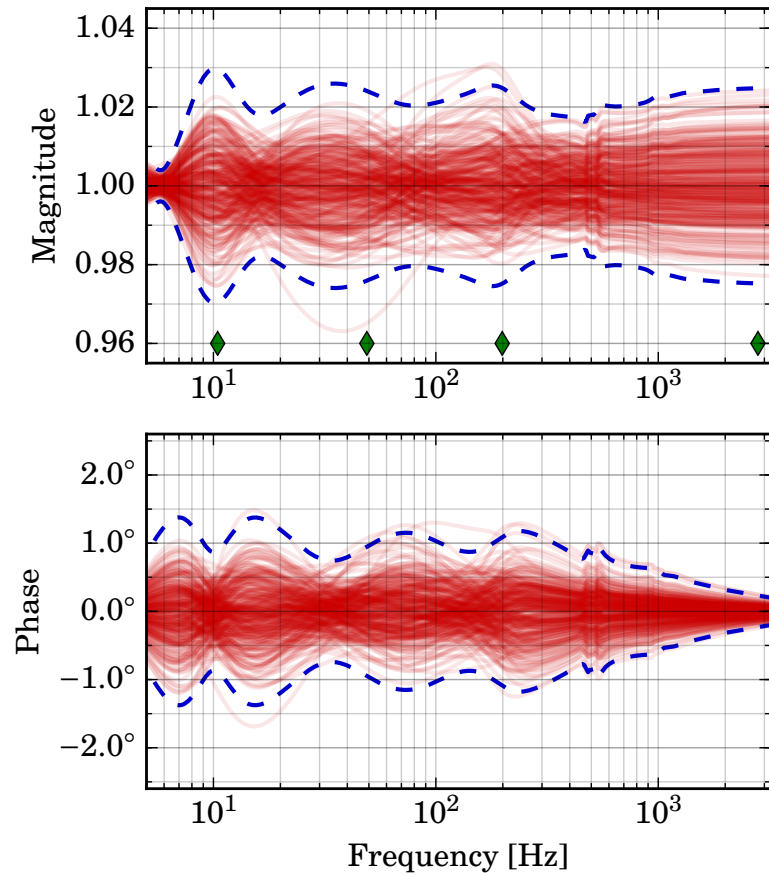


Figure 5.10: Response function errors (analogous to figure 5.8) for four optimized calibration line frequencies for an O2-like configuration. Compared to the hand-picked frequencies in figure 5.9, the optimized frequency choice improves the response function magnitude uncertainty around 200 Hz and improves the phase uncertainty between 30 and 500 Hz.

# 6 Searching for dark matter with laser interferometers

This chapter considers the possible use of laser interferometers to detect large macroscopic dark matter objects interacting gravitationally with the interferometer test masses. Numerical simulations are presented showing detection rates for both a Newtonian gravitational coupling and a Yukawa coupling. The work presented here also appears in a preprint by Hall et al.<sup>139</sup>

## 6.1 Previous work

Laser interferometers have already received some consideration as dark matter detectors, either because of possible GW signatures of dark matter, or because of the possibility of local dark matter interaction with the interferometer itself.

In terms of GW signatures of dark matter, Bird et al.<sup>140</sup> argue that some of the universe's dark matter density may consist of primordial black holes (PBHs) with masses between  $20 M_{\odot}$  and  $100 M_{\odot}$ , and that GW150914 could have been generated from a binary system of two such black holes. A PBH scenario was also considered by Sasaki et al.<sup>141</sup>

Brown<sup>142</sup> and Hanna<sup>143</sup> conducted searches in Initial LIGO data for sub-solar-mass binary systems; these searches are motivated in part by the possibility of binary MACHOs, which may have component masses from  $0.15 M_{\odot}$  to  $0.9 M_{\odot}$  based on microlensing surveys.

In terms of non-GW tests of dark matter using laser interferometers, Stadnik and Flambaum<sup>144</sup> consider the case of a dark matter scalar field which couples quadratically to the electromagnetic field in a laser interferometer. Additionally, Seto and Cooray (whose results we will quote below) considered direct Newtonian pertur-

bations of LISA test masses from PBH flybys, with masses of order  $10^{14}$  kg ( $\sim 10^{-17} M_\odot$ ).<sup>145</sup>

Rather than a primordial black hole or an aggregation of baryonic matter, a macroscopic dark matter object could be a gravitationally bound aggregate of nonbaryonic particles. Such macroscopic objects can form from the gravitational infall of dark matter particles into primordial overdensities, and these objects can subsequently be broken apart by tidal disruption.<sup>146</sup>

## 6.2 Newtonian and Yukawa-type interactions

In this chapter we consider the possibility of Yukawa gravitational interactions between standard and dark matter particles, with a potential

$$V_{ij}(r) = -\frac{Gm_i m_j}{r} \left[ 1 + (-1)^s \delta_i \delta_j e^{-r/\lambda} \right], \quad (6.1)$$

where  $i$  and  $j$  may each refer to either standard matter (SM) or dark matter (DM).  $m_i$  and  $m_j$  are the masses of the particles. If the interaction is mediated by a scalar, then  $s = 0$ ; if it is mediated by a vector, then  $s = 1$ .  $\delta_{\text{SM}}$  and  $\delta_{\text{DM}}$  are Yukawa couplings for SM and DM, and  $\lambda$  is a Yukawa screening length. For the problem of detecting a DM object with a test mass made of SM, we are particularly interested in the SM–DM coupling  $g = \delta_{\text{SM}} \delta_{\text{DM}}$ . Note that this Yukawa interaction reduces to the usual Newtonian interaction for either  $\delta_{\text{SM}} = 0$  or  $\delta_{\text{DM}} = 0$ . This potential leads to a central force

$$\mathbf{F}_{ij}(r) = -\frac{\partial V_{ij}}{\partial r} \hat{\mathbf{r}} = -\frac{Gm_i m_j}{r^2} \left[ 1 + \left(1 + \frac{r}{\lambda}\right) (-1)^s \delta_{\text{SM}} \delta_{\text{DM}} e^{-r/\lambda} \right] \hat{\mathbf{r}}. \quad (6.2)$$

Torsion balance tests of the equivalence principle by, for example, Schlaminger et al.<sup>147</sup> set an upper limit of  $10^{-3}$  for  $\delta_{\text{SM}}$ , assuming  $\lambda > 10$  m.

A limit on  $\delta_{\text{DM}}$  is set by the self-interaction cross section  $\sigma_{\text{DD}}$  of dark matter, which is constrained by structure formation to be  $\sigma_{\text{DD}}/m \lesssim 0.1 \text{ m}^2/\text{kg}$  for  $v/c \simeq 10^3$ . This leads to a constraint

$$\delta_{\text{DM}} \lesssim 5 \times 10^9 \times \left( \frac{1 \text{ kg}}{m_{\text{DM}}} \right)^{1/4}. \quad (6.3)$$

Here and below we assume that the radius  $r_{\text{DM}}$  of the dark matter objects are much less than the interferometer arm length, and that the Yukawa screening length is much less than  $n_{\text{DM}}^{1/3}$ , where  $n_{\text{DM}}$  is the number density of dark matter objects in the universe.

## 6.3 Detection with laser interferometers

### Analytical Newtonian case

Seto and Cooray<sup>145</sup> considered the Newtonian interaction of primordial-mass black holes ( $10^{13}$  to  $10^{17}$  kg) with test masses of a LISA-like detector (arm length  $L = 5 \times 10^6$  km), and derived the expected event rate given the measured local dark matter density in the galaxy ( $\rho = 0.011 M_\odot/\text{pc}^3 = 7 \times 10^{-22} \text{ kg/m}^3$ ). We will briefly review their analysis and results before moving on to the new numerical analysis performed in this work.

They performed an analytical analysis in which each black hole (with mass  $M$ ) flies at normal incidence through the plane of the detector, with a fixed speed  $v = 350$  km/s. If the distance of closest approach to a particular test mass is  $R$ , then the acceleration time series of the test mass is

$$a(t) = \frac{GMR}{[R^2 + (vt)^2]^{3/2}}, \quad (6.4)$$

which in the frequency domain is

$$a(f) = \frac{2GM}{Rv} K_1\left(\frac{2\pi f R}{v}\right), \quad (6.5)$$

where  $K_1$  is the first modified Bessel function of the second kind. With the frequency-domain acceleration in hand, the optimal matched-filter SNR  $\varrho$  can be computed via

$$\varrho^2 = 4 \int_0^\infty df \frac{|a(f)|^2}{S_{aa}(f)}, \quad (6.6)$$

where  $S_{aa}(f)$  is the PSD of the detector's acceleration noise. Seto and Coray assume a flat acceleration noise of  $S_{aa}^{1/2} = 3 \times 10^{-15} \text{ m s}^{-2} \text{ Hz}^{-1/2}$ , so that  $\varrho$  can be computed analytically in terms of  $M$ ,  $R$ , and  $L$ .<sup>a</sup>

To compute the expected rate  $\dot{\eta}$  (in events per year) of events above a certain critical SNR  $\varrho_*$ , Seto and Cooray assume that the entire dark matter halo consists of black holes of a particular mass  $M$ . If  $R_*$  is the radius which yields an SNR of  $\varrho_*$ , then

---

<sup>a</sup>The derivation and rates quoted here implicitly assume  $R < L$ , since the acceleration of only one test mass is considered; Seto and Cooray refer to this as the “close-approach” regime. They additionally give a derivation for the “tidal” regime in which  $R > L$  and the accelerations of all test masses must be considered.

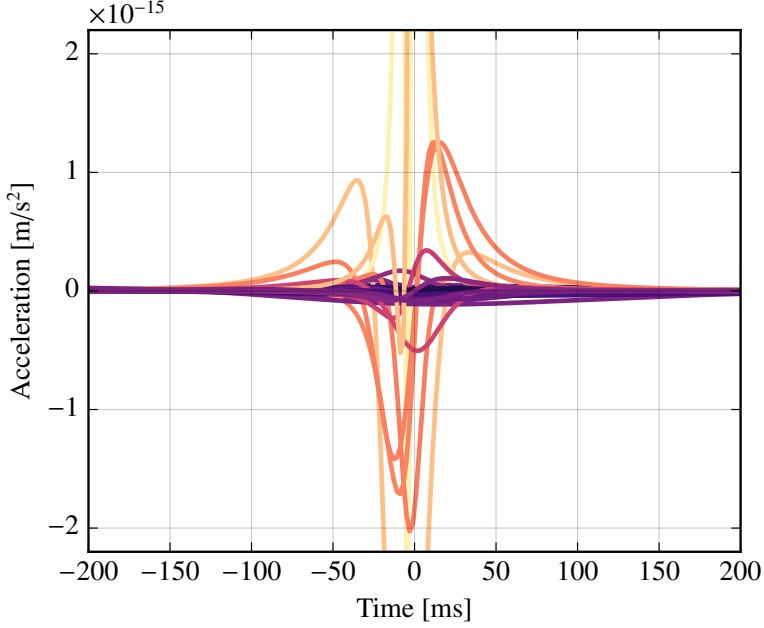


Figure 6.1: Example acceleration time series for dark matter interactions with Advanced LIGO, here shown for 1000 kg objects.

the number of flybys per unit time with SNR  $\varrho \geq \varrho_*$  is  $\pi R_*^2 F \equiv \dot{\eta}(\varrho_*)$ , where  $F = \varrho v/M$  is the event flux. Seto and Cooray derive the following formula for this rate:

$$\begin{aligned} \dot{\eta}(\varrho) = & (0.01 \text{ yr}^{-1}) \left( \frac{1 \times 10^{14} \text{ kg}}{M} \right)^{1/5} \left( \frac{5}{\varrho} \right)^{4/5} \left( \frac{v}{350 \text{ km/s}} \right)^{3/5} \left( \frac{\rho}{7 \times 10^{-22} \text{ kg/m}^3} \right) \\ & \left( \frac{3 \times 10^{-15} \text{ m s}^{-2} \text{ Hz}^{-1/2}}{S_{aa}^{1/2}} \right)^{4/5} \left( \frac{L}{5 \times 10^6 \text{ km}} \right), \end{aligned} \quad (6.7)$$

suggesting that the prospects for primordial black hole detection with LISA are quite marginal, with less than one high-SNR event expected even after 10 years of observation.

## Numerical Newtonian analysis

We performed a Monte Carlo simulation of the interaction of compact objects (such as primordial mass black holes) with laser interferometer test masses, both for Advanced LIGO and for LISA.

In this simulation, a dark matter object is incident on the plane of the detector with a random impact parameter and random angles of incidence. The speed is chosen from a distribution that takes into account both the zero-mean, randomly oriented thermal velocity distribution of the dark matter in the halo as well as the nonzero,

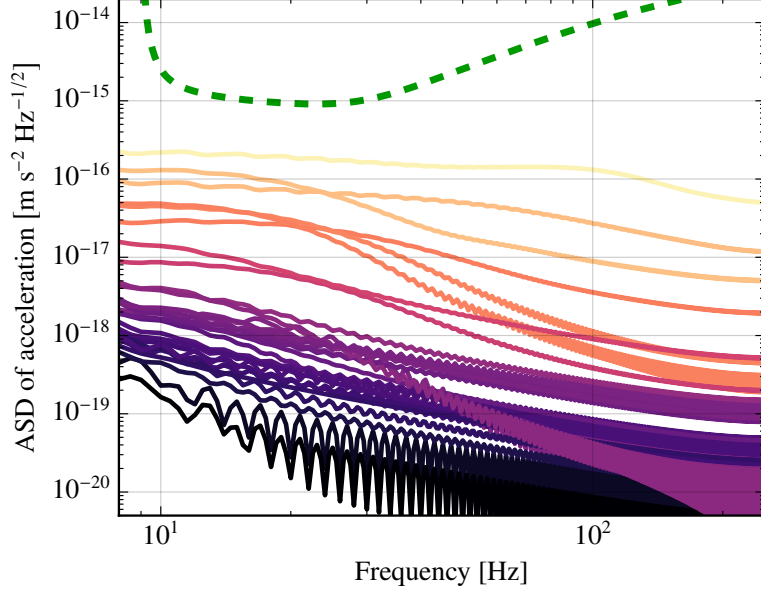


Figure 6.2: Example acceleration spectra for dark matter interactions with Advanced LIGO, corresponding to the time series in figure 6.1. The dashed line shows the assumed acceleration noise of Advanced LIGO for the purposes of the simulations in this chapter.

nonrandom velocity of the solar system through the halo. This distribution is a displaced Maxwell–Boltzmann distribution (that is, the three-dimensional analog of a Rice distribution), which we now derive. The joint distribution for the individual components  $\dot{x}$ ,  $\dot{y}$ , and  $\dot{z}$  of the clump velocities is

$$p(\dot{x}, \dot{y}, \dot{z}) = \frac{1}{(2\pi\sigma^2)^{3/2}} \exp \left[ -\frac{(\dot{x}_\odot - \dot{x})^2 + (\dot{y}_\odot - \dot{y})^2 + (\dot{z}_\odot - \dot{z})^2}{2\sigma^2} \right], \quad (6.8)$$

where  $v_\odot = \sqrt{\dot{x}_\odot^2 + \dot{y}_\odot^2 + \dot{z}_\odot^2} = 220$  km/s is the speed of the solar system, and  $\sigma = 270$  km/s is the thermal velocity spread of the clumps in the halo. The corresponding speed distribution  $p(v)$  can be found by changing variables into spherical coordinates ( $\dot{x} = v \cos\phi \sin\theta$ ,  $\dot{y} = v \sin\phi \sin\theta$ , and  $\dot{z} = v \cos\theta$ ), and assuming (without loss of gen-

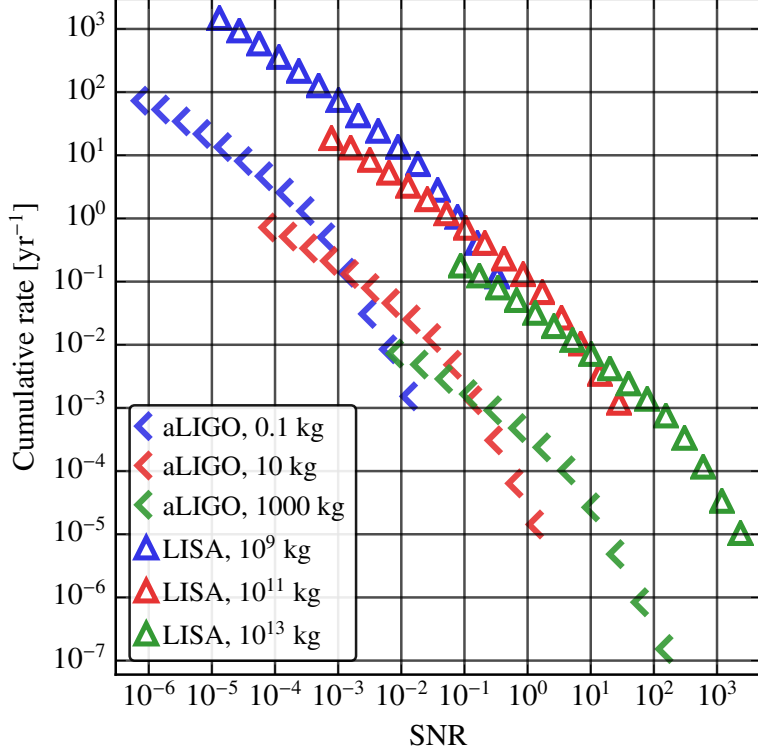


Figure 6.3: Cumulative event rate  $\dot{\eta}(\varrho)$  for the number of dark matter events per year with SNR of at least  $\varrho$ , assuming a Newtonian interaction.

erality) that the solar system velocity lies entirely in the  $z$  direction. Then

$$1 = \int_{-\infty}^{\infty} dx \int_{-\infty}^{\infty} dy \int_{-\infty}^{\infty} dz p(x, y, z) \quad (6.9a)$$

$$= \int_0^{2\pi} d\phi \int_0^\pi d\theta \int_0^\infty dv v^2 \sin \theta \frac{1}{(2\pi\sigma^2)^{3/2}} \exp \left[ -\frac{\dot{x}^2 + \dot{y}^2 + (v_\odot - \dot{z})^2}{2\sigma^2} \right] \quad (6.9b)$$

$$= \int_0^\infty dv \underbrace{\left( \frac{2}{\pi} \right)^{1/2} \frac{v}{\sigma v_\odot} \exp \left( -\frac{v_\odot^2 + v^2}{2\sigma^2} \right)}_{\equiv p(v)} \sinh \left( \frac{v_\odot v}{\sigma^2} \right), \quad (6.9c)$$

where the integrand in the last line is the expression for the speed distribution  $p(v)$ . Example acceleration time series for 10 kg objects interaction with an Advanced LIGO detector are shown in figure 6.1, and the corresponding spectra are shown in figure 6.2.

Additionally, in this simulation the effect of the flyby on all test masses is accounted for when computing the differential acceleration, and the matched-filter SNR is computed using the full, frequency-dependent acceleration noise PSD.

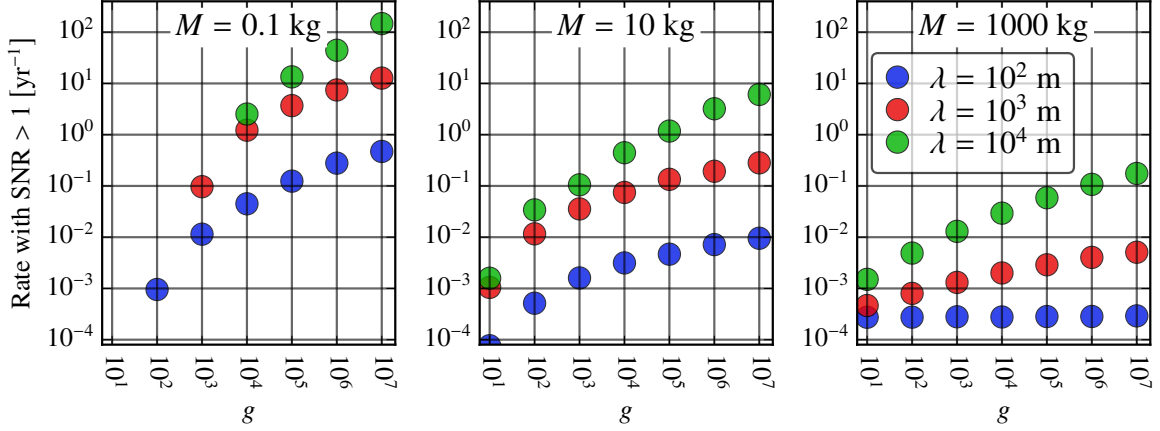


Figure 6.4: Cumulative event rate  $\dot{\eta}(1)$  in Advanced LIGO for the number of dark matter events per year with SNR of at least 1, as a function of Yukawa coupling  $g$  and screening length  $\lambda$ .

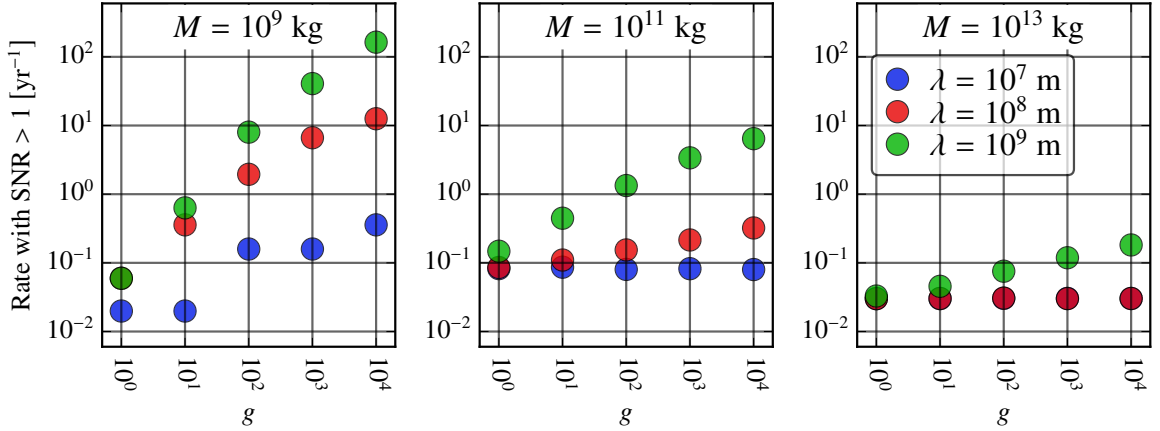


Figure 6.5: Cumulative event rate  $\dot{\eta}(1)$  in LISA for the number of dark matter events per year with SNR of at least 1, as a function of Yukawa coupling  $g$  and screening length  $\lambda$ .

For each detector and each DM object mass, several thousand events are simulated, and the histogram of SNRs is recorded. From this, the cumulative event rate  $\dot{\eta}(q)$  is computed. The results are shown in figure 6.3. Consistent with the Seto and Cooray analysis, the prospects for DM detection with LISA are not promising. Further, the prospects for DM detection with Advanced LIGO are even less promising.

## Numerical Yukawa analysis

The numerical Yukawa analysis is similar to the numerical Newtonian analysis, with the Newtonian force law replaced with the Yukawa force law given in equa-

tion 6.2. For each value of the DM mass, the simulation is run for several values of coupling  $g$  and screening length  $\lambda$ , and the unity-SNR event rate  $\dot{\eta}(1)$  is recorded. The results are shown in figure 6.4 for Advanced LIGO and 6.5 for LISA. In the lightest-mass case considered ( $M = 0.1\text{kg}$ ), detection rates become promising for  $g \gtrsim 10^4$ , with a screening length  $\lambda \sim 1\text{km}$ .

## Shapiro delay

One effect not considered in the above analysis and simulation is the Shapiro delay in the interferometer arms. Shapiro delay in laser interferometers has already been analyzed, for example, in the context of intentional modulation for Fabry–Pérot cavities by Ballmer et al.<sup>148</sup> and in the context of asteroid flybys for LISA by Chauvineau et al.<sup>149</sup>

In the simple case of a stationary mass  $M$  located a distance  $d$  along an arm of length  $L$  at an impact parameter  $b$ , the round-trip time delay is<sup>150</sup>

$$\Delta t = -\frac{2GM}{c^3} \ln \frac{4d(L-d)}{b^2}. \quad (6.10)$$

For a given mass and impact parameter, the delay is maximized for  $d = L/2$ , giving  $\Delta t = -(4GM/c^3) \ln(L/b)$ . For Advanced LIGO, a 1000 kg mass located 1 m from the midpoint of an arm (corresponding to a characteristic interaction frequency  $v/b \sim 300\text{Hz}$ ) would produce a peak displacement  $c\Delta t$  of about  $10^{-23}\text{m}$ , which is too small to be detected. The logarithmic dependence of the time delay on  $b$  means that a peak displacement of  $1 \times 10^{-21}\text{m}$  (which might be detectable) would require an impact parameter that is smaller than the Planck length.

## 6.4 Search strategy

A significant practical impediment to this kind of search in Advanced LIGO is the lack of colocated interferometers. The screening lengths considered here ( $\lambda \lesssim 10\text{km}$ ) are much smaller than the current (and planned) baseline separations of advanced laser interferometers (typically thousands of kilometers). Therefore, a putative DM interaction event would register in only one interferometer at a time. However, a search could be conducted over data from the H1 and H2 initial LIGO interferometers. Additionally, some third-generation interferometers such as the Einstein Telescope<sup>151</sup> and LISA<sup>6</sup> are planned to have colocated interferometers.

# 7 Future work

In this chapter we give a few suggestions for how to improve the current Advanced LIGO detectors and what to think about for future detectors.

## 7.1 Interferometry

Suggestions for sensitivity improvements have been given by Miller et al.<sup>152</sup> Some possible minor alterations to the interferometer configuration or sensing are as follows:

- The use of paired in-vacuum length sensors to facilitate out-of-loop and cross-correlation noise estimates. An out-of-loop reflection sensor would be particularly useful, since it is difficult to estimate the residual frequency noise by other methods.
- The inclusion of pick-off sensors for the signal recycling cavity.
- Greater jitter suppression before the laser is injected into the vacuum system. Pointing noise from the injection-locked oscillator greatly contaminated the interferometer's differential sensitivity. While one can attempt to mitigate the jitter coupling through careful thermal tuning and alignment offset adjustment, it is much less painful to mitigate the jitter itself by using a higher-finesse pre-modecleaner, or two pre-modecleaners in series.
- Active optical stabilization of the rf sideband amplitudes. Residual amplitude modulation (RAM) has the potential to introduce extra sensing noise into length and angular control loops, including dc error point offsets.<sup>153</sup> Active RAM suppression could be achieved via heterodyned electrical and thermal EOM feedback<sup>154</sup> or direct rf feedback to the EOM.<sup>155</sup>

A more drastic configuration change may be made by removing the signal-recycling mirror in order to alleviate some technical issues associated with the presence of

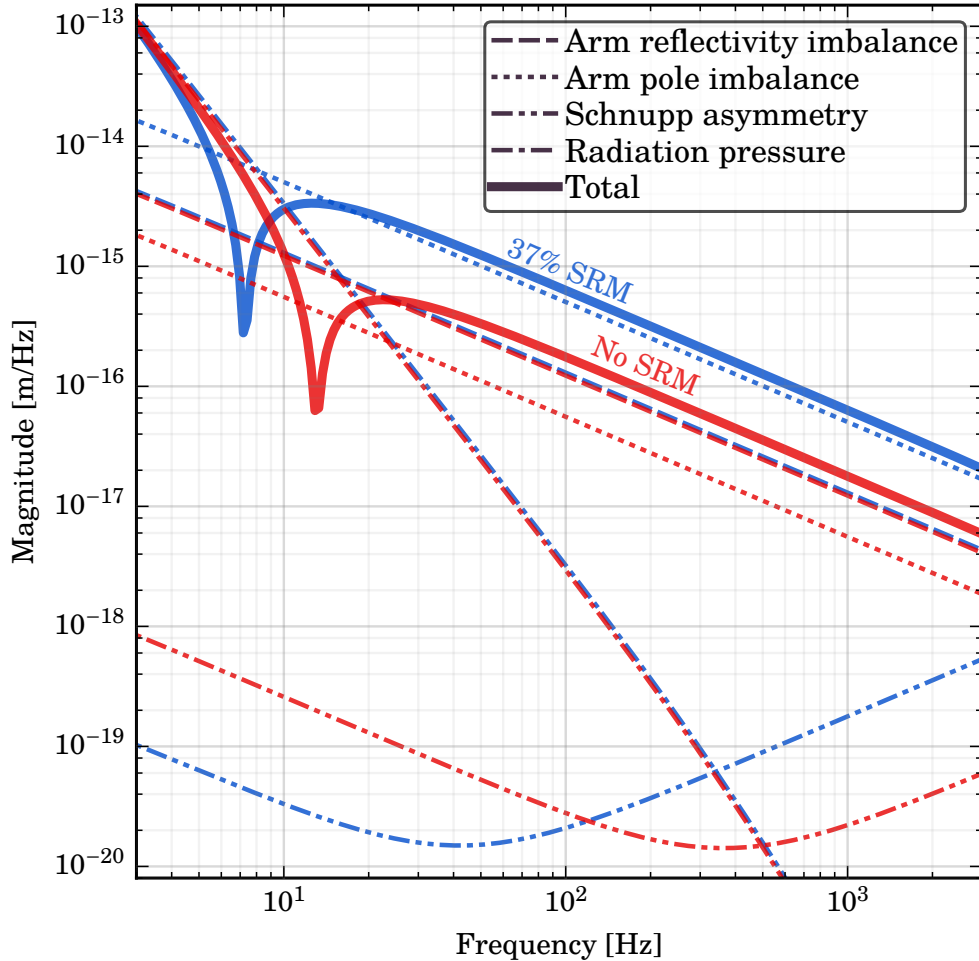


Figure 7.1: Expected frequency noise coupling into differential arm length for the case of a 37 % signal recycling mirror and for the case of no signal recycling mirror. In each case the input test mass transmissivities have been adjusted as described in the text to give a differential arm pole  $f_- \approx 350$  Hz. The assumed input power is 25 W. The calculation is done according to equation 29 in Izumi et al.<sup>21</sup> The assumed arm reflectivity imbalance is  $\delta r_a = 0.0029$ , the arm pole imbalance is  $\delta f_a = 0.24$  Hz, the differential reduced mass is  $\delta\mu = 5$  g, and the differential arm amplitude gain is  $\delta g_a = -0.036$ .

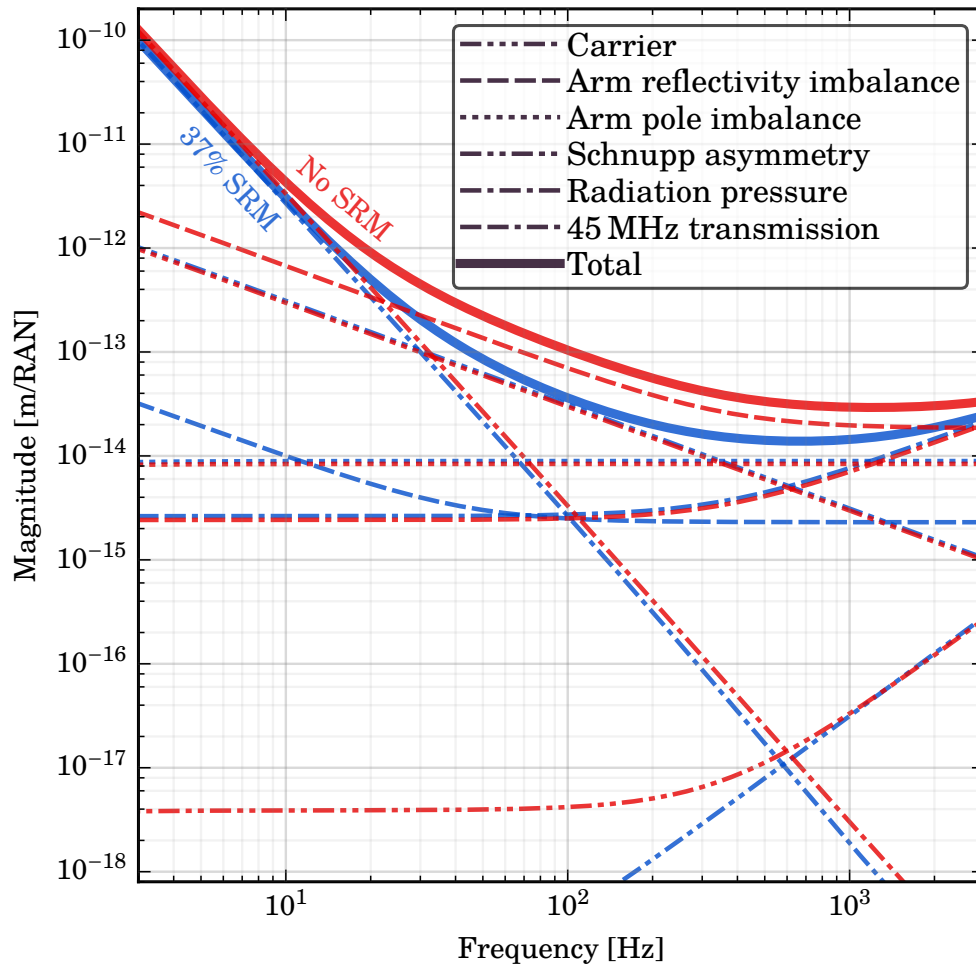


Figure 7.2: Expected intensity noise coupling into differential arm length for the case of a 37% signal recycling mirror and for the case of no signal recycling mirror. In each case the input test mass transmissivities have been adjusted as described in the text to give a differential arm pole  $f_- \approx 350$  Hz. The assumed input power is 25 W. The calculation is done according to equation 26 in Izumi et al.<sup>21</sup>

a signal recycling cavity. Here we consider a scenario in which the interferometer is operated at O1 power (25 W) with no signal recycling mirror. To maintain the differential arm pole at  $f_- \approx 350$  Hz, the input test mass transmissivity can be set to  $T_i = 11.5\%$ , giving an arm finesse  $\mathcal{F} = 52$ . Some consequences of this optical configuration change are as follows.

- **Sensing and control issues.** Eliminating the SRM simplifies the interferometer sensing-and-control scheme by removes the signal-recycling length degree of freedom and the two angular degrees of freedom of the mirror.
- **Frequency and intensity noise couplings.** Removing the SRM (and subsequently altering the input test mass transmissivities) makes the interferometer less susceptible to frequency noise, but more susceptible to intensity noise (figures 7.1 and 7.2). However, the changes in susceptibility are modest (about a factor of 5 at most).
- **Modematching.** With the SRM, the signal-recycling cavity must be mode-matched to the arms, and the output modecleaner must be matched to the signal-recycling cavity. Eliminating the SRM simplifies this problem, requiring only that the output modecleaner be matched to the arms. This reduces the potential for modematching-induced output port losses, which degrade the shot-noise-limited SNR and limit the achievable amount of squeezing.
- **Power-recycling losses.** With the lower arm finesse, the circulating power in the interferometer becomes more sensitive to losses in the power-recycling cavity. To ensure the circulating arm power drops by no more than a few percent of its zero-loss value, a PRC loss on the order of  $10^{-4}$  or less is required (equation 2.17b).
- **Michelson motion.** The coupling  $\Xi_m = \pi/2\mathcal{F}$  of Michelson motion into differential arm length readout increases by roughly a factor of 10. Since the shot noise of the Michelson sensor can be subtracted from the GW readout signal with feedforward, this means that the Michelson displacement noise must be kept sufficiently small.

Looking further into the future, we can ask how the frequency coupling transfer function could look for a 40 km interferometer of the type considered for the so-called Cosmic Explorer.<sup>156</sup> We consider a dual-recycled Fabry–Pérot Michelson with input test mass transmissivity  $T_i = 7\%$ , PRM transmissivity  $T_p = 0.5\%$ , SRM transmissivity  $T_s = 10\%$ , a circulating arm power  $P_a = 2$  MW, test masses weighing 320 kg, and a Schnupp asymmetry  $\bar{L}_M = 0.8$  m. The frequency-to-displacement coupling transfer function is shown in figure 7.3. For the chosen parameters, the

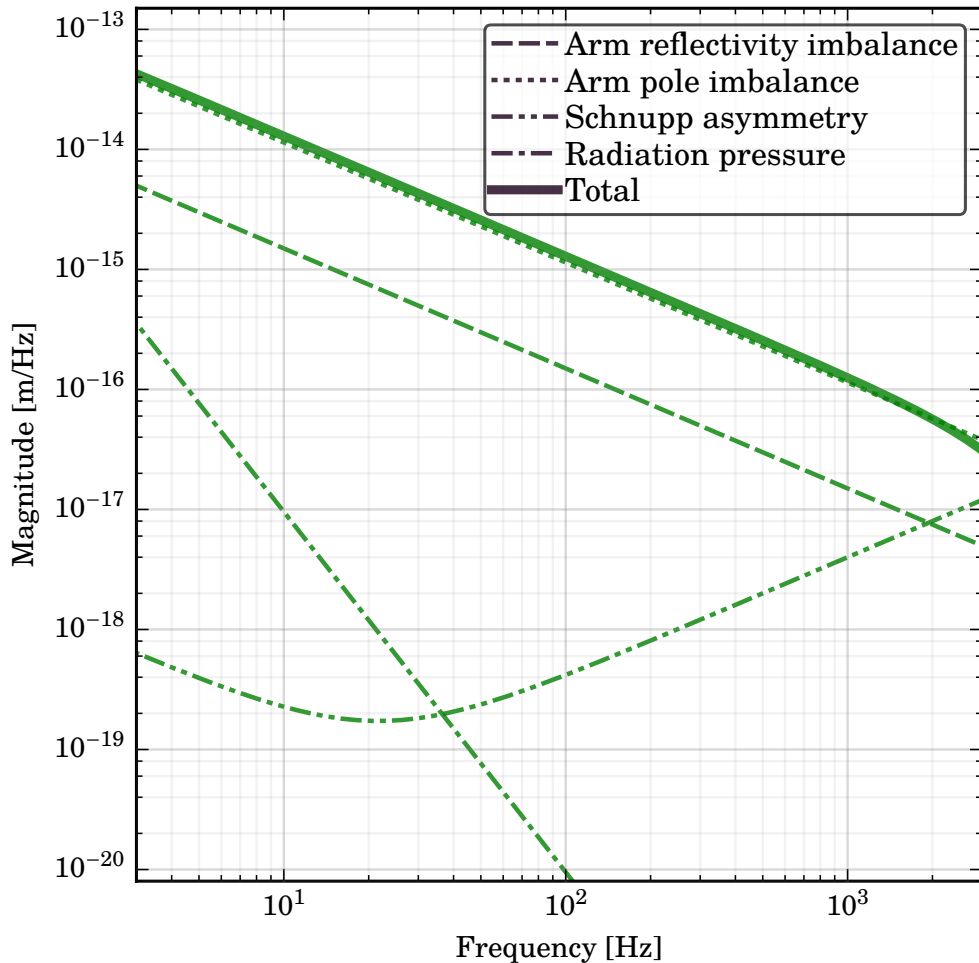


Figure 7.3: Expected frequency noise coupling into differential arm length for a possible 40 km detector as described in the text. The calculation is again done according to equation 29 in Izumi et al.<sup>21</sup> The various imbalances are the same as the imbalances assumed for the Advanced LIGO coupling transfer functions described above. The magnitude of the coupling for the 40 km detector is similar to the magnitude of the Advanced LIGO coupling. If the displacement noise of the 40 km detector is similar to the displacement noise of Advanced LIGO, this indicates that the laser frequency noise requirement need not be significantly more stringent than the current Advanced LIGO requirement.

transfer function is well approximated by  $(10^{-15} \text{ m/Hz}) \times (100 \text{ Hz}/f)$ . If the sensitivity of the Cosmic Explorer is about  $8 \times 10^{-21} \text{ m/Hz}^{1/2}$  between 20 Hz and 1 kHz, then the required frequency noise at the interferometer input must be less than  $(1 \mu\text{Hz}/\text{Hz}^{1/2}) \times (100 \text{ Hz}/f)$  in order to contribute negligibly to the total displacement sensitivity. In fact this is not so different from the requirements for Advanced LIGO.<sup>35</sup> However, the controls problem must also be considered. For a 40 km interferometer the interferometer's response to frequency fluctuations (using PDH reflection locking) will have infinitely deep notches at positive integer multiples of the arm FSR  $c/2L = 3.7 \text{ kHz}$ . This restricts the bandwidth of the common-mode frequency stabilization loop to less than a few kilohertz, and hence restricts the amount of suppression that can be achieved. However, if a macroscopic differential arm length offset  $\bar{L}_-$  is incorporated into the interferometer topology, the FSR notches acquire a finite depth. Either  $\bar{L}_-$  could be made large enough to make the notches negligibly deep, or the first few notches could be electronically compensated to produce a stable servo loop.

## 7.2 Calibration

Some possible future directions in interferometer calibration are as follows:

- Repeating the analysis given in chapter 5 using waveforms that include merger and ringdown signals (for example, those described by Ajith et al.<sup>157</sup>).
- Investigating other methods of optimizing calibration line placement. In chapter 5 we minimized the volume of the covariance of the interferometer's optomechanical plant parameters. However, in the end we are actually interested in minimizing the volume of the covariance of the astrophysical parameters (mass, spin, and so on) of a particular signal. To this end, we may want to minimize a different quantity, such as the uncertainty in the interferometer response function in a particular frequency band.

Additionally, the line optimization technique described in the calibration chapter could be put to work more generally as a way to optimally extract information about the dynamics of LTI systems. For example, this technique could be applied to optical plant measurement for angular control loops, where the timescale of the dynamics (seconds or tens of seconds) typically require long transfer function measurements.

# A Preliminary notions about loops

This appendix presents a basic overview of feedback loops. Deeper discussion can be found in various controls textbooks and review articles, such as the article by Bechhoefer.<sup>158</sup>

## A.1 Introduction

Let  $P(f)$  denote the transfer function of some linear, time-invariant system (the **plant**) which we want to control. The plant takes some input  $x(f)$  and produces some output  $y(f) = P(f)x(f)$ . We want to take  $y$  (in this context called the **error signal**), pass it through some filter  $K(f)$  (the **compensator**) to produce a control signal  $k(f)$ , and feed this control signal back into the input of  $P(f)$ .

The resulting servo loop is characterized by its **open-loop transfer function (OLTF)**  $H(f) = K(f)P(f)$ . The OLTF indicates to what extent (and at what frequencies) the feedback system can suppress external fluctuations. If an external fluctuation  $x(f)$  is injected into the loop, then after one trip around the loop it will arrive just before the injection point as a fluctuation  $b(f) = H(f)x(f)/[1 - H(f)]$ . Just after the excitation point, the fluctuation is  $a(f) = b(f) + x(f) = x(f)/[1 - H(f)]$ . We call  $H/(1 - H)$  the system's **closed-loop transfer function** and denote it as  $\bar{H}$ . We call  $1/(1 - H)$  the system's **loop suppression function** and denote it as  $\underline{H}$ .<sup>a</sup>

For the feedback system to be stable, an external perturbation  $x(f)$  must not produce an infinite in-loop perturbation  $a(f)$ ; that is, we must have  $a/x = 1/(1 - H) \neq \infty$ , or

$$H(f) \neq +1. \quad (\text{A.1})$$

---

<sup>a</sup> Sometimes  $1/(1 - H)$  is referred to as the closed-loop transfer function.<sup>159</sup>

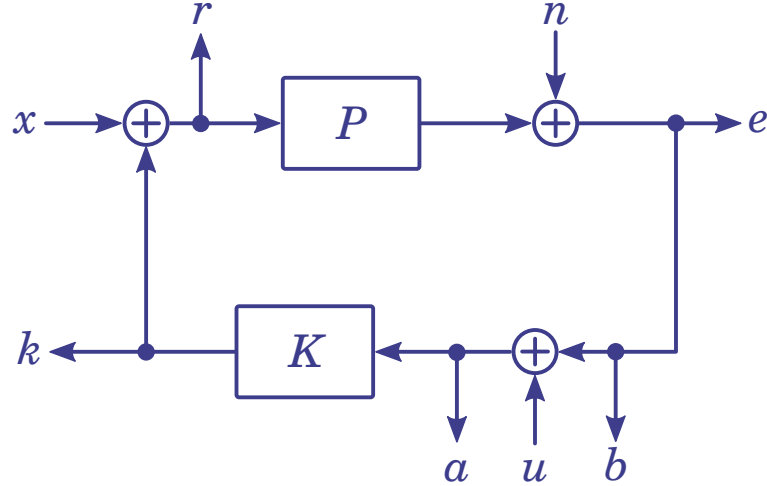


Figure A.1: Anatomy of a generalized servo loop, consisting of a plant  $P$  and a compensator  $K$ , which together form an open-loop transfer function  $H = PK$ . Any external noise  $x$  injected into the loop causes a fluctuation in the error signal  $e$ . The error signal is fed through  $K$  to produce a control signal  $k$ , which is summed back into the loop in order to suppress the external noise, so that its contribution to the residual loop noise  $r$  is  $x/(1-H)$ . In general, the equipment used to construct the servo loop will also introduce sensing noise  $n$ , which appears in the residual loop noise as  $Hn/(1-H)$ . Also depicted is a loop excitation point  $u$ ; the OLTF  $H$  can be measured by monitoring the signals  $a$  and  $b$  just after and just before this excitation.

Said another way, if the OLTF has unity gain ( $|H(f)| = 1$ ), the phase must not be zero ( $\arg H(f) \neq 0^\circ$ ).<sup>b</sup>

Any frequency  $f_0$  for which  $|H(f_0)| = 1$  is called a **unity-gain frequency** (UGF) for  $H$ , and  $\arg H(f_0)$  is called the **phase margin** at that particular UGF. A small phase margin causes the magnitude of the loop suppression function  $\underline{H}$  to exceed 1 around the UGF, meaning that the loop amplifies noise rather than suppressing it; this is called **gain peaking**. Additionally, at any frequency  $f_1$  for which  $\arg H(f_1) = 0^\circ$ , the quantity  $|H(f_1)|$  is called the **gain margin** at that particular frequency.

---

<sup>b</sup> Warning: there exist two popular sign conventions for loop analysis, depending on how the control signal  $k$  is fed back into the loop. This appendix is written with the convention that  $k$  is *summed* into the loop, as depicted in figure A.1. If instead one uses the convention that  $k$  is *differenced* into the loop, then a number of statements made in this appendix must be modified. Among other things, loop instability occurs when  $H = -1$  (that is,  $|H| = 1$  and  $\arg H = \pm 180^\circ$ ), and the expressions for the closed-loop transfer function and loop suppression function are  $\bar{H} = H/(1+H)$  and  $\underline{H} = 1/(1+H)$ .

## A.2 Crossovers

Sometimes, a feedback loop employs multiple LTI blocks in parallel. Such loops are common in systems which rely on multiple actuators to provide feedback. For example, when frequency-locking a solid-state laser such as an NPRO to an optical cavity, feedback to the length of the laser crystal can be applied using a PZT to strain the crystal, or a heater to control the thermal expansion of the crystal. The former provides several megahertz of actuation range with a bandwidth of a few tens of kilohertz, and the latter provides several gigahertz of actuation range with a bandwidth of a few hertz. For robust, long-lived locks, both actuators are needed.

Consider a loop with OLTF  $H = H_1 + H_2$  (i.e., two blocks  $H_1$  and  $H_2$  are added in parallel). The usual loop stability condition requires  $H(f) = H_1(f) + H_2(f) \neq +1$ ; i.e.,  $H_1/(1 - H_2) \neq +1$ . We define

$$\Xi \equiv H_1/(1 - H_2) \quad (\text{A.2})$$

to be the **crossover transfer function** of  $H_1$  and  $H_2$ ; it characterizes the relative strength of  $H_1$  versus  $H_2$  at various frequencies. Any frequency  $f_0$  for which  $|\Xi(f_0)| = 1$  is a **crossover frequency** between  $H_1$  and  $H_2$ .<sup>c</sup>

## A.3 Measurements

We now turn to some topics in how to measure transfer functions. Again let  $P(f)$  denote some LTI system, with an input and output. The canonical measurement of the transfer function  $P(f)$  is done by injecting random noise  $x(f)$  into the output, which will generate a signal  $y(f) = P(f)x(f)$  at the output. The estimate  $\hat{P}(f)$  of  $P(f)$  is made by computing<sup>160</sup>

$$\hat{P}(f) = \frac{S_{xy}(f)}{S_{xx}(f)}, \quad (\text{A.3})$$

where  $S_{xy}(f)$  is the (complex) cross-spectral density of  $x$  and  $y$ , and  $S_{xx}(f)$  is the (real) auto-spectral density (or power spectral density) of  $x$ . Equivalently, we will write the cross-spectral density as  $\langle x^* y \rangle$ , as this notation is more suggestive of how spectral densities are estimated in practice. A common figure of merit for the quality of a particular measurement is the **coherence**

$$\gamma_{xy}^2(f) = \frac{|S_{xy}(f)|^2}{S_{xx}(f)S_{yy}(f)}, \quad (\text{A.4})$$

---

<sup>c</sup> Sometimes the crossover transfer function is instead defined as  $H_1/H_2$ .<sup>159</sup>

which can attain any value from 0 (no correlation between  $x$  and  $y$ ) to 1 (perfect correlation between  $x$  and  $y$ ).

We consider a loop whose OLTF  $H(f)$  we would like to measure. In order to do this, we inject some excitation  $u$  into the loop, and we measure just after ( $a$ ) and just before ( $b$ ) the excitation (see figure A.1). As mentioned above, these test points are given (in the frequency domain) by

$$a = \frac{u}{1-H} \quad (\text{A.5})$$

$$b = \frac{Hu}{1-H}. \quad (\text{A.6})$$

With  $a$ ,  $b$ , and  $u$  in hand, one can see that there are (at least) four ways to extract the OLTF.

1. Compute an estimate of the CLTF

$$\hat{\overline{H}} = \frac{\langle u^* b \rangle}{\langle u^* u \rangle} \quad (\text{A.7})$$

and then do algebra to compute  $\hat{H}$ .

2. Compute an estimate of the loop suppression function

$$\underline{\hat{H}} = \frac{\langle u^* a \rangle}{\langle u^* u \rangle} \quad (\text{A.8})$$

and then do algebra to compute  $\hat{H}$ .

3. Compute an estimate of the OLTF directly using  $a$  and  $b$  only

$$\hat{H} = \frac{\langle a^* b \rangle}{\langle a^* a \rangle}. \quad (\text{A.9})$$

This is the technique used with network analyzers (such as DTT<sup>161</sup>) when making Fourier-based (for example, broadband) transfer function measurements.

4. Compute an estimate of the OLTF directly using  $a$ ,  $b$ , and  $u$ :

$$\hat{H}' = \frac{\langle u^* b \rangle}{\langle u^* a \rangle}. \quad (\text{A.10})$$

This is the technique used with network analyzers when making demodulation-based (for example, swept-sine) transfer function measurements.

The last of two these is often the most convenient: the estimated OLTF can be read directly off a network analyzer, with no algebra required. However, we will now

show that the third estimator ( $\hat{H}$ ) has the drawback of being biased, while the other three do not.

All realistic loops have some noise  $x$  which is also injected into (or generated within) the system under feedback control. In the presence of both noise  $x$  and excitation  $u$ , the test points for our measurement are

$$a = \frac{u + x}{1 - H} \quad (\text{A.11})$$

$$b = \frac{Hu + x}{1 - H}, \quad (\text{A.12})$$

and so, assuming that  $x$  and  $u$  are uncorrelated, the direct OTLF estimate is

$$\hat{H} = \frac{\langle a^* b \rangle}{\langle a^* a \rangle} = \frac{H \langle u^* u \rangle + \langle x^* x \rangle}{\langle u^* u \rangle + \langle x^* x \rangle}. \quad (\text{A.13})$$

This equation is telling us that *attempting to directly estimate  $H$  in this fashion will succeed only if the excitation  $u$  is much stronger than the other noise  $x$  in the loop*. If  $|u| \gg |x|$ , then  $\hat{H} \rightarrow H$ , as desired. But if  $|u| \ll |x|$ , then  $\hat{H} \rightarrow 1$ , regardless of the true value of  $H$ . In other words,  $\hat{H}$  is a biased estimator of  $H$ . Moreover, examining the coherence of the test points may be misleading, since in the limit  $u \rightarrow 0$ ,  $a$  and  $b$  are both perfectly correlated with  $x$ . Then  $\gamma_{ab}^2 \rightarrow 1$ .

One can show that  $\hat{H}$ ,  $\underline{H}$ , and  $\hat{H}'$  are all *unbiased* estimators, converging respectively to  $\overline{H}$ ,  $\underline{H}$ , and  $H$  for any  $u \neq 0$ , regardless of the relative strength of  $u$  and  $x$ .<sup>d</sup> In situations where it is hard to satisfy  $|u| \gg |x|$  (for example, angular loops which cannot tolerate much excitation beyond the quiescent noise level of the loop), it may be advantageous to use these alternative estimators if possible.

## A.4 Noise

Let us again focus on the example of locking a laser to an optical cavity by monitoring the phase fluctuation  $\phi(f)$  of the light in reflection. The phase fluctuation may arise either from length fluctuation  $L(f)$  of the cavity, or from frequency fluctuation  $v(f)$  of the laser light:

$$\phi(f) = (2\pi/c)[v(0)L(f) + v(f)L(0)]. \quad (\text{A.14})$$

The former noise is an example of a **displacement noise** — a noise in the error signal arising from actual motion of the system of interest. The latter noise is an

---

<sup>d</sup> Of course, if  $|u| \ll |x|$  by many orders of magnitude, extracting a good transfer function estimate may be impractical.

example of a **sensing noise** — a noise in the error signal arising from whatever is used to sense the system of interest.

A closely related concept has to do with what kinds of noise limit the performance of a servo loop. Consider again loop with OLTF  $H$ . Suppose the loop has a certain amount of displacement noise  $x(f)$ , as well as some sensing noise  $n(f)$  injected after the displacement noise. Now suppose we were able to measure the true residual  $r(f)$  between  $x$  and  $n$ . We would find

$$r = \frac{x}{1-H} + \frac{Hn}{1-H}. \quad (\text{A.15})$$

This first term on the right-hand side of this equation says that as the gain  $|H|$  is increased, the loop's displacement noise is more aggressively suppressed. The second term says that when  $|H| > 1$ , the sensing noise is impressed onto the residual. If the first term dominates the residual, the loop is said to be **gain limited**, and the residual  $r$  within the loop bandwidth can be reduced by increasing the loop gain. If the second term dominates the residual, the loop is said to be **sensing-noise limited**, and the residual  $r$  within the loop bandwidth cannot be reduced by increasing the loop gain.

Note that the loop's error signal  $e(f)$  in general does *not* accurately represent the true in-loop residual, since

$$e = \frac{x}{1-H} + \frac{n}{1-H} \neq r. \quad (\text{A.16})$$

In other words, continuing to increase the loop gain  $|H|$  will make the error signal smaller, even if the loop's actual residual is sensing-noise limited. This is the motivation for placing an “out-of-loop” sensor at nearly the same place as the in-loop sensor; this out-of-loop sensor will see the true in-loop residual in combination with the sensor's own sensing noise.<sup>e</sup>

---

<sup>e</sup> However, the out-of-loop sensor will not see sensing noises common to both sensors.

## B Median estimation of amplitude spectral densities

Bin-by-bin median averaging of amplitude spectral densities (ASDs) is sometimes preferred over traditional rms averaging for its increased robustness against transients.<sup>162</sup> In this note we examine some of the subtleties of median averaging techniques, with a particular focus on Gaussian noise.

The central result of this appendix—that in the limit of large sample size, the median is biased downward from the mean by a factor of  $(\ln 2)^{1/2}$ —is already known in the gravitational-wave data analysis community.<sup>163–165</sup> Here we give a simple demonstration of this fact using the aLIGO H1 OMC null stream.

### B.1 Problem statement

Given a time series  $h(t)$ , how does one arrive at an estimate of the ASD  $S_{hh}(f)^{1/2}$ ? Spectrum analyzers, DTT, Matlab’s `pwelch`, etc., usually produce an ASD estimate using some flavor of the Welch method:<sup>166</sup>

1. Split  $h(t)$  into  $N$  segments, each of length  $T$ . The segments can be chosen to overlap by some factor (often 50 %).
2. Apply a windowing function  $w(t)$  to each segment  $h_i(t)$  and compute the Fourier transform  $H_i(f)$  of  $w(t)h_i(t)$ .
3. At each Fourier frequency  $f$ , compute the rms of the magnitudes of the Fourier transforms (and then apply a normalization factor  $\mathcal{C}$ ) in order to arrive at an estimate of the ASD:

$$\hat{S}_{hh}(f)^{1/2} = \mathcal{C} \left( \frac{1}{N} \sum_{i=0}^{N-1} |H_i(f)|^2 \right)^{1/2}. \quad (\text{B.1})$$

Note that rms averaging of the ASDs amounts to mean averaging of the PSDs, so this step is often referred to as “mean averaging”.

## B.2 Gauss and Rayleigh distributions

When one says that  $h(t)$  consists of Gaussian noise, one means that in each frequency bin, the quadrature components  $x = \text{Re } H(f)$  and  $y = \text{Im } H(f)$  of the noise are independent, identically distributed, Gaussian random variables with zero mean and variance  $\sigma^2$ . That is, their joint pdf is

$$p(x, y) = p(x)p(y) = \frac{1}{2\pi\sigma^2} \exp\left(-\frac{x^2 + y^2}{2\sigma^2}\right). \quad (\text{B.2})$$

When estimating the ASD, we are interested not in  $x$  or  $y$  individually, but rather the quantity  $r = (x^2 + y^2)^{1/2}$ . (We often discard the phase information  $\phi = \arctan y/x$ .) This quantity does not follow a Gaussian distribution, but rather a Rayleigh distribution:<sup>160;a;b</sup>

$$p(r) = \frac{r}{\sigma^2} \exp\left(-\frac{r^2}{2\sigma^2}\right) \quad \text{for } r \geq 0, \quad (\text{B.3})$$

and  $p(r) = 0$  otherwise. For this distribution, we will be interested in the following quantities:

- the mode

$$M = \max_r p(r) = \sigma; \quad (\text{B.4})$$

- the mean

$$\mu = \int_0^\infty r p(r) dr = \left(\frac{\pi}{2}\right)^{1/2} \sigma \approx 1.25\sigma; \quad (\text{B.5})$$

- the rms

$$\psi = \left( \int_0^\infty r^2 p(r) dr \right)^{1/2} = \sqrt{2}\sigma \approx 1.41\sigma; \quad (\text{B.6})$$

and

---

<sup>a</sup> Explicitly: writing  $x = r\cos\phi$  and  $y = r\sin\phi$ , the pdf  $p(x, y)$  transforms to  $p(r\cos\phi, r\sin\phi)|\det J(r, \phi)|$ , where  $J(r, \phi)$  is the Jacobian of the coordinate transformation. Integrating over  $\phi$  gives the Rayleigh distribution  $p(r)$ .

<sup>b</sup> If one recasts this analysis in terms of PSDs rather than ASDs, then the quantity  $s = r^2$  follows an exponential distribution, with  $p(s) = \exp(-s/\zeta)/\zeta$  and  $\zeta = 2\sigma^2$ .<sup>163,164</sup>

- the median  $m$ , which is defined as follows:

$$\frac{1}{2} = \int_0^m p(r) dr = 1 - \exp\left(-\frac{m^2}{2\sigma^2}\right) \quad (\text{B.7})$$

$$\Rightarrow m = (\ln 4)^{1/2} \sigma \simeq 1.18\sigma. \quad (\text{B.8})$$

For the Rayleigh distribution, these four quantities are distinct, with  $\sigma < m < \mu < \psi$ .<sup>c</sup>

### B.3 rms versus median averaging

The usual algorithm for estimating an averaged ASD from multiple data segments is to compute the rms: that is, for each bin, we compute a quantity proportional to  $\bar{r} = (r_0^2 + r_1^2 + \dots + r_{N-1}^2)^{1/2}/N$ . Therefore, this estimate  $\bar{r}$  is an estimate of  $\psi$ , as defined above (and hence we can write this estimate as  $\hat{\psi}$ ). Conversely, the median estimate  $\hat{m} = \text{med}\{r_0, r_1, \dots, r_{N-1}\}$  converges to  $m$ .<sup>d</sup> Therefore, *in each frequency bin of a Gaussian-noise ASD, the median value is biased downward from the corresponding rms value by a factor  $b_\infty = m/\psi = (\ln 2)^{1/2} \simeq 0.83$ , in the limit of an infinite number of non-overlapping segments.*

The papers by Abbott et al.<sup>163</sup> and Allen et al.<sup>164</sup> discuss the value of the bias when the two foregoing assumptions are not satisfied. For a finite number of non-overlapping segments, the sample median is not equal to the true median of the underlying Rayleigh distribution. Instead, the bias is given by

$$b(N) = \begin{cases} \left[ \sum_{n=1}^N \frac{(-1)^{n+1}}{n} \right]^{1/2} & \text{if } N \text{ is odd,} \\ b(N-1) & \text{if } N \text{ is even.} \end{cases} \quad (\text{B.10})$$

As one might anticipate,  $b(N) \rightarrow (\ln 2)^{1/2}$  as  $N \rightarrow \infty$ . Table B.1 gives the value of  $b$  for several values of  $N$ .

---

<sup>c</sup> We note in passing that in the case of Gaussian noise superimposed on a coherent line—for example, shot noise superimposed on the vibrational mode from some optic—the ASD will instead follow a Rice distribution:

$$p(r) = \frac{r}{\sigma^2} \exp\left(-\frac{r^2 + v^2}{2\sigma^2}\right) I_0\left(\frac{rv}{\sigma^2}\right), \quad (\text{B.9})$$

where  $I_0$  is the modified Bessel function of the first kind, and  $v$  describes the height of the line in the ASD.

<sup>d</sup> Note that since the function  $x \mapsto x^2$  is strictly increasing for  $x \geq 0$ , one does *not* need to square the ASDs before computing the median.

$N$	$b$
1	1.0000
3	0.9128
10	0.8635
30	0.8427
100	0.8356
300	0.8336
1000	0.8328
$\infty$	0.8326

Table B.1: Median bias factor  $b$  (to four decimal places) for  $N$  non-overlapping segments.

In the case of overlapping segments, the above formula for  $b$  is still not correct, since the data in adjacent segments are correlated (i.e., one does not truly have  $N$  independent samples from the underlying distribution). If median averaging with overlap is desired (and the overlap is  $\leq 50\%$ ), Allen et al. suggest computing the medians  $m$  and  $m'$  of the  $k$  even-numbered and  $k'$  odd-numbered segments individually, correcting by the appropriate bias factors  $b$  and  $b'$ , and then taking the weighted rms of the two values:

$$\hat{\psi} = \left[ \frac{k(m/b)^2 + k'(m'/b')^2}{N} \right]^{1/2}. \quad (\text{B.11})$$

This prescription is referred to as *mean–median averaging*.

## B.4 Real-world example

We now demonstrate some of the above claims using data from the Advanced LIGO H1 null stream.

The Advanced LIGO instruments read out the light at the antisymmetric port using two photodiodes (labeled A and B), each with photocurrent  $I_A(t)$  and  $I_B(t)$ . The sum  $I_+ = I_A + I_B$  is the error signal for the differential arm length. The difference  $I_- = I_A - I_B$  is the null stream. Since A and B are balanced, the null stream should contain only those noises which are uncorrelated between the two photodiodes.<sup>e</sup>

<sup>e</sup> Of course, it is only approximately true that A and B are balanced. In practice, the balancing of A and B is tuned digitally in order to minimize the appearance of correlated noise in the null stream. For H1 the required digital balancing is 0.3 %.

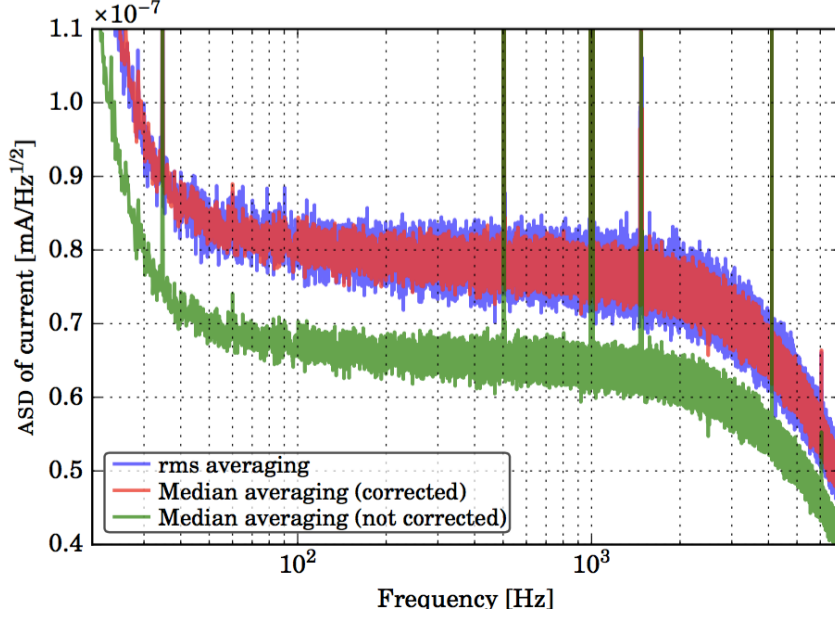


Figure B.1: Three ASD estimates of the H1 OMC null stream. The first is the usual bin-by-bin rms averaging of the 720 individual ASDs. The second is the bin-by-bin median estimate, divided by  $(\ln 2)^{1/2}$ . The third is the bin-by-bin median estimate, without this correction factor incorporated.

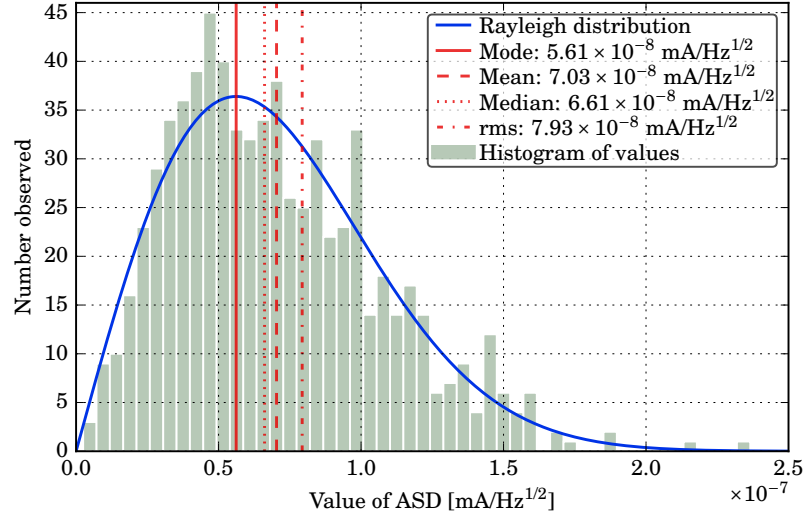


Figure B.2: Histogram of the H1 OMC null stream ASD at  $f = 100$  Hz, assembled from  $N = 720$  individual segments. The observed median  $m$  was used to estimate the parameter  $\sigma$  for the underlying Rayleigh distribution.

In particular, the null stream should be dominated by (1) the shot noise of the light from the interferometer, and (2) the electronics noise of the photodiodes and

their readout chains. In both cases we can reasonably expect that the noise in each quadrature of each frequency bin is Gaussian.

We have taken two hours of raw H1 null stream data ( $f_{\text{samp}} = 16384 \text{ Hz}$ )<sup>f</sup> and processed it as follows using gwpy:

1. We split the data record into  $N = 720$  segments (with 50 % overlap and  $T = 10 \text{ s}$ ).
2. We apply a Hann window to each segment, and then apply a discrete Fourier transform.
3. We take the magnitude of each DFT and normalize it, thereby producing 720 individual ASD estimates (with units of  $\text{mA}/\text{Hz}^{1/2}$ ). (The time stream  $I_-$  is already calibrated into millamps.)
4. We produce averaged ASD estimates, either by rms averaging, or median averaging. No rebinning is performed.
5. We undo the magnitude of the digital decimation filter, which otherwise produces significant rippling of the spectrum above 1 kHz.

Figure B.1 shows the rms and median ASD estimates for these two hours of null stream data. The median is plotted twice, both with and without the  $(\ln 2)^{1/2}$  correction. Only with the correction factor applied does the median estimate coincide with the rms estimate for this Gaussian channel.

Figure B.2 shows a histogram of the 720 ASD estimates at  $f = 100 \text{ Hz}$ . We compute the mean, median, and rms values, and use the median to estimate the parameter  $\sigma$  (i.e., the mode) of the underlying Rayleigh distribution. The Rayleigh distribution is then plotted on top of the histogram.

---

<sup>f</sup>More specifically, the data record is H1:OMC-DCPD\_NULL\_OUT\_DQ, from 00:00:00Z to 02:00:00Z 2015-06-07.

# C Optical cavities

In this appendix we will review some concepts related to optical cavities and Pound–Drever–Hall locking.

## C.1 Definitions

We consider a Fabry–Pérot interferometer of length  $L$ , and with optics of reflectivity  $r_a$  and  $r_b$ .

The circulating field  $E_{\text{circ}}$ , the reflected field  $E_{\text{refl}}$ , and the transmitted field  $E_{\text{tr}}$  are given by

$$E_{\text{circ}}(\omega) = E_0(\omega) \frac{t_a}{1 - r_a r_b e^{2i\omega L/c}} \quad (\text{C.1})$$

$$E_{\text{refl}}(\omega) = E_0(\omega) \frac{-r_a + r_b e^{2i\omega L/c}}{1 - r_a r_b e^{2i\omega L/c}} \quad (\text{C.2})$$

$$E_{\text{tr}}(\omega) = E_0(\omega) \frac{t_a t_b e^{i\omega L/c}}{1 - r_a r_b e^{2i\omega L/c}}. \quad (\text{C.3})$$

By examining (C.1), we see that the frequency response is characterized by periodic resonance: when  $e^{2i\omega L/c} = 1$ , the denominator becomes very small since  $r_a r_b \simeq 1$  for reasonably reflective mirrors.

We now define some commonly-used quantities relating to Fabry–Pérot cavities. The periodicity of the frequency response is called the **free spectral range** (FSR):

$$f_{\text{FSR}} = c/2L. \quad (\text{C.4})$$

The width of the resonance is characterized by the **cavity pole**  $f_p = \omega_p/2\pi$ , which is found by setting the denominator of (C.1) to zero and solving for  $\omega$ . The result is<sup>18,37</sup>

$$2\pi i f_p = -\frac{c}{2L} |\ln r_a r_b|; \quad (\text{C.5})$$

in other words, it is a single, real pole on the left-hand side of the  $s$ -plane. To derive the next three quantities, we examine the circulating power

$$\frac{P_{\text{circ}}(\omega)}{P_0(\omega)} = \left| \frac{E_{\text{circ}}(\omega)}{E_0(\omega)} \right|^2 = \frac{t_a^2}{|1 - r_a r_b e^{2i\omega L/c}|^2} = \frac{t_a^2 / (1 - r_a r_b)^2}{1 + \frac{4r_a r_b}{(1 - r_a r_b)^2} \sin^2\left(\frac{\omega L}{c}\right)}. \quad (\text{C.6})$$

The ratio  $E_{\text{circ}}(0)/E_0(0)$  is the **cavity amplitude gain**

$$g = \frac{t_a}{1 - r_a r_b}, \quad (\text{C.7})$$

and the **cavity power gain** is  $G = g^2$ . The frequency for which  $P_{\text{circ}}/P_0 = 1/2$  is the **half-width half-max frequency**:

$$f_{\text{HWHM}} = \frac{c}{2L} \times \frac{1}{\pi} \arcsin \left[ \frac{1 - r_a r_b}{2(r_a r_b)^{1/2}} \right]. \quad (\text{C.8})$$

In combination with the FSR, we can now define the **finesse**

$$\mathcal{F} = \frac{f_{\text{FSR}}}{2f_{\text{HWHM}}} = \frac{\pi/2}{\arcsin \left[ \frac{1 - r_a r_b}{2(r_a r_b)^{1/2}} \right]}. \quad (\text{C.9})$$

In the high-finesse limit, we have

$$f_{\text{HWHM}} \approx f_p \quad (\text{C.10})$$

and

$$\mathcal{F} \approx \frac{\pi(r_a r_b)^{1/2}}{1 - r_a r_b} \approx \frac{2\pi}{\mathcal{L}}, \quad (\text{C.11})$$

where  $\mathcal{L}$  is the round-trip loss in the cavity (including transmission loss). This last approximation follows by writing  $r_a = \sqrt{1 - \mathcal{L}_a}$  and  $r_b = \sqrt{1 - \mathcal{L}_b}$ , with  $\mathcal{L}_a, \mathcal{L}_b \ll 1$ , and  $\mathcal{L} = \mathcal{L}_a + \mathcal{L}_b$ .

Finally, some words about coupling. If  $r_a < r_b$ , the cavity is said to be **overcoupled**; if  $r_a = r_b$  the cavity is said to be **critically coupled**, and if  $r_a > r_b$ , the cavity is said to be **undercoupled**.

In the high-finesse limit,  $G$  and  $\mathcal{F}$  have the following relationships in the strongly overcoupled ( $r_b = 1$ ) and critically coupled cases:

$$G \approx 2\mathcal{F}/\pi \quad (\text{strongly overcoupled}) \quad (\text{C.12a})$$

$$G \approx \mathcal{F}/\pi \quad (\text{critically coupled}). \quad (\text{C.12b})$$

Another important quantity is the **visibility**:

$$v = 1 - \frac{P_{\text{refl}}(0)}{P_{\text{refl}}(f_{\text{FSR}}/2)}. \quad (\text{C.13})$$

## C.2 Pound–Drever–Hall locking

In the Pound–Drever–Hall technique,<sup>167</sup> the light into the cavity is phase-modulated with an index  $\Gamma$  at an rf frequency  $\Omega/2\pi$ , and the rf beatnote is read out in reflection of the cavity.

We assume the cavity is on resonance at dc, and is subject to a phase modulation of index  $\gamma$  at audio-band frequency  $\omega/2\pi$ .

The field into the cavity is

$$E_{\text{in}} = \sqrt{2}E_0 \cos [\omega_0 t + \Gamma \cos \Omega t + \gamma \cos \omega t] \quad (\text{C.14a})$$

$$= \frac{E_0}{\sqrt{2}} e^{i\omega_0 t} e^{i\Gamma \cos \Omega t} e^{i\gamma \cos \omega t} + \text{cc} \quad (\text{C.14b})$$

$$\approx \frac{E_0}{\sqrt{2}} e^{i\omega_0 t} \left\{ 1 + \frac{i\Gamma}{2} e^{i\Omega t} + \frac{i\Gamma}{2} e^{-i\Omega t} + \frac{i\gamma}{2} e^{i\omega t} + \frac{i\gamma}{2} e^{-i\omega t} - \frac{\Gamma\gamma}{4} \left[ e^{i(\Omega+\omega)t} + e^{i(\Omega-\omega)t} + e^{i(-\Omega-\omega)t} + e^{i(-\Omega+\omega)t} \right] \right\} + \text{cc}, \quad (\text{C.14c})$$

where we have kept terms of order 1,  $\Gamma$ ,  $\gamma$ , and  $\Gamma\gamma$ .

Upon reflection from the cavity,

$$E_{\text{refl}} = \frac{E_0}{\sqrt{2}} e^{i\omega_0 t} \left\{ r_0 + \frac{i\Gamma}{2} r_\Omega e^{i\Omega t} + \frac{i\Gamma}{2} r_{-\Omega} e^{-i\Omega t} + \frac{i\gamma}{2} r_\omega e^{i\omega t} + \frac{i\gamma}{2} r_{-\omega} e^{-i\omega t} - \frac{\Gamma\gamma}{4} \left[ r_{\Omega+\omega} e^{i(\Omega+\omega)t} + r_{\Omega-\omega} e^{i(\Omega-\omega)t} + r_{-\Omega-\omega} e^{i(-\Omega-\omega)t} + r_{-\Omega+\omega} e^{i(-\Omega+\omega)t} \right] \right\} + \text{cc}. \quad (\text{C.15})$$

We have made the assumption that the carrier is exactly resonant, so  $r_0$  is real. We further assume the rf sidebands are exactly antiresonant, so  $r_\Omega$  is real and equal to  $r_{-\Omega}$ . This means additionally that  $r_{-\omega} = r_\omega^*$  and  $r_{\Omega-\omega} = r_{\Omega+\omega}^*$ . Then

$$E_{\text{refl}} = \frac{E_0}{\sqrt{2}} e^{i\omega_0 t} \left\{ r_0 + i\Gamma r_\Omega \cos \Omega t + i\gamma \operatorname{Re}(r_\omega) \cos \omega t - i\gamma \operatorname{Im}(r_\omega) \sin \omega t - \Gamma\gamma \cos(\Omega t) [\operatorname{Re}(r_{\Omega+\omega}) \cos \omega t - \operatorname{Im}(r_{\Omega+\omega}) \sin \omega t] \right\} + \text{cc} \quad (\text{C.16})$$

$$\equiv \frac{E_0}{\sqrt{2}} e^{i\omega_0 t} \psi + \text{cc}, \quad (\text{C.17})$$

where  $\psi$  refers to the terms in curly brackets. Then the detected optical power is

$$P_{\text{refl}} = E_{\text{refl}}^2 \quad (\text{C.18a})$$

$$= \frac{E_0^2}{2} \left[ e^{i\omega_0 t} \psi + e^{-i\omega_0 t} \psi^* \right]^2 \quad (\text{C.18b})$$

$$= \frac{P_0}{2} \times 2\psi^* \psi + (\text{terms at } 2\omega_0) \quad (\text{C.18c})$$

$$= P_0 \psi^* \psi. \quad (\text{C.18d})$$

The PDH error signal is made by demodulating the reflected power  $P_{\text{refl}}$  at the rf frequency  $\Omega/2\pi$ . If we are interested at the error signal response at audio frequency  $\omega/2\pi$ , then when computing  $P_{\text{refl}}$  we therefore need only to consider terms that oscillate at  $\pm\Omega \pm \omega$ . Then

$$\begin{aligned} P_{\text{refl}} = 2P_0\Gamma\gamma\cos(\Omega t)\{ &[-r_0\text{Re}(r_{\Omega+\omega}) + r_\Omega\text{Re}(r_\omega)]\cos\omega t \\ &+ [r_0\text{Im}(r_{\Omega+\omega}) - r_\Omega\text{Im}(r_\omega)]\sin\omega t \} + (\text{other terms}). \end{aligned} \quad (\text{C.19a})$$

Demodulating at  $\Omega/2\pi$  and low-pass filtering yields the following phase-to-power transfer function:

$$\frac{\langle P_{\text{refl}} \rangle_\Omega}{\gamma} = P_0\Gamma(-r_0r_{\Omega+\omega}^* + r_\Omega r_\omega^*). \quad (\text{C.20})$$

We can recast this as a frequency-to-power transfer function by recalling the Laplace-domain relation  $2\pi v(s) = \dot{v}(s) = s\gamma(s)$ . Additionally, in the more general case that  $\Gamma$  is not much smaller than 1, we can replace  $\Gamma$  by  $2J_0(\Gamma)J_1(\Gamma)$ . Therefore, the PDH reflection transfer function is

$$\mathcal{D}(f) = \frac{P(f)}{v(f)} = 2P_0J_0(\Gamma)J_1(\Gamma) \frac{-r(0)r(f_{\text{FSR}}/2+f)^* + r(f_{\text{FSR}}/2)r(f)^*}{if}. \quad (\text{C.21})$$

To calculate the expected dc gain  $|\mathcal{D}(0)|$ , we apply L'Hôpital's rule to the fraction in equation C.21. We can write  $r(f) \approx (\partial r/\partial f)|_0 f$ . The derivative is

$$\left. \frac{\partial r}{\partial f} \right|_0 = 2\pi \left. \frac{\partial r}{\partial \Phi} \frac{\partial \Phi}{\partial \omega} \right|_0 = 2\pi \underbrace{\frac{t_a^2 r_b}{(1 - r_a r_b)^2}}_{\equiv r'_0} \times \left( i \frac{2L}{c} \right) = \frac{2\pi i r'_0}{f_{\text{FSR}}}, \quad (\text{C.22})$$

where  $\Phi = 2\omega L/c$  is the round-trip phase of the cavity, and hence  $r'_0 = \partial r/\partial \Phi|_0$  is the derivative of the reflectivity with respect to the phase. Therefore,

$$\mathcal{D}(0) = -2P_0J_0(\Gamma)J_1(\Gamma) \frac{2\pi r_\Omega r'_0}{f_{\text{FSR}}}. \quad (\text{C.23})$$

We now want to derive the frequency dependence of  $\mathcal{D}(f)$  for  $f \ll f_{\text{FSR}}$ . In this limit, we have  $r(f_{\text{FSR}}/2+f) \approx r(f_{\text{FSR}}/2)$ , so the numerator in equation C.21 becomes approximately

$$r(f_{\text{FSR}}/2)[-r(0) + r(f)^*], \quad (\text{C.24})$$

which has 0 as its lowest-order zero and  $f_p$  as its lowest-order pole. This means that equation C.21 behaves as a single-pole filter with dc gain  $|\mathcal{D}(0)|$  and pole  $f_p$ :

$$\mathcal{D}(f) \approx \frac{\mathcal{D}(0)}{1 + if/f_p}. \quad (\text{C.25})$$

In the limit of critical coupling ( $r_a = r_b \equiv r$ ) and high finesse ( $1 - r^2 \ll 1$ ), we have  $r'_0 = r/(1 - r^2) = \mathcal{F}/\pi = f_{\text{FSR}}/2\pi f_p$  and  $r_\Omega \approx 1$ , so

$$\mathcal{D}^{(\text{CC})}(0) = -2P_0 J_0(\Gamma) J_1(\Gamma)/f_p. \quad (\text{C.26})$$

On the other hand, in the case of strong overcoupling ( $r_b = 1$ ), one finds  $r'_0 = 2\mathcal{F}/\pi$ , and hence

$$\mathcal{D}^{(\text{OC})}(0) = -4P_0 J_0(\Gamma) J_1(\Gamma)/f_p. \quad (\text{C.27})$$

### C.3 Michelson locking

Here we examine rf Michelson locking. Again the input light is phase modulated with an index  $\Gamma$  at an rf frequency  $\Omega$ . The field incident on the Michelson's symmetric port is

$$E_{\text{in}}(t) = \sqrt{2}E_0 \cos[\omega_0 t + \Gamma \cos \Omega t] \quad (\text{C.28a})$$

$$\simeq \frac{E_0}{\sqrt{2}} e^{i\omega_0 t} \left[ 1 + \frac{i\Gamma}{2} e^{i\Omega t} + \frac{i\Gamma}{2} e^{-i\Omega t} \right] + \text{cc}. \quad (\text{C.28b})$$

Upon transmission through the Michelson, the field at the antisymmetric port is

$$E_{\text{as}}(t) = \frac{iE_0}{\sqrt{2}} e^{i\omega_0 t} \left\{ e^{i\omega_0 \ell_+/c} \sin\left(\frac{\omega_0 \ell_-}{c}\right) + \frac{i\Gamma}{2} e^{i(\omega_0 + \Omega)\ell_+/c} \sin\left(\frac{(\omega_0 + \Omega)\ell_-}{c}\right) e^{i\Omega t} \right. \\ \left. + \frac{i\Gamma}{2} e^{i(\omega_0 - \Omega)\ell_+/c} \sin\left(\frac{(\omega_0 - \Omega)\ell_-}{c}\right) e^{-i\Omega t} \right\} + \text{cc}. \quad (\text{C.29})$$

We assume that the interferometer is operated close to a dark fringe; that is, the microscopic phase offset  $\delta\phi_- = \omega_0 \delta \ell_- / c \simeq \sin(\omega_0 \ell_- / c)$  is small. However, the macroscopic phase offset (Schnupp asymmetry) is large, so that we have non-negligible sideband transmission to the antisymmetric port.

We want to keep all terms only to linear order in  $\delta\phi_-$ . The carrier term itself is linear in  $\delta\phi_-$ , so we will keep only the dc sideband terms. To that end, we note that (to zeroth order in  $\delta\phi_-$ ) we have

$$\sin\left(\frac{(\omega_0 \pm \Omega)\ell_-}{c}\right) = \sin\left(\frac{\omega_0 \ell_-}{c}\right) \cos\left(\frac{\Omega \ell_-}{c}\right) \pm \cos\left(\frac{\omega_0 \ell_-}{c}\right) \sin\left(\frac{\Omega \ell_-}{c}\right) \quad (\text{C.30a})$$

$$\simeq \sin\left(\frac{\Omega \ell_-}{c}\right) \quad (\text{C.30b})$$

$$\equiv \Phi_-, \quad (\text{C.30c})$$

so

$$E_{\text{as}}(t) \simeq \frac{iE_0}{\sqrt{2}} e^{i\omega_0 t} e^{i\omega_0 \ell_+/c} \left[ \delta\phi_- + \frac{i\Gamma}{2} \Phi_- e^{i\Omega \ell_+/c} e^{i\Omega t} - \frac{i\Gamma}{2} \Phi_- e^{-i\Omega \ell_+/c} e^{-i\Omega t} \right] + \text{cc} \quad (\text{C.31a})$$

$$= -\sqrt{2} E_0 \sin(\omega_0 t + \omega_0 \ell_+/c) [\delta\phi_- - \Gamma \Phi_- \sin(\Omega t + \Omega \ell_+/c)]. \quad (\text{C.31b})$$

The power sensed by the photodiode is

$$P_{\text{as}} = \langle E_{\text{as}}^2 \rangle_{\omega_0} \quad (\text{C.32a})$$

$$= P_0 [\delta\phi_- - \Gamma \Phi_- \sin \Omega t]^2 \quad (\text{C.32b})$$

$$= P_0 [\delta\phi_-^2 - 2\Gamma \Phi_- \delta\phi_- \sin \Omega t + \Gamma^2 \Phi_-^2 \sin^2 \Omega t] \quad (\text{C.32c})$$

with  $P_0 = E_0^2$ . Therefore, demodulating at  $\Omega/2\pi$  yields

$$\langle P_{\text{as}} \rangle_\Omega = P_0 \Gamma \sin(\Omega \ell_-/c) \delta\phi_-. \quad (\text{C.33})$$

## D Some algebra for the differential arm length plant

This section records some algebra for transforming the optomechanical plant for detuned resonant sideband extraction from the Buonanno and Chen formalism to a version that is more friendly to hands-on control room measurements and calibration (chapter 5).

We start with the transfer function extracted by Ward from the Buonanno/Chen input/output relations:

$$\frac{\delta P}{\delta h} \propto \frac{t_s e^{i\beta} [(1 - r_s e^{2i\beta}) \cos \phi \cos \zeta - (1 + r_s e^{2i\beta}) \sin \phi \sin \zeta]}{1 + r_s^2 e^{4i\beta} - 2r_s e^{2i\beta} [\cos 2\phi + (\mathcal{K}/2) \sin 2\phi]} \sqrt{\frac{2P_{bs}\omega_0^2}{\omega_a^2 + \omega^2}} \quad (\text{D.1})$$

with  $\beta = -\arctan \omega/\omega_a \equiv \arctan(-x)$  and

$$\mathcal{K} = \frac{8P_{bs}}{ML^2} \frac{\omega_0}{\omega^2(\omega_a^2 + \omega^2)} = \frac{8P_{bs}}{ML^2} \frac{\omega_0}{\omega_a^2 \omega^2} \frac{1}{(1 + ix)(1 - ix)}. \quad (\text{D.2})$$

Note

$$e^{i\beta} = \sqrt{\frac{1 - ix}{1 + ix}}. \quad (\text{D.3})$$

The prefactor in equation D.1 can be rewritten as

$$t_s \sqrt{\frac{1 - ix}{1 + ix}} \sqrt{\frac{2P_{bs}\omega_0^2}{\omega_a^2(1 + ix)(1 - ix)}} = \frac{t_s \sqrt{2P_{bs}} \omega_0 / \omega_a}{1 + ix}. \quad (\text{D.4})$$

The numerator in equation D.1 can be rewritten as

$$\left(1 - r_s \frac{1 - ix}{1 + ix}\right) \cos \phi \cos \zeta - \left(1 + r_s \frac{1 - ix}{1 + ix}\right) \sin \phi \sin \zeta \quad (\text{D.5a})$$

$$= \cos(\phi + \zeta) - r_s \frac{1 - ix}{1 + ix} \cos(\phi - \zeta) \quad (\text{D.5b})$$

$$= \frac{1}{1 + ix} [(1 + ix) \cos(\phi + \zeta) - r_s (1 - ix) \cos(\phi - \zeta)] \quad (\text{D.5c})$$

$$= \frac{\cos(\phi + \zeta) - r_s \cos(\phi - \zeta)}{1 + ix} \left[ 1 + ix \times \frac{\cos(\phi + \zeta) + r_s \cos(\phi - \zeta)}{\cos(\phi + \zeta) - r_s \cos(\phi - \zeta)} \right]. \quad (\text{D.5d})$$

The denominator can be rewritten as

$$1 + r_s^2 \left( \frac{1 - ix}{1 + ix} \right)^2 - 2r_s \frac{1 - ix}{1 + ix} \left[ \cos 2\phi + \frac{\alpha}{x^2(1 - ix)(1 + ix)} \sin 2\phi \right] \quad (\text{D.6a})$$

$$= \frac{1}{(1 + ix)^2} \left[ (1 + ix)^2 + r_s^2 (1 - ix)^2 - 2r_s (1 - ix)(1 + ix) \cos 2\phi - 2r_s \frac{\alpha}{x^2} \sin 2\phi \right] \quad (\text{D.6b})$$

$$= \frac{1}{(1 + ix)^2} \left\{ \left[ (1 + ix) - r_s e^{2i\phi} (1 - ix) \right] \left[ (1 + ix) - r_s e^{-2i\phi} (1 - ix) \right] - ir_s \left( e^{2i\phi} - e^{-2i\phi} \right) \frac{\alpha}{x^2} \right\} \quad (\text{D.6c})$$

$$= \frac{1}{(1 + ix)^2} \left\{ [(1 - p) + (1 + p)ix] [(1 - p^*) + (1 + p^*)ix] - i(p - p^*) \frac{\alpha}{x^2} \right\} \quad (\text{D.6d})$$

$$= \frac{1}{(1 + ix)^2} \left\{ (1 - p)(1 - p^*) \left[ 1 + ix \times \frac{1 + p}{1 - p} \right] \left[ 1 + ix \times \frac{1 + p^*}{1 - p^*} \right] - i(p - p^*) \frac{\alpha}{x^2} \right\} \quad (\text{D.6e})$$

$$= \frac{(1 - p)(1 - p^*)}{(1 + ix)^2} \left\{ \left[ 1 + ix \times \frac{1 + p}{1 - p} \right] \left[ 1 + ix \times \frac{1 + p^*}{1 - p^*} \right] - \frac{i(p - p^*)}{(1 - p)(1 - p^*)} \frac{\alpha}{x^2} \right\}, \quad (\text{D.6f})$$

where  $p = r_s e^{2i\phi}$  and  $\alpha = 4P_{\text{bs}}\omega_0/(\omega_a^4 M L^2)$ .

Therefore, an equivalent representation of equation D.1 is

$$\begin{aligned} \frac{\delta P}{\delta h} &\propto \frac{t_s \sqrt{2P_{\text{bs}}} \omega_0}{\omega_a} \times \frac{\cos(\phi + \zeta) - r_s \cos(\phi - \zeta)}{1 - 2r_s \cos 2\phi + r_s^2} \\ &\times \left\{ \frac{1 + \frac{if}{f_a} \times \frac{\cos(\phi + \zeta) + r_s \cos(\phi - \zeta)}{\cos(\phi + \zeta) - r_s \cos(\phi - \zeta)}}{\left[ 1 + \frac{if}{f_a} \times \frac{1 + r_s e^{2i\phi}}{1 - r_s e^{2i\phi}} \right] \left[ 1 + \frac{if}{f_a} \times \frac{1 + r_s e^{-2i\phi}}{1 - r_s e^{-2i\phi}} \right] - \frac{2\alpha r_s \sin 2\phi}{1 - 2r_s \cos 2\phi + r_s^2} \frac{f_a^2}{f^2}} \right\}. \end{aligned} \quad (\text{D.7})$$

We can tidy this up by defining the complex RSE pole

$$p = f_a \times \frac{1 - r_s e^{2i\phi}}{1 + r_s e^{2i\phi}}, \quad (\text{D.8})$$

the square of the spring frequency

$$\xi^2 = f_a^2 \times \frac{2\alpha r_s \sin 2\phi}{1 - 2r_s \cos 2\phi + r_s^2}, \quad (\text{D.9})$$

which may be positive or negative, and the (real) RSE zero

$$z = f_a \times \frac{\cos(\phi + \zeta) - r_s \cos(\phi - \zeta)}{\cos(\phi + \zeta) + r_s \cos(\phi - \zeta)} \quad (\text{D.10})$$

so that equation D.7 becomes

$$\frac{\delta P}{\delta h} \propto \frac{t_s \sqrt{2P_{bs}} \omega_0}{\omega_a} \times \frac{\cos(\phi + \zeta) - r_s \cos(\phi - \zeta)}{1 - 2r_s \cos 2\phi + r_s^2} \times \left[ \frac{1 + if/z}{(1 + if/p)(1 + if/p^*) - \xi^2/f^2} \right]. \quad (\text{D.11})$$

## E In-situ test mass ringdown measurement

Here we present an in-situ estimate of the coating and substrate thermal noise of an Advanced LIGO test mass, determined from the ringdown times of several of the test mass body modes.

The loss angle  $\phi = 1/Q$  of a particular test mass mode is related to the loss angle of the substrate and of the coating by

$$\phi = \frac{U_s\phi_s + U_c\phi_c}{U_s + U_c}, \quad (\text{E.1})$$

where  $U_s$  is the portion of the mode's strain energy stored in the substrate, and  $U_c$  is the portion in the coating. Because the volume of the coating is much smaller than the volume of the substrate, it is almost always the case that  $U_s \gg U_c$ , and in this situation we can say to very good approximation

$$\phi = \phi_s + \frac{U_c}{U_s}\phi_c. \quad (\text{E.2})$$

If we know the loss angles and energy configurations of several modes, we can estimate the underlying loss angles  $\phi_s$  and  $\phi_c$ .

Three modes were measured: a butterfly mode, the lowest-order drumhead mode, and the next-lowest-order drumhead mode (with a horizontal nodal line). Each mode was excited electrostatically using the high-frequency actuation path normally used to damp parametric instabilities;<sup>168</sup> the ringdown was observed in the differential arm length readout. The  $Q$  factor of each mode was determined with least-squares fitting and the uncertainty was determined by examining the  $\chi^2$  of the fit. The energy configurations were determined by finite element analysis: a simple Comsol model of a cylindrical piece of fused silica (with dimensions matching the test mass) was used to extract the bulk energy  $U_s$  of the optic (in joules)

	$f$ (Hz)	$Q$	$\frac{\partial U_c/\partial z}{U_s}$ (m <sup>-1</sup> )
Butterfly	6054	$2.53(26) \times 10^7$	13.3
Drumhead 1	8158	$2.13(45) \times 10^7$	13.9
Drumhead 2	9830	$4.69(59) \times 10^7$	3.3

Table E.1: Data for determining the test mass coating and substrate loss from measured end Y optic ringdowns. The frequencies and  $Q$  factors are measured, and the energy ratios are determined via finite-element analysis.

and the surface energy  $\partial U_c/\partial z$  of the optic face (in joules per meter). The energy in the coating is then  $U_c = (\partial U_c/\partial z)d$ , where  $d = 6.2\mu\text{m}$  is the thickness of the end test mass coating. The measured frequencies, modeled energy configurations, and measured  $Q$  factors are given in table E.1.

To estimate  $\phi_s$  and  $\phi_c$ , we now turn to Bayesian analysis. As usual, our goal is to compute a posterior probability on  $\phi_s$  and  $\phi_c$  given our measurements  $\{\phi_i\}$ :

$$p(\phi_s, \phi_c | \{\phi_i\}) = \frac{p(\{\phi_i\} | \phi_s, \phi_c) p(\phi_s, \phi_c)}{Z}. \quad (\text{E.3})$$

Since in principle either  $\phi_c$  or  $\phi_s$  could range over several orders of magnitude, we choose the log-uniform prior

$$p(\phi_s, \phi_c) = \frac{1}{\phi_s \phi_c}. \quad (\text{E.4})$$

Our log-likelihood function is

$$\ln \mathcal{L} \propto \ln p(\{\phi_i\} | \phi_s, \phi_c) \propto - \sum_i \frac{(\phi_i - \hat{\phi}_i)^2}{2\sigma_i^2}, \quad (\text{E.5})$$

where  $\phi_i$  is the measured loss angle of mode  $i$ ,  $\sigma_i$  is the uncertainty of the measurement, and

$$\hat{\phi}_i = \phi_s + \frac{\partial U_c/\partial z}{U_s} d \phi_c. \quad (\text{E.6})$$

Here we are assuming that both the coating and the substrate losses are structural. Our overall log-probability function for the Monte–Carlo simulation is then proportional to  $\ln \mathcal{L} + \ln p(\phi_s, \phi_c)$ . The simulation yields the joint posterior shown in figure E.1. The 1D marginalizations of the posterior yield the following median values (with  $1\sigma$  uncertainties):

$$\phi_s = 1.56(39) \times 10^{-8} \quad \text{and} \quad \phi_c = 2.8(8) \times 10^{-4}. \quad (\text{E.7})$$

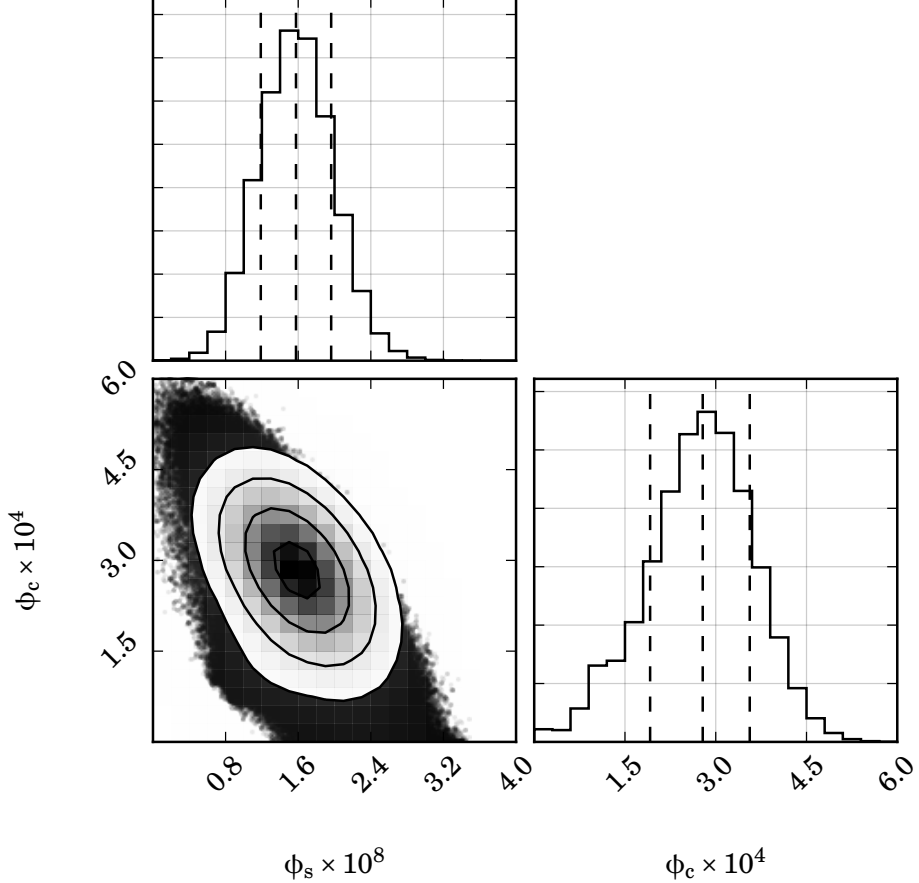


Figure E.1: Posterior pdf of Advanced LIGO test mass loss angles  $\phi_s$  and  $\phi_c$ , as determined from end Y ringdown data. Dashed lines in the 1D (marginalized) posteriors show 16th, 50th, and 84th percentiles of the posterior. The solid contours in the 2D (joint) posterior show  $0.5\sigma$ ,  $1\sigma$ , and  $1.5\sigma$  contours.

With our knowledge of  $\phi_s$  and  $\phi_c$ , we can estimate the expected coating thermal noise level in Advanced LIGO. Implicit in our finite-element analysis is the assumption that the coating has the same material properties as the substrate. This is not correct (nor is it correct to speak of a single “loss angle” common to both bulk and shear strain),<sup>89</sup> but nonetheless it is consistent with the theoretical analysis of Nakagawa et al.,<sup>169</sup> who computed the Brownian noise of a test mass coated with a single lossy layer whose material properties match those of the substrate. In terms of displacement noise, their result is

$$S_{xx}(f) = \frac{k_B T(1-\sigma^2)}{\pi^{3/2} f w E} \left[ \phi_s + \frac{2}{\pi^{1/2}} \frac{(1-2\sigma)}{(1-\sigma)} \frac{d}{w} \phi_c \right]. \quad (\text{E.8})$$

With  $E = 72 \text{ GPa}$ ,  $\sigma = 0.17$ ,  $w = 62 \text{ mm}$ , and  $T = 300 \text{ K}$ , and with the loss angles

inferred in this appendix, this yields

$$S_{xx}(f)^{1/2} = [8.1(8) \times 10^{-21} \text{ m/Hz}^{1/2}] \times \left( \frac{100 \text{ Hz}}{f} \right)^{1/2} \quad (\text{E.9})$$

for the end Y test mass. This is somewhat higher than—but consistent with—direct audio-band measurements by Gras et al.<sup>90</sup> on end test mass coating witness samples, where the reported value is  $S_{xx}(f)^{1/2} = [7.1(3) \times 10^{-21} \text{ m/Hz}^{1/2}] \times (100 \text{ Hz}/f)^{1/2}$ .

# Bibliography

1. J. D. E. Creighton and W. G. Anderson. *Gravitational-Wave Physics and Astronomy*. Wiley-VCH, 2011 (cit. on pp. 1, 4).
2. A. Zee. *Einstein Gravity in a Nutshell*. Princeton University Press, 2013 (cit. on p. 1).
3. M. Bartelmann. **The dark universe**. *Rev. Mod. Phys.* 82(1) (2010), pp. 331–382 (cit. on p. 2).
4. F. Acernese, M. Alshourbagy, P. Amico, F. Antonucci, S. Aoudia, P. Astone, S. Avino, D. Babusci, L. Baggio, G. Ballardin, et al. **First joint gravitational wave search by the AURIGA–EXPLORER–NAUTILUS–Virgo collaboration**. *Classical and Quantum Gravity* 25(20) (2008), p. 205007 (cit. on pp. 4, 5).
5. S. Sato, S. Kawamura, M. Ando, T. Nakamura, K. Tsubono, A. Araya, I. Funaki, K. Ioka, N. Kanda, S. Moriwaki, et al. **DECIGO: the Japanese space gravitational wave antenna**. *Journal of Physics: Conference Series* 154(1) (2009), p. 012040 (cit. on p. 5).
6. A. Sesana, W. J. Weber, C. J. Killow, M. Perreur-Lloyd, D. I. Robertson, H. Ward, E. D. Fitzsimons, J. Bryant, A. M. Cruise, G. Dixon, et al. **Space-based detectors**. *General Relativity and Gravitation* 46(12) (2014), pp. 1–13. ISSN: 1572-9532 (cit. on pp. 5, 118).
7. F. J. Dyson. **Seismic response of the earth to a gravitational wave in the 1-Hz band**. *Ap. J.* 156 (1969), p. 529 (cit. on p. 4).
8. M. Coughlin and J. Harms. **Upper limit on a stochastic background of gravitational waves from seismic measurements in the range 0.05–1 Hz**. *Phys. Rev. Lett.* 112(10) (2014), p. 101102 (cit. on p. 4).
9. M. Coughlin and J. Harms. **Constraining the gravitational-wave energy density of the universe in the range 0.1 Hz to 1 Hz using the apollo seismic array**. *Phys. Rev. D* 90(10) (2014), p. 102001 (cit. on p. 4).
10. P. R. Saulson. **If light waves are stretched by gravitational waves, how can we use light as a ruler to detect gravitational waves?** *American Journal of Physics* 65(6) (1997), pp. 501–505 (cit. on p. 6).

11. R. van Haasteren. *Gravitational Wave Detection & Data Analysis for Pulsar Timing Arrays*. PhD thesis. University of Leiden, 2011 (cit. on p. 7).
12. P. D. Lasky, C. M. F. Mingarelli, T. L. Smith, J. T. Giblin, E. Thrane, D. J. Reardon, R. Caldwell, M. Bailes, N. D. R. Bhat, S. Burke-Spolaor, et al. *Gravitational-wave cosmology across 29 decades in frequency*. *Phys. Rev. X* 6(1) (2016), p. 011035 (cit. on p. 7).
13. M. Kamionkowski and E. D. Kovetz. *The quest for B modes from inflationary gravitational waves*. *Annual Review of Astronomy and Astrophysics* 54(1) (2016), pp. 227–269 (cit. on p. 7).
14. A. Staley, D. Martynov, R. Abbott, R. X. Adhikari, K. Arai, S. Ballmer, L. Barsotti, A. F. Brooks, R. T. DeRosa, S. Dwyer, et al. *Achieving resonance in the advanced LIGO gravitational-wave interferometer*. *Classical and Quantum Gravity* 31(24) (2014), p. 245010 (cit. on p. 8).
15. A. N. Staley. *Locking the Advanced LIGO Gravitational Wave Detector: with a focus on the Arm Length Stabilization Technique*. PhD thesis. Columbia University, 2015 (cit. on p. 8).
16. D. V. Martynov. *Lock Acquisition and Sensitivity Analysis of Advanced LIGO Interferometers*. PhD thesis. California Institute of Technology, 2015 (cit. on pp. 8, 50, 51, 55).
17. D. Sigg. *Frequency Response of the LIGO Interferometer*. Tech. rep. LIGO-T970084-v1. LIGO Caltech, 1997 (cit. on p. 8).
18. K. Izumi and D. Sigg. Advanced LIGO: length sensing and control in a dual recycled interferometric gravitational wave antenna. *In prep.* (2016) (cit. on pp. 8, 13, 15, 23, 27, 34, 37, 72, 137).
19. K. Izumi and D. Sigg. *Frequency response of the aLIGO interferometer: part 1*. Tech. rep. LIGO-T1500325-v3. LIGO Caltech, 2016 (cit. on p. 8).
20. K. Izumi, D. Sigg, and K. Kawabe. *Frequency response of the aLIGO interferometer: part 2*. Tech. rep. LIGO-T1500461-v3. LIGO Caltech, 2016 (cit. on pp. 8, 72).
21. K. Izumi, D. Sigg, and K. Kawabe. *Frequency response of the aLIGO interferometer: part 3*. Tech. rep. LIGO-T1500559-v3. LIGO Caltech, 2016 (cit. on pp. 8, 72, 120, 121, 123).
22. J. C. Mather, E. S. Cheng, D. A. Cottingham, R. E. Eplee Jr., D. J. Fixsen, T. Hewagama, R. B. Isaacman, K. A. Jensen, S. S. Meyer, P. D. Noerdlinger, et al. *Measurement of the cosmic microwave background spectrum by the COBE FIRAS instrument*. *Ap. J.* 420 (1994), pp. 439–44 (cit. on p. 10).
23. P. K. Fritschel. *Techniques for Laser Interferometer Gravitational Wave Detectors*. PhD thesis. Massachusetts Institute of Technology, 1992 (cit. on p. 10).

24. T. M. Niebauer, R. Schilling, K. Danzmann, A. Rüdiger, and W. Winkler. Nonstationary shot noise and its effect on the sensitivity of interferometers. *Phys. Rev. A* 43(9) (1991), pp. 5022–5029 (cit. on p. 11).
25. T. T. Fricke. *Homodyne detection for laser-interferometric gravitational wave detectors*. PhD thesis. Louisiana State University, 2011 (cit. on p. 11).
26. N. D. Smith. *Techniques for Improving the Readout Sensitivity of Gravitational Wave Antennae*. PhD thesis. Massachusetts Institute of Technology, 2012 (cit. on pp. 12, 48).
27. R. Abbott, R. Adhikari, S. Ballmer, L. Barsotti, M. Evans, P. Fritschel, V. Frolov, G. Mueller, B. Slagmolen, and S. Waldman. *Advanced LIGO Length Sensing and Control Final Design*. Tech. rep. LIGO-T1000298-v2. LIGO, 2010 (cit. on pp. 14, 15, 36, 37).
28. P. Fritschel, R. Adhikari, S. Ballmer, and M. Evans. *Arm Cavity Finesse for Advanced LIGO*. Tech. rep. LIGO-T070303-v1. LIGO, 2007 (cit. on p. 14).
29. A. Staley, D. Hoak, A. Effler, K. Izumi, S. Dwyer, K. Kawabe, E. J. King, M. Rakhmanov, R. L. Savage, and D. Sigg. High precision optical cavity length and width measurements using double modulation. *Opt. Express* 23(15) (2015), pp. 19417–19431 (cit. on p. 18).
30. K. Arai. Tech. rep. LIGO-T1000276-v5. LIGO Caltech, 2013 (cit. on p. 18).
31. E. Hall. *LHO Logbook Entry #18988*. 2015 (cit. on p. 18).
32. T. Chalermongsak, F. Seifert, E. D. Hall, K. Arai, E. K. Gustafson, and R. X. Adhikari. Broadband measurement of coating thermal noise in rigid Fabry–Pérot cavities. *Metrologia* 52(1) (2015), p. 17 (cit. on pp. 19, 21, 69).
33. J. Aasi et al. Advanced LIGO. *Class. Quantum Grav.* 32(7) (2015), p. 074001 (cit. on p. 19).
34. P. Fritschel and E. Gustafson. *Advanced LIGO Optical Layout*. Tech. rep. LIGO-D0902838. LIGO, 2008 (cit. on p. 19).
35. R. Adhikari, S. Ballmer, and P. Fritschel. *Interferometer Sensing and Control Design Requirements*. Tech. rep. LIGO-T070236. LIGO, 2008 (cit. on pp. 19, 32, 34, 53, 124).
36. P. Kwee, C. Bogan, K. Danzmann, M. Frede, H. Kim, P. King, J. Pöld, O. Puncken, R. L. Savage, F. Seifert, et al. Stabilized high-power laser system for the gravitational wave detector Advanced LIGO. *Opt. Express* 20(10) (2012), pp. 10617–10634 (cit. on pp. 19, 21, 53, 68).
37. M. Rakhmanov, R. Savage, D. Reitze, and D. Tanner. Dynamic resonance of light in Fabry–Perot cavities. *Physics Letters A* 305(5) (2002), pp. 239–244 (cit. on pp. 20, 30, 137).

38. E. A. Donley, T. P. Heavner, F. Levi, M. O. Tataw, and S. R. Jefferts. *Double-pass acousto-optic modulator system*. *Review of Scientific Instruments* 76 (6), 063112 (2005) (cit. on p. 22).
39. N. Robertson and J. Kissel. *ETM/ITM Quad Suspension Actuator Control Ranges*. Tech. rep. LIGO-T1100595. LIGO, 2011 (cit. on p. 25).
40. F. Matichard, B. Lantz, R. Mittleman, K. Mason, J. Kissel, B. Abbott, S. Biscans, J. McIver, R. Abbott, S. Abbott, et al. Seismic isolation of advanced LIGO: review of strategy, instrumentation and performance. *Class. Quantum Grav.* 32 (18) (2015), p. 185003 (cit. on pp. 25, 49, 66).
41. A. Buonanno and Y. Chen. Quantum noise in second generation, signal-recycled laser interferometric gravitational-wave detectors. *Phys. Rev. D* 64 (4) (2001), p. 042006 (cit. on pp. 27, 55, 89).
42. T. T. Fricke, N. D. Smith-Lefebvre, R. Abbott, R. Adhikari, K. L. Dooley, M. Evans, P. Fritschel, V. V. Frolov, K. Kawabe, J. S. Kissel, et al. DC readout experiment in Enhanced LIGO. *Class. Quantum Grav.* 29 (6) (2012), p. 065005 (cit. on p. 27).
43. D. V. Martynov, E. D. Hall, B. P. Abbott, R. Abbott, T. D. Abbott, C. Adams, R. X. Adhikari, R. A. Anderson, S. B. Anderson, K. Arai, et al. Sensitivity of the Advanced LIGO detectors at the beginning of gravitational wave astronomy. *Phys. Rev. D* 93 (11) (2016), p. 112004. (Cit. on pp. 30, 55, 86).
44. E. Hall. *LHO Logbook Entry #27675*. 2016 (cit. on p. 30).
45. E. Hall. *LHO Logbook Entry #21489*. 2015 (cit. on p. 30).
46. J. Kissel. *LHO Logbook Entry #22117*. 2015 (cit. on p. 30).
47. P. Fritschel. *LHO Logbook Entry #22513*. 2015 (cit. on pp. 30, 32).
48. J. Kissel. *Calibration Measurement / DARM Loop Time Delay Diagrams*. Tech. rep. LIGO-G1601472. LIGO, 2016 (cit. on p. 30).
49. R. Abbott. *Split ISC Whitening Filter Interface Board*. Tech. rep. LIGO-D1300520. LIGO, 2013 (cit. on p. 29).
50. R. Abbott. *In-vacuum DCPD for OMC*. Tech. rep. LIGO-D060572. LIGO, 2006 (cit. on p. 29).
51. The LIGO Scientific Collaboration. Calibration of the Advanced LIGO detectors for the discovery of the binary black-hole merger GW150914. *ArXiv e-prints* (2016) (cit. on pp. 31, 87).
52. S. Dwyer. *LHO Logbook Entry #25053*. 2016 (cit. on p. 32).
53. G. Vajente. *Simulation of SRCL coupling to DARM and DARM pole frequency*. Tech. rep. LIGO-G1500641-v2. LIGO, 2015 (cit. on p. 38).

54. B. Swinkels, E. Campagna, G. Vajente, L. Barsotti, and M. Evans. *Longitudinal noise subtraction: the alpha-, beta- and gamma-technique*. Tech. rep. VIR-050A-08. Virgo, 2008 (cit. on p. 39).
55. E. Morrison, B. J. Meers, D. I. Robertson, and H. Ward. *Automatic alignment of optical interferometers*. *Appl. Opt.* 33(22) (1994), pp. 5041–5049 (cit. on p. 41).
56. N. Mavalvala. *Alignment issues in laser interferometric gravitational-wave detectors*. PhD thesis. Massachusetts Institute of Technology, 1997 (cit. on p. 41).
57. J. A. Sidles and D. Sigg. *Optical torques in suspended Fabry–Perot interferometers*. *Physics Letters A* 354(3) (2006), pp. 167–172. ISSN: 0375-9601 (cit. on p. 42).
58. L. Barsotti, M. Evans, and P. Fritschel. *Alignment sensing and control in Advanced LIGO*. *Classical and Quantum Gravity* 27(8) (2010), p. 084026 (cit. on pp. 42, 44, 49).
59. S. J. Waldman. *The Advanced LIGO ETM transmission monitor*. Tech. rep. LIGO-T0900385-v7. LIGO, 2009 (cit. on p. 45).
60. D. Hoak. *Gravitational Wave Astrophysics: Instrumentation, Detector Characterization, and a Search for Gravitational Signals from Gamma-ray Bursts*. PhD thesis. University of Massachusetts Amherst, 2015 (cit. on p. 48).
61. K. Arai, D. Hoak, and N. Smith-Lefebvre. *Matrix calculations for the angular control of H1 OMC*. Tech. rep. LIGO-T1400585. LIGO, 2014 (cit. on p. 48).
62. S. Kawamura and M. E. Zucker. *Mirror-orientation noise in a Fabry–Perot interferometer gravitational wave detector*. *Appl. Opt.* 33(18) (1994), pp. 3912–3918 (cit. on p. 49).
63. M. Barton. *Dissipation Dilution*. Tech. rep. LIGO-T070101. LIGO, 2007 (cit. on p. 51).
64. H. Radkins. *LHO Logbook Entry #14876*. 2014 (cit. on p. 52).
65. K. Kawabe. *LHO Logbook Entry #19649*. 2015 (cit. on p. 52).
66. E. Hall. *LHO Logbook Entry #26758*. 2016 (cit. on p. 53).
67. E. Hall. *LHO Logbook Entry #26773*. 2016 (cit. on p. 53).
68. J. Driggers, S. Dwyer, S. Ballmer, and K. Izumi. *Modeling the instability at LHO*. Tech. rep. LIGO-G1600864. LIGO, 2016 (cit. on p. 54).
69. K. Kawabe. *LHO Logbook Entry #27898*. 2016 (cit. on p. 54).
70. K. Izumi. *LHO Logbook Entry #27940*. 2016 (cit. on p. 54).
71. R. Adhikari. *Sensitivity and noise analysis of 4 km laser interferometric gravitational wave antennae*. PhD thesis. Massachusetts Institute of Technology, 2004 (cit. on p. 55).

72. S. W. Ballmer. *LIGO interferometer operating at design sensitivity with application to gravitational radiometry*. PhD thesis. Massachusetts Institute of Technology, 2006 (cit. on p. 55).
73. C. M. Caves. Quantum-mechanical radiation-pressure fluctuations in an interferometer. *Phys. Rev. Lett.* 45(2) (1980), pp. 75–79 (cit. on p. 55).
74. H. Miao. *Exploring Macroscopic Quantum Mechanics in Optomechanical Devices*. PhD thesis. University of Western Australia, 2012 (cit. on p. 55).
75. H. B. Callen and T. A. Welton. Irreversibility and generalized noise. *Physical Review* 83(1) (1951), p. 34 (cit. on p. 57).
76. M. Aspelmeyer, T. J. Kippenberg, and F. Marquardt. Cavity optomechanics. *Rev. Mod. Phys.* 86(4) (2014), pp. 1391–1452 (cit. on p. 58).
77. P. R. Saulson. Thermal noise in mechanical experiments. *Phys. Rev. D* 42(8) (1990), pp. 2437–2445 (cit. on pp. 58, 65).
78. R. Nawrodt, S. Rowan, J. Hough, M. Punturo, F. Ricci, and J.-Y. Vinet. Challenges in thermal noise for 3rd generation of gravitational wave detectors. *General Relativity and Gravitation* 43(2) (2011), pp. 593–622. ISSN: 1572-9532 (cit. on p. 58).
79. V. Braginsky, M. Gorodetsky, and S. Vyatchanin. Thermodynamical fluctuations and photo-thermal shot noise in gravitational wave antennae. *Physics Letters A* 264(1) (1999), pp. 1–10. ISSN: 0375-9601 (cit. on pp. 59, 62, 63).
80. J. B. Johnson. Thermal agitation of electricity in conductors. *Phys. Rev.* 32(1) (1928), pp. 97–109 (cit. on p. 59).
81. H. Nyquist. Thermal agitation of electric charge in conductors. *Phys. Rev.* 32(1) (1928), pp. 110–113 (cit. on p. 59).
82. A. V. Cumming, A. S. Bell, L. Barsotti, M. A. Barton, G. Cagnoli, D. Cook, L. Cunningham, M. Evans, G. D. Hammond, G. M. Harry, et al. Design and development of the Advanced LIGO monolithic fused silica suspension. *Class. Quantum Grav.* 29(3) (2012), p. 035003 (cit. on pp. 60, 61).
83. Y. Levin. Internal thermal noise in the LIGO test masses: a direct approach. *Phys. Rev. D* 57(2) (1998), pp. 659–663 (cit. on p. 61).
84. F. Bondu, P. Hello, and J.-Y. Vinet. Thermal noise in mirrors of interferometric gravitational wave antennas. *Physics Letters A* 246(3) (1998), pp. 227–236. ISSN: 0375-9601 (cit. on p. 61).
85. Y. T. Liu and K. S. Thorne. Thermoelastic noise and homogeneous thermal noise in finite sized gravitational-wave test masses. *Phys. Rev. D* 62(12) (2000), p. 122002 (cit. on pp. 61, 62).
86. *Gravitational Wave Interferometer Noise Calculator*. URL: <https://awiki.ligo-wa.caltech.edu/aLIGO/GWINC> (cit. on pp. 61, 82).

87. M. Cerdonio, L. Conti, A. Heidmann, and M. Pinard. Thermoelastic effects at low temperatures and quantum limits in displacement measurements. *Phys. Rev. D* 63(8) (2001), p. 082003 (cit. on pp. 62, 63).
88. K. Somiya, K. Kokeyama, and R. Nawrodt. Remarks on thermoelastic effects at low temperatures and quantum limits in displacement measurements. *Phys. Rev. D* 82(12) (2010), p. 127101 (cit. on p. 62).
89. T. Hong, H. Yang, E. K. Gustafson, R. X. Adhikari, and Y. Chen. Brownian thermal noise in multilayer coated mirrors. *Phys. Rev. D* 87(8) (2013), p. 082001 (cit. on pp. 62, 148).
90. S. Gras, H. Yu, W. Yam, D. Martynov, and M. Evans. Audio-band coating thermal noise measurement for Advanced LIGO with a multimode optical resonator. *Phys. Rev. D* 95(2) (2017), p. 022001 (cit. on pp. 62, 149).
91. Y. Levin. Fluctuation–dissipation theorem for thermo-refractive noise. *Physics Letters A* 372(12) (2008), pp. 1941–4. ISSN: 0375-9601 (cit. on p. 62).
92. M. Evans, S. Ballmer, M. Fejer, P. Fritschel, G. Harry, and G. Ogin. Thermo-optic noise in coated mirrors for high-precision optical measurements. *Phys. Rev. D* 78(10) (2008), p. 102003 (cit. on pp. 62, 63).
93. M. J. Martin. *Quantum Metrology and Many-Body Physics: Pushing the Frontier of the Optical Lattice Clock*. PhD thesis. 2013 (cit. on p. 62).
94. T. Chalermsongsak, E. D. Hall, G. D. Cole, D. Follman, F. Seifert, K. Arai, E. K. Gustafson, J. R. Smith, M. Aspelmeyer, and R. X. Adhikari. Coherent cancellation of photothermal noise in GaAs/Al<sub>0.92</sub>Ga<sub>0.08</sub> as Bragg mirrors. *Metrologia* 53(2) (2016), p. 860 (cit. on p. 63).
95. A. Farsi, M. S. de Cumis, F. Marino, and F. Marin. Photothermal and thermo-refractive effects in high reflectivity mirrors at room and cryogenic temperature. *Journal of Applied Physics* 111(4) (2012), p. 043101 (cit. on pp. 63, 64).
96. C. Torrie. LHO Logbook Entry #27493. 2016 (cit. on p. 65).
97. R. Adhikari. LHO Logbook Entry #27488. 2016 (cit. on p. 65).
98. R. Derosa. LLO Logbook Entry #26735. 2016 (cit. on p. 65).
99. P. Fritschel. LHO Logbook Entry #27510. 2016 (cit. on p. 65).
100. E. J. Daw, J. A. Giaime, D. Lormand, M. Lubinski, and J. Zweizig. Long-term study of the seismic environment at LIGO. *Classical and Quantum Gravity* 21(9) (2004), pp. 2255–2273. ISSN: 1361-6382 (cit. on p. 65).
101. R. X. Adhikari. Gravitational radiation detection with laser interferometry. *Rev. Mod. Phys.* 86(1) (2014), pp. 121–151 (cit. on pp. 65, 66).
102. J. Harms. Terrestrial gravity fluctuations. *Living Reviews in Relativity* 18(3) (2015) (cit. on p. 66).

103. J. C. Driggers. *Noise Cancellation for Gravitational Wave Detectors*. PhD thesis. California Institute of Technology, 2015 (cit. on p. 66).
104. M. Zucker. *The LIGO Vacuum Equipment and Beam Tubes: Retrospective and Prospective*. Tech. rep. LIGO-G1300176. LIGO, 2013 (cit. on p. 66).
105. M. E. Zucker and S. E. Whitcomb. Measurement of optical path fluctuations due to residual gas in the LIGO 40 meter interferometer. *Proceedings of the Seventh Marcel Grossman Meeting on recent developments in theoretical and experimental general relativity, gravitation, and relativistic field theories* (1994) (cit. on p. 66).
106. R. Dolesi, M. Hueller, D. Nicolodi, D. Tombolato, S. Vitale, P. J. Wass, W. J. Weber, M. Evans, P. Fritschel, R. Weiss, et al. Brownian force noise from molecular collisions and the sensitivity of advanced gravitational wave observatories. *Phys. Rev. D* 84(6) (2011), p. 063007 (cit. on p. 67).
107. R. Weiss. *Gas Damping of the Final Stage in the Advanced LIGO Suspensions*. Tech. rep. LIGO-T0900509. LIGO, 2009 (cit. on p. 67).
108. M. Evans, P. Fritschel, and R. Weiss. *Gas Damping Monte Carlo*. Tech. rep. LIGO-T0900582. LIGO, 2009 (cit. on p. 67).
109. P. Fritschel, T. J. Kane, and A. Jeffries. Frequency fluctuations of a diode-pumped Nd:YAG ring laser. *Opt. Lett.* 14(18) (1989), pp. 993–995 (cit. on p. 68).
110. T. Chalermongsak. *High fidelity probe and mitigation of mirror thermal fluctuations*. PhD thesis. California Institute of Technology, 2014 (cit. on p. 69).
111. D. Sigg. *Frequency Difference Divider*. Tech. rep. LIGO-T0900138. LIGO, 2009 (cit. on p. 69).
112. I. Angert and D. Sigg. *Characterization of a Voltage Controlled Oscillator*. Tech. rep. LIGO-T0900451. LIGO, 2009 (cit. on p. 69).
113. D. Hoak. *LHO Logbook Entry #16656*. 2015 (cit. on p. 74).
114. P. Fritschel. *DAC Noise Update II (General Standards 18 bit)*. Tech. rep. LIGO-G1401399. LIGO, 2014 (cit. on p. 75).
115. M. Evans and J. Miller. *Summary of ESD Force Coefficient Simulations*. Tech. rep. LIGO-T1000119-v1. LIGO, 2010 (cit. on p. 76).
116. H. Grote. *LLO Logbook Entry #14541*. 2014 (cit. on p. 77).
117. N. Smith. *LLO Logbook Entry #14566*. 2014 (cit. on p. 77).
118. B. P. Abbott, R. Abbott, T. D. Abbott, M. R. Abernathy, F. Acernese, K. Ackley, C. Adams, T. Adams, P. Addesso, R. X. Adhikari, et al. Observation of gravitational waves from a binary black hole merger. *Phys. Rev. Lett.* 116(6) (2016) (cit. on pp. 84, 85).

119. B. P. Abbott, R. Abbott, T. D. Abbott, M. R. Abernathy, F. Acernese, K. Ackley, C. Adams, T. Adams, P. Addesso, R. X. Adhikari, et al. **GW151226: observation of gravitational waves from a 22-solar-mass binary black hole coalescence.** *Phys. Rev. Lett.* 116(24) (2016) (cit. on pp. 84, 85).
120. B. P. Abbott, R. Abbott, T. D. Abbott, M. R. Abernathy, F. Acernese, K. Ackley, C. Adams, T. Adams, P. Addesso, R. X. Adhikari, et al. **Astrophysical implications of the binary black hole merger GW150914.** *The Astrophysical Journal* 818(2) (2016), p. L22. ISSN: 2041-8213 (cit. on p. 84).
121. R. Schofield. **LHO Logbook Entry #22497.** 2015 (cit. on p. 86).
122. B. P. Abbott, R. Abbott, T. D. Abbott, M. R. Abernathy, F. Acernese, K. Ackley, C. Adams, T. Adams, P. Addesso, R. X. Adhikari, et al. **Binary black hole mergers in the first Advanced LIGO observing run.** *Phys. Rev. X* 6(4) (2016), p. 041015 (cit. on pp. 84, 85).
123. B. P. Abbott, R. Abbott, T. D. Abbott, M. R. Abernathy, F. Acernese, K. Ackley, C. Adams, T. Adams, P. Addesso, R. X. Adhikari, et al. **Observing gravitational-wave transient GW150914 with minimal assumptions.** *Phys. Rev. D* 93(12) (2016), p. 122004 (cit. on p. 84).
124. B. P. Abbott, R. Abbott, T. D. Abbott, M. R. Abernathy, F. Acernese, K. Ackley, C. Adams, T. Adams, P. Addesso, R. X. Adhikari, et al. **GW150914: first results from the search for binary black hole coalescence with advanced LIGO.** *Phys. Rev. D* 93(12) (2016), p. 122003 (cit. on p. 84).
125. B. P. Abbott, R. Abbott, T. D. Abbott, M. R. Abernathy, F. Acernese, K. Ackley, C. Adams, T. Adams, P. Addesso, R. X. Adhikari, et al. **Properties of the binary black hole merger gw150914.** *Phys. Rev. Lett.* 116(24) (2016), p. 241102 (cit. on p. 84).
126. B. P. Abbott, R. Abbott, T. D. Abbott, M. R. Abernathy, F. Acernese, K. Ackley, C. Adams, T. Adams, P. Addesso, R. X. Adhikari, et al. **Tests of general relativity with GW150914.** *Phys. Rev. Lett.* 116(22) (2016), p. 221101 (cit. on pp. 84, 97, 98).
127. B. P. Abbott et al. **The rate of binary black hole mergers inferred from Advanced LIGO observations surrounding GW150914.** *Ap. J. L.* 833(1) (2016), p. L1 (cit. on p. 84).
128. B. P. Abbott et al. **Supplement: “The rate of binary black hole mergers inferred from Advanced LIGO observations surrounding GW150914”** (2016, ApJL, 833, L1). *Ap. J. S.* 227(2) (2016), p. 14 (cit. on p. 84).
129. S. Karki et al. **The Advanced LIGO photon calibrators.** *In prep.* (2016) (cit. on p. 89).
130. R. L. Ward. ***Length Sensing and Control of a Prototype Advanced Interferometric Gravitational Wave Detector.*** PhD thesis. California Institute of Technology, 2010 (cit. on p. 90).

131. U. von Toussaint. Bayesian inference in physics. *Rev. Mod. Phys.* 83(3) (2011), pp. 943–999 (cit. on p. 93).
132. C. Röver, R. Meyer, and N. Christensen. Bayesian inference on compact binary inspiral gravitational radiation signals in interferometric data. *Classical and Quantum Gravity* 23(15) (2006), p. 4895 (cit. on pp. 95, 96).
133. N. Cornish, L. Sampson, N. Yunes, and F. Pretorius. Gravitational wave tests of general relativity with the parameterized post-einsteinian framework. *Phys. Rev. D* 84(6) (2011), p. 062003 (cit. on p. 97).
134. C. M. Will. Bounding the mass of the graviton using gravitational-wave observations of inspiralling compact binaries. *Phys. Rev. D* 57(4) (1998), pp. 2061–2068 (cit. on pp. 97, 98).
135. L. Price. *Optimal Experimental Design: Introduction and Application to System Identification*. Tech. rep. LIGO-G1400084-v1. LIGO Caltech, 2014 (cit. on pp. 100, 102).
136. D. Wittman. *Fisher Matrix for Beginners*. URL: <http://wittman.physics.ucdavis.edu/Fisher-matrix-guide.pdf> (cit. on p. 100).
137. A. Albrecht, G. Bernstein, R. Cahn, W. L. Freedman, J. Hewitt, W. Hu, J. Huth, M. Kamionkowski, E. W. Kolb, L. Knox, et al. Report of the Dark Energy Task Force. *ArXiv Astrophysics e-prints* (2006) (cit. on p. 100).
138. B. Efron and D. V. Hinkley. Assessing the accuracy of the maximum likelihood estimator: observed versus expected fisher information. *Biometrika* 65(3) (1978), pp. 457–483 (cit. on p. 101).
139. E. D. Hall, V. V. Frolov, T. Callister, H. Müller, M. Pospelov, and R. X. Adhikari. Laser interferometers as dark matter detectors. *ArXiv e-prints* (2016). (Cit. on p. 111).
140. S. Bird, I. Cholis, J. B. Muñoz, Y. Ali-Haïmoud, M. Kamionkowski, E. D. Kovetz, A. Raccanelli, and A. G. Riess. Did LIGO detect dark matter? *Phys. Rev. Lett.* 116(20) (2016), p. 201301 (cit. on p. 111).
141. M. Sasaki, T. Suyama, T. Tanaka, and S. Yokoyama. Primordial black hole scenario for the gravitational-wave event gw150914. *Phys. Rev. Lett.* 117(6) (2016), p. 061101 (cit. on p. 111).
142. D. A. Brown. *Searching for Gravitational Radiation from Binary Black Hole MACHOs in the Galactic Halo*. PhD thesis. University of Wisconsin–Milwaukee, 2004 (cit. on p. 111).
143. C. Hanna. *Searching for Gravitational Waves from Binary Systems in Non-Stationary Data*. PhD thesis. Louisiana State University, 2006 (cit. on p. 111).
144. Y. V. Stadnik and V. V. Flambaum. Searching for dark matter and variation of fundamental constants with laser and maser interferometry. *Phys. Rev. Lett.* 114(16) (2015), p. 161301 (cit. on p. 111).

145. N. Seto and A. Cooray. **Search for small-mass black-hole dark matter with space-based gravitational wave detectors.** *Phys. Rev. D* 70(6) (2004), p. 063512 (cit. on pp. 112, 113).
146. V. S. Berezinsky, V. I. Dokuchaev, and Y. N. Eroshenko. **Small-scale clumps of dark matter.** *Physics-Uspekhi* 57(1) (2014), p. 1 (cit. on p. 112).
147. S. Schlamminger, K.-Y. Choi, T. A. Wagner, J. H. Gundlach, and E. G. Adelberger. **Test of the equivalence principle using a rotating torsion balance.** *Phys. Rev. Lett.* 100(4) (2008), p. 041101 (cit. on p. 112).
148. S. Ballmer, S. Márka, and P. Shawhan. **Feasibility of measuring the Shapiro time delay over meter-scale distances.** *Classical and Quantum Gravity* 27(18) (2010), p. 185018 (cit. on p. 118).
149. B. Chauvineau, S. Pireaux, and T. Regimbau. **Shapiro delay of asteroids on LISA.** *Classical and Quantum Gravity* 24(11) (2007), p. 3005 (cit. on p. 118).
150. I. I. Shapiro. **Fourth test of general relativity.** *Phys. Rev. Lett.* 13(26) (1964), pp. 789–791 (cit. on p. 118).
151. M. Punturo, H. Lück, and M. Beker. **A Third Generation Gravitational Wave Observatory: The Einstein Telescope.** *Advanced Interferometers and the Search for Gravitational Waves: Lectures from the First VESF School on Advanced Detectors for Gravitational Waves.* Ed. by M. Bassan. Springer International Publishing, 2014, pp. 333–362. ISBN: 978-3-319-03792-9 (cit. on p. 118).
152. J. Miller, L. Barsotti, S. Vitale, P. Fritschel, M. Evans, and D. Sigg. **Prospects for doubling the range of Advanced LIGO.** *Phys. Rev. D* 91(6) (2015), p. 062005 (cit. on p. 119).
153. K. Kokeyama, K. Izumi, W. Z. Korth, N. Smith-Lefebvre, K. Arai, and R. X. Adhikari. **Residual amplitude modulation in interferometric gravitational wave detectors.** *J. Opt. Soc. Am. A* 31(1) (2014), pp. 81–88 (cit. on p. 119).
154. W. Zhang, M. J. Martin, C. Benko, J. L. Hall, J. Ye, C. Hagemann, T. Legero, U. Sterr, F. Riehle, G. D. Cole, et al. **Reduction of residual amplitude modulation to  $1 \times 10^{-6}$  for frequency modulation and laser stabilization.** *Opt. Lett.* 39(7) (2014), pp. 1980–1983 (cit. on p. 119).
155. J. L. Hall, W. Zhang, and J. Ye. **Accurate Removal of RAM from FM Laser Beams.** *Frequency Control Symposium & the European Frequency and Time Forum.* IEEE, 2015 (cit. on p. 119).
156. B. P. Abbott, R. Abbott, T. D. Abbott, M. R. Abernathy, K. Ackley, C. Adams, P. Addesso, R. X. Adhikari, V. B. Adya, C. Affeldt, et al. **Exploring the sensitivity of next generation gravitational wave detectors.** *ArXiv e-prints* (2016) (cit. on p. 122).
157. P. Ajith, M. Hannam, S. Husa, Y. Chen, B. Brügmann, N. Dorband, D. Müller, F. Ohme, D. Pollney, C. Reisswig, et al. **Inspiral-merger-ringdown waveforms for black-hole binaries with nonprecessing spins.** *Phys. Rev. Lett.* 106(24) (2011), p. 241101 (cit. on p. 124).

158. J. Bechhoefer. *Feedback for physicists: a tutorial essay on control*. *Rev. Mod. Phys.* 77(3) (2005), pp. 783–836 (cit. on p. 125).
159. J. R. Smith. *Formulation of Instrument Noise Analysis Techniques and Their Use in the Commissioning of the Gravitational Wave Observatory, GEO 600*. PhD thesis. Leibniz Universität Hannover, 2006 (cit. on pp. 125, 127).
160. J. Bendat and A. Piersol. *Random Data: Analysis and Measurement Procedures*. 4th. Wiley, 2011. ISBN: 9781118210826 (cit. on pp. 127, 132).
161. D. Sigg and P. Fritschel. *Diagnostics Test Tool (DTT) Software Manual*. Tech. rep. LIGO-T990013. LIGO, 1999 (cit. on p. 128).
162. S. Gonugondla, D. Martynov, J. Harms, and R. Adhikari. *Notes on median spectra*. Tech. rep. LIGO-T1300859. LIGO/Caltech, 2013 (cit. on p. 131).
163. B. Abbott et al. *First all-sky upper limits from LIGO on the strength of periodic gravitational waves using the Hough transform*. *Phys. Rev. D* 72(10) (2005), p. 102004 (cit. on pp. 131–133).
164. B. Allen, W. G. Anderson, P. R. Brady, D. A. Brown, and J. D. E. Creighton. *FINDCHIRP: an algorithm for detection of gravitational waves from inspiraling compact binaries*. *Phys. Rev. D* 85(12) (2012), p. 122006 (cit. on pp. 131–133).
165. D. Hoak. *Comparison of Detector Sensitivity to Rayleigh-distributed Noise for S6 Epochs*. <https://wiki.ligo.org/DetChar/S6RayleighDistributions>. 2013 (cit. on p. 131).
166. G. Heinzel, A. Rüdiger, and R. Schilling. *Spectrum and spectral density estimation by the Discrete Fourier transform (DFT), including a comprehensive list of window functions and some new flat-top windows*. Tech. rep. LIGO-T1400010. Max-Planck-Institut für Gravitationsphysik, 2002 (cit. on p. 131).
167. R. W. P. Drever, J. L. Hall, F. V. Kowalski, J. Hough, G. M. Ford, A. J. Munley, and H. Ward. *Laser phase and frequency stabilization using an optical resonator*. *Applied Physics B* 31(2) (1983), pp. 97–105. ISSN: 1432-0649 (cit. on p. 139).
168. C. Blair, S. Gras, R. Abbott, S. Aston, J. Betzwieser, D. Blair, R. DeRosa, M. Evans, V. Frolov, P. Fritschel, et al. *First demonstration of electrostatic damping of parametric instability at Advanced LIGO*. *ArXiv e-prints* (2016) (cit. on p. 146).
169. N. Nakagawa, A. M. Gretarsson, E. K. Gustafson, and M. M. Fejer. *Thermal noise in half-infinite mirrors with nonuniform loss: a slab of excess loss in a half-infinite mirror*. *Phys. Rev. D* 65(10) (2002), p. 102001 (cit. on p. 148).